

Self-Healing of Open-Circuit Faults in Organic Thin-Film Transistor-Based Flexible Electronics

Li Ding
Queens' College

Nanoscience Centre
Department of Engineering
University of Cambridge

This dissertation is submitted for the degree of
Doctor of Philosophy
September 2021

Declaration

I hereby declare that his dissertation is my own work and contains nothing which is the outcome of work done in collaboration with others, except as specified in the text and Acknowledgements.

I further state that except where specific reference is made to the work of others, the contents of this dissertation are original and no substantial part of my dissertation has already been submitted, or, is being concurrently submitted for any such degree, diploma or other qualification at the University of Cambridge or any other University or similar institution.

In accordance with the University of Cambridge regulations, this dissertation contains less than 65,000 words, including appendices, bibliography, footnotes, tables and equations and has fewer than 150 figures.

Li Ding

Department of Engineering

University of Cambridge

Self-Healing of Open-Circuit Faults in Organic Thin-Film Transistor-Based Flexible Electronics

Li Ding

Abstract

Flexible electronics has attracted tremendous attention due to the fast-growing market for portable devices and sensors. However, these devices usually suffer from internal and external forces, which can lead to the failure of interconnects in the circuit. To address this issue, some passive and active strategies have been developed for improving the reliability of interconnects in circuits. Although all these strategies are effective in tackling problems related to the mechanical stress, they have inherent limit in dealing with other failure causes or repairing the open fault. Therefore, in this dissertation, a particle-based self-healing (PBSH) technique has been developed.

The detailed study starts with an overall review of the state of the art in techniques developed for improving the reliability of interconnects in flexible circuits. Then the mechanisms of the PBSH technique are analysed and the chemical treatment of metal particles are explored. The physical modelling of the healing is established, and relations between the healing time with the suspension concentration, electric field, length of open gap, and external resistance are verified by experimental results. In addition, to avoid the inherent conductivity of the suspension and the aggregation of micro-particles, they are modified by the oleic acid. This chemical treatment of metal particles improves the uniformity of the suspension and sets a threshold electric field for the occurrence of self-healing.

As a key component in flexible circuits, an organic thin-film transistor (OTFT) fabricated by all inkjet-printing process has been developed and characterised in this study. This transistor uses 6,13-bis(triisopropylsilylethynyl)-pentacene (TIPS-Pentacene) as the semiconductor, poly (vinyl cinnamate) (PVC) as the dielectric, silver as the electrodes, and CYTOP as the encapsulation. Based on this device, two basic

circuits: the current mirror and the common-source (CS) amplifier have been successfully built on flexible substrates. The proper functioning of the printed devices and circuits becomes the base for the study of the self-healing in flexible circuits.

Subsequently, the PBSH in OTFT device and circuit interconnects is verified. This technique can successfully repair open faults at both source and drain sides in OTFT device interconnects. Simultaneously, it can heal open faults occurring at different locations in flexible current mirror and common-source amplifier circuits biased at the static state. Moreover, the self-healing is also proved to be effective and stable in common-source amplifier when processing alternating current (AC) signals.

In order to demonstrate the feasibility of the PBSH technique in real-world applications, more performance characterisations have been conducted. The bending test shows the reliability and stability of the healing in the bent condition. And the dual-faults test verifies the ability of the PBSH technique for healing more than one open fault in interconnects. In addition, methods of packaging the circuit and confining the healing material in the expected region are also developed, which prove the feasibility and manufacturability of the PBSH technique in integrated circuits. This study sets a new benchmark for improving the reliability of inkjet-printed flexible circuits.

Acknowledgements

First and foremost, I would like to express my sincere gratitude to my academic supervisor, Dr. Sanjiv Sambandan, for his patient and organised research supervision in my doctoral project. He treated me not only as his student, but also as a good friend. As a supervisor, he provided precise guidance, good research environment and sufficient experiment facilities for my project. As a colleague and friend, he gave me advice and help on extending academic network and planning my future career. Without his help, I could hardly finish my doctoral study and complete this dissertation.

I would like to thank Prof. Arokia Nathan, who recognised my academic ability and helped me step into this dream campus. His generous help is a ticket, with which I can start this Ph.D. journey.

I would also like to acknowledge my advisor, Dr. Colm Durkan. I would never forget the day of the formal meeting for my first year report. To attend the meeting on time, he changed the schedule of his business trip and travelled for hours back to Cambridge. When he entered the room at the very last minute before the meeting, I felt really lucky and proud for having such a nice advisor.

Furthermore, I want to thank my colleague Dr. Pushkaraj Joshi. During his post-doctoral year in Cambridge, we collaborated a lot. I remember our meaningful discussions and every exciting moment when we got the good experiment results. Pushkaraj is a nice colleague and working with him is quite happy.

In addition, I would like to say thanks to all friends and colleagues in CAPE and Nanoscience. Dr. Chen Jiang: thank you for your support all the time, your useful suggestions smooth my Ph.D. road. Dr. Hyung Woo Choi: you are like my elder brother in Cambridge. You always ask me if I need any help and generously offer your help. I was really touched by your selfless support. Dr. Zhuocong Xiao, Dr. Dongyang Chen, Dr. Duo Zhang, Xiao Liu, Dr. Qifang Wan, Dr. Canlin Ou, Dr. Hanbin Ma, Dr. Xiang Cheng, Dr. Guangyu Yao, Dr. Yang Su, and Dr. Constantinos Tsangarides: thank you all for your concern and assistance in the past four years.

I am also grateful for the support from my friends outside of Cambridge. Prof. Xiaojun Guo: you are always my advisor, both in academic and in career life. Dr. Linrun Feng and Dr. Wei Tang: I will always remember how you guided me into the research world and told me to be an honest researcher seeking the truth of the science. Dr.

Qiaofeng Li and Dr. Yukun Huang: you always have enough patience to listen to my questions and provide remote assistance or suggestions. I want to express my gratitude to the China Scholarship Council (CSC), who provides the scholarship to support my doctoral project.

I also want to thank my home in Cambridge – Queens’ College. I would like to say thank you to all staffs and friends in Queens’. Dr. Laurence Tiley and Dr. Andrew Marsham: thank you for being my tutor and help me solve various questions and problems. Shijia Pan, Qinyi Xu, Shruti Dhaundiyal, Hongjia Zhu: you are my closest friends in Cambridge and thank you for your companionship for these years. Finally, my deepest gratitude goes to my loved family. Your endless love is always my firmest support in this wonderful Ph.D. journey.

CONTENTS

LIST OF FIGURES	X
LIST OF TABLES	XV
LIST OF PUBLICATIONS	XVI
LIST OF SYMBOLS	XVII
LIST OF ABBREVIATIONS	XX
1 INTRODUCTION	1
1.1 LARGE AREA FLEXIBLE ELECTRONICS	1
1.2 INTERCONNECTS IN FLEXIBLE ELECTRONICS	3
1.2.1 METAL FOILS	4
1.2.2 WIRE BONDING	4
1.3 RELIABILITY OF INTERCONNECTS IN FLEXIBLE ELECTRONICS	5
1.3.1 MECHANICAL STRESS	6
1.3.2 ELECTRO-MIGRATION (EM).....	7
1.3.3 CHEMICAL CORROSION.....	8
1.3.4 THERMAL STRESS.....	10
1.4 IMPROVING THE RELIABILITY OF INTERCONNECTS	10
1.5 OBJECTIVES	11
1.6 DISSERTATION OUTLINE	12
2 TECHNIQUES FOR IMPROVING THE RELIABILITY OF INTERCONNECTS	14
2.1 PASSIVE TECHNIQUES	14
2.1.1 HELICAL COILS AND MEANDER DESIGN.....	14
2.1.2 GEOMETRIC PATTERNING OF SUBSTRATES	17
2.1.3 NOVEL MATERIALS	19
2.2 ACTIVE TECHNIQUES	21
2.2.1 LIQUID METALS.....	21
2.2.2 CONDUCTIVE INK IN MICROCAPSULES.....	23
2.3 THEORETICAL MODELS OF THE PBSH TECHNIQUE	24

2.4 ADVANTAGES AND LIMITATIONS OF THE PBSH TECHNIQUE.....	29
2.5 CHEMICAL COATING OF METAL PARTICLES	31
2.5.1 PREPARATION OF THE SUSPENSION.....	32
2.5.2 MECHANISM OF MODIFICATION	32
2.6 SUMMARY.....	38
3 INKJET-PRINTED ORGANIC THIN-FILM TRANSISTORS	39
3.1 CARRIER TRANSPORT IN ORGANIC SEMICONDUCTOR MATERIALS.....	39
3.1.1 HOPPING MODEL.....	40
3.1.2 MULTIPLE TRAPPING AND RELEASE MODEL	41
3.2 OTFT STRUCTURES.....	42
3.3 OTFT MATERIALS	43
3.3.1 SUBSTRATE.....	43
3.3.2 ELECTRODES	45
3.3.3 ORGANIC SEMICONDUCTOR (OSC)	47
3.3.4 DIELECTRICS	51
3.3.5 ENCAPSULATION.....	53
3.4 INKJET PRINTING PROCESS	54
3.5 EXPERIMENT	55
3.5.1 PREPARATION OF INKS.....	55
3.5.2 DEVICE FABRICATION.....	56
3.5.3 DEVICE CHARACTERISATION.....	57
3.6 PROPERTIES OF OTFTS.....	58
3.6.1 FILM THICKNESS	58
3.6.2 ELECTRICAL PROPERTIES	60
3.7 SUMMARY.....	63
4 SELF-HEALING OF INKJET PRINTED INTERCONNECTS.....	65
4.1 SELF-HEALING OF OPEN-FAULT IN THE WIRE	65
4.1.1 EXPERIMENTAL SET-UP	65
4.1.2 SELF-HEALING IN THE OPEN GAP	66
4.2 DEPENDENCE OF HEALING TIME ON SUSPENSION CONCENTRATIONS	68
4.3 DEPENDENCE OF HEALING TIME ON ELECTRIC FIELD.....	71
4.4 DEPENDENCE OF HEALING TIME ON OPEN GAP	72
4.5 DEPENDENCE OF HEALING TIME ON EXTERNAL RESISTANCE	73

4.6 STABILITY OF THE HEALING.....	74
4.7 SUMMARY.....	76
5 SELF-HEALING IN OTFT INTERCONNECTS	77
5.1 EXPERIMENTAL SET-UP	77
5.2 SELF-HEALING OF THE FAULT LOCATED AT THE SOURCE SIDE	78
5.3 SELF-HEALING OF THE FAULT LOCATED AT THE DRAIN SIDE	81
5.4 SUMMARY.....	85
6 SELF-HEALING IN OTFT-BASED CIRCUITS.....	86
6.1 SELF-HEALING IN THE CURRENT MIRROR.....	86
6.1.1 CIRCUIT AND CHARACTERISTICS	87
6.1.2 SELF-HEALING IN THE CURRENT MIRROR CIRCUIT	88
6.2 SELF-HEALING IN THE COMMON-SOURCE AMPLIFIER (DC)	93
6.2.1 CIRCUIT AND CHARACTERISTICS	93
6.2.2 SELF-HEALING IN THE COMMON-SOURCE AMPLIFIER CIRCUIT (DC).....	97
6.3 SELF-HEALING IN THE COMMON-SOURCE AMPLIFIER (AC)	100
6.4 SUMMARY.....	103
7 PERFORMANCE CHARACTERISATIONS OF THE PBSH TECHNIQUE.....	104
7.1 BENDING	104
7.2 DOUBLE FAULTS.....	105
7.3 PACKAGING	107
7.4 NOISE	111
7.5 SUMMARY.....	115
8 CONCLUSIONS AND FUTURE WORK.....	116
APPENDIX.....	121
REFERENCES.....	126

LIST OF FIGURES

- 1.1 Asia Pacific flexible electronics market size, 2013 – 2024.
- 1.2 (a) Flexible OLED display with OTFT backplane by SonyTM, (b) SamsungTM Galaxy Fold; (c) Illustration and photo of a thin large-area active-matrix sensor with 12×12 tactile pixels, (d) Schematic of the artificial mechanoreceptor system composed of a pressure-sensitive tactile element and an organic ring oscillator.
- 1.3 Micrograph of the Ag wire on PEN substrate.
- 1.4 (a) Two forces act on metal ions when applying an electrical field in a conductive material. (b) Void and Hillock failures in wires due to EM.
- 2.1 Two stretchable and twistable sensor systems using helical wires: (a) The fabric artificial skin, and (b) The tactile sensing array.
- 2.2 Simulated von Mises stress in (a) straight and (b) helical Nylon wires while being stretched to extend by 1%.
- 2.3 Simulated von Mises stress in (a) straight and (b) horseshoe-shaped wires while being stretched to extend by 1%.
- 2.4 (a) Scheme for the preparation of conductive composites. (b) Bending (c) Compressing (d) Stretching tests of conductive composites. (e) Stretching test of the LED array using PU-CuAg-PDMS conductive composites.
- 2.5 (a) SEM image of the dense AgNW network structure and (b) The hierarchical multiscale AgNW/CNT hybrid nanocomposite (c) Conductivities of PEDOT:PSS films treated with different chemicals (d) Twisting reliability of the gravure-printed PEDOT:PSS electrode.
- 2.6 (a) The mechanism of the self-healing using LM–elastomer composite. (b)

- A four-channel serial clock display connected by the LM–elastomer composite (c) The disconnection and reconnection of a LED circuit using a self-healing wire.
- 2.7 (a) SEM image and (b) optical micrograph of microcapsules containing SWNTs (0.05 wt%) suspended in PhCl (c) reaction equation of the formation of the TTF/TCNQ charge-transfer salt.
- 2.8 Illustration of the PBSH occurred at an open gap.
- 2.9 Simulated heat distribution in the particle-based bridge.
- 2.10 SEM image of the sintered particle-particle binding.
- 2.11 (a)Molecular structure of the oleic acid. (b) Formation of the covalent bond between the central atom (Ag^+) and ligand ($-\text{COO}^-$).
- 2.12 FTIR spectra of oleic acid-treated Cu and Ag particles and the oleic acid-olamine mixture.
- 2.13 FESEM images of (a) untreated and (b) oleic acid treated Ag particles suspended in hexane and drop-casted on silicon wafer.
- 2.14 (a) Photographs illustrating the settling behavior of untreated and oleic acid treated Ag particles suspended in silicone oil with varying concentrations observed on day 0, 3, and 7. (b) UV-Visible absorbance of the freshly prepared and 35-day settled untreated and oleic acid treated Ag particles.
- 3.1 sp^2 hybridisation of two carbon atoms, sp^2 orbitals are connected by σ -bond in one plane, while pz orbitals (perpendicular to sp^2) plane are connected by π -bond.
- 3.2 Temperature dependence of the electron drift mobility μ_0 (Inset) Model of the electronic-state distribution in an amorphous solid.
- 3.3 Illustration of the OTFT device structures.
- 3.4 Molecular structures of four plastic substrates.
- 3.5 The AFM topographic images of the surface of: (a) PEN film, (b) Corning™ glass.
- 3.6 The contact angles of the DI water droplets on the surface of: (a) PEN film, (b) Corning™ glass.
- 3.7 Molecular structures of two SAMs materials.

- 3.8 Molecular structures of typical OSCs.
- 3.9 Molecular structures of typical organic dielectric materials for OTFTs.
- 3.10 The cross-linking process of PVC under UV exposure.
- 3.11 Photographs of (a) Dimatix DMP-2831 inkjet printer, (b) Dimatix DMPLCP-11610 cartridge.
- 3.12 (a) Schematic image of an OTFT with the BGBC structure, (b) Photograph of a flexible sample and microscopic image of a single OTFT.
- 3.13 Thickness of the printed films.
- 3.14 (a) Measured transfer characteristics of 46 OTFTs, (b) Typical output characteristics of one OTFT.
- 3.15 Histograms of 46 inkjet-printed OTFTs over the 4 cm × 4 cm size flexible substrate.

- 4.1 Schematic of the experimental set-up for measuring the self-healing in printed interconnects.
- 4.2 Self-healing of inkjet-printed interconnects on flexible substrates.
- 4.3 (a)-(e) Optical micro-photos showing the formation of the conductive bridge (f) SEM image of the healed particle-based conductive bridge.
- 4.4 (a) Typical dynamics of current for suspension concentrations of 10, 20, and 40 mg/mL (b) The dependence of the healing time on suspension concentrations.
- 4.5 (a) Typical dynamics of current for the self-healing occurred under electric fields of 1.0, 1.1, 1.2, and 1.3 V/μm (b) The dependence of the healing time on electric field strengths.
- 4.6 (a) Distribution of the healing time against the external resistance in different open gaps (b) Analysis of the dipole-dipole attraction force in Ag particles.
- 4.7 Dynamics of the healing current for different external resistances for (a) 80 and (b) 28 μm open gaps.
- 4.8 (a) The stability of the healing when the external voltage is sequentially lowered (b) The histogram of resistances for steady-state healed bridges.

- 5.1 (a) Schematic and microscopic image of an OTFT printed on flexible

- substrate. (b) Layout and patterns of various layers in printed OTFT.
- 5.2 Schematic of the circuit for simulating the healing of the open fault at the source side of an OTFT.
 - 5.3 The (a) transfer and (b) output characteristics of the OTFT before and after the healing of the open fault at source side.
 - 5.4 Dynamics of the source-drain current (I_{ds}) in the OTFT during self-healing of the open fault at the source side when applying (a) various drain voltages (V_d) and (b) various gate voltages (V_g).
 - 5.5 Schematic of the circuit for simulating the healing of the open fault at the drain side of an OTFT.
 - 5.6 The (a) transfer and (b) output characteristics of the OTFT before and after the healing of the open fault at drain side.
 - 5.7 Dynamics of the source-drain current (I_{ds}) in the OTFT during self-healing of the open fault at the drain side when applying (a) various drain voltages (V_d) and (b) various gate voltages (V_g).
 - 5.8 Impact of the electric field on the healing time with various gate voltages.
- 6.1 (a) Schematic circuit diagram and (b) Photo of an inkjet-printed current mirror.
 - 6.2 Schematic circuit diagram of a current mirror with faults located at various locations as defined by six cases.
 - 6.3 Self-healing in the current mirror circuit with the fault located at various locations as defined by six cases.
 - 6.4 (a) Schematic circuit diagram and (b) Photo of an inkjet-printed common-source amplifier.
 - 6.5 The (a) simulated and (b) measured curves of output voltage (V_{out}) and gain ($\Delta V_{out}/\Delta V_{in}$) as a function of input voltage (V_{in}) in the common-source amplifier.
 - 6.6 Schematic circuit diagram of a CS amplifier with faults located at various locations as defined by three cases.
 - 6.7 Self-healing in the common-source voltage amplifier circuit (left: $V_{out} - V_{in}$, right: Gain) with the fault located at various locations as defined by three cases.

- 6.8 Schematic of the experimental setup for measuring the frequency response of the inkjet-printed CS amplifier.
- 6.9 Frequency response of the CS amplifier before the fault and after the healing for each case.

- 7.1 Self-healing with bending (bending radius ≈ 7 cm) and the demonstration of the healing stability after 100 bending cycles.
- 7.2 Schematic of the experimental setup for measuring the self-healing in printed interconnects with dual open faults.
- 7.3 Dynamics of current showing the healing of dual faults for external resistors of 0.47, 0.99, and 10.56 M Ω (Inset) Microscopic images of open gaps in various interconnects.
- 7.4 Method to package the suspension using an inkjet-printing compatible process and add self-healing ability to a circuit.
- 7.5 (a)The microscope photo and (b) The cross-sectional image demonstrating the containment of the suspension between silane-treated regions.
- 7.6 The transfer characteristics of the OTFT showing the successful self-healing with the silane-based packaging.
- 7.7 Schematic of the experimental setup for noise measurement (a)without the direct current (b)with the direct current.
- 7.8 Measured noise current in different cases.

LIST OF TABLES

- 2.1 The comparison of the PBSH technique with other reliability-improving techniques.
- 2.2 Parameters and calculated Hamaker constant for different materials.
- 3.1 Average values of extracted parameters for inkjet-printed OTFTs.
- 6.1 AIM-spice simulation: Parameters for OTFTs in current mirror.
- 6.2 The simulated and measured currents in the current mirror.
- 6.3 AIM-spice simulation: Parameters for OTFTs in CS amplifier.

LIST OF PUBLICATIONS

- [1] **Li Ding**, Pushkaraj Joshi, James Macdonald, Virendra Parab, and Sanjiv Sambandan. Self-healing Thin-film Transistor Circuits on Flexible Substrates. *Advanced Electronic Materials*, 7(3):2001023, 2021. ISSN: 2199-160X. doi: 10.1002/aelm.202001023.
- [2] Pushkaraj Joshi, **Li Ding**, James Macdonald, and Sanjiv Sambandan. Self-Healing of Thin Film Transistor Circuits, *IEEE International Conference on Flexible & Printable Sensors & Systems (IEEE FLEPS 2021)*, doi: 10.1109/FLEPS-51544.2021.9469703
- [3] Chen Jiang, Constantions P. Tsangarides, Xiang Cheng, **Li Ding**, Hanbin Ma, and Arokia Nathan. High Stretchability Ultralow-Power All-Printed Thin Film Transistor Amplifier on Strip-Helix-Fiber, *IEEE International Electron Devices Meeting (IEEE IEDM 2021)*, in press.
- [4] Amit Kumar, Virendra Parab, Arindan Handu, **Li Ding**, Pushkaraj Joshi, Chen Jiang, and Sanjiv Sambandan. Self-healing Interconnects with Nearly Plastic Stretching of Repairs. *Physical Review Applied*, 11(1) 2019. ISSN: 2331-7019. doi: 10.1103/PhysRevApplied.11.014057.
- [5] Virendra Parab, **Li Ding**, Amit Kumar, Vaddi Yaswant, and Sanjiv Sambandan. Self-Healing Interconnects for Reliable Flexible Electronics. *ECS Transactions*, 85(13):825-831, 2018. ISSN: 1938-6737. doi: 10.1149/08513.0825ecst.

LIST OF SYMBOLS

A_i	Hamaker constant
C_i	gate dielectric capacitance per unit area
d	thickness of the film
d_p	initial distance between particles
D_S	drop space
D_H	drop height
E_F	Fermi energy level
E_{Fi}	intrinsic Fermi level
F_D	dipole–dipole attractive force
F_e	electrostatic force
F_{eff}	effective force
F_v	viscous drag force
f	frequency
g_m	trans-conductance
h	Planck constant
$\langle i_{th}^2 \rangle$	thermal noise density
$\langle i_{1/f}^2 \rangle$	flicker noise density
$\langle i_s^2 \rangle$	shot noise density
I_{DS}	drain-to-source current
I_{on}	current at the ON state (for TFT)
I_{off}	current at the OFF state (for TFT)
I_{in}	input current
I_{out}	output current

J	current density
k	dielectric constant
k_0	permittivity of vacuum
k_B	Boltzman's constant
L	channel length
M_r	relative molecular mass
n_p	number of particles in unit volume
N_{SS}	trap density
p	dipole moment
q	elementary charge
Q	Joule heating
r_p	effective radius of the particles
R_p	mean impedance of the single metal particle
R_{ext}	external resistance
s	length of the open gap
S_{\square}	unit area
T	absolute temperature
V_{th}	threshold voltage
V_{DS}	drain-to-source voltage
V_{GS}	gate-to-source voltage
V_{in}	input voltage
V_{out}	output voltage
W	channel width
$x(t)$	distance between particles at time t
Z_0	impedance of the external circuit
z_h	impedance of the healed bridge
α	ratio of the effective density of states
β	Claussius-Mossotti factor
ξ	electric field
ξ_{th}	threshold electric field
ϵ_f	permittivity of the fluid
λ	wavelength of the electromagnetic wave

η_f	viscosity of the fluid
μ	mobility
μ_0	mobility in delocalised band
μ_{lin}	mobility in the linear region
μ_{sat}	mobility in the saturation region
ϕ	activation energy
ϕ_s	surface potential
ϕ_{fp}	difference between intrinsic Fermi level and Fermi energy level
ϕ_{Ag}	concentration of Ag particles in suspension
ϕ_{Cu}	concentration of Cu particles in suspension
ρ_{Ag}	mass density of Ag
ρ_{Cu}	mass density of Cu
τ_h	healing time
v	drift velocity of the charge carriers
ν_e	electronic absorption frequency

LIST OF ABBREVIATIONS

2D	two-dimensional
3D	three-dimensional
a-Si	amorphous silicon
AC	alternating current
AFM	atomic force microscopy
AIM-Spice	Automatic Integrated Circuit Modelling Spice
Al	aluminium
Al ₂ O ₃	alumina
ALD	atomic layer deposition
Ag	silver
AgNW	silver nanowire
APC	amorphous polycarbonate
APS	average particle size
BGBC	bottom-gate bottom -contact
BGTC	bottom-gate top-contact
CAD	computer aided design
CCD	charge coupled device
CNT	carbon nanotube
CPU	central processing unit
CS	common-source
CTE	coefficients of thermal expansion
Cu	copper
C8-BTBT	2,7-alkyl[1]benzo-thieno[3,2-b][1]benzothiophene
C ₁₆ IDT-BT	indacenodithiophene-co-benzothiadiazole

diF-TES-ADT	2,8-difluoro-5,11-bis(triethyl-silylethynyl) anthradithiophene
CDT-BTZ	poly[2,6-(4,4-bis-alkyl-4H-cyclopenta[2,1-b;3,4-b']-dithiophene)-alt-4,7-(2,1,3-benzothiadiazole)]
CYTOP	poly(perfluoro-alkenylvinyl ether)
D	drain electrode
DC	direct current
DNTT	dinaphtho[2,3-b:2',3'-f]thieno[3,2-b]thiophene
EDA	Electronic Design Automation
EGaIn	eutectic gallium–indium
EM	electro-migration
F8BT	poly[(9,9-din-octylfluorenyl-2,7-diyl)-alt-(benzo[2,1,3]-thiadiazol-4,8-diyl)]
FEA	finite element analysis
FESEM	field emission scanning electron microscope
FET	field effect transistor
FTIR	Fourier transform infrared
G	gate electrode
Ga	gallium
Ge	germanium
GND	ground
HfO ₂	hafnium oxide
HOMO	highest occupied molecular orbital
IPA	isopropyl alcohol
LMs	liquid metals
LTPS	low-temperature polycrystalline
LUMO	lowest unoccupied molecular orbital
MTF	mean time to failure
O ₂	oxygen
OA	oleic acid
OLED	organic light-emitting diode
OSC	organic semiconductor
OTFT	organic thin-film transistor
PAN	polyacrylonitrile

P α MS	poly(α -methylstyrene)
PBSH	particle-based self-healing
PBTTT	poly[2,5-bis(3-dodecylthiophen-2-yl)thieno[3,2-b]thiophene]
PCB	printed circuit board
PCDTPT	poly[(4,4-bis(2-ethylhexyl)cyclopenta[2,1-b:3,4-b ₀]dithio- phene)-2,6-diyl-alt-[1,2,5]-thiadiazolo[3,4-c]pyridine]
PDMS	polydimethylsiloxane
PEN	polyethylene Naphthalate
PET	polyethylene Terephthalate
PFBT	pentafluoro-benzenethiol
PFDT	1H,1H,2H,2H-Perfluorodecanethiol
PI	polyimide
PMMA	polymethyl-methacrylate
P(METAC-co- MPTS)	poly[2-(methacryloyloxy)ethyl trimethylammonium chloride- co-3-(trimethoxysilyl)propyl methacrylate]
PS	polystyrene
PTAA	polymer poly(triarylamine)
PTFE	poly(tetrafluoroethylene)
PU	polyurethane
PUF	poly(urea-formaldehyde)
PVA	poly (vinyl alcohol)
PVC	poly (vinyl cinnamate)
PVP	poly (4-vinylphenol)
P(VDF-TrFE-CFE)	poly[(vinylidene-fluoride-co-trifluoroethylene)]
rms	root-mean-squared
rr-P3HT	regioregular poly (3-hexylthiophene-2,5-diyl)
rr-PQTs	regioregular poly-quaterthiophenes
RFID	radio frequency identification
S	source electrode
SAM	self-assembled monolayer
SCS	semiconductor characterisation system
SEM	scanning electron microscope
SID	Society for Information Display

Si	silicon
Si ₃ N ₄	silicon nitride
SiO ₂	silicon oxide
SMU	source measure unit
SPICE	simulation program with integrated circuit emphasis
SS	subthreshold swing
SWCNT	single-walled carbon nanotube
TFT	thin-film transistor
TGBC	top-gate bottom-contact
TGTC	top-gate top-contact
TiO ₂	titania
TIPS-pentacene	6,13-Bis(triisopropylsilylethynyl)pentacene
TTF-TCNQ	tetrathiafulvalene–tetracyanoquino-dimethane
VLSI	very large-scale integration
ULSI	ultra large-scale integration
UV	ultraviolet

1 INTRODUCTION

This chapter provides the background for large area flexible electronics and self-healing techniques. Further the motivation to develop the particle-based self-healing (PBSH) technique for flexible circuits is discussed. Section 1.1 reviews the development and promising applications of flexible electronics. Section 1.2 introduces major types of interconnects in flexible circuits. Section 1.3 describes several factors threatening the reliability of interconnects in flexible circuits. To improve the reliability, some passive and active healing techniques are introduced, meanwhile, advantages of the PBSH technique developed in this work over these healing techniques are described in Section 1.4. The objectives of this dissertation are revealed in Section 1.5. Finally, the overall outline of this dissertation is listed in Section 1.6.

1.1 Large Area Flexible Electronics

Flexible electronics has attracted tremendous attention due to the increasing demand for portable devices and sensors [1-8]. The popularity of the new concepts, such as flexible display screens [1], printed radio frequency identification (RFID) tags [5], disposable medical sensors [6, 7], and artificial e-skin [8-10], has bloomed the flexible electronics market dramatically. According to a report from Grand View Research, in Asia-Pacific region, the market size has expanded over three times in the past 8 years, increasing from USD 4 billion to 13 billion, and is estimated to reach USD 28 billion in 2024 (shown in Fig. 1.1). As the key element for functional large-area circuits such as displays and sensors, thin-film transistor (TFT) has been widely researched and developed. In flat-panel display industry, amorphous silicon (a-Si), low-temperature polycrystalline (LTPS) and oxide TFTs have been well developed and applied in commercial products for years. Compared to these inorganic counterparts,

organic TFTs (OTFTs) hold several advantages for its mechanical flexibility [11], low-temperature processibility [12, 13], and roll-to-roll compatibility [14]. These unique features make OTFT a promising candidate for fabricating flexible circuits.

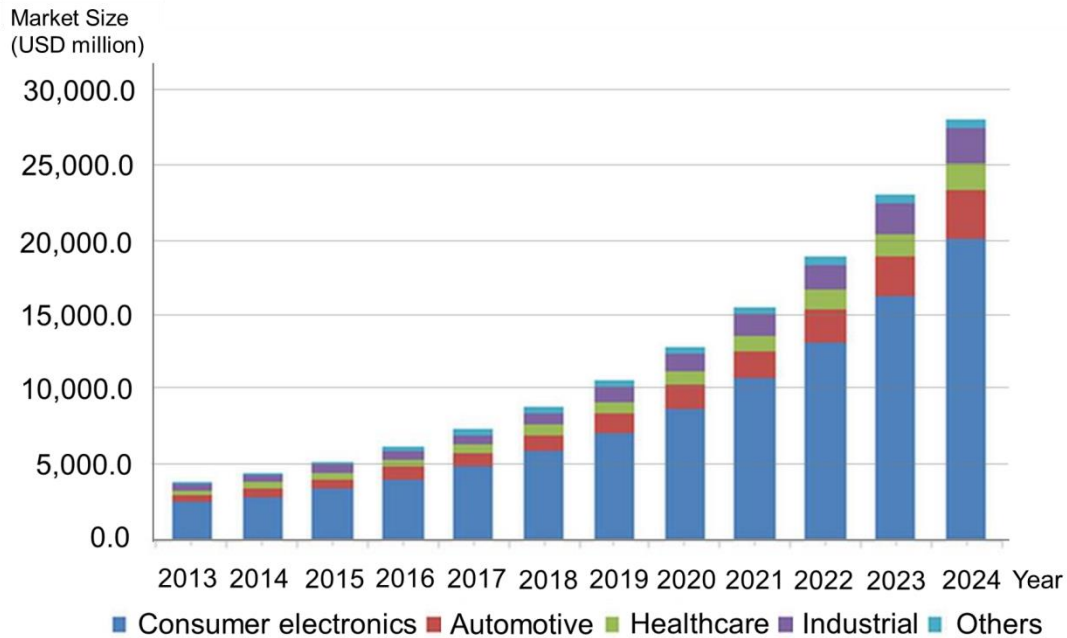


Figure 1.1. Asia-Pacific flexible electronics market size, 2013 – 2024. Source: Grand View Research

In the display industry, flexible screens have been developed for years and become the symbol of flagship products for smartphone manufacturers. In 2010, Sony™ unveiled an 80 μm-thick, 4.1-inch, 121 ppi, OTFT-driven full colour organic light-emitting diode (OLED) display at the Society for Information Display (SID) International Symposium. The proper functioning and rollable capability of this OLED panel represent the future of the display technology [15]. In 2019, Samsung™ [16] and Huawei™ announced their first foldable smartphones, which have 7.3-inch and 8-inch foldable displays, respectively. Following them, other manufacturers publicised or plan to develop their foldable products. The prosperity of this market shows the trend for the development of portable device industry in the future.

Flexible electronics also dominate the research in the wearable device area. In 2013, Someya et al. published the design of an ultrathin active-matrix sensor array [4]. Each sensor pixel consists of a resistive tactile sensor and a dinaphtho[2,3-b:2',3'-f]thieno[3,2-b]thiophene (DNTT)-based OTFT. This sensor array is as light as a feather

and remains fully functional when being bent and stretched. In 2015, Bao et al. demonstrated a skin-inspired artificial mechanoreceptor system, which is composed of a pressure-sensitive tactile element and an organic three-stage ring oscillator [8]. The tactile element is a piezoresistor, whose impedance is changed by the external pressure. The changing impedance affects the supply voltage to the ring oscillator, deciding the frequency of the output signal. The large-scale integration of this system can be potentially used as electronic skins for conventional neural prosthetics.

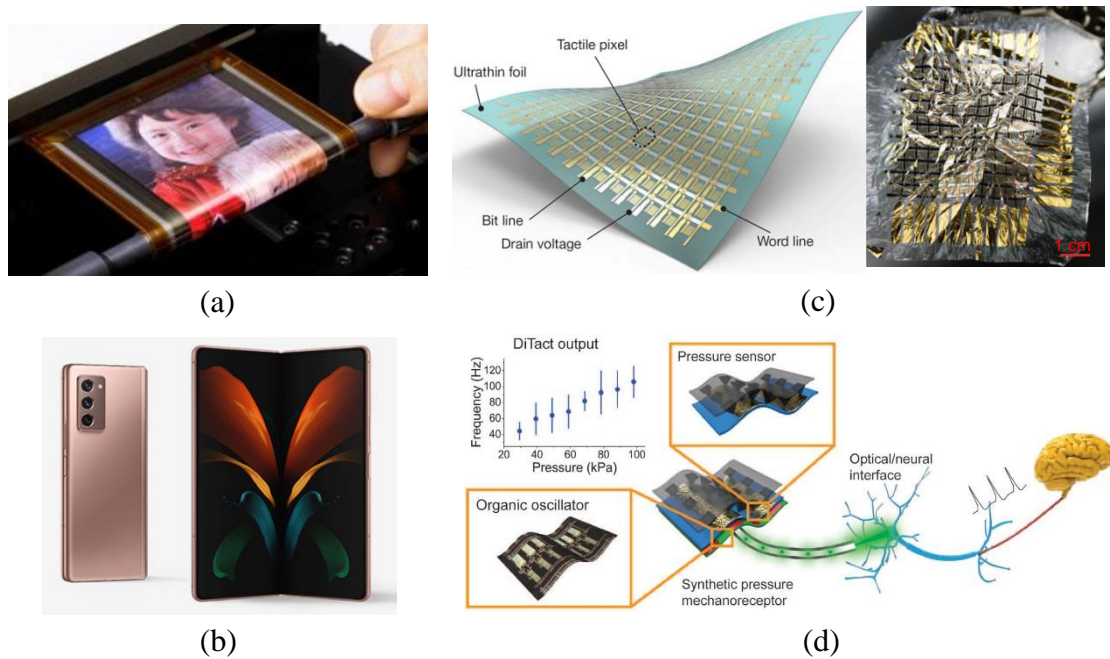


Figure 1.2. (a) Flexible OLED display with OTFT backplane by SonyTM [15]; (b) SamsungTM Galaxy Z Fold2 [16]; (c) Illustration and photo of a thin large-area active-matrix sensor with 12×12 tactile pixels [4]; (d) Schematic of the artificial mechanoreceptor system composed of a pressure-sensitive tactile element and an organic ring oscillator [8].

Flexible electronics are promising for next-generation displays and sensors. However, this technique faces several challenges, and the biggest one is its reliability.

1.2 Interconnects in Flexible Electronics

In conventional printed circuit board (PCB) circuits, there are various types of interconnects, and two of them are also widely-used in flexible electronics: one is metal foils connection, which is used to connect most devices and components; the other one

is wire bonding, which mainly acts as the first-level chip interconnects or the jump wire in flexible circuits.

1.2.1 Metal Foils

Metal foils are the most dominant form of interconnects in both PCB circuits and flexible circuits. Metals for fabricating these conductive foils include copper (Cu), silver (Ag), and aluminium (Al), etc., and they are embedded in or directly deposited on the substrates. In PCB circuits, metal foils are deposited on the entire surface of the substrate, the interconnect is formed by removing the unwanted part through etching, ablation or other mechanical processes. However, in flexible circuits, the interconnect is formed by additive processes, including the thermal evaporation, sputtering, ink-printing and direct transferring of the patterned foils onto the substrate. The advantages of applying metal foils interconnects in flexible circuits include: (a) High conductivity. Metal foils deposited on the flexible substrates have similar conductivity to metal wires used in PCB circuits. Compared to most basic components in circuits (e.g., large resistor, transistor, capacitor, etc.), the impedance of metal foils interconnects can be neglected. (b) High flexibility. Because of the low thickness of metal foils, when they are tightly adhered to flexible substrates, they can be bent, compressed and stretched together with substrates. (c) High utilisation rate of materials. In most cases, the deposition of metal foils on flexible substrate is an additive process, which means “manufacturing-on-demand” can be realised and few materials are wasted in this process.

1.2.2 Wire Bonding

Wire-bonding is the most widely-used method for first-level chip or integration circuit interconnect throughout the electronics industry. Compared to other first-level microelectronic interconnect method, wire-bonding is reliable and low-cost. The failure rate is typically at the single digit parts per million level [17]. In PCB circuits, wire-bonded interconnects are usually applied to connect pins of integrated circuit (IC) chips with the package or substrate. While in flexible circuits, except for that used as the first-level chip interconnects, wire-bonding is applied to create the jump wire as well, connecting pads which are non-connectable in two-dimensional (2D) plane. Materials for bonding wires include a variety of pure and alloy metals. The major materials are

pure gold (Au), aluminium (Al), copper (Cu), aluminium (Al) with 1% silicon (Si), and aluminium (Al)-magnesium (Mg) alloy.

Three major techniques have been developed for microelectronic wire-bonding: thermo-compression bonding, ultrasonic bonding, and thermo-sonic bonding. The thermo-compression bonding brings the surface of bonding wire and pad together to form an intimate contact with controlled temperature, pressure, and time. In this process, the bonding wire and metal pad undergo plastic deformation and interdiffusion in the atomic scale. If the bonding wire and pad have the same composition, the atomic interdiffusion can result in a uniform welded interface. Otherwise, if the bonding wire and pad have different compositions, the atomic interdiffusion can lead to the formation of intermetallics [17]. The ultrasonic bonding uses the ultrasonic energy to weld metals. In this process, a transducer vibrates the bonding wedge in the frequency range of 20-300 kHz, and the direction of vibration is parallel to the bonding pad. One main advantage of ultrasonic bonding is the ability to form the strong bonds with little or no extra heat, which is mild with the plastic substrate for flexible circuits. Another advantage is the possibility of performing the bonding at narrower space or finer pitches, as the shape of bond is narrower and more elongated compared to the ball bonding method [17]. The third microelectronic wire-bonding technique is the thermo-sonic bonding, it combines the ultrasonic energy with the ball bonding capillary technique in thermo-compression bonding, and is performed in a way similar to the thermo-compression bonding. The difference is that in thermo-compression bonding the capillary is heated at a high temperature to create a melted soft ball at the end of bonding wire; in thermo-sonic bonding, the high-temperature heating is not required, and the interfacial heat needed for welding is mainly generated by short bursts (10-100 milliseconds level) of ultrasonic energy. Because of the existence of both heat and ultrasonic energy, the applied temperature and ultrasonic energy in thermo-sonic bonding can be much lower than those in thermo-compression bonding and ultrasonic bonding, respectively. This advantage makes thermo-sonic bonding an ideal technique for bonding metals with large hardness, such as Au, Cu, etc.

1.3 Reliability of Interconnects in Flexible Electronics

Flexible displays and sensors are commonly based on ultra-thin plastic or glass substrates. During their lifetime, these devices will suffer from internal and external

forces and corrosions, which can lead to the failure of interconnects in the circuit. The typical reasons causing reliability problem include:

1.3.1 Mechanical Stress

Mechanical stress refers to the force per unit area in the cross-section of the interconnect. It can be caused by the external-applied force during bending and stretching [18], or the different thermal expansion of the adjacent components when heating up and cooling down (due to the different coefficients of thermal expansion (CTE) of the respective materials). If a material is repeatedly loaded with the external force, it would continuously transform between the deformed and non-deformed states, leading to the weakening of the material named as fatigue. The structural failure normally goes through three stages: (1) The formation of the crack. At the point which bearing large stress or the region with a high density of defects, the nucleation of a crack occurs. From this nucleus, the cracks start to grow. (2) The growth of the crack. In the early stage these cracks propagate slowly along the crystallographic planes, where the shear stress is highest. When the size of the cracks reaches a threshold value, these cracks propagate quickly, along the direction perpendicular to the applied external force. (3) The permanent failure. As these cracks grow to a detectable size, the metal materials are split in two parts and the permanent deformation occurs in polymer materials.

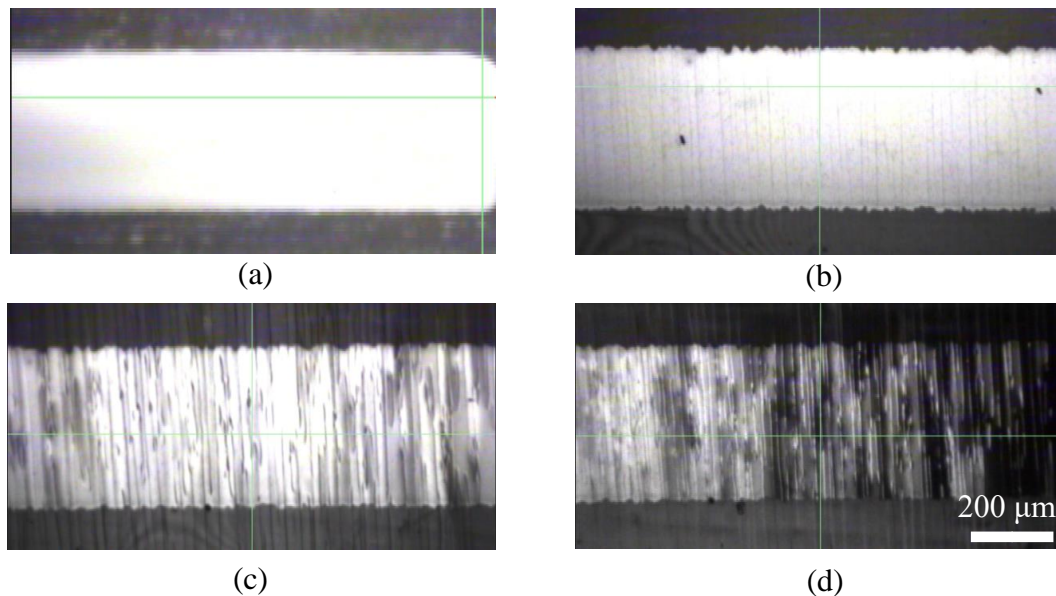


Figure 1.3. Micrograph of Ag wire on PEN substrate (a) Before the flexural test (b) Bending for 1000 cycles. (c) Bending for 2000 cycles (d) Bending for 3000 cycles.

To reveal the influence of the mechanical stress on flexible substrates, the flexural test was conducted using the Polyethylene Naphthalate (PEN) substrate. Fig. 1.3 shows the micrograph of the printed silver (Ag) wire on PEN substrate (thickness: 125 μm), which was bent for 3000 times. In these micrographs, after being bent for 1000 times, some tiny cracks were found on the surface of the Ag wire. When being bent for 2000 times, obvious cracks appeared on both Ag wire and PEN substrate. The Ag wire was split into flakes, as shown in Fig. 1.3(d), when the number of bending cycles reached 3000. The average width of cracks was measured to be 8 μm and these cracks lead to the open fault in the Ag wire. The result of this flexural test indicates that the mechanical stress is a huge threat to flexible devices and circuits.

1.3.2 Electro-migration (EM)

Electro-migration (EM) is caused by the momentum transfer between electrons and ionised metal atoms. When an electrical field is applied in the conductor, there are two forces affecting the ionised atoms: One is the electrostatic force F_e . The ionised atoms carry the positive charge, so they will be motivated by a field force, which has the same direction with the electrical field. The other one, F_p , is the force arising from the collision with electrons, resulting in the exchange of momentum between ionised atoms and electrons. The direction of this force is opposite to the electrical field. Therefore, the effective force upon an ionised atom is calculated as:

$$F_{eff} = F_e - F_p \quad (1-1)$$

When the EM occurs, a large number of moving electrons, which are called *Ion Wind*, transfer momentum to nearby ionised atoms, leading to the displacement of these atoms from their original positions. There are two cases: one is the accumulation of such displacement, creating voids in some regions. Then these voids expand and connect to each other, and finally generate an open fault in the conductor. This is called the void failure or the internal failure. Another case is that the moving ionised atoms stack at one point, making the undesired connection between two separated parts and causing the short in the circuit. This is called the hillock failure or whisker failure.

To estimate the failure speed of the EM, an empirical model was developed to calculate the MTF (mean time to failure, in hours) [19]:

$$MTF = AJ^{-2} \exp\left(\frac{\phi}{kT}\right) \quad (1-2)$$

where A is a constant, which is related to the cross-sectional area of the wire. J is the current density (A/cm^2). ϕ is an activation energy (eV). k is Boltzman's constant, and T is wire's temperature (K). For the higher current density and higher temperature, the failure in the conductor would be accelerated. That is because the high current density increases the number of electrons in a unit area and the high temperature accelerates the thermal motion of carriers, causing an increase in the amount of electron scattering against the atoms and the momentum transfer between these two charge carriers. Hence the displacement of the ionised atoms is accelerated and the MTF is shorten.

In Very Large-scale Integration (VLSI) or Ultra Large-scale Integration (ULSI) systems, the influence of the EM becomes more severe, as the size of devices and wires in these systems are commonly at micrometer (μm) or even nanometer (nm) level. The small cross-sectional area of the wire or device significantly increases the current density, and the high power consumption increases the temperature in the whole system, raising the probability of failure caused by the EM in this system [20]. To solve this problem, people apply the high conductive metals for the wire and optimise the layout of circuits by using Electronic Design Automation (EDA) tools to avoid the EM problems [21].

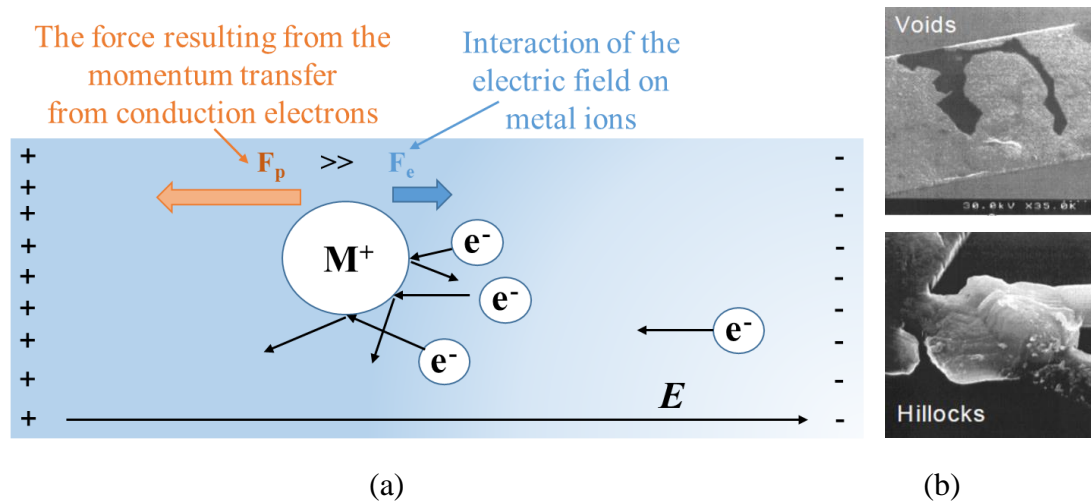


Figure 1.4. (a) Two forces act on metal ions when applying an electrical field in a conductive material. (b) Void and Hillock failures in wires due to EM [21].

1.3.3 Chemical Corrosion

Wearable devices are usually exposed to the ambient environment and are prone to be permeated by oxygen and moisture, so they are easily influenced by chemical

corrosions. Corrosion is a process converting the pure metal into a more chemically stable form, such as oxide, chloride or sulphide. It is a gradual destruction of the metal caused by the chemical or electrochemical reactions. One common example of the corrosion is rusting, the oxidation of the metal surface. The mechanism of corrosion can be simplified as an electrochemical process. Taking the oxidation as an example, in ambient environment it originally takes place at a particular spot on the surface of the metal, then this spot acts as an anode. The metal atom M turns into the ion M^{n+} , releasing electrons to adjacent regions. If the water film dissolving the carbon dioxide (CO_2), sulphur dioxide (SO_2), or hydrogen sulphide (H_2S) gas exists at these regions, the spots inside would act as the cathode and the reaction is: $2H^+ + 2e^- == H_2 \uparrow$. In this case the metal is damaged like being etched by the acid. If the ambient environment is not in acid condition, the electrons combine with the oxygen (O_2) in the water film and the reaction occurring at the cathode is: $2H_2O + O_2 + 4e^- == 4OH^-$. Then the hydroxyl ions combine with the metal ions and form the metallic oxide.

Apart from the hydrogen evolution reaction and oxygen abstraction reaction introduced above, there are other forms of corrosion. One is the galvanic corrosion, it occurs when two types of metals contact with each other (physically or electrically), immersing in the common electrolyte, or when a metal is immersed in the electrolyte with different concentrations. In the galvanic corrosion, two different parts are named as the galvanic couple, in which the more active component acts as the anode and releases electrons, and this part corrodes at an accelerated rate. On the contrary, the more noble component acts as the cathode and corrodes at a slower rate. The mechanism of the galvanic corrosion can be used to protect one metal by adding a more active metal as the sacrificial anode, so it is usually used in the marine and hydropower industries. However, in the electronic industry, the contact of different metals (metals for bonding wires, printed circuit board (PCB) wires, soldering spots) may lead to unexpected damage of the interconnects under the ambient environment.

Another type of corrosion is the high-temperature corrosion. It is a chemical destruction occurring when the metal is exposed to a high-temperature atmosphere containing oxygen, sulphur, chlorine or similar gas capable of oxidising metals. In the electronic industry, the high-temperature commonly exists in resistive devices and large-scale integrated circuits, like central processing unit (CPU). And it can accelerate the oxidation of metal on the surface, leading to the degradation of conductivity. If

the size of wires in the circuits is extremely small, the high-temperature corrosion may oxidise the whole wire and permanently damage the interconnects, causing the failure of the entire circuit.

1.3.4 Thermal Stress

Thermal stress refers to the mechanical stress caused by the change of temperature in one material or two contacted materials. In a solid or liquid, under a specific temperature, the cohesive forces between atoms or molecules are kept in a dynamic balance, thus the distance between them can remain constant. The increase of temperature results in longer distance between atoms or molecules, causing the volume expansion of a material. If the crystalline material has the same structural configuration in all dimensions, it is defined as an isotropic crystal and the deformation will be uniform in all directions. For an anisotropic crystalline material, its structural configuration varies in different directions, leading to different expansion coefficients along these directions. When the temperature changes, this anisotropic characteristic can cause the inner stress in solid material, resulting in the change of shape or even the breakdown of crystalline structure.

For two different materials, the cohesive forces maintaining dynamic balance between atoms or molecules are different. Therefore, different materials normally have variations in their expansion coefficients. This poses a great threat to interconnects between two or more materials (e.g. the bonding between Cu wire and Al pad). When the temperature changes, different expansion coefficients lead to the difference in thermo-mechanical distortions of two contacted materials, causing the mechanical stress at the contact interface. When this stress grows larger than the binding force between two crystalline materials, cracks and the failure of interconnects may take place. Therefore, when designing the interconnects in circuits, especially in high-power circuits, the selection of materials with matched coefficient of thermal expansion (CTE) is critical.

1.4 Improving the Reliability of Interconnects

To improve the reliability of the whole system, several strategies have been developed and adopted, which can be divided into two categories: passive strategies and active strategies.

In passive strategies, novel geometric structures or materials are applied to make the circuit more robust to the mechanical stress. The special geometric structures include helical coils [22, 23], meandered wires [24-26] and three-dimensional (3D) mogul-patterned or porous spongy structures [27-30]. The novel materials include metal or carbon based composites [31-33], nano-particles [34], nano-wires [35-39], and conductive polymers [40-42]. These materials have high conductivity and can bear large strain or stress.

In active strategies, conductive particles or powders dispersed in insulating microcapsules or liquid are widely applied. These suspensions can permit the real-time repair of the open fault. One typical approach is to encapsulate the conductive ink into microcapsules [43-46]. When the external force breaks the interconnect, the microcapsules are ruptured and the inner conductive ink is released. This ink fills up the open gap and repairs the interconnect.

Details about these strategies will be discussed in Chapter 2. While all these strategies can improve the reliability of systems, they have inherent shortcomings. Passive strategies using novel geometric structures or materials cannot heal the open fault after the break of the interconnect. Active strategies usually use relatively rare materials (e.g., Ga and In) [47] or complex fabrication processing (e.g., chemical reaction to form the polymer shell) [46], and can only repair the mechanical force-caused disconnection. To avoid these shortcomings, a particle-based self-healing (PBSH) technique that is of interest to this study is developed [48]. This approach can heal the disconnection caused by various reasons and does not need the rare materials or complex fabrication process. The mechanism and the breakthrough of this technique will be discussed in Chapter 2 as well.

1.5 Objectives

There are two sub-objectives in this dissertation: one is to understand and develop the PBSH technique. The other one is to design, fabricate and characterise the inkjet-printed OTFT devices and circuits. The final objective is to prove the feasibility of applying the PBSH technique in OTFT-based flexible circuits. The main challenges include:

- To understand the mechanism and establish the theoretical model of the PBSH technique.

- To achieve the homogenous and insulating suspension.
- To select the proper materials and optimise the fabrication process for inkjet-printed OTFTs.
- To design, fabricate and characterise the OTFT-based flexible circuits.
- To characterise and evaluate the PBSH at the wire, device and circuit levels.
- To realise the packaging of the circuit and confine the suspension in the expected region.
- To evaluate the reliability and stability of the PBSH after the open fault is repaired.

1.6 Dissertation Outline

This dissertation investigates the feasibility of applying the PBSH technique in OTFT-based flexible circuits. The outline of this dissertation is shown as follows:

Chapter 2 reviews the state of the art in techniques developed for improving the reliability of interconnects. Then the mechanism of the PBSH technique investigated in this work is explained. A theoretical model is established, and advantages of the PBSH technique over other reliability-improving techniques are discussed. Limitations of this technique are also introduced and to address these issues, a chemical coating process to modify the surface of conductive particles is developed.

Chapter 3 introduces the inkjet-printed OTFT devices. OTFTs are basic component for flexible circuits in this study, thus material properties, device structures and fabrication process of this key component are discussed in detail. The challenges in achieving stable OTFTs are also discussed in this chapter.

Chapter 4 describes the PBSH in inkjet-printed interconnects. Relationships between the healing time with the concentration, electric field strength, length of the open gap and external resistance are analysed in this chapter, proving the feasibility of the PBSH at the wire level. Part of the chemical and electrical experimental results in Chapter 2 and Chapter 4 were collected with the assistance from Dr. Pushkaraj Joshi, here I acknowledge Dr. Joshi's contributions to this study.

Chapter 5 investigates the PBSH in OTFT electrodes. The healings of the open faults occurring at Source (S) and Drain (D) electrodes are analysed, which show the feasibility of the PBSH at the device level.

Chapter 6 explores the PBSH in OTFT-based flexible circuits. Two types of circuits are analysed: current-mirror and common-source (CS) amplifier. The circuit performance before and after the open fault is analysed and the effect of the PBSH is evaluated. This chapter reveals the feasibility of the PBSH at the circuit level.

Chapter 7 characterises the performance of the healed interconnection. The influence of the repeated bending, the ability of healing the multi-open-faults, and the noise of the healed part are analysed. In addition, as PBSH is a particle-based and fluid-carried healing technique, the healing materials are expected to appear in the damageable regions. Therefore, the packaging of the circuits which can confine the healing materials in the expected region and the self-healing in the confined region are also included in this study.

Chapter 8 summarises the conclusions obtained from this dissertation. The technological outlook for future exploration of this study are proposed as well.

2 TECHNIQUES FOR IMPROVING THE RELIABILITY OF INTERCONNECTS

This chapter introduces the passive and active strategies developed for improving the reliability of interconnects. Then the particle-based self-healing (PBSH) technique investigated in this work is discussed in detail. The mechanism of this technique is analysed and its advantages over other reliability-improving techniques are listed. Section 2.1 and Section 2.2 review the typical passive and active techniques, respectively. Section 2.3 describes the theoretical models of the PBSH technique developed in this work. The advantages and limitations of this PBSH technique are summarised in Section 2.4. Finally, to address the technique limitation, a pre-treatment of metal particles is introduced in Section 2.5.

2.1 Passive Techniques

In this section several passive techniques developed for improving the reliability of interconnects are reviewed. These techniques use novel geometric structures or materials to make the circuit more robust to mechanical stress.

2.1.1 Helical Coils and Meander Design

In recent years, stretchable and twistable wires have been developed for artificial skin and fabric electronics. Among this research, wire shaped in helical coils is a promising candidate for flexible and stretchable electronics. Compared with a straight wire, helical wires are more robust to stretching and twisting. A structure of helical wire-based sensor is shown in Fig. 2.1(a). Conductive wires are wound around a

stretchable insulating core, and a piezo-resistive layer is coated as the outer layer. There are two functions of this piezo-resistive outer layer: one is to prevent the direct contact of two conductive wires, and the other is to form a sandwich structure (conductor - piezo-resistive layer - conductor) acting as a sensor unit to detect pressure on it. Fig 2.1(a) shows helical conductive wires used in a stretchable fabric artificial skin. The length of these wires can increase up to 200% and the sensing unit can maintain its functionality for up to 100,000 cycles [22]. Fig. 2.1(b) shows the helical conductive wires applied in a twistable tactile sensing array, which can withstand a twisting angle of 70° without any damage in structure or functionality [23]. In these examples, the mechanical properties and the reliability of the whole system are significantly improved by using helical wires.

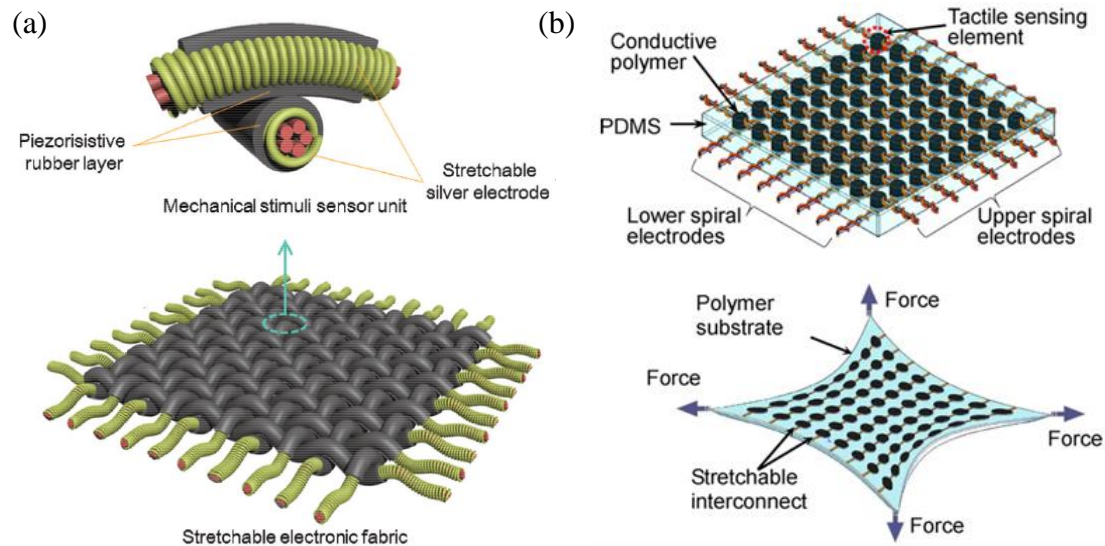


Figure 2.1. Two stretchable and twistable sensor systems using helical wires: (a) The fabric artificial skin [22], and (b) The tactile sensing array [23].

The reason helical wires can improve the reliability is that the helical coil structure can help release internal stress in the wire while being stretched. Here a simulation was conducted using a commercial finite element analysis (FEA) software COMSOLTM Multiphysics 5.3. In this simulation, a straight wire with the length of 0.1 m and a helical coil with the axis length of 0.1 m were stretched to extend by 1%, simultaneously, the radius and material of these wires were set to be the same. Fig. 2.2 shows the simulated results of the internal stress in these wires while being stretched. When the Nylon wire was set to be stretched by 1%, the simulated von Mises stress inside the straight wire

was 15 ~ 20 MPa, and inside the helical wire the result was 0.5 ~ 2 MPa. With the same load, the von Mises stress in the straight wire was 10 times larger than that in the helical wire. As the internal stress is the main factor leading to the mechanical failure in the interconnect, the helical coil structure shows a remarkable advantage in enhancing the reliability.

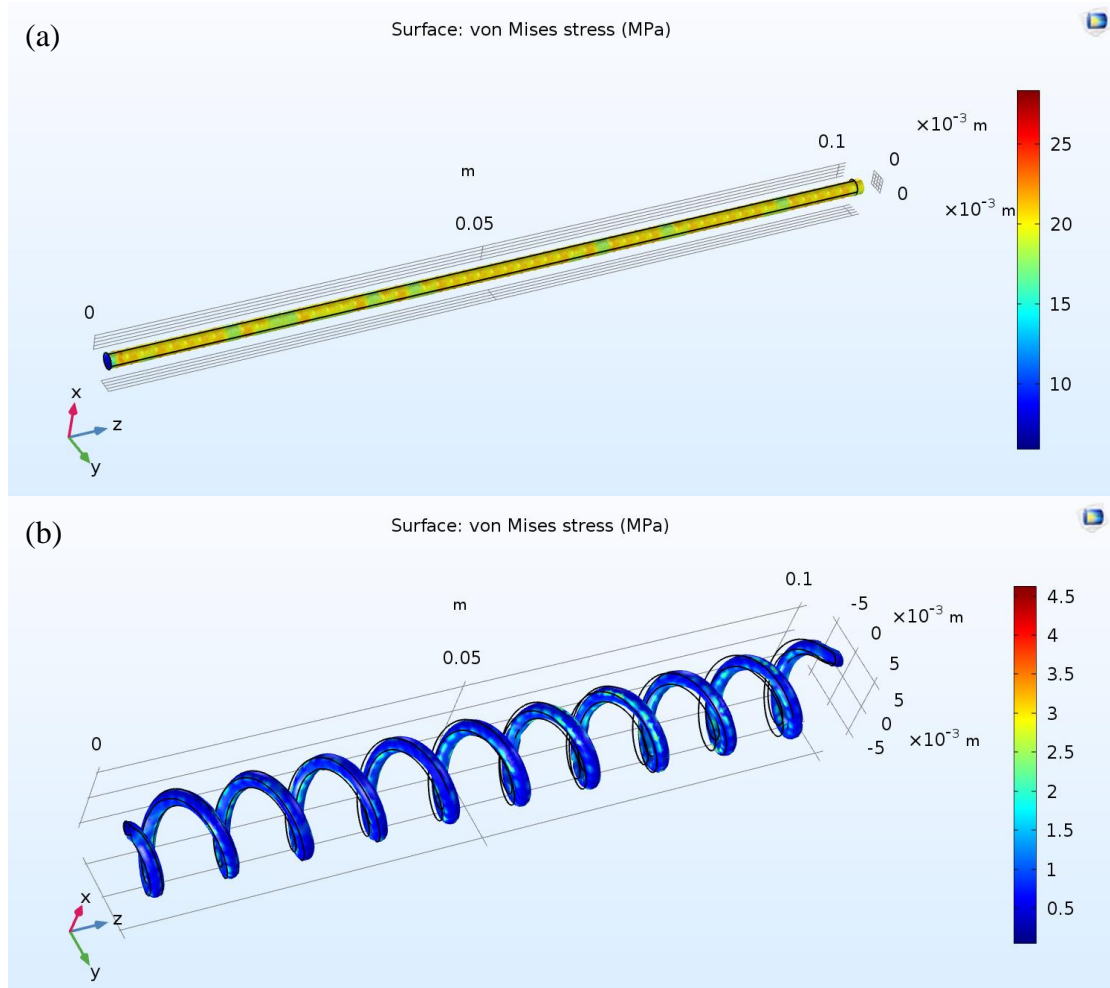


Figure 2.2. Simulated von Mises stress in (a) straight and (b) helical Nylon wires while being stretched to extend by 1%.

Another geometric design for releasing internal stress in wires is the meander design. Different from the helical coil structure, the meander design is mainly for two-dimensional (2D) layouts of interconnection, but their physical principle is the same: using the meandering or helical structure to release the internal stress in the interconnection wire. The meander designs are usually applied to membrane electrodes and wires on the flexible substrates [24, 25, 49]. Fig. 2.3 shows the von Mises stress in

2D wires shaped in the straight and horseshoe patterning. The material and width of these wires were set to be the same, and they were set to be stretched by 1%.

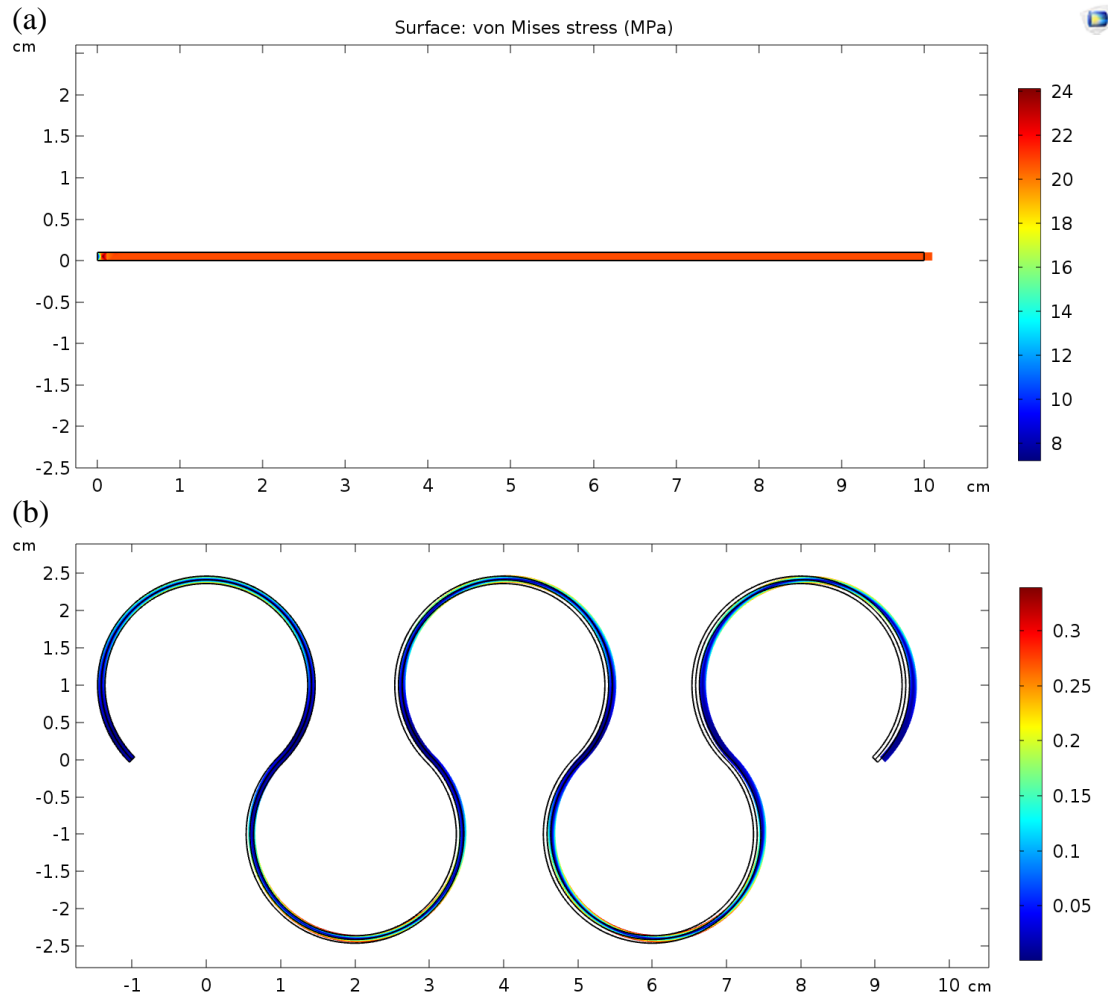


Figure 2.3. Simulated von Mises stress in (a) straight and (b) horseshoe-shaped wires while being stretched to extend by 1%.

In Fig. 2.3 the von Mises stress in the horseshoe-shaped wire was not more than 0.3 MPa, while it was 60 times larger in the straight wire, reaching 20 MPa. The result of the simulation reveals advantages of the meander design for the 2D layout of wires in flexible circuits.

2.1.2 Geometric Patterning of Substrates

This method is utilised in flexible circuits which use a part or whole substrate as the conductive path. By changing the substrate into a porous structure and coating conductive materials inside or at the surface of it, the interconnection can be more stable

when the whole circuit suffers repeated stretching, compressing, or twisting [27, 29, 30, 50]. Fig. 2.4 describes work using the functionalised metal-coated porous polyurethane (PU) sponge as the conductive flexible substrate [27].

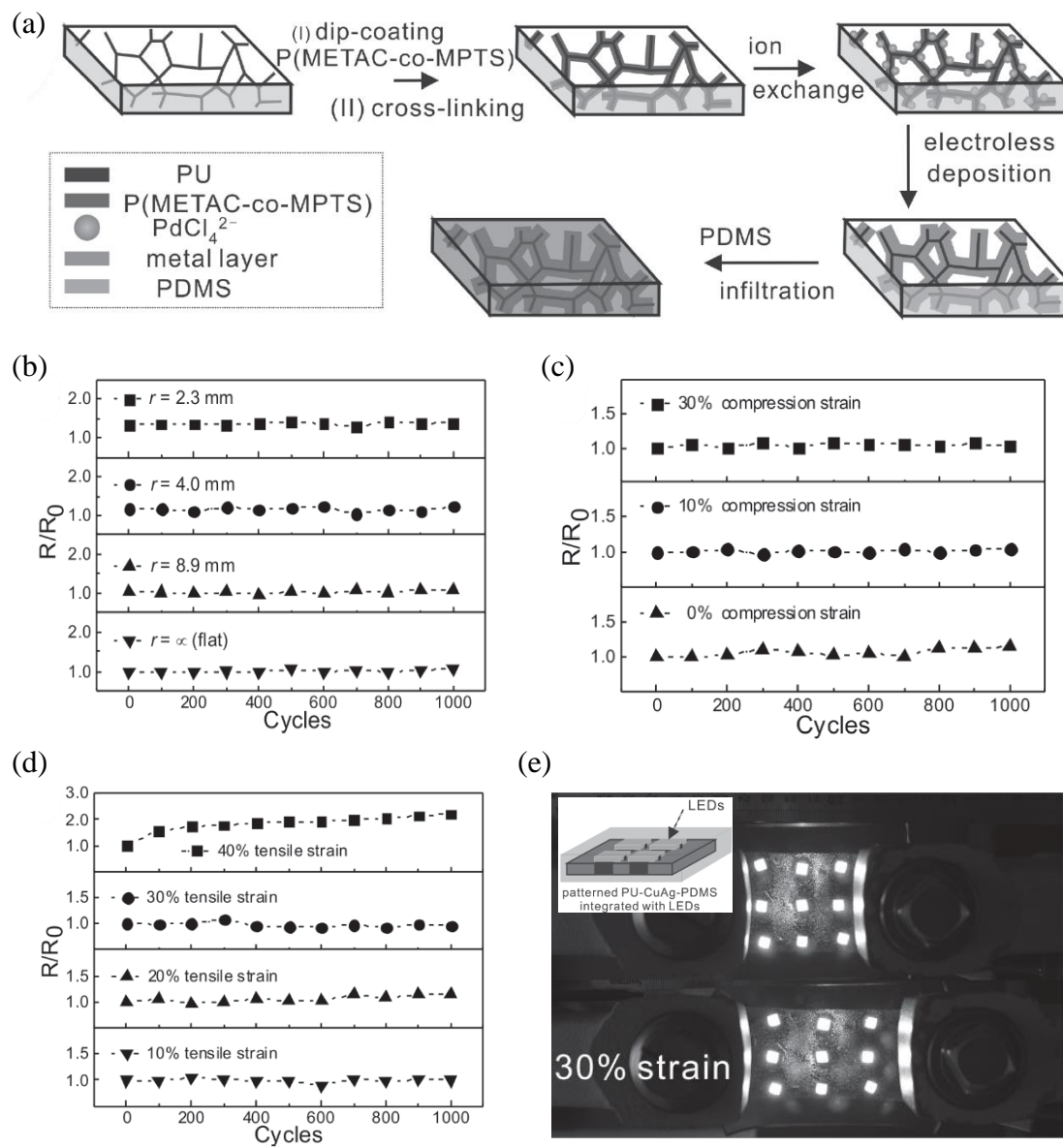


Figure 2.4. (a) Scheme for the preparation of conductive composites. (b) Bending (c) Compressing (d) Stretching tests of conductive composites. (e) Stretching test of the LED array using PU-CuAg-PDMS conductive composites. [27]

Fig. 2.4(a) illustrates the fabrication process of this flexible substrate. The PdCl₄²⁻ moieties loaded on the poly[2-(methacryloyloxy)ethyl trimethylammonium chloride-co-3-(trimethoxysilyl)propyl methacrylate] P(METAC-co-MPTS) copolymer layer act as the adhesion layer between the substrate surface and the thin metal film. The

precursors of polydimethylsiloxane (PDMS) were infiltrated into the PU-metal sponge to form the PU-metal-PDMS conductive composite. Fig. 2.4(b)-(d) demonstrate the variation of the resistance in bending, compressing, and stretching tests. From these figures, it can be concluded that when the radius of curvature was not less than 4 mm, or when the compression strain and the stretching strain were not more than 30%, the normalised resistance (R/R_0) remained stable at ca. 1.0. Simultaneously, this conductive composite can resist over 1000 cycles of bending, compressing or stretching without any change in resistance. Fig. 2.4(e) shows a flexible and stretchable LED array using PU-CuAg-PDMS conductive composite as the interconnect. This array can maintain remarkable stability upon stretching by 30%, proving the effectiveness of this conductive composite in improving the reliability of the system.

2.1.3 Novel Materials

To replace the metal interconnects in flexible circuits, which are easily damaged by mechanical, electrical, and chemical factors. Some new conductive materials have been researched and developed as interconnects for flexible electronics. Features of these materials include good stretchability, conductivity, and chemical stability. Materials which can meet these requirements are metal- or carbon-based composites [31, 32, 35], nano particles or wires [36, 39, 51], and conductive polymers [40, 42, 52].

Silver nanowire (AgNW) is a widely-used conductive material to fabricate stretchable electrodes. The good electrical and mechanical properties of the AgNW-based bulk or film come from the dense network structure shown in Fig. 2.5(a). When being stretched or bended, although the mesh space in the network expands, the high-density and the large length-to-diameter aspect ratio of the AgNW guarantees the complete connection between these nano-wires and maintains the conductivity of the network. Advantages of AgNW include high conductivity, high visual transparency, and good mechanical compliancy, making this material a popular choice for transparent electrodes. However, the impedance of the AgNW-based film changes with increasing strain, influencing the current flowing in interconnects. Although this characteristic has a reverse effect on the electrical stability of the circuit, some studies use it to fabricate high-performance strain sensors [53, 54].

Another type of under-researched material for better reliability are carbon-based composites. One such material is the carbon nanotube (CNT), which has several unique

advantages: First, it can be solution processed, which means it can be patterned to form uniform films. Second, it is inert in biomedical applications. These advantages make CNTs a good alternative for biomedical electrodes or sensors. However, the weakness of this material is also obvious: it has a relatively large sheet resistance ($>100 \Omega/\text{sq}$) [55]. To address this shortcoming, research has been conducted to combine CNTs with other materials to synthesize hybrid nanocomposites. Fig. 2.5(b) shows a hierarchical multiscale AgNW/CNT hybrid nanocomposite for highly stretchable conductors [31]. In this structure, the highly conductive AgNWs act as a backbone for fast electron transport, while the elastic but relatively resistive CNT network provides high stretchability and flexibility. In addition, the CNT network can further enhance the conductivity of the whole composite as it fills the mesh space of the backbone, providing more local paths for electron transport.

Conductive polymers are also investigated to improve the reliability. Among these polymers the conductive PEDOT:PSS has been an attractive material [42, 52]. One feature of this material is that its conductivity can be modified by post-treatment with different solvents. Fig. 2.5(c) illustrates the modified conductivity of PEDOT:PSS treated by methanol (MeOH), ethanol (EtOH), isopropyl alcohol (IPA), and i-butanol. The pure PEDOT:PSS has a low conductivity of only 0.3 S/cm, while being treated by MeOH, the maximum conductivity can reach 1015 S/cm. This makes PEDOT:PSS a good candidate for making electrodes or wires. In terms of the stability, the resistance change during the twist test is shown in Fig. 2.5(d). After being twisted for 2000 cycles, the resistance remained constant with small variation ($\Delta R/R \approx 0$). This result indicates that the post-treated PEDOT:PSS is an outstanding conductive polymer for stable interconnects in flexible circuits.

To summarise, passive techniques utilise the mechanical and electrical properties of unique geometric structures or materials to achieve the improved reliability in flexible electronics. However, these methods can only deal with issues caused by mechanical stress, and they cannot provide the real-time repair (healing) for open-circuit faults. Therefore, some conductive liquid-based new techniques are developed to complement these shortcomings.

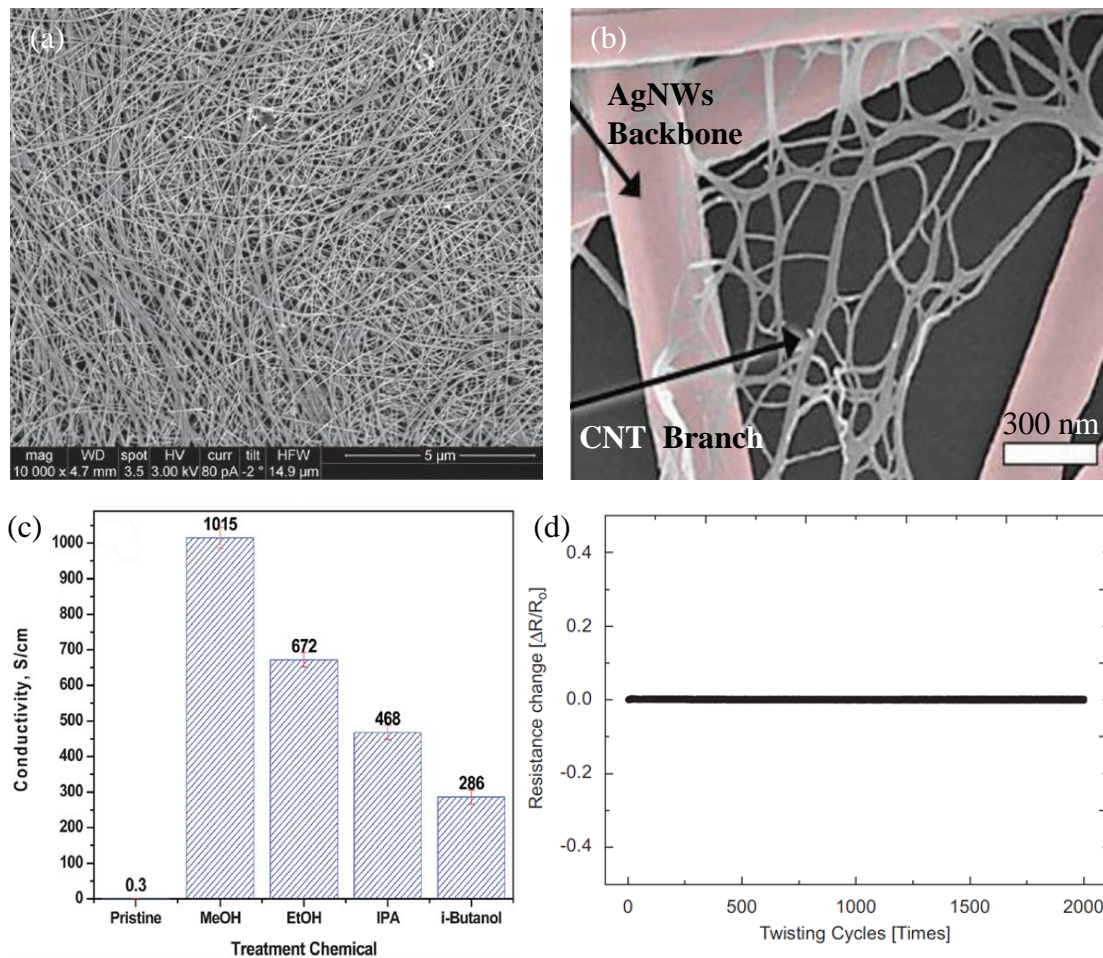


Figure 2.5. (a) SEM image of the dense AgNW network structure [36] and (b) The hierarchical multiscale AgNW/CNT hybrid nanocomposite [31] (c) Conductivities of PEDOT:PSS films treated with different chemicals [52] (d) Twisting reliability of the gravure-printed PEDOT:PSS electrode [42].

2.2 Active Techniques

In this section several active techniques developed for strengthening the robustness of flexible circuits are reviewed. These techniques utilise novel materials to provide the real-time repair for open-circuit faults.

2.2.1 Liquid Metals

Some synthesised liquid metals (LMs) are used to fabricate stretchable interconnects, which can heal an open-circuit fault after being damaged. Fig. 2.6(a) shows a kind of LM–elastomer composite which is composed of droplets of gallium (Ga)-based LM alloy (eutectic gallium–indium, EGaIn) embedded in a silicone

elastomer [47]. This composite is intrinsically insulating, while applying the external forces, the local stress in the composite can rupture the LM droplets and form conductive pathways. The conductivity of this pathway is determined by the volume ratio of the LM alloy in the composite. When the volume ratio is 50%, the conductivity of the pathway can reach 1370 S/cm. Fig. 2.6(b) is a four-channel serial clock display connected to the power (V_{cc} and GND), data and clock signal terminals by the LM–elastomer composite. Although these four lines experienced extreme mechanical damage (tearing, cutting and the complete removal of material), the clock display continues to work.

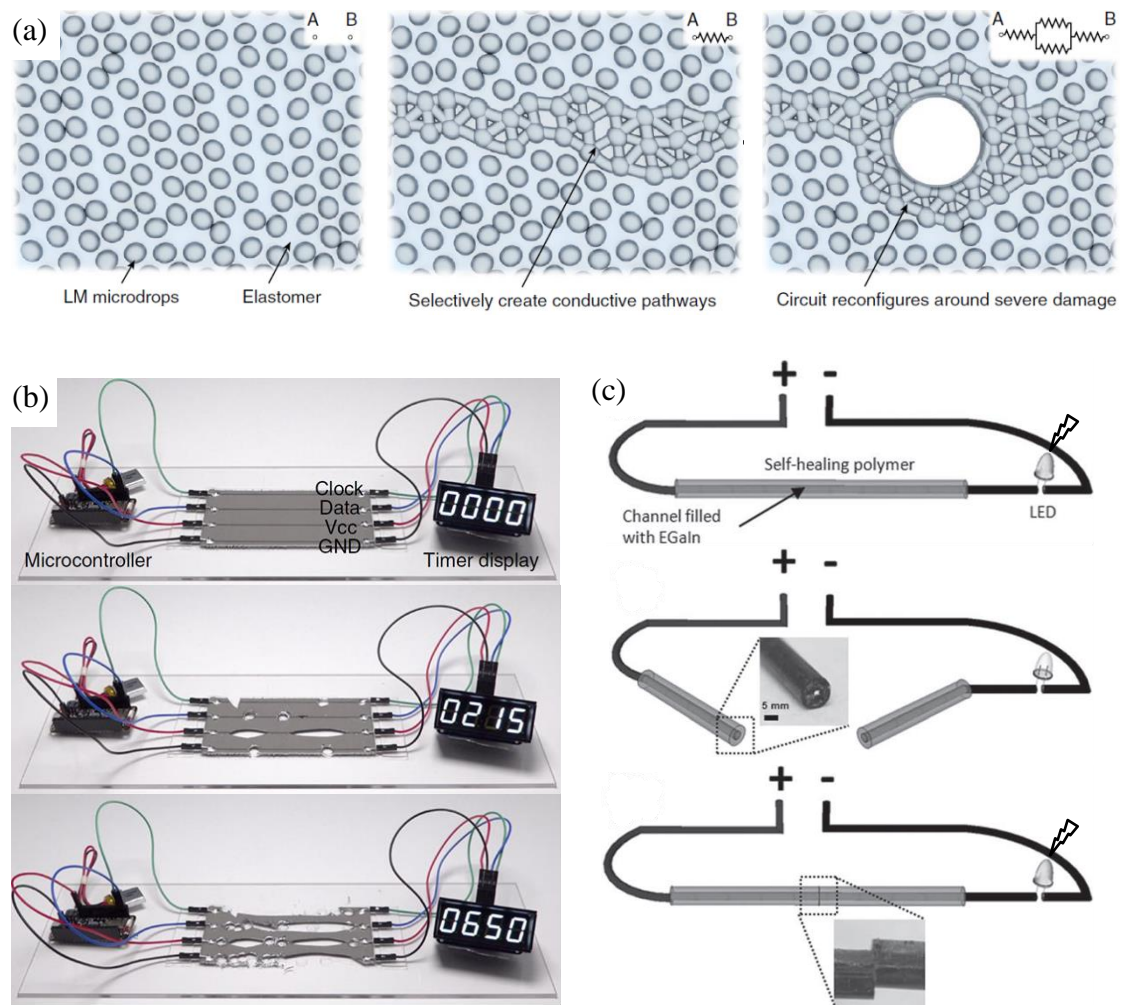


Figure 2.6. (a) The mechanism of the self-healing using LM–elastomer composite. (b) A four-channel serial clock display connected by the LM–elastomer composite [47] (c) The disconnection and reconnection of a LED circuit using a self-healing wire [56].

Fig. 2.6(c) shows a stretchable self-healing coaxial wire, which is fabricated by injecting EGaIn LM into the polymer microchannel [56]. When rejoining two severed wires, the inner liquid metal components merge together, forming the conductive path again. Meanwhile, functional groups grafted in the polymer generate strong hydrogen bonding and permits the polymer to self-heal in minutes [57]. Therefore, this self-healing wire can enable both mechanical and electrical healing of an open fault in interconnects.

2.2.2 Conductive Ink in Microcapsules

Microcapsules with conductive ink inside is another active technique used to repair open faults caused by mechanical damage. Materials for conductive ink include single-walled carbon nanotubes (SWCNTs) [43, 44], graphene [44], tetrathiafulvalene-tetracyanoquinodimethane (TTF-TCNQ) [45], carbon black [46] and metal particles [58]. Materials for the outer capsule are molecule-level polymer materials like poly(urea-formaldehyde) (PUF) or polyurethane (PU). These polymers are intrinsically insulating so the whole suspension is non-conductive until microcapsules are ruptured by an external force. There are two approaches to release the conductive solution. One is directly encapsulating the conductive particles into insulating polymer shells [43]. When the outer shell is damaged, the conductive solution inside is released and fills up the open gap in interconnects. Another one is to separately embed the non-conductive components (e.g. TTF and TCNQ) into insulating microcapsules (e.g. PUF) [45]. Rupture of TTF-containing and TCNQ-containing microcapsules leads to the release of these two materials and the reaction between them results in the formation of the conductive crystalline salt. The conductivity of the crystalline TTF-TCNQ salt formed by the solution reaction can reach 5-10 S/cm, which is comparable to that of vacuum-deposited TTF-TCNQ films. The non-conductive precursors and damage-triggered reactions make this microcapsule system a promising technique for the restoration of conductivity in mechanically damaged electronic devices.

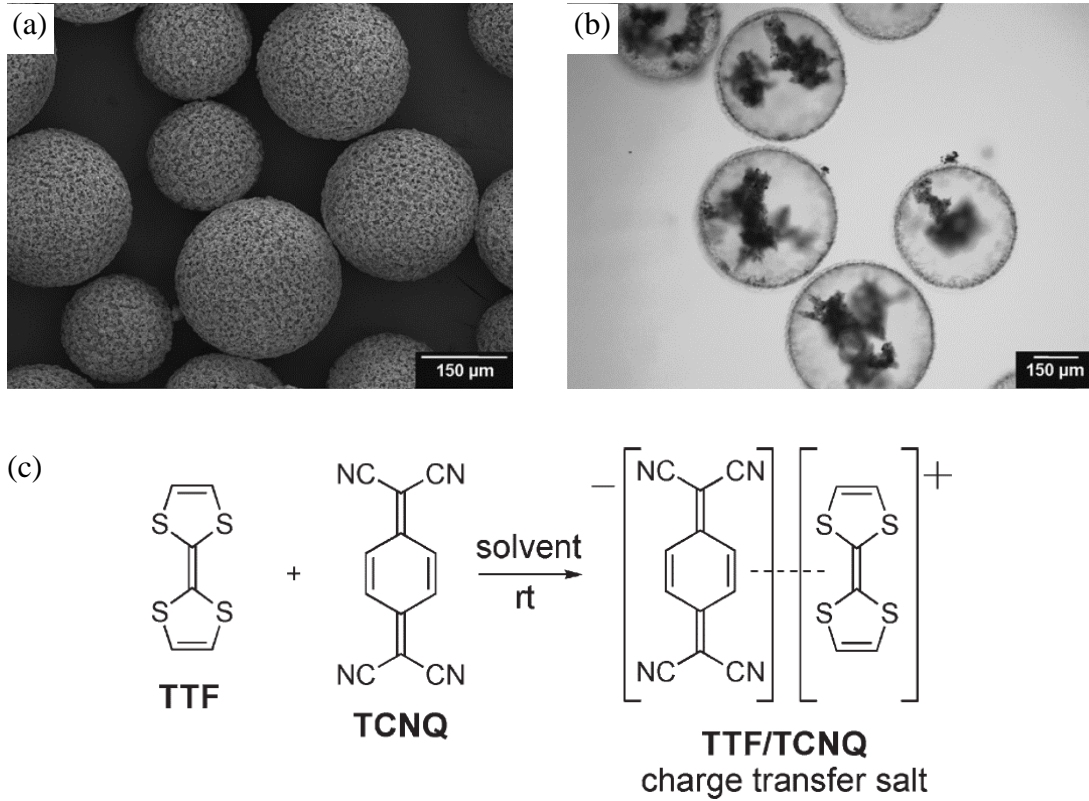


Figure 2.7 (a) SEM image and (b) optical micrograph of microcapsules containing SWNTs (0.05 wt%) suspended in PhCl [43] (c) reaction equation of the formation of the TTF/TCNQ charge-transfer salt [45].

2.3 Theoretical Models of the PBSH Technique

To understand the mechanism of the PBSH, we consider the case of an open-circuit fault taking place in a current-carrying interconnection. Before establishing the stable healing, conductive micro-particles have to go through three stages:

Stage 1: The formation of the single bridge

When the circuit suffers from mechanical stress, thermal stress, chemical corrosion or other external factors, an open circuit fault occurs in the interconnection. Upon the occurrence of this fault, an electric field (ξ_0), forms in the open gap:

$$\xi_0 = \frac{V}{L} \quad (2.1)$$

where V is the initial potential difference across the open gap and L is the length of this gap. Because of the existence of this electric field, the conductive particles in the suspension present in the open gap are polarised to have a dipole moment (p), which is calculated as:

$$|p| = 4\pi\beta\epsilon_f r_p^3 \xi \quad (2.2)$$

where ϵ_f is the permittivity of the fluid, β is the Claussius-Mossotti factor and r_p is the effective radius of the particles. The polarised particles in the suspension now experience dipole–dipole attractive forces (F_D), and this attractive force between two particles is scaled as:

$$F_D(t) \sim \frac{|p|^2}{\epsilon_f x(t)^4} \quad (2.3)$$

where $x(t)$ is the distance between particles at time t . This attractive force can drive particles moving in the suspension, causing a viscous drag force (F_v) opposing to the moving direction. According to Stoke's law, this drag force is scaled as:

$$F_v \sim \eta_f r_p \frac{dx}{dt} \quad (2.4)$$

with η_f being the viscosity of the fluid. By equating F_D and F_v , the time taken for the chaining up of one conductive bridge can be got:

$$t \sim \frac{\eta_f}{\epsilon_f \xi^2} \left(\frac{x}{r_p} \right)^5 \quad (2.5)$$

According to Equation 2.5, the chaining time for one bridge is proportional to x^5 . Replacing x with the initial distance between particles $d_p = x(t = 0)$, the chaining time can be scaled as:

$$t \sim \frac{\eta_f}{\epsilon_f \xi^2} \left(\frac{d_p}{r_p} \right)^5 \quad (2.6)$$

If the number of particles in unit volume is n_p , then d_p can be represented as:

$$d_p \sim (1/n_p)^{1/3} \quad (2.7)$$

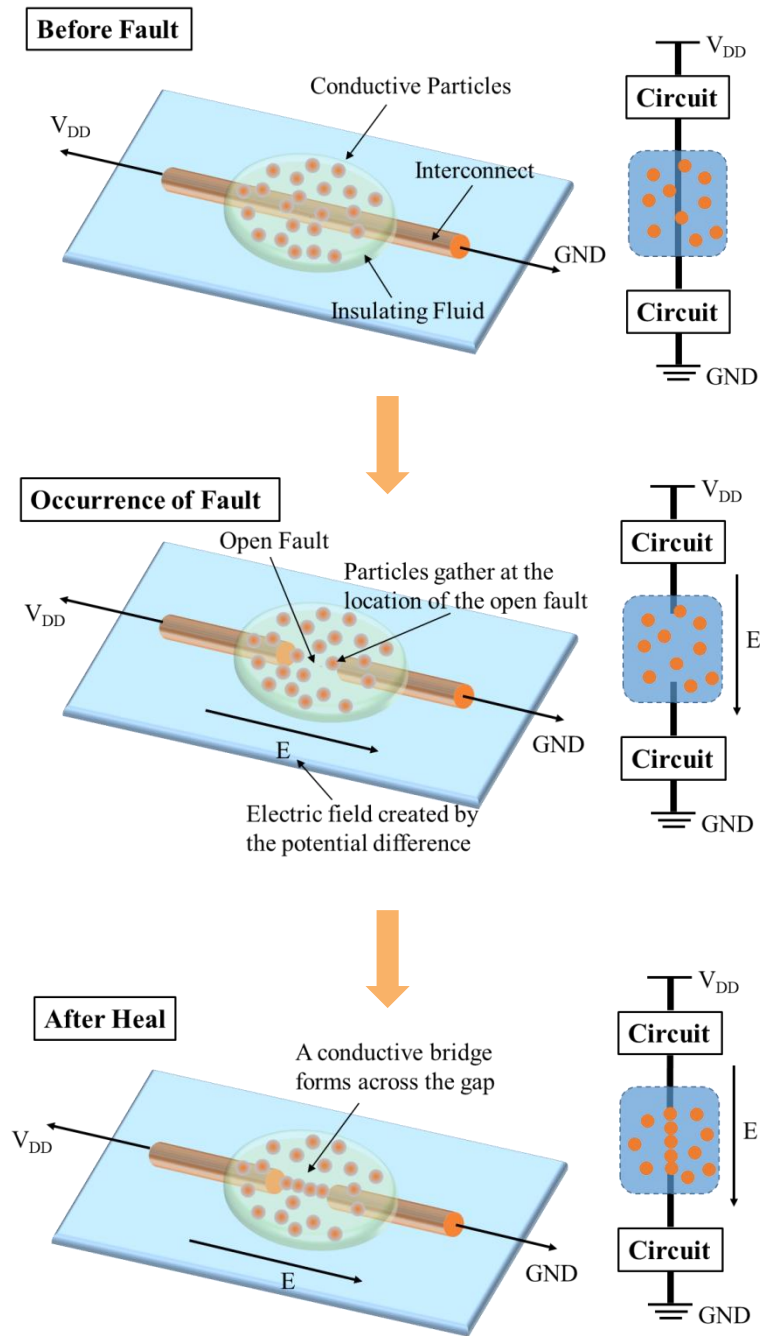


Figure 2.8. Illustration of the PBSH occurred at an open gap.

Stage 2: The formation of stable bridges

Generally, after the formation of the first conductive pathway, the strength of the electric field across the gap decreases. But the field still remains in the gap and drive particles to form new bridges. Eventually, multi-bridges can form across the gap and become the stable connection for the failed interconnects. While the impedance of the external circuit is Z_0 and the impedance of the healed bridge is Z_h , the electric field reduces by a factor of α :

$$\alpha = \frac{Z_h}{Z_0 + Z_h} \quad (2.8)$$

After the formation of the first healed bridge, the initial electric field ξ_0 reduces to $\alpha\xi_0$. And upon the formation of the j th bridge, the electric field changes to $\alpha^j\xi_0$. Thus, the effective time taken to stably heal the open gap is scaled as:

$$\begin{aligned} t_{eff} &= \sum_{n=0}^j t_n \sim \frac{\eta_f}{\epsilon_f} \frac{1}{\xi_0^2} \left(\frac{d_p}{r_p}\right)^5 \sum_{n=0}^j \frac{1}{\alpha^{2n}} \\ &\sim \frac{\eta_f}{\epsilon_f} \frac{1}{\xi_0^2} \left(\frac{d_p}{r_p}\right)^5 \frac{\alpha^2}{\alpha^{2j}(1-\alpha^2)} \end{aligned} \quad (2.9)$$

Stage 3: Sintering

Upon the formation of bridges across the open gap, the current flows through each of them. With time, in each bridge, the current causes Joule heating (Q), which is scaled as:

$$Q = \int_0^{t_1} \frac{L}{2r_p} R_p I^2 dt \quad (2.10)$$

where R_p is the mean impedance of the single metal particle. I is the current flowing through the bridge. This Joule heating leads to two changes in the healed bridge:

(a) The first change is the sintering of particles in the bridge. The current-caused heating accumulates in the bridge, especially at the contact points of the adjacent particles. Fig. 2.9 reveals the simulated result of the heat distribution in the particle-based bridge when a current flows through this bridge. The simulation was conducted by COMSOLTM Multiphysics 5.3.

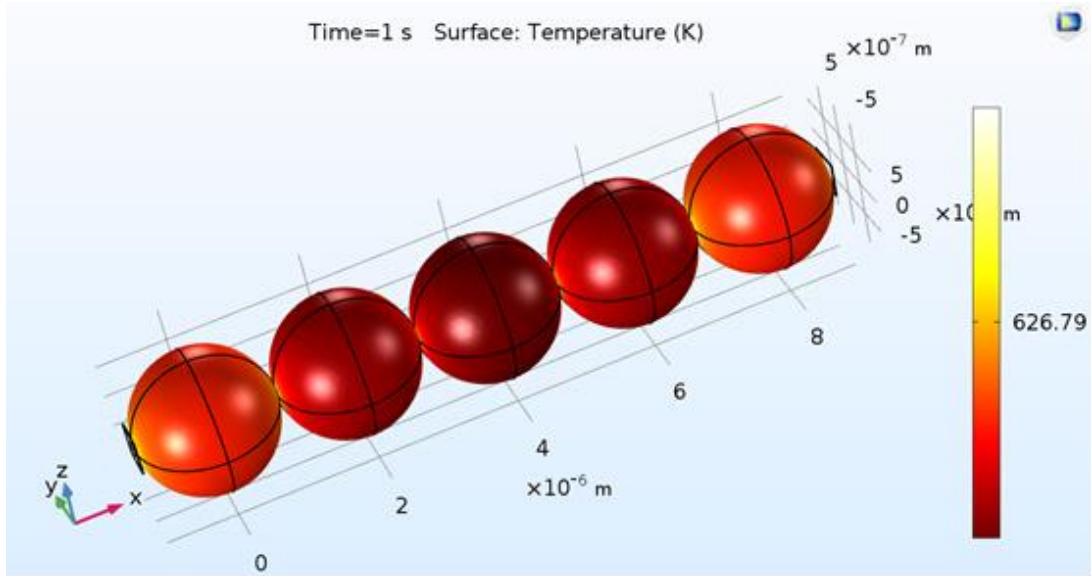


Figure 2.9. Simulated heat distribution in the particle-based bridge.

The yellow or white parts represent the extremely high density of heat and these parts are distributed at the contact points of the adjacent particles in Fig. 2.9. The high temperature melts a small amount of metal at the contact points and welds two particles together. The sintering creates a more stable structure for the healed bridge, and makes the bridge able to resist the repeated bending after the healing.

(b) The second change is the oxidation at the surface of metal particles. The heating accelerates the combination of oxygen molecules with metal atoms and the generation of the metallic oxide at the metal surface. The metallic oxide layer acts as a shell to protect the sintered bridge and make it stable against the ambient environment.

Fig 2.10 shows the scanning electron microscope (SEM) image of the sintered particle-particle binding [59]. In this image the melted particle-particle joint and the metallic oxide shell are observed, indicating the sintering and oxidation occurred in the healed bridge. With these changes, the discrete metal particles can unite together and form firm bridges across the open gap. These strengthened bridges can heal the open faults in interconnects and help the circuit resist mechanical or electrical stress.

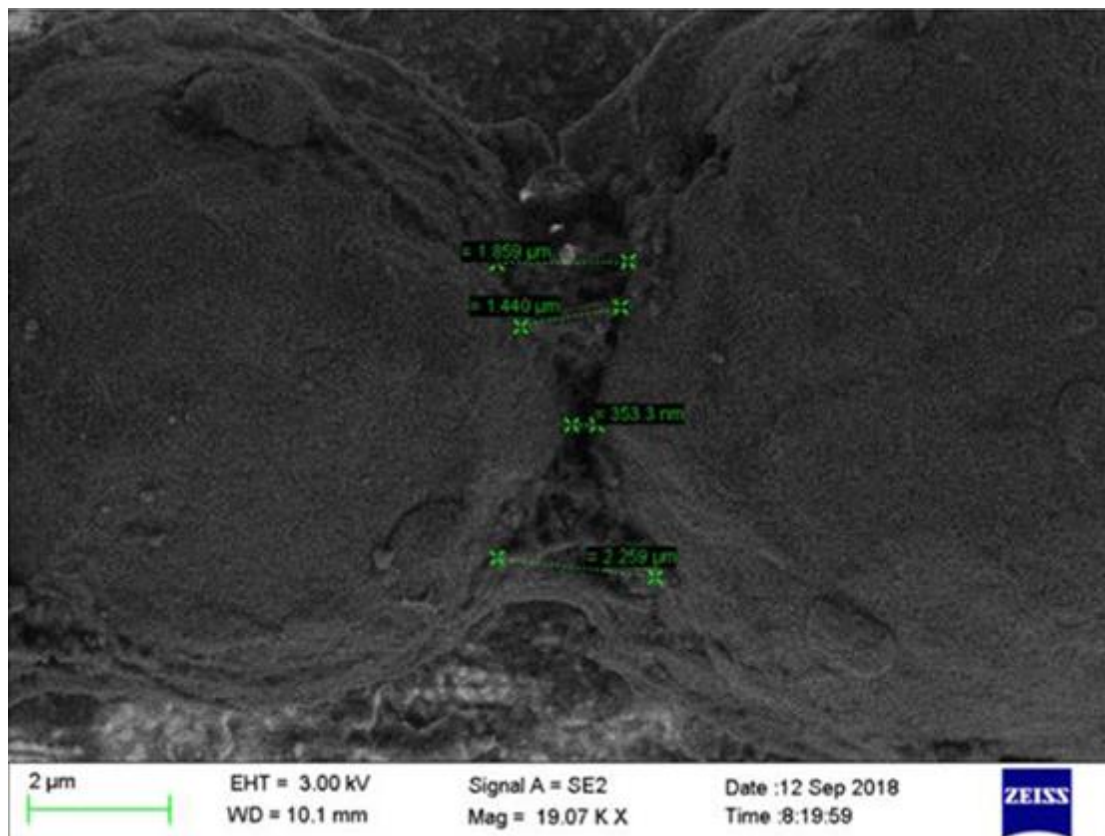


Figure 2.10. SEM image of the sintered particle-particle binding [59].

2.4 Advantages and Limitations of the PBSH Technique

The comparison of the PBSH technique with other reliability-improving techniques is summarised in Table 2.1.

Compared with all passive techniques, the PBSH technique has some obvious advantages. Firstly, passive techniques can only handle issues related to the mechanical stress, while the PBSH technique can deal with all interconnection failures caused by mechanical stress, electrical stress and chemical erosion. Secondly, passive techniques improve reliability by releasing mechanical stress in interconnects, but they cannot repair the open gap when open failure occurs in interconnects. As introduced in Section 2.3, the main function of the PBSH technique is to improve the reliability by realising the real-time repair in the open gap. So compared with passive techniques, the PBSH technique can provide longer range protection for the circuit.

The PBSH technique also has some advantages over other active techniques. Liquid metals use relatively rare materials (e.g., Ga, In), which are in the eutectic state. These increase the complexity of preparing materials. For the PBSH technique, the commonly-used materials are Ag or Cu particles, and insulating liquids like silicon oil. These materials are easily-achieved in the commercial market, making the PBSH an accessible technique for common users. In addition, LM–elastomer composite can only address mechanical-stress-related faults, while the PBSH technique can handle interconnect failures caused by other reasons.

The preparation of the conductive ink in microcapsules requires complex chemical reactions, making the fabrication process of the ink-filled microcapsules more complex than that of the suspension used in the PBSH technique. Moreover, this material faces the same challenge as liquid metals. Because the rupture of microcapsules can only be triggered by external force, the ink-filled microcapsules can only repair open faults caused by mechanical stress. Another challenge for this technique is that after the rupture of microcapsules, the insulating suspension turns into a conductive liquid. Different from using electric field-driven conductive particles to connect the open gap, this technique fills up the open gap with the conductive ink. However, if the suspension covers more than one wires, the conductive ink may lead to short failure in the circuit. Therefore, the suspension should only cover one wire and the confinement of the liquid should be conducted when applying it in the circuit.

Table 2.1 The comparison of the PBSH technique with other reliability-improving techniques.

	Simple Material	Simple Structure	Simple Fabrication Process	Resistant to the Mechanical Stress	Resistant to Other Stress	Healing Ability	Reference
Helical Coils	○	○	○	○	×	×	[22,23]
Meanders Design	○	○	○	○	×	×	[24,25,49]
Geometric Patterning of Substrates	×	×	×	○	×	×	[27,29,30,50]
Novel Materials	×	○	○	○	×	×	[31-36,40, 42,51,52]
Liquid Metals	×	○	×	○	×	○	[47,56]
Conductive Ink in Microcapsules	×	×	×	○	×	○	[43-46,58]
PBSH Technique	○	○	○	○	○	○	[48]

Each technique has its own strength and weakness. The PBSH technique has many advantages over other reliability-improving techniques, but it still faces some challenges before it can be put into real-world applications. The major one is the risk of short failure when applying the metallic micro-particle suspension in the circuit. As introduced in Section 2.3, metal particles in the open gap are driven by dipole–dipole attractive forces, which are generated by the potential difference across the open gap. However, in a working circuit, potential difference may exist not only in the open gap, but also between the neighbouring wires. The potential difference between the adjacent wires can generate an electric field and drive metal particles in the suspension to form an unexpected conductive bridge, leading to short failure in the working circuit. In addition, if the concentration of metal particles in the suspension is too high, conductive particles may contact to each other, making the suspension intrinsically conductive. To address this problem, it is necessary to set a threshold value of the electric field for the start of self-healing and to maintain the insulativity of the suspension. In this work, a chemical pre-treatment was used to coat metal particles with an insulating layer. This layer impedes the direct contact of the conductive particles, guaranteeing the intrinsic insulation of the suspension. Moreover, the electric field needed for driving metal particles with the insulating layer is higher than that for driving untreated metal particles, increasing the threshold value of the electric field for the start of the self-healing.

2.5 Chemical Coating of Metal Particles

To realise the practical application of healing an open fault in interconnects, a uniform and stable micro-particle suspension is required. When metal particles are directly added into the fluid media, these particles usually aggregate and sediment because of the poor compatibility between the metal particles and the fluid media. When applying such suspension in the failed circuit, the agglomerated particles are likely to cause an unexpected short. Therefore, an appropriate surface modification process is needed for the preparation of a uniform and stable suspension.

In this study, an effective way for the modification of particle surface was developed using the oleic acid (OA) as the ligand and silicon oil as the liquid for suspension. After this surface modification, the uniform dispersion of metal particles within silicon oil was achieved.

2.5.1 Preparation of the Suspension

A suspension of silver (Ag) particles in oleic acid with a concentration of 10 mg/mL was stirred furiously by a magnetic stirrer at 35 °C for 24 h. Then it was centrifuged at 4500 rpm for 20 min to remove the supernatant. The Ag particles were re-suspended in ethanol then centrifuged with the same setting (4500 rpm for 20 min) to remove the excess oleic acid. After three complete washing cycles in ethanol, Ag particles are dried overnight. Before using for self-healing, the optimised amount of oleic acid-coated Ag particles was added to silicone oil and mixed with a vortex mixer at 1000 rpm for 1 min. Then the suspension was sonicated in a water bath for 5 min.

2.5.2 Mechanism of Modification

The surface modification of the metal particle is a coordination reaction. In this reaction, the central metal atom or ion and the surrounding molecules or ions are linked by the metal–ligand bond, forming a coordination complex. The central metal atom or ion is known as the coordination centre and the surrounding molecules or ions are named as ligands or complexing agents. In addition, the atom within in the ligand which is bonded to the coordination centre is called the donor atom. Unlike the covalent compound, in which each atom contributes one electron to form the covalent bond, in coordination complex, the donor atom donates a pair of electrons and the central metal atom or ion accepts this electron pair to form the coordinate bond. In this work, the Ag ions (Ag^+) act as the coordination centre and oleic acid molecules and ions are served as ligands. The molecular structure of the oleic acid is shown in Fig. 2.11(a), the carboxylate radical $-\text{COOH}$ in molecular can be ionised to $-\text{COO}^-$ and H^+ .

The distribution of peripheral electrons for $-\text{COO}^-$ are shown in Fig. 2.11(b). In this radical ion, both oxygen atoms can act as the donor atom: they have the peripheral electron pairs which can be provided to form the covalent bond between the central atom (Ag^+) and ligand ($-\text{COO}^-$). So there are two types of single-bonded COOAg coordination complex. When the two donor atoms are linked with the same central atom and form a closed-loop structure, this mode of coordination is named as the bidentate coordination. Furthermore, the two donor atoms within the ligand can connect two central atoms, this type of connection is called a bridging coordination and the ligand in this connection is known as the bridging ligand.

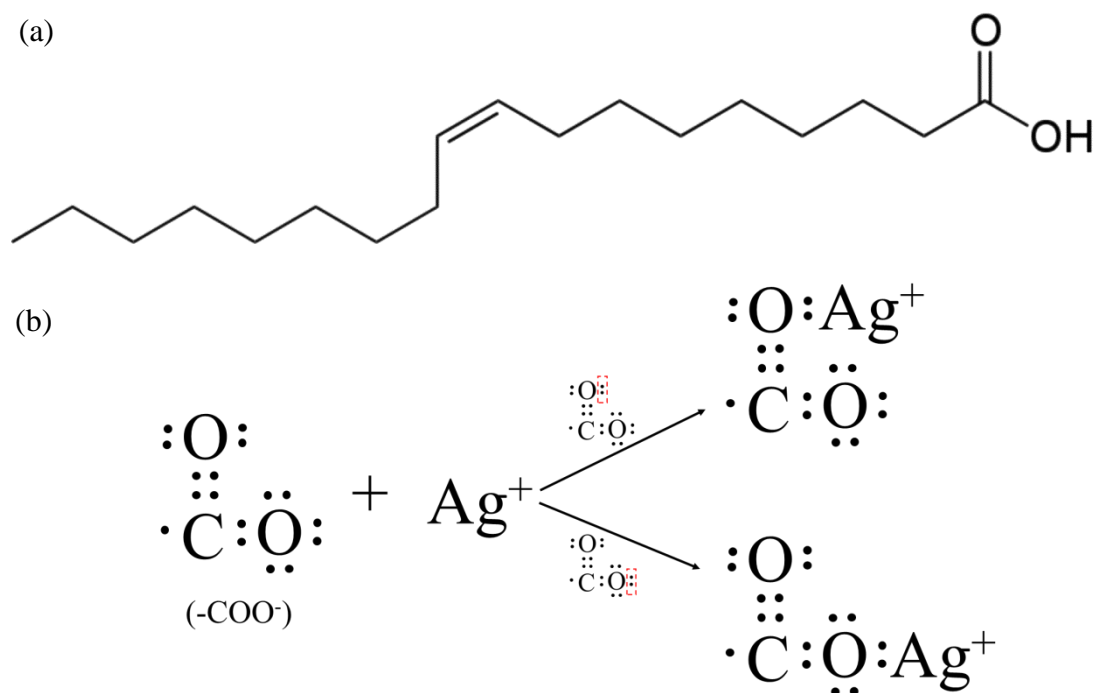


Figure 2.11. (a)Molecular structure of the oleic acid. (b) Formation of the covalent bond between the central atom (Ag^+) and ligand ($-\text{COO}^-$).

Fourier transform infrared (FTIR) spectra of Cu and Ag particles treated by oleic acid and the oleic acid-olamine mixture were recorded and shown in Fig. 2.12. The range of the wave number is from 400 cm^{-1} to 4000 cm^{-1} . Two conclusions can be drawn from this FTIR spectra. The first one is the correspondence of wave peaks. The oleic acid-treated metal particles have the similar FTIR spectra with the oleic acid, indicating the successful modification of the metallic surface. The second conclusion which can be drawn from the FTIR spectra is the mode of the coordination. The absorption bands of the $-\text{COO}^-$ group in the FTIR spectra are 1630 , 1562 , 1463 , 1420 cm^{-1} . The carboxylate coordination mode can be deduced from the position and separation (Δ) of $-\text{COO}^-$ bands in the $1300 - 1700\text{ cm}^{-1}$ region [60-63]. These modes include the ionic, unidentate, bidentate, and bridging coordination. For $\Delta < 110\text{ cm}^{-1}$, the bidentate mode is confirmed, whereas for $140 < \Delta < 200\text{ cm}^{-1}$, the bridging coordination is expected. When $\Delta > 200\text{ cm}^{-1}$, the unidentate ligands exist in the coordination complex. For oleic acid-treated Ag particles used in this work, the separation of the two major peaks at 1420 and 1562 cm^{-1} is 142 cm^{-1} , indicating that the major mode of the oleic acid-Ag coordination is the bridging coordination. The difference between the two shoulder

peaks 1463 and 1630 cm^{-1} is 167 cm^{-1} , further proving that the bridging mode dominates the oleic acid-Ag coordination.

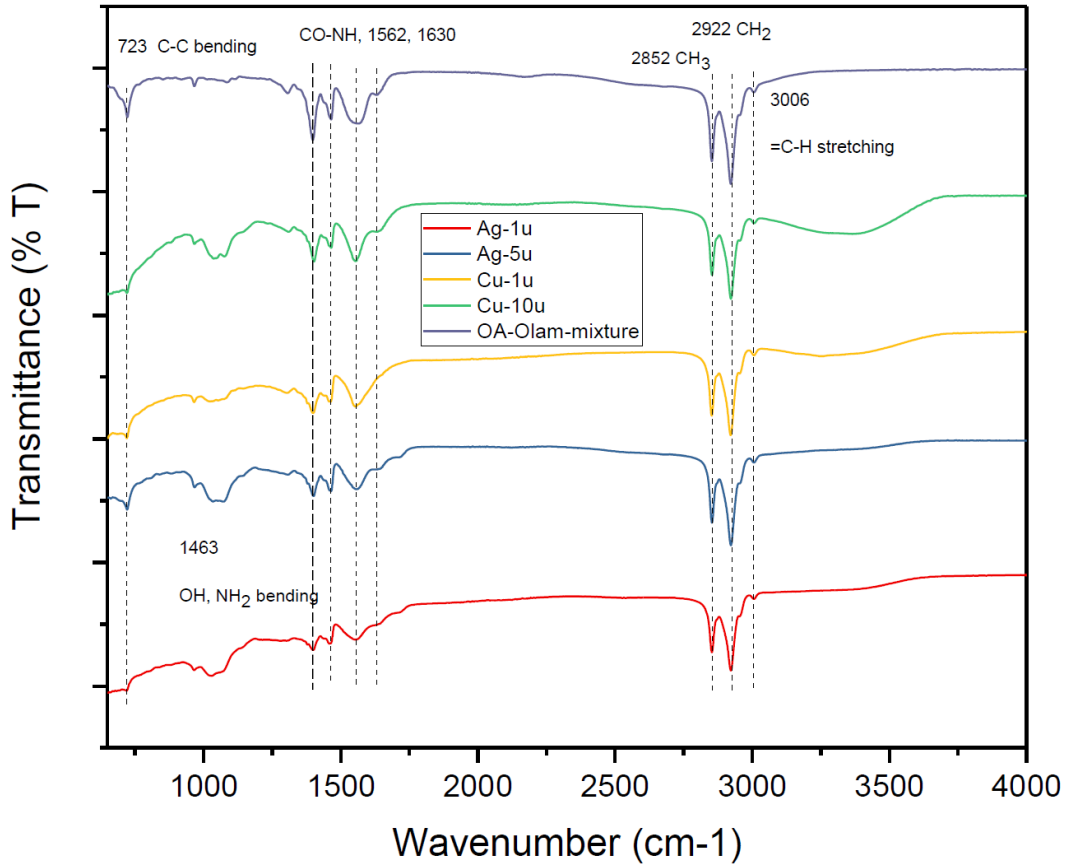


Figure 2.12. FTIR spectra of oleic acid-treated Cu and Ag particles and the oleic acid-olamine mixture.

The surface modification of the metal particle can improve its suspension behaviour in the fluid media. In the suspension system, the dominant factor affecting the suspension behaviour is the surface forces between particles. In the particle-based suspension system, van der Waals attraction between neighbouring particles is the main driving force triggering agglomeration of particles. If particles agglomerate and form the larger cluster, the force exerted on the agglomerated cluster (mainly the gravity) becomes the dominant force, resulting in the sedimentation of the agglomerated particles. The van der Waals attraction between two particles can be calculated as:

$$F_{vdW} \cong -\frac{r}{12} \left[\frac{(\sqrt{A_{medium}} - \sqrt{A_{ligand}})^2}{D} + \frac{(\sqrt{A_{ligand}} - \sqrt{A_{particle}})^2}{D+2L} + \frac{(\sqrt{A_{medium}} - \sqrt{A_{ligand}})(\sqrt{A_{ligand}} - \sqrt{A_{particle}})}{D+L} \right] \quad (2.11)$$

where r is the radius of particles, L is the layer thickness of the treatment agent, D is the distance of the neighbouring particles, and A_i ($i = \text{medium, ligand, and particle}$) is the Hamaker constant of corresponding materials [64, 65]. This constant is calculated by the following equation:

$$A_i = \frac{3}{4} k_B T \left(\frac{\varepsilon_i - \varepsilon_{vac}}{\varepsilon_i + \varepsilon_{vac}} \right)^2 + \frac{3h\nu_e(n_i^2 - n_{vac}^2)^2}{16\sqrt{2}(n_i^2 + n_{vac}^2)^{3/2}} \quad (2.12)$$

where k_B is the Boltzmann constant (1.38×10^{-23} J/K), T is the absolute temperature, ε_i and ε_{vac} are the static dielectric constant of corresponding materials and vacuum. h is the Planck constant (6.626×10^{-34} J·s) and ν_e is the electronic absorption frequency ($\sim 3 \times 10^{15}$ s⁻¹). n_i and n_{vac} are the refractive index of corresponding materials and vacuum. The specific parameters for different materials and the calculated Hamaker constant values are listed in Table 2.2.

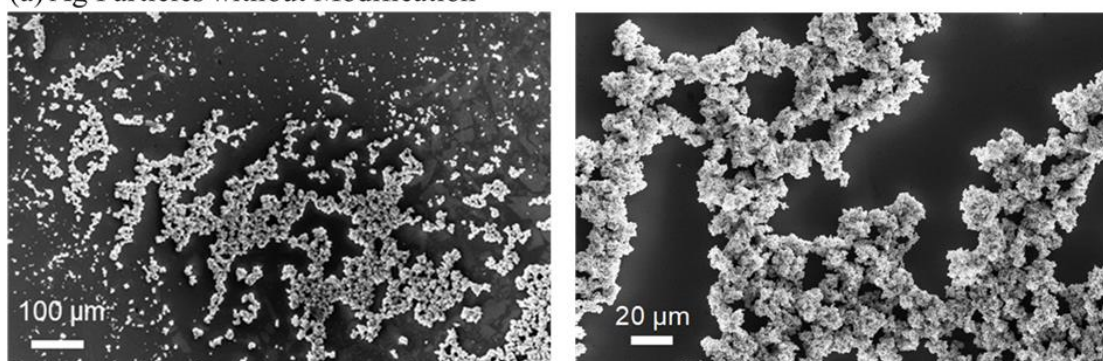
Table 2.2 Parameters and calculated Hamaker constant for different materials.

	ε_i	n_i	A (10^{-20} J)
Ag	3.45	0.12	25.15
Oleic Acid	2.46	1.38	4.39
Silicon Oil	2.40	1.41	5.03

Using the parameters in Table 2.2, assuming the separation distance between the adjacent particles to be $D \approx 1 \mu\text{m}$, and ignoring the thickness of the ligand layer, the van der Waals attraction force between neighbouring particles can be calculated by Equation 2.11. Without the surface modification, the van der Waals attraction force between Ag particles is calculated as $3.81k_B T$. After the surface modification, this attraction force decays to $1.63k_B T$. Therefore, the possibility of the agglomeration and the sedimentation can be reduced and the suspension with better uniformity and stability can be achieved. Fig. 2.13 gives the images taken by the field emission scanning electron microscope (FESEM). The untreated Ag particles agglomerated and formed the clusters with large size ($APS > 20 \mu\text{m}$). After the oleic acid modification, Ag particles were observed to be uniformly dispersed ($APS < 4 \mu\text{m}$) in the hexane. To evaluate the stability of the suspension, the untreated and treated suspensions with different Ag particle concentrations (10, 20, 40 mg/mL) were prepared and settled for 35 days. Fig. 2.14(a) shows the settling behaviour of the untreated and oleic acid treated Ag particles suspended in silicone oil observed on day 0, 3 and 7. It could be observed

that the obviously faster sedimentation of Ag particles occurred in the suspension with untreated Ag particles. The stability of the suspension with oleic acid treated Ag particles could be further proved by the UV-Visible absorption spectra shown in Fig. 2.14(b). The light absorption of the suspension with oleic acid treated Ag particles was 7 times higher than that of the suspension with untreated Ag particles, on both day 0 and day 35, indicating the larger range of the distribution of particles in the fluid. These results evidenced the lower agglomeration and sedimentation rate of the modified Ag particles, thus further proved the better stability of this suspension.

(a) Ag Particles without Modification



(b) Ag Particles with Oleic-acid Modification

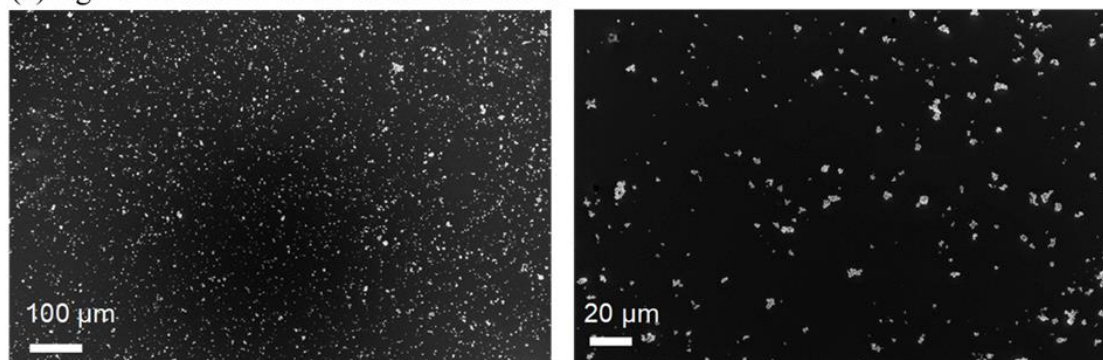


Figure 2.13. FESEM images of (a) untreated and (b) oleic acid treated Ag particles suspended in hexane and drop-casted on silicon wafer.

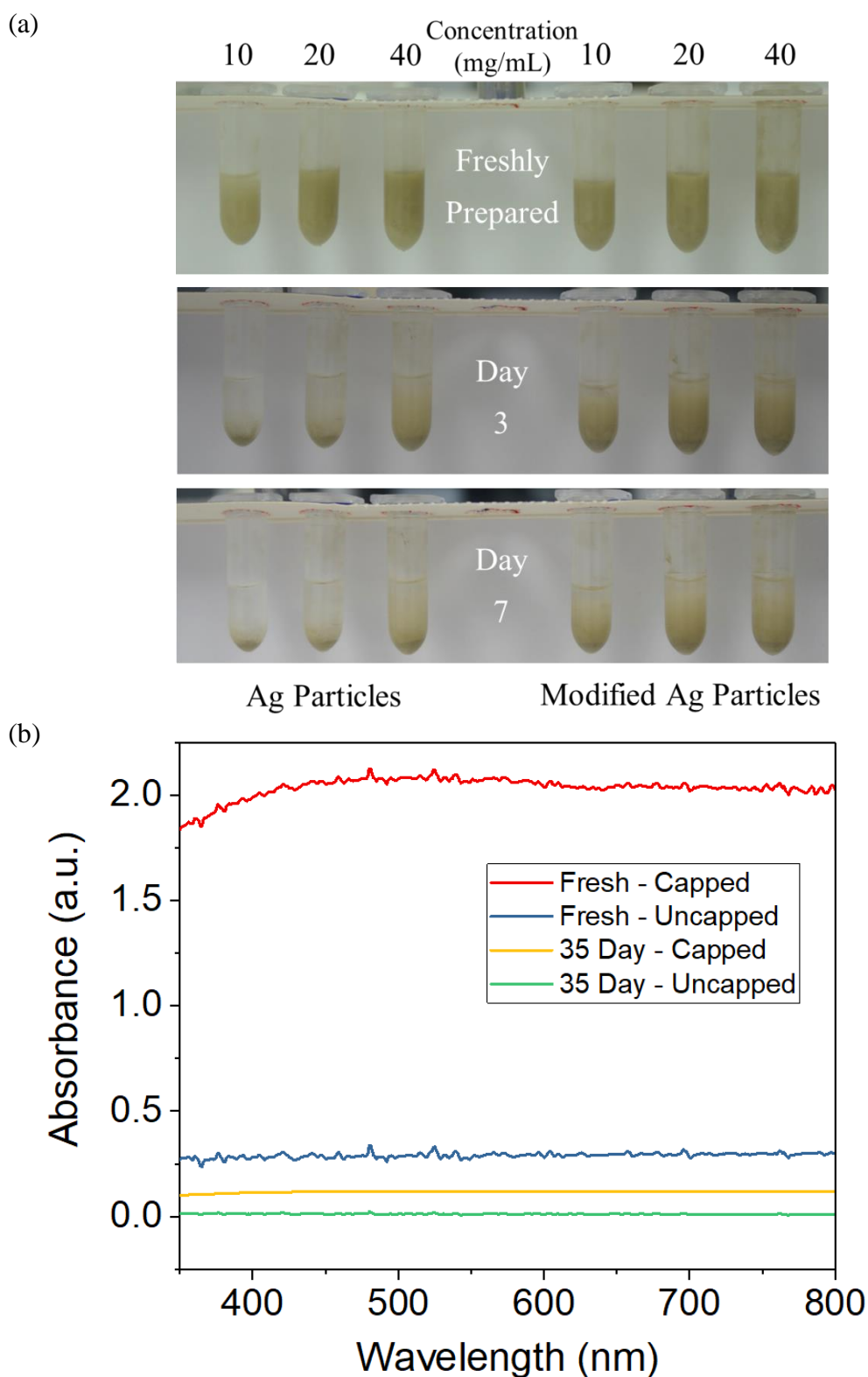


Figure 2.14. (a) Photographs illustrating the settling behavior of untreated and oleic acid treated Ag particles suspended in silicone oil with varying concentrations observed on day 0, 3, and 7. (b) UV-Visible absorbance of the freshly prepared and 35-day settled untreated and oleic acid treated Ag particles.

2.6 Summary

In this chapter, some passive and active strategies developed for improving the reliability of interconnects are reviewed. The mechanism of the PBSH technique developed in this work is analysed and the physical models are built in this chapter. To achieve the uniform and stable suspension, a method of modifying the particle surface using the oleic acid (OA) has been developed in this study. After the modification, Ag particles become inherently insulating, which can avoid the unexpected short of the adjacent interconnects when applying a particle-based suspension in the circuit. Simultaneously, the agglomeration and sedimentation rate of particles can be slowed down by surface modification. The suspension containing the modified Ag particles and silicon oil are the basic chemicals for healing open faults in interconnects, and the detailed process of healing will be analysed in the following chapters.

3 INKJET-PRINTED ORGANIC THIN-FILM TRANSISTORS

As described in Chapter 1, due to the advantages of the mechanical flexibility and the low-temperature processibility, the OTFT becomes an ideal candidate for manufacturing flexible circuits, thus it is selected as the key component in this study. For the fabrication of OTFT devices and circuits, inkjet printing technique is applied.

In this chapter, basic factors about the OTFT are reviewed. These include the carrier transport in organic semiconductor (OSC) materials, device structures, basic materials and fabrication processes. Moreover, the inkjet printing process and the characterisation of OTFTs fabricated in this work are described in detail.

3.1 Carrier Transport in Organic Semiconductor Materials

In conventional semiconductors like silicon (Si) or germanium (Ge), atoms are connected by the covalent bond, the charge carriers are transported in delocalised states. In that case their transport is mainly limited by the thermally induced lattice deformations [66]. But in low conductive organic semiconductors, its semiconductivity is caused by the sp^2 hybridisation of carbon atoms. The electron structure of a carbon atom is $1s^2 2s^2 2p^2$. There are two electrons in the third orbit, which is also the outermost orbit of the carbon atom. When carbon atoms are connected in the organic molecules, the orbital hybridisation occurs because of the interaction of the electron wave function. As shown in Figure 3.1, one 2s orbit and two 2p orbits hybridise, forming three equivalent hybrid orbits. These orbits are in one plane (with 120° angles) and they are called sp^2 hybrid orbits. The remaining 2p orbit forms a p_z orbit which is perpendicular to the plane of sp^2 orbits. The sp^2 hybrid orbits can form a strong covalent bond with

the adjacent carbon atoms, which is named as the σ -bond. The bonding force in the σ -bond is so strong that electrons can hardly transport in this bond. However, the bond between the adjacent p_z orbitals, which is called the π -bond, is much weaker than the σ -bond. The weak force in π -bond makes it easy for electrons to transport inside it, thus contributing to the semiconductive characteristics of the organic semiconductor.

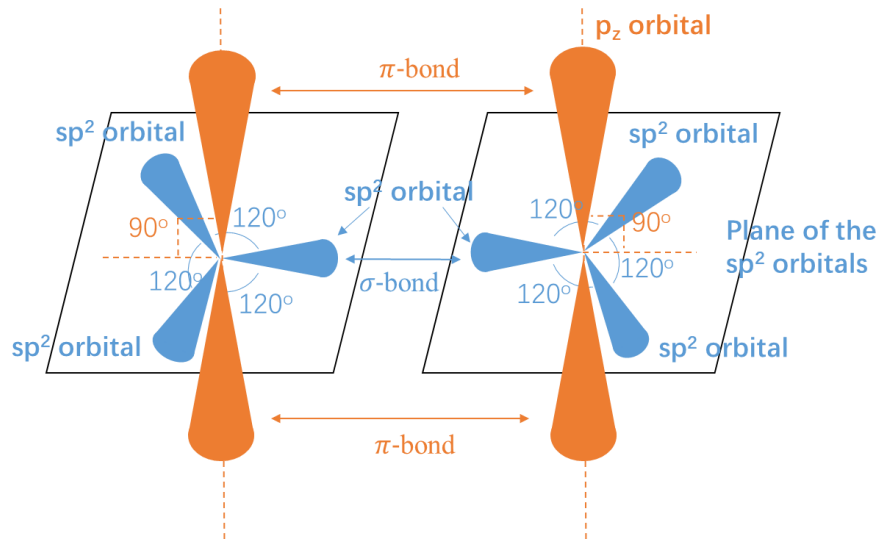


Figure 3.1. sp^2 hybridisation of two carbon atoms, sp^2 orbitals are connected by σ -bond in one plane, while p_z orbitals (perpendicular to sp^2 plane) are connected by π -bond.

To describe the charge carrier transport in the OSC material, a range of physical models have been developed over the past 30 years, and two widely-accepted models are listed as follows:

3.1.1 Hopping Model

The first model is the *Hopping model*. In this model it simply estimates that the mean free path of charge carriers is shorter than the average atomic distance. So the hopping of charge carriers between the localised states is the main transport method in OSC materials. Compared with the conventional Si semiconductor whose charge carrier transport occurs in delocalised states, the OSC material has the inverse temperature response. That is because in delocalised transport, the charge carrier transport is limited by phonon scattering, here phonons are mainly created by thermally induced lattice deformations [66]. But in localised transport, the charge carrier transport is assisted by phonons. So in the Hopping model, charge mobility increases with

temperature in OSC materials, and the temperature dependence of the mobility is described as:

$$\mu = \mu_0 \exp[-(T_0/T)^{1/\alpha}] \quad (3.1)$$

where α is a constant ranging from 1 to 4.

3.1.2 Multiple Trapping and Release Model

In the *Multiple Trapping and Release (MTR) model*, during charge carriers' transport through the delocalised levels, they interact with the localised levels by trapping and thermal release [66]. In this transport process two assumptions are made: one is that carriers arriving at a trap will be trapped instantaneously, the other one is that the release of trapped carriers is a thermally-related process. The electrons drift in the extended states near E_c , and the time a charge carrier takes in the localised states is included in the total transport time, so the drift mobility in this model is described as:

$$\mu_D = \mu_0 \alpha \exp(-\frac{E_t}{kT}) \quad (3.2)$$

where μ_0 is the mobility in the delocalised band, which is near the bottom of the extended states. α is the ratio of the effective density of states at the delocalised band edge to the density of traps. E_t equals to $E_c - E$, which is the difference between the delocalised band edge and the trap level.

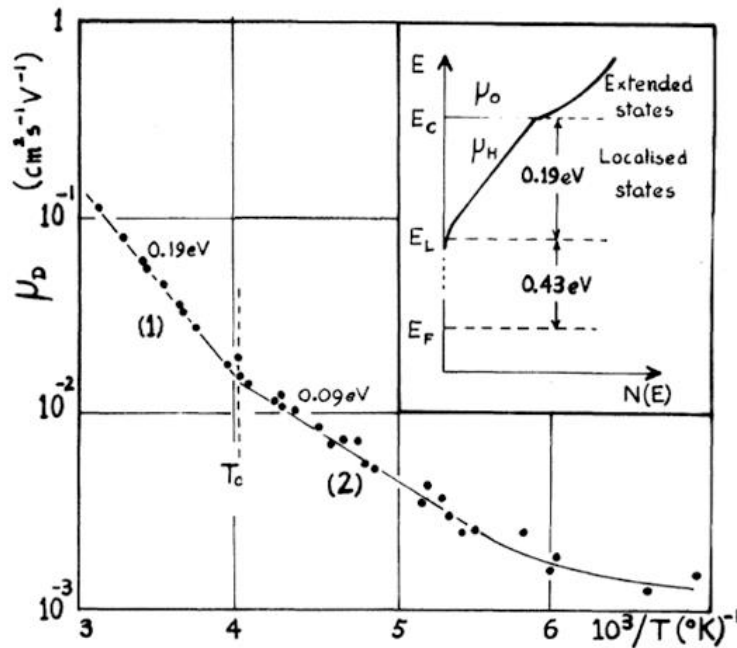


Figure 3.2. Temperature dependence of the electron drift mobility μ_0 (Inset) model of the electronic-state distribution in an amorphous solid [64].

3.2 OTFT Structures

Conventionally, OTFT devices have six parts: substrate, gate (G) electrode, dielectric layer, source (S) and drain (D) electrodes, semiconductor layer and passivation layer. If the gate electrode is deposited before the source/drain electrodes, the device is classified as a bottom-gate structure, conversely, it is a top-gate structure. If source/drain electrodes are deposited on the semiconductor layer, the device is defined as a top-contact structure, conversely, it is a bottom-contact structure. As shown in Fig. 3.3, depending on the relative location of these layers, the device structure can be divided into four categories: the inverted staggered (bottom-gate top-contact, BGTC), the coplanar (top-gate top-contact, TGTC), the inverted coplanar (bottom-gate bottom-contact, BGBC) and the staggered (top-gate bottom-contact, TGBC) structures.

When selecting the device structure in this study, the first choice is to decide whether to use the bottom-gate (inverted coplanar and inverted staggered) structures or the top-gate (coplanar and staggered) structures. In solution processes, bottom-gate structures are preferred because they are more process-compatible. In OTFT the semiconductor layer is the most sensitive and can easily be affected by impurities from other layers. And in bottom-gate structures, the semiconductor layer is deposited after the deposition of the dielectric layer, so these structures can avoid the influence on the semiconductor from other layers. When comparing the inverted staggered (top-contact) structure and the inverted coplanar (bottom-contact) structure, the former one has a larger effective contact area between source/drain electrodes and the semiconductor layer [67, 68]. So the carrier injection is more efficient and many reported OTFTs with high-mobility have been fabricated using this structure [69, 70]. However, in solution-based processes, when depositing metal electrodes onto the semiconductor layer, it is easy to implant impurities into the semiconductor material. In addition, the conventional photolithography patterning process may damage the semiconductor layer (for example, when etching or lifting off the photoresist layer). These unexpected circumstances may cause the failure of the semiconductor material. So top-contact structures bring a big challenge to the fabrication process. For bottom-contact structures, semiconductor layer is formed after the deposition of metal electrodes, avoiding the impurities from the post-process. Another advantage of bottom-contact structures is that a thiol self-assembled monolayer (SAM) can be applied to the metal surface to lower the contact barrier and get a better ohmic metal/semiconductor contact [71]. In

this work, the inverted coplanar (BGBC) structure was selected. Because the dielectric layer is formed before the deposition of the semiconductor layer and the dielectric material can be cross-linked. In this structure materials in different layers do not interfere and can maintain their functionalities well.

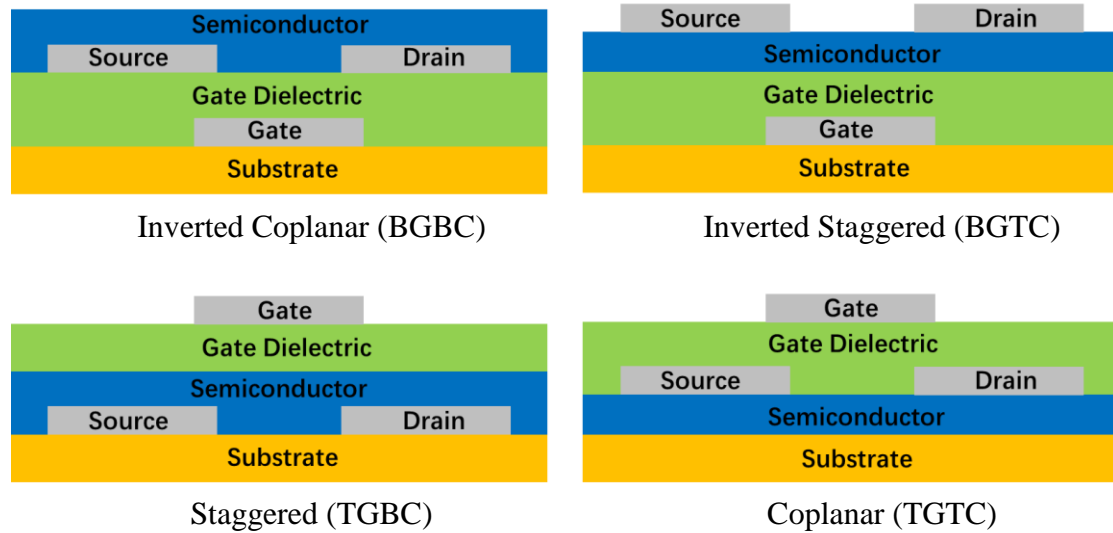


Figure 3.3. Illustration of the OTFT device structures.

3.3 OTFT Materials

As described in the above section, OTFTs typically have six parts: substrate, gate electrode, dielectric layer, source/drain electrodes, organic semiconductor (OSC) layer and passivation layer. In this section, materials for respective parts are introduced.

3.3.1 Substrate

Like other TFTs, the commonly-used substrates for fabricating OTFT devices are glass slides or silicon (Si) wafers. In recent years to meet the requirement in flexible and wearable electronics, OTFT devices and circuits are frequently manufactured on plastic [3, 72, 73] and paper [74, 75] substrates. Fig. 3.4 gives some examples of plastic substrates. For plastic and paper substrates, the main threat in the device fabrication process is the damage caused by high temperatures. Therefore, low-temperature processibility of OTFT makes it an ideal candidate to eliminate this threat.

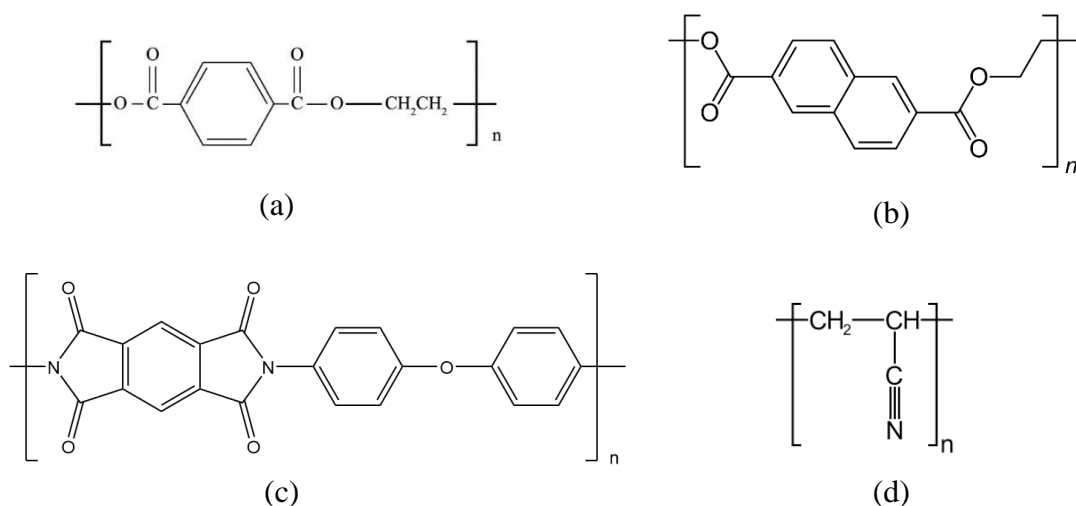


Figure 3.4. Molecular structures of four plastic substrates: (a) Polyethylene Terephthalate (PET), (b) Polyethylene Naphthalate (PEN), (c) Polyimide (PI), (d) Polyacrylonitrile (PAN).

In this work, there are several requirements for the substrate. First, to prove the compatibility with flexible displays and sensors, a transparent film with no colour is preferred. In this regard PAN and PI are excluded since they are non-transparent or have colours. Second, the surface roughness is significant as it determines the morphology of the deposited film. The rough surface of the film generates defects at the interface which degrade the device performance. Therefore, a substrate with low surface roughness is expected. Third, in the solution process, the wettability of the substrate surface is also important as it determines the uniformity of the film formed by the deposition of the liquid drops. With these considerations, a 125 μm -thick transparent PEN film is selected in this work. Fig. 3.5 shows the atomic force microscopy (AFM) image of PEN and CorningTM glass. The root-mean-squared (rms) roughness for PEN and glass are 1.6 nm and 0.8 nm. This means in terms of the surface roughness, PEN film is comparable with CorningTM glass, which is widely used in the display industry to manufacture panels. Fig. 3.6 shows the contact angles of deionised (DI) water droplets on the two substrates. The average contact angles of 80.60° on the PEN film and the 34.67° on the CorningTM glass indicate that both substrates are hydrophilic, and the PEN surface has a smaller interfacial surface energy. In the inkjet printing process, a hydrophilic substrate with smaller interfacial surface energy is expected, as the spread of the ink droplets would be limited, which can help with the

control of the morphology of printed patterns. So a more precise pattern and uniform film can be achieved on the PEN substrate when applying solution process.

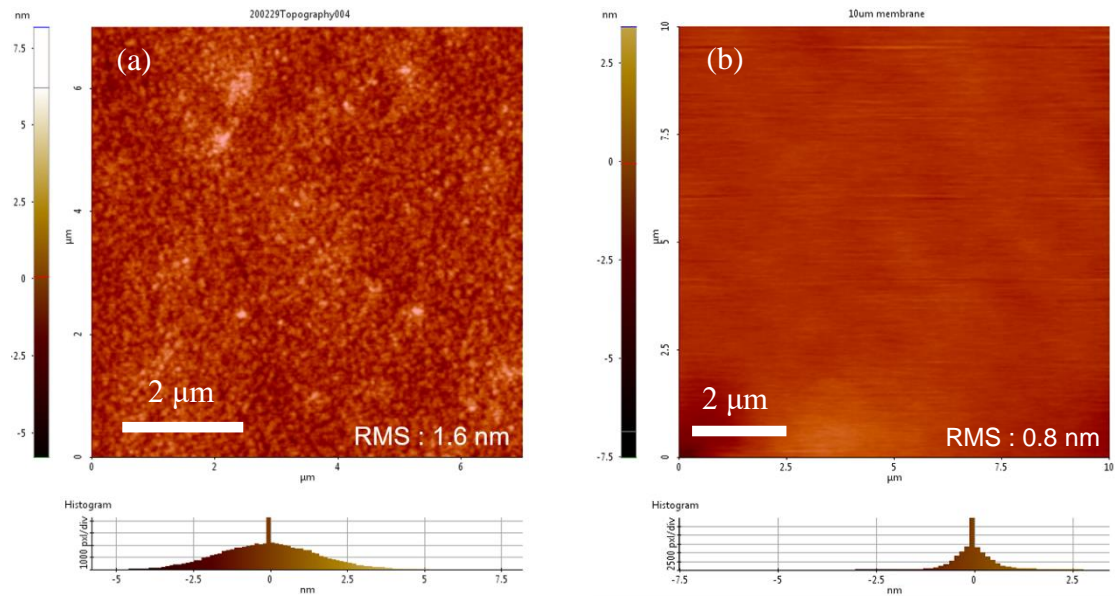


Figure 3.5. The AFM topographic images of the surface of: (a) PEN film, (b) Corning™ glass.

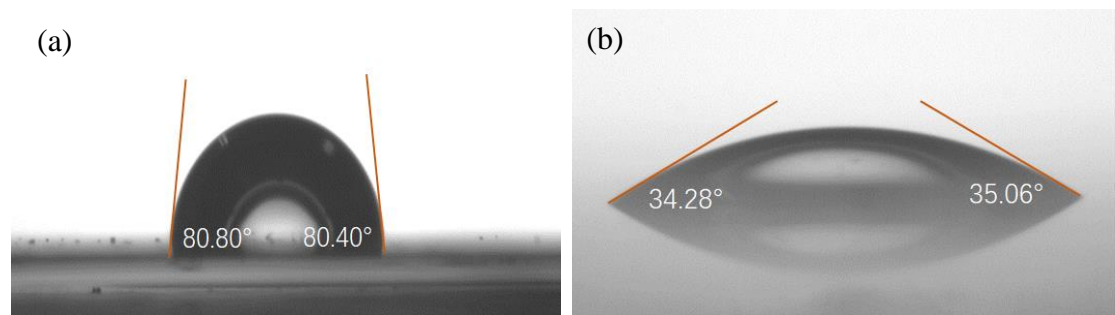


Figure 3.6. The contact angles of the DI water droplets on the surface of: (a) PEN film, (b) Corning™ glass.

3.3.2 Electrodes

The most popular and widely-used electrode materials in industry are metals (such as gold (Au), silver (Ag), copper (Cu), aluminium (Al), etc.). Metals have high conductivity and are abundant in the nature. Since these materials are generally in bulk forms in the natural state, electrode films are usually deposited by the thermal evaporation. In this process precisely-patterned shadow masks or photoresist layers are needed, and an ultra-high vacuum environment is required, increasing the complexity

and the cost of fabrication. To address this issue, researchers have worked on making metals into printable inks. Generally, there are two strategies: synthesising nanoparticles and metallising metal salts. The former one is to use chemical reactions to synthesise nano-scale particles, which are dispersed in the liquid. By annealing this nanoparticle suspension, the conductive metal bulk can be achieved [76-78]. The later method is to apply a metal salt, which is highly dissolved in the solvent. With the redox reaction, the metal salt can be transferred into metals [79, 80]. Comparing these two methods, the former one is preferred because residues of salts are unavoidable in the solvent and these impurities can influence device performance.

In an OTFT device, the gate electrode controls the depth of the channel and the density of charge carriers in the channel. Source/drain electrodes directly contact the semiconductor, controlling the injection and collection of charge carriers. The ideal assumption is that there is no barrier at the metal-semiconductor junction, which is called the ohmic semiconductor/metal contact. In that case the work function of the source/drain electrodes should match the highest occupied molecular orbital (HOMO) level in p-type OSC or the lowest unoccupied molecular orbital (LUMO) level in n-type OSC. However, a contact barrier exists between most OSCs and metals (for example, most p-type OSCs' HOMO levels are higher than 5 eV while most metal work functions are lower than 5 eV), so in real circumstances, the contact between source/drain electrodes and the OSC is a Schottky semiconductor/metal contact. To lower the Schottky-barrier height, source/drain electrodes are treated by self-assembled monolayers (SAMs) [81, 82]. Fig. 3.7 shows two types of SAMs materials. SAMs can increase or lower the work function of the electrode metal due to the dipole moment of the molecule [83].

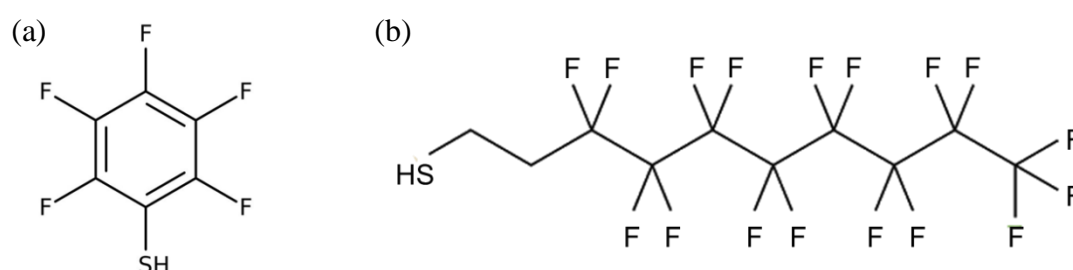


Figure 3.7. Molecular structures of two SAMs materials: (a) Pentfluoro-benzenethiol (PFBT), (b) 1H,1H,2H,2H-Perfluorodecanethiol (PFDT).

In this work, a commercially synthesised Ag nanoparticle ink was selected. And Pentafluorobenzenethiol (PFBT) was used to modify the Ag source/drain electrodes. The work function of the bare Ag is 4.26 eV, and after the PFBT treatment the work function increases to 5.2 eV. Given the HOMO of TIPS-pentacene as 5.4 eV [84, 85], the height of Schottky-barrier between Ag and TIPS-pentacene narrows from 1.14 eV to 0.2 eV after the PFBT treatment of the Ag electrode. In addition, the sheet resistance of the printed Ag bulk is measured as 25 ~ 30 Ω /sq.

3.3.3 Organic Semiconductor (OSC)

The OSC layer is a critical component in OTFTs, since it provides the channel for the transport of charge carriers. According to the type of major charge carriers, OSC materials can be categorised into n-type and p-type semiconductors. And based on the molecule size, OSC materials can be categorised into small molecule and polymer semiconductors. The p-type OSCs were developed earlier than n-type OSCs, and they are also the most common for both small molecule and polymer semiconductors. One reason is that electrons are prone to being trapped at the interface of the gate dielectric, and that the barrier for electron injection is higher than that for the hole injection because the work function of accessible materials for the electrode is relatively high [86, 87]. In 1986 the first OTFT was fabricated utilising a p-type OSC, polythiophene. At that time the carrier mobility was only 10^{-5} cm^2/Vs [88]. Later a lot of OSC materials were synthesised and the material performance has been greatly improved. Typical OSC materials including both small molecule and polymer semiconductors are summarised in Fig. 3.8. In these materials, regioregular poly (3-hexylthiophene-2,5-diyl) (rr-P3HT) was a widely-used polymer OSC in the 1990's, and its carrier mobility ranged from 0.001 to 0.1 cm^2/Vs [89, 90]. The requirement for higher mobility has pushed the development of more polymer OSCs. These newly-developed materials include regioregular poly-quaterthiophenes (rr-PQTs) (0.14 cm^2/Vs) [91], poly[2,5-bis(3-dodecylthiophen-2-yl)thieno[3,2-b]thiophene] (PBTTT) (0.1 - 0.6 cm^2/Vs) [92, 93], poly[(9,9-din-octylfluorenyl-2,7-diyl)-alt-(benzo[2,1,3]-thiadiazol-4,8-diyl)] (F8BT) (0.4 cm^2/Vs) [94], and poly[(4,4-bis(2-ethylhexyl)cyclo-penta[2,1-b:3,4-b']dithiophene)-2,6-diyl-alt-[1,2,5]-thiadiazolo[3,4-c]pyridine] (PCD-TPT) (0.45 cm^2/Vs) [95]. Compared with the early OSCs like rr-P3HT, these polymer OSCs have made large progress in the material performance. But their mobilities still did not

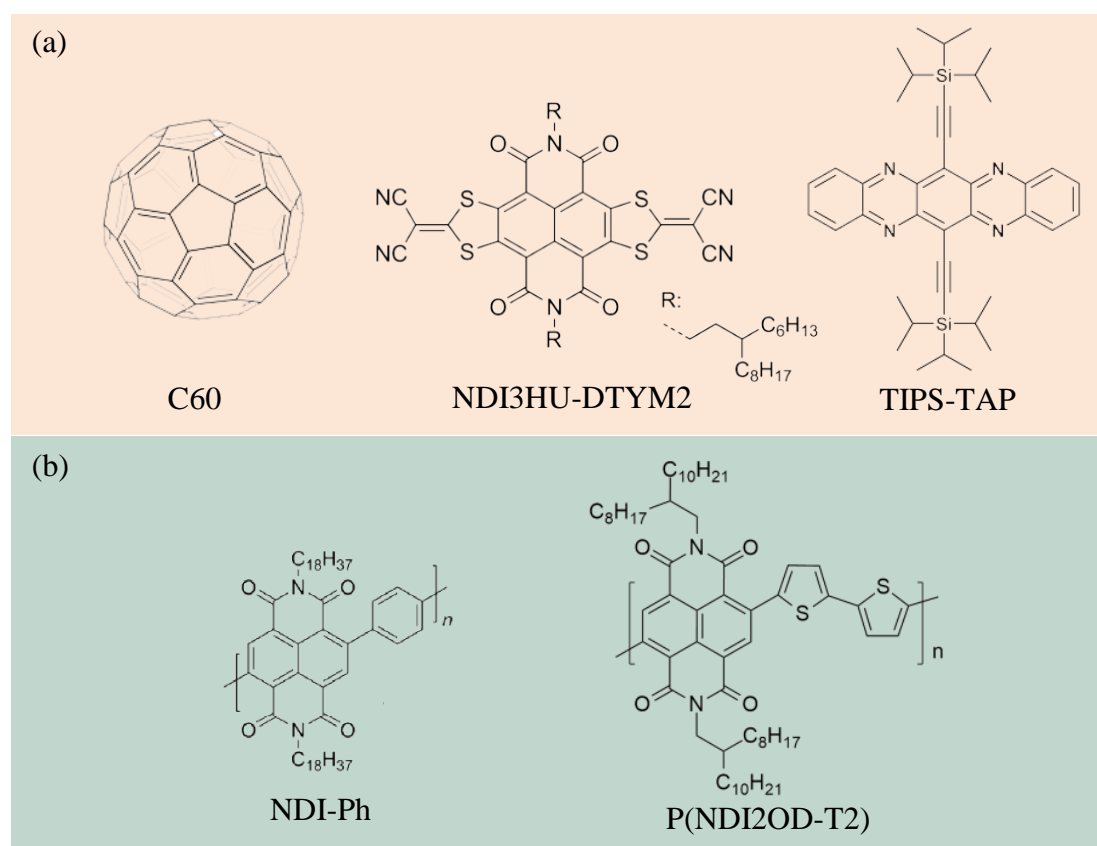
exceed $1 \text{ cm}^2/\text{Vs}$. To solve this issue, donor–acceptor (D–A) copolymer OSC materials have been developed. Among these materials the representative and widely-used ones are indacenodithiophene-co-benzothiadiazole ($\text{C}_{16}\text{IDT-BT}$) ($1.5 - 3.6 \text{ cm}^2/\text{Vs}$) [96, 97] and poly[2,6-(4,4-bis-alkyl-4H-cyclopenta[2,1-b;3,4-b']-dithiophene)-alt-4,7-(2,1,3-benzothiadiazole)] (CDT-BTZ) ($3.3 \text{ cm}^2/\text{Vs}$) [98]. Mobilities of these D-A copolymer OSCs are generally over $1 \text{ cm}^2/\text{Vs}$, but their cost is much higher than other polymer OSCs.

To balance the performance and the cost, some researchers tend to choose small molecule OSCs. Mobilities of small molecule OSCs are generally comparable to those of polymer OSCs, and most of these small molecule OSCs are available in the market and the price is normally acceptable. Popular small molecule OSCs reported in other works include 6,13-Bis(triisopropylsilylethynyl)pentacene (TIPS-Pentacene) ($0.01 - 1.2 \text{ cm}^2/\text{Vs}$) [12, 99-104], 2,7-alkyl[1]benzo-thieno[3,2-b][1]benzothiophene (C8-BTBT) ($0.42 - 5 \text{ cm}^2/\text{Vs}$) [85, 105, 106], and 2,8-difluoro-5,11-bis(triethyl-silylethynyl)anthradithiophene (diF-TES-ADT) ($0.13 - 2.41 \text{ cm}^2/\text{Vs}$) [71, 107-109]. These materials show high performance when they form crystals with good morphology. To grow large crystals, two strategies are taken:

(a) The first strategy is to control the growth of semiconductor crystals, which is usually realised by applying specific film deposition processes. In these processes, a unidirectional moving meniscus [12, 100, 110-112] or nozzle [113, 114] is used to control the crystallographic orientation. This moving guide carries the OSC solution forward, making it gradually exposed to the ambient environment and controlling the volatilisation rate with moving speed and ambient temperature. The control of volatilisation rate is critical as it determines the size of crystalline grains. The growth of the crystalline grain occurs in the solvent and starts from the nucleation. If the volatilisation rate is too high, there is no carrier for the growth of crystalline grains. If the volatilisation rate is too low, part of the grown crystalline grain is re-dissolved by the solvent and a new nucleus forms, leading to an increasing number of crystalline grains and grain boundaries in the unit area. For OTFTs, the larger crystalline grain size and less grain boundaries in the channel region are preferred because grain boundaries act as barriers blocking the transport of charge carriers. As a consequence, controlling the volatilisation rate of the solvent to match it with the growth rate of the crystalline grain is critical in this method.

(b) The second strategy is to blend polymer binders with OSC solutions. According to Flory-Huggins theory, the difference between solubility parameters of these two materials can lead to vertical phase separation when the blended solution evaporates on a surface [115, 116]. A sandwich-like structure (semiconductor-polymer-semiconductor) forms inside the semiconductor layer, and this vertical phase separation can induce a better crystallisation of the semiconductor phase [117]. To achieve better crystallisation, polymer materials with large relative molecular mass ($M_r > 20000$) are preferred, and reported polymer binders used to facilitate OSC crystallisation include polystyrene (PS) [12, 48, 69, 78], polymer poly(triarylamine) (PTAA) [107, 109, 111], amorphous polycarbonate (APC) [115], and poly(α -methylstyrene) (P α MS) [116-118].

In this work, a p-type small molecule OSC TIPS-pentacene blended with PS was used. TIPS-pentacene is a relatively high-performance and market-available OSC material, and PS is a polymer with large molecular mass ($M_r \approx 35000$). These material properties make this blended system an ideal choice for fabricating OTFTs.



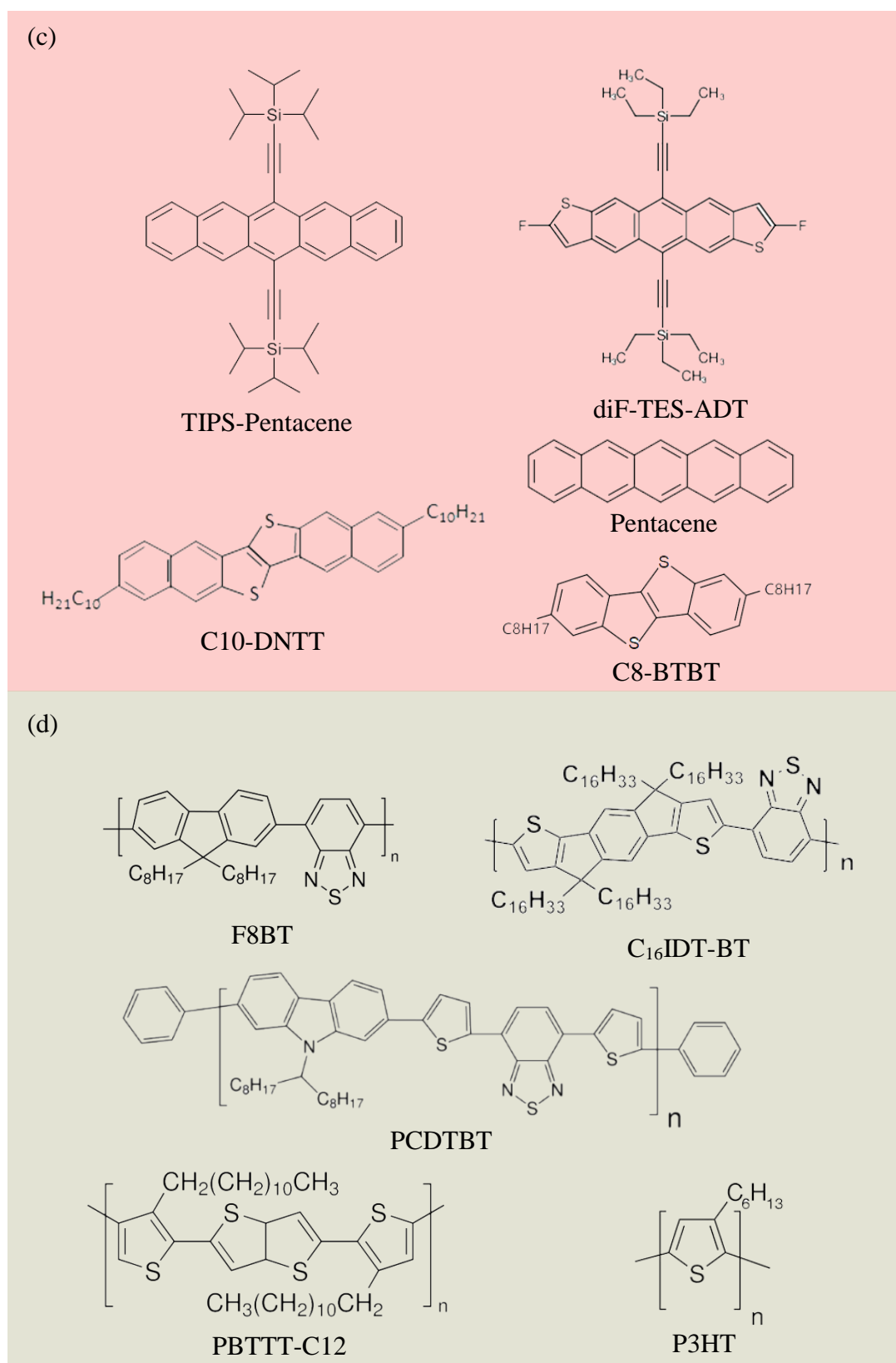


Figure 3.8. Molecular structures of typical OSCs: (a) n-type small molecule OSCs, (b) n-type polymer OSCs, (c) p-type small molecule OSCs, (d) p-type polymer OSCs.

3.3.4 Dielectrics

Dielectric layer is another critical component in OTFTs. The function of this layer is to separate the gate (G) electrode with the source/drain (S/D) electrodes and the semiconductor layer. It blocks the leakage current from gate to source/drain electrodes. This layer also prevents the direct contact of the gate electrode with the semiconductor layer, blocking the charge carrier injection from the gate electrode into the semiconductor. For OTFTs, organic polymer materials and inorganic oxide/nitride materials are commonly utilised for the dielectric layer. Typical organic dielectric materials include poly (vinyl alcohol) (PVA) [78, 119], poly (4-vinylphenol) (PVP) [74, 99, 103], poly (vinyl cinnamate) (PVC) [12], polymethyl-methacrylate (PMMA) [70, 93, 120], poly[(vinylidene-fluoride-co-trifluoroethylene) (P(VDF-TrFE-CFE)) [121], and poly(perfluoro-alkenylvinyl ether) (CYTOP) [75, 107], etc. And popular inorganic oxide/nitride materials for dielectric layers include silicon oxide (SiO₂) [112], silicon nitride (Si₃N₄) [122], alumina (Al₂O₃) [123], and hafnium oxide (HfO₂) [124], etc.

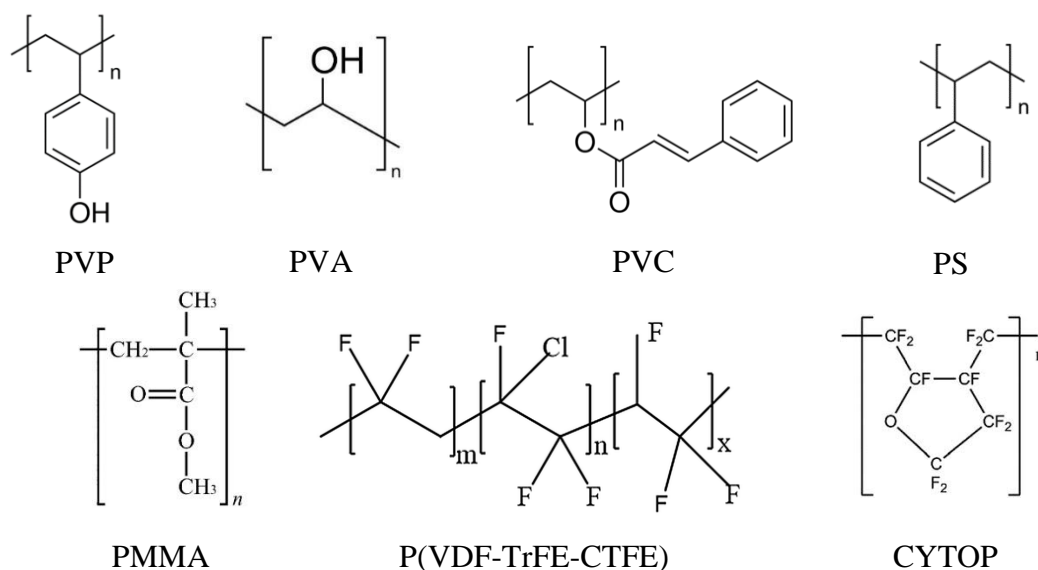


Figure 3.9. Molecular structures of typical organic dielectric materials for OTFTs.

In this study, as organic polymer materials are compatible with the inkjet printing process, they are chosen as the candidate for the dielectric layer. Regarding the selection of the specific organic dielectric material, there are two factors to be considered:

(a) The organic polymer material for the dielectric layer should be able to be cross-linked. Most polymer materials are in the form of independent chains, which are soluble in compatible solvents. As OTFT is a multi-layer structure, the solvents of other layers may dissolve the dielectric polymers. To solve this issue, a cross-linking process is used to link the polymer chains by covalent or ionic bonds. With these bonds, the independent chains are weaved into a mesh, increasing the mass of the polymer molecular and making it more resistible to its compatible solvents.

(b) The dielectric constant (k) of the polymer material for the dielectric layer should be moderate. According to the physical theory in Field Effect Transistor (FET), the subthreshold swing (SS), which is defined as the change in gate voltage needed to increase the drain current by one order of magnitude, can be described as:

$$SS = \ln(10) \frac{k_B T}{q} \left(1 + \frac{q^2 N_{SS}}{C_i} \right) \quad (3.3)$$

where k_B is Boltzman's constant, T is absolute temperature, q is the elementary charge, N_{SS} is the trap density, and C_i is the gate dielectric capacitance per unit area, which is calculated as:

$$C_i = \frac{k k_0 S_{\square}}{d} \quad (3.4)$$

where k is the relative dielectric constant for the dielectric material, k_0 is the permittivity of vacuum, S_{\square} is the unit area, and d is the thickness of the dielectric layer.

A high-performance OTFT is expected to have a large on/off current ratio and a steep slope in the transfer curve. So a small value of SS is required. In Equation 3.3, $\frac{k_B T}{q}$ is a constant, so the value of SS depends on N_{SS} and C_i , and a lower N_{SS} and large C_i is required. As mentioned in Section 3.3.3, N_{SS} can be lowered by improving the crystallisation of the semiconductor. And derived from Equation 3.4, C_i can be increased by choosing the material with high- k value. However, the large C_i may limit the frequency response of OTFTs [125]. The trade-off between SS and the response speed has to be balanced when choosing the polymer material for the dielectric layer.

Taking all factors into consideration, PVC was selected as the dielectric material in this work. The main reason is that it can be cross-linked under ultraviolet (UV) exposure. The cross-linking in PVC is known as (2+2) cycloaddition [126], which is shown in Fig. 3.10.

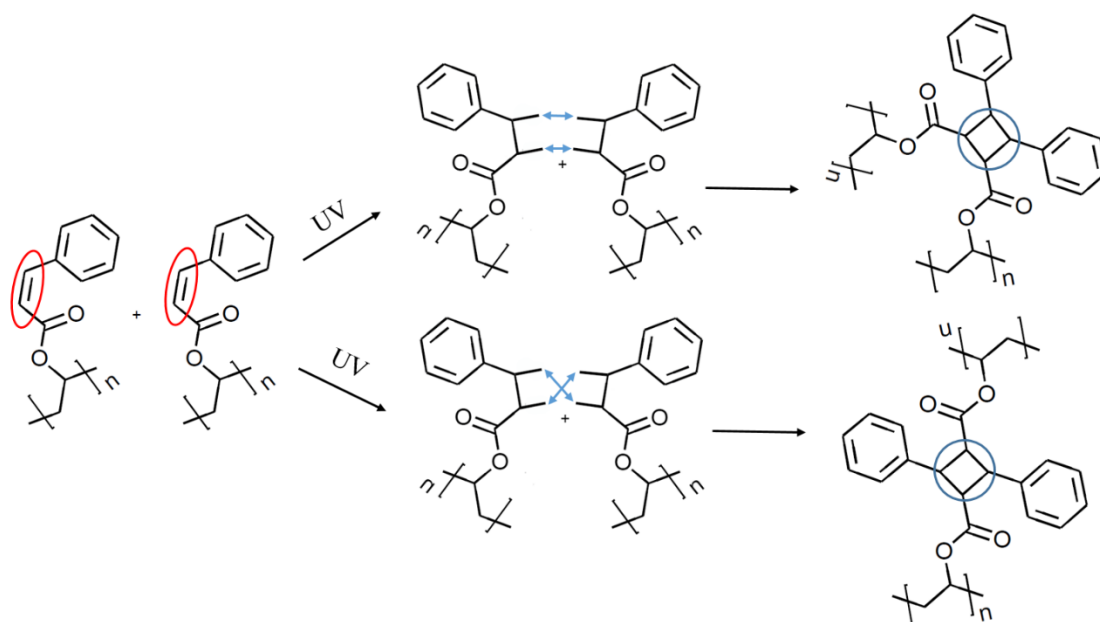


Figure 3.10. The cross-linking process of PVC under UV exposure.

In this process, the C=C bonds (red circle) break due to the energy of the UV rays and two free C- bonds are formed in the cinnamoyl chain. Then free bonds in adjacent molecules connect as the C-C bonds and form cyclobutane rings (blue circle). Depends on the combination mode of the C-C bonds, cyclobutane rings can be classified into trans isomer and cis isomer. These cyclobutane rings act as the cross-links in the polymer mesh, and the existence of the different isomers makes PVC prone to being cross-linked and becoming more chemically inert.

3.3.5 Encapsulation

Oxygen and moisture are major factors threatening the stability of OTFTs, as they can cause the oxidation of the electrodes and degradation of the OSC materials [127]. To prevent the permeation of the oxygen and moisture and improve the stability of the OTFTs, a passivation layer is needed on the top of the device. Materials for the encapsulation include organic materials like polytetrafluoroethylene (PTFE) [128], CYTOP [99] and inorganic materials such as alumina/titania ($\text{Al}_2\text{O}_3/\text{TiO}_2$) composites [129] and glass [130].

In this study, CYTOP is selected for the passivation layer. The first reason is that CYTOP is a fluoropolymer, and the rich fluorine atoms in polymer chains make it intrinsically hydrophobic and effective in preventing the moisture diffusion. In addition, the main solvent for CYTOP is perfluorotributylamine, which is also a fluoropolymer

[131]. An important requirement for passivation material is that it should not dissolve any prepositive materials, and this fluorinated solvent does not dissolve the non-fluorinated semiconductor and dielectric materials. These factors make CYTOP solution a good candidate for the passivation layer.

3.4 Inkjet Printing Process

To fabricate OTFTs, a range of thin film deposition techniques have been developed.

For electrodes, vacuum thermal evaporation is the most common-used process for the film deposition. In this process, a high vacuum level and designed shadow masks with high precision are required. For OTFTs with short channel ($< 10 \mu\text{m}$), a photolithography technique is needed and the photoresist material should be carefully chosen as the organic photoresist may dissolve or blend with the organic dielectrics or semiconductors, influencing the device performance of OTFTs.

For dielectrics, both organic and inorganic materials are used. One popular inorganic dielectric material is aluminium oxide (AlO_x), and the processes for depositing the AlO_x film include sputtering [132], oxygen (O_2) plasma treatment [3], and atomic layer deposition (ALD) [5]. For organic solutions, spin-coating is the most widely-used process for the formation of films [12, 119, 133, 134]. However, this process has two drawbacks: One is the nonuniformity of the film thickness caused by the different tangential velocities. The other one is the high possibility of having defects in the film because particles easily enter the film when the substrate rotates at a high speed.

Many studies have focused on the deposition of semiconductor layers, as this layer is the most critical layer deciding the device performance of OTFTs. The reported solution-based processes include spin-coating [71, 107, 119, 135], slot-die coating [110], solution shearing [100, 112], and blade-coating [12], etc. These processes used a high-speed spin coater or designed guide-blade to spread the OSC solution and form the semiconductor film.

In this work, an inkjet printing process was utilised to deposit all layers in OTFTs. This process used a functional materials printer (Dimatix DMP-2831, Fujifilm), accompanied with an organic-compatible cartridge (DMPLCP-11610, Dimatix, Fujifilm), to print functional inks at the designed positions. This cartridge has 16

nozzles and the drop size is 10 pL. Fig. 3.11 shows the functional inkjet printer and cartridge used in this study.

Compared with other film deposition techniques, this process has several advantages. First, in this process, the precise shadow masks or photoresist are not needed. Patterns for each layer are designed in computer aided design (CAD) softwares. With the ultra-small size of the ink drop from one single nozzle and the ability of precise positioning of the cartridge, high-resolution patterns can be achieved. Second, this process does not require a vacuum environment and all layers can be printed in the ambient-air environment, which can reduce the cost of device fabrication. Third, inkjet printing is an additive process and all layers are printed-on-demand, so there is almost no waste of ink in this process. The high utilisation efficiency of materials also makes this process an economical choice for manufacturing OTFTs.

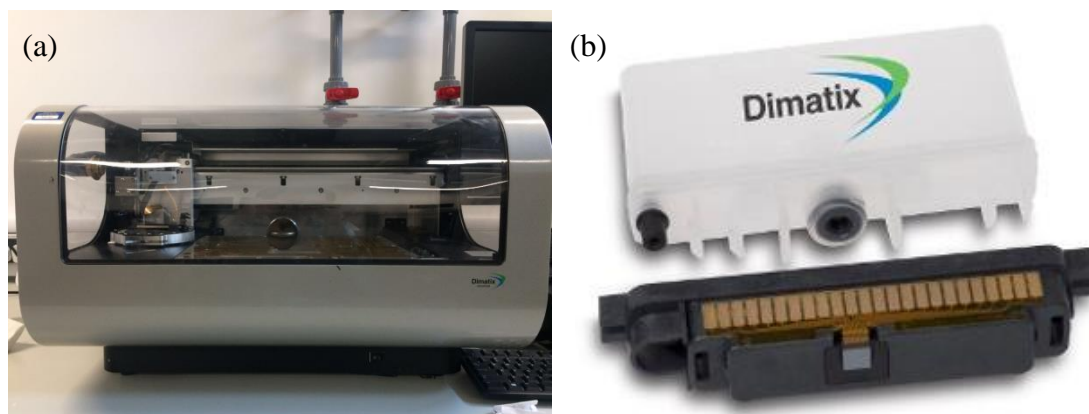


Figure 3.11. Photographs of (a) Dimatix DMP-2831 inkjet printer, (b) Dimatix DMPLCP-11610 cartridge.

3.5 Experiment

3.5.1 Preparation of Inks

Electrode: A type of commercial Ag ink (JET-605C) provided by Hisense Electronics, Kunshan, China, was used in this work. As the solvent for this Ag ink is an alcohol, an organic-compatible cartridge (DMPLCP-11610, Dimatix) was used to hold the ink. To remove large particles and solid impurities in the Ag ink, it was injected into the cartridge through a 0.2 μm poly(tetrafluoroethylene) (PTFE) filter.

Dielectric: The PVC powder (CAS NO. 9050-06-0, Sigma-Aldrich) was dissolved in anisole (CAS NO. 100-66-3, Sigma-Aldrich) with a concentration of 45 mg/mL.

Since PVC is sensitive to UV rays, the solution should be kept in an amber bottle wrapped with the aluminum foil. The dielectric ink was stirred by a magnetic stirrer for 12 h, then it was injected into the DMPLCP-11610 cartridge through a 0.2 μm PTFE filter.

Semiconductor: TIPS-pentacene (CAS NO. 373596-08-8 Sigma-Aldrich) and PS (CAS NO. 9003-53-6, Sigma-Aldrich) powders were dissolved in anisole with a concentration of 10 mg/mL, respectively. Then they were mixed with a volume to volume ratio of 3:1 (TIPS-pentacene:PS =3:1). The blended semiconductor ink was also kept in an amber bottle and stirred by a magnetic stirrer for 12 h. After the intensive mixing, it was injected into the DMPLCP-11610 cartridge through a 0.2 μm PTFE filter.

Encapsulation: The blending system of CYTOP (CTL-809M) and its thinner (CT-Solv. 180) were utilised as the ink for passivation layer. Both of them were supplied by Asahi Glass, Japan. They were mixed at a mass ratio of 1:3 (CYTOP:thinner = 1:3) and the blending system was stirred by a magnetic stirrer for 2 h.

3.5.2 Device Fabrication

As shown in Fig. 3.12(a), an inverted coplanar (BGBC) device architecture was applied in this work. At the bottom a 4 cm \times 3 cm PEN film (Teonex Q65HA, 125 μm , Pütz GmbH & Co. Folien KG) was used as the substrate. The Ag ink was deposited onto the PEN substrate to pattern the gate electrode. The drop space (D_S) and the distance from the cartridge nozzles to substrate surface (D_H) were set as 50 μm and 1 mm, respectively. After the deposition of the Ag ink, the substrate was transferred to a hot plate and annealed at 130 $^{\circ}\text{C}$ for 15 min. By this treatment a uniform conductive film with sheet resistance of 25–30 Ω/sq can be obtained. Then the PVC solution was printed onto the substrate with a D_S of 10 μm and a D_H of 1 mm, covering the whole gate electrode, followed by a 30 min UV ($\lambda \sim 254 \text{ nm}$) exposure and 30 min annealing at 100 $^{\circ}\text{C}$ for the cross-linking of the PVC molecules. Subsequently, the source/drain electrodes were formed by printing Ag ink onto the dielectric layer with the same jetting parameters when printing the gate electrode, and then annealed at 120 $^{\circ}\text{C}$ for 15 min. All OTFTs fabricated in this work were designed to have a constant aspect ratio for their channels, with a width of 1600 μm and a length of 80 μm . To lower the Schottky-barrier height between source/drain electrodes and semiconductors, the sample was immersed into the PFBT solution (volume to volume ratio: PFBT:ethanol = 1:1000)

for 15 min and rinsed with pure ethanol. This treatment attaches self-assembled monolayers onto the surface of source/drain electrodes, lowering the difference of the work function between source/drain electrodes and semiconductors. The semiconductor ink was then printed on the sample, covering both source/drain electrodes and the whole channel region. The D_S and the D_H were set to be 10 μm and 1 mm, and the platen temperature in the printer was set to be 40 $^\circ\text{C}$ to control the volatilisation rate of the solvent in the OSC ink. After the formation of OSC crystalline grains, the sample was annealed at 100 $^\circ\text{C}$ for 15 min. Finally, the CYTOP ink was deposited onto the sample as the passivation layer, covering the whole device (except the extended pads of gate/source/drain electrodes for testing). After the annealing at 100 $^\circ\text{C}$ for 15 min, the sample was ready for the measurement. The fabricated sample and the single OTFT device is shown in Fig 3.12(b).

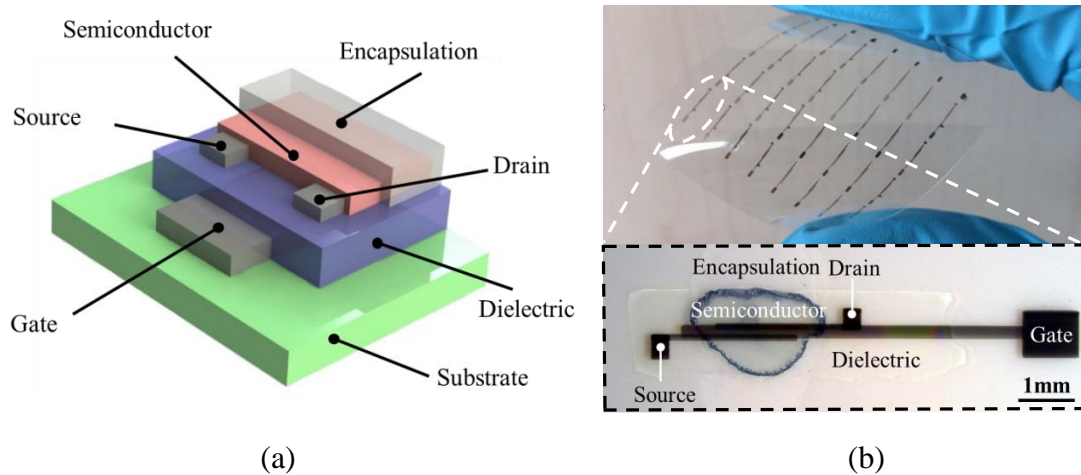


Figure 3.12. (a) Schematic image of an OTFT with the BGBC structure, (b) Photograph of a flexible sample and microscopic image of a single OTFT.

3.5.3 Device Characterisation

The electrical characteristics of OTFTs were measured by the KeithleyTM 4200 Semiconductor Characterisation System (SCS). A probe station system supplied by SEL-TEK Ltd. was connected with KeithleyTM 4200 SCS, and probe tips in the probe station contact the extended pads for gate/source/drain electrodes. The film thickness was measured by the Dektak 6M stylus profilometer. All measurements were conducted in an ambient-air environment.

3.6 Properties of OTFTs

3.6.1 Film Thickness

As shown in 3.5.2, the OTFT fabricated in this work has a BGBC architecture, so the thickness of the bottom layers has great influence on the device performance. For the gate electrode, its thickness should not influence the surface morphology of the dielectric layer covering it. Therefore, the gate electrode should have a relatively small thickness compared with the dielectric layer. In addition, for the dielectric layer, there is a trade-off when deciding the thickness of the film:

On the one hand, a thick dielectric layer is expected as it has to prevent the gate leakage current flowing from gate electrode to source or drain electrode.

On the other hand, the large thickness of the dielectric layer would degrade the device performance, which can be explained by the threshold voltage (V_{th}) and subthreshold slope (SS) relations:

$$V_{th} = V_{th,theoretical} + \frac{Q_t}{C_i} \quad (3.5)$$

$$SS = SS_{theoretical} \left(1 + \frac{q^2 N_{SS}}{C_i}\right) \quad (3.6)$$

where $V_{th,theoretical}$ and $SS_{theoretical}$ are the theoretical threshold voltage and subthreshold slope without defects, Q_t is the charge density of defect-trapped carriers, N_{SS} is the density of defect trap (per eV and unit area), and C_i is the gate insulator capacitance per unit area, which is calculated by Equation 3.4. According to Equation 3.4, the increase of the film thickness would lead to the decrease of the gate insulator capacitance C_i , causing an increase of the V_{th} and SS values. The large value of V_{th} means larger gate-source voltage (V_{gs}) is needed for the operation of the device. And the large value of SS means the slower increase of the working current (I_{ds}) with the rise of the gate-source voltage (V_{gs}) in the transfer characteristic. Because of these influences, a thin dielectric layer is expected for the better device performance.

To modulate the thickness of the dielectric layer, the inkjet printer was set to deposit the single- and double-layer PVC film. The thicknesses of the single- and double-layer films were measured by the profilometer and the result is shown in Fig. 3.13. The average thickness of the single-layer PVC film was measured to be 236 nm while for the double-layer PVC film, the value was measured as 486 nm. However, when the relatively high voltage was applied on the gate electrode ($V_{gs} \geq 25$ V) of the

OTFT with the single dielectric layer, it was highly possible that the dielectric layer broke down and lost its function of isolating the gate voltage and modulating the channel region. Meanwhile, in the experiments, most of OTFTs with double-layer dielectric film could resist high voltages. Therefore, at least two layers of the dielectric film were needed for the fabrication of OTFTs.

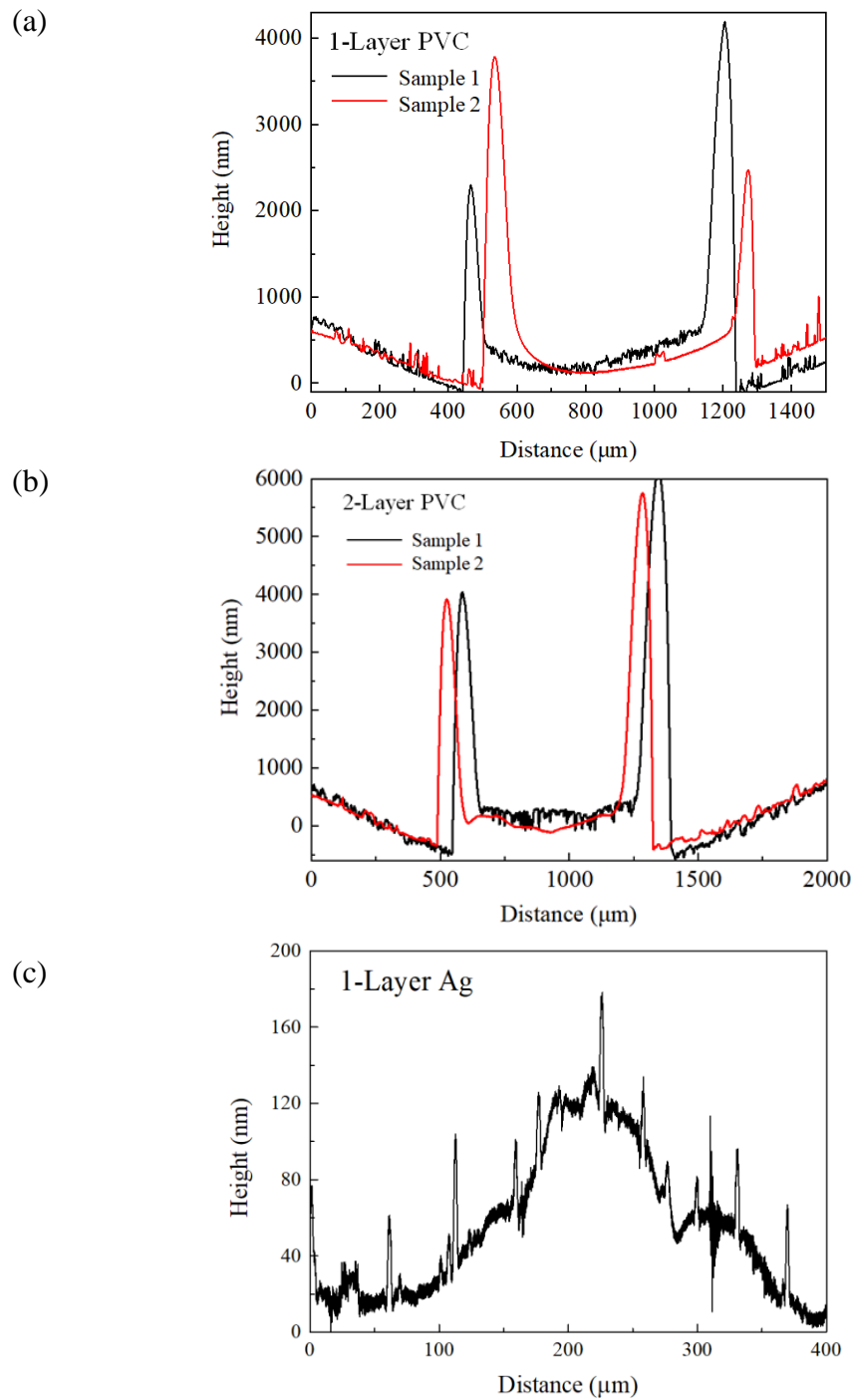


Figure 3.13. Thickness of the printed films: (a) single-layer PVC (b) double-layer PVC (c) single-layer Ag.

The thickness of the Ag electrode film is shown in Fig. 3.13(c). The average value is calculated as 57.1 nm, and the peak of the film is less than 140 nm. Therefore, it can be concluded that compared with the dielectric layer, the electrode film is thin enough and has no influence on the surface morphology of the dielectric layer.

3.6.2 Electrical Properties

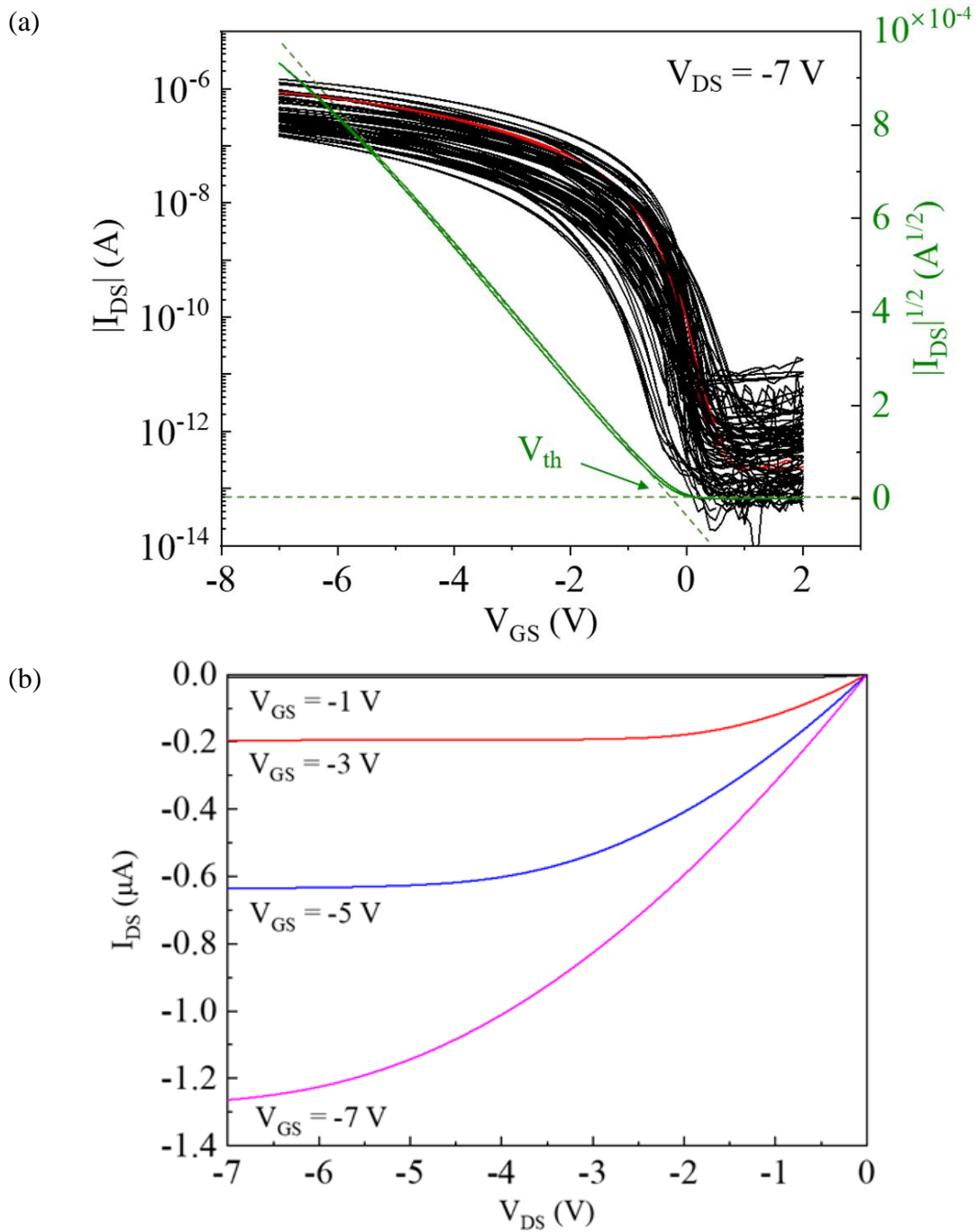


Figure 3.14. (a) Measured transfer characteristics of 46 OTFTs, (b) Typical output characteristics of one OTFT.

The total number of fabricated devices was 54 and when the functional device was defined as having an on/off current ratio over 10^3 , the yield of these OTFTs was 85.19% (46 out of 54). The transfer characteristics of these functional OTFTs are shown in Fig. 3.14(a). In this figure the red line represents the typical transfer curve for the p-type OTFT, and the typical output characteristic is shown in Fig. 3.14(b).

To evaluate the device performance of manufactured OTFTs, the threshold voltage (V_{th}), device mobility (μ), on/off current ratio and SS were extracted and counted. The extraction methods of these parameters are summarised below:

Mobility (μ): The mobility is defined as the average drift velocity of the charge carriers under an electric field:

$$\mu = \frac{v}{E} \quad (3.7)$$

where v is the drift velocity of the charge carriers in the semiconductor and E is the external electric field. It describes how well the charge carriers in the semiconductor can move due to an electric field, and its unit is expressed as cm^2/Vs . When voltages applied on the S/D/G electrodes meet the condition: $|V_{DS}| < |V_{GS} - V_{th}|$, the OTFT is operating in the linear region. In this region the current from the Source to the Drain (I_{DS}) is calculated as:

$$I_{DS} = \mu_{lin} C_i \frac{W}{L} \left(V_{GS} - V_{th} - \frac{V_{DS}}{2} \right) V_{DS} \quad (3.8)$$

where μ_{lin} is the mobility in the linear region, C_i is the dielectric capacitance per unit area, and W/L is the aspect ratio of the channel. When voltages meet the condition: $|V_{DS}| > |V_{GS} - V_{th}|$, the OTFT is biased in the saturation mode region, and I_{DS} is calculated as:

$$I_{DS} = \frac{1}{2} \mu_{sat} C_i \frac{W}{L} (V_{GS} - V_{th})^2 \quad (3.9)$$

here μ_{sat} is the mobility in the saturation region. Based on Equation 3.8 and Equation 3.9, μ_{lin} and μ_{sat} can be calculated as:

$$\mu_{lin} = \frac{L}{C_i W V_{DS}} \frac{\partial I_{DS}}{\partial V_{GS}} \quad (3.10)$$

$$\mu_{sat} = \frac{2L}{C_i W} \left(\frac{\partial \sqrt{|I_{DS}|}}{\partial V_{GS}} \right)^2 \quad (3.11)$$

In this work, the OTFT was usually biased in the saturation region, so the mobility μ appearing in this dissertation is μ_{sat} . In addition, based on Equation 3.11, μ can be extracted from the transfer characteristics curve ($|I_{DS}|^{1/2} - V_{GS}$). The value of $\frac{\partial \sqrt{|I_{DS}|}}{\partial V_{GS}}$

can be achieved by calculating the average slope of tangents to several specific points on the curve.

Threshold Voltage (V_{th}): V_{th} is defined as the gate voltage required to meet the condition: $\phi_s = 2\phi_{fp}$, here ϕ_s is the surface potential and ϕ_{fp} is the difference between the intrinsic Fermi level (E_{Fi}) and Fermi energy level (E_F) in a p-type semiconductor. Based on Equation 3.9, V_{th} can be calculated as:

$$V_{th} = V_{GS} - \left(\frac{2LI_{DS}}{C_i W \mu_{sat}}\right)^{1/2} \quad (3.12)$$

V_{th} can be extracted from the $|I_{DS}|^{1/2} - V_{GS}$ curve, as shown in Fig.3.14(a). It is determined as the intersection of the X-axis and the tangent extended from the curve.

Subthreshold Swing (SS): SS is defined as the change in gate voltage needed to increase the drain current by one order of magnitude. It is calculated by Equation 3.3, and is extracted from the transfer characteristics curve ($I_{DS} - V_{GS}$). The value of SS equals to the reciprocal of the slope of the tangent derived from the curve. In addition, based on Equation 3.3, at the room temperature (300 K), the theoretical limit of SS for OTFT is $\ln(10) \frac{k_B T}{q} \approx 60$ mV/dec.

On/Off Current Ratio: The value of the on/off current ratio is usually used to evaluate the switch performance of the OTFT device. It is extracted from the transfer characteristics curve ($I_{DS} - V_{GS}$) and is calculated as:

$$\text{On/Off current ratio} = \frac{I_{on}}{I_{off}} \quad (3.13)$$

The average values and histograms of these extracted parameters are shown in Table 3.1 and Fig. 3.15, respectively.

Table 3.1 Average values of extracted parameters for inkjet-printed OTFTs

	Mobility (cm^2/Vs)	V_{th} (V)	On/off ratio	SS (mV/decade)	Yield
Average Values	0.125	-0.53	3.17×10^6	240.8	85.19%

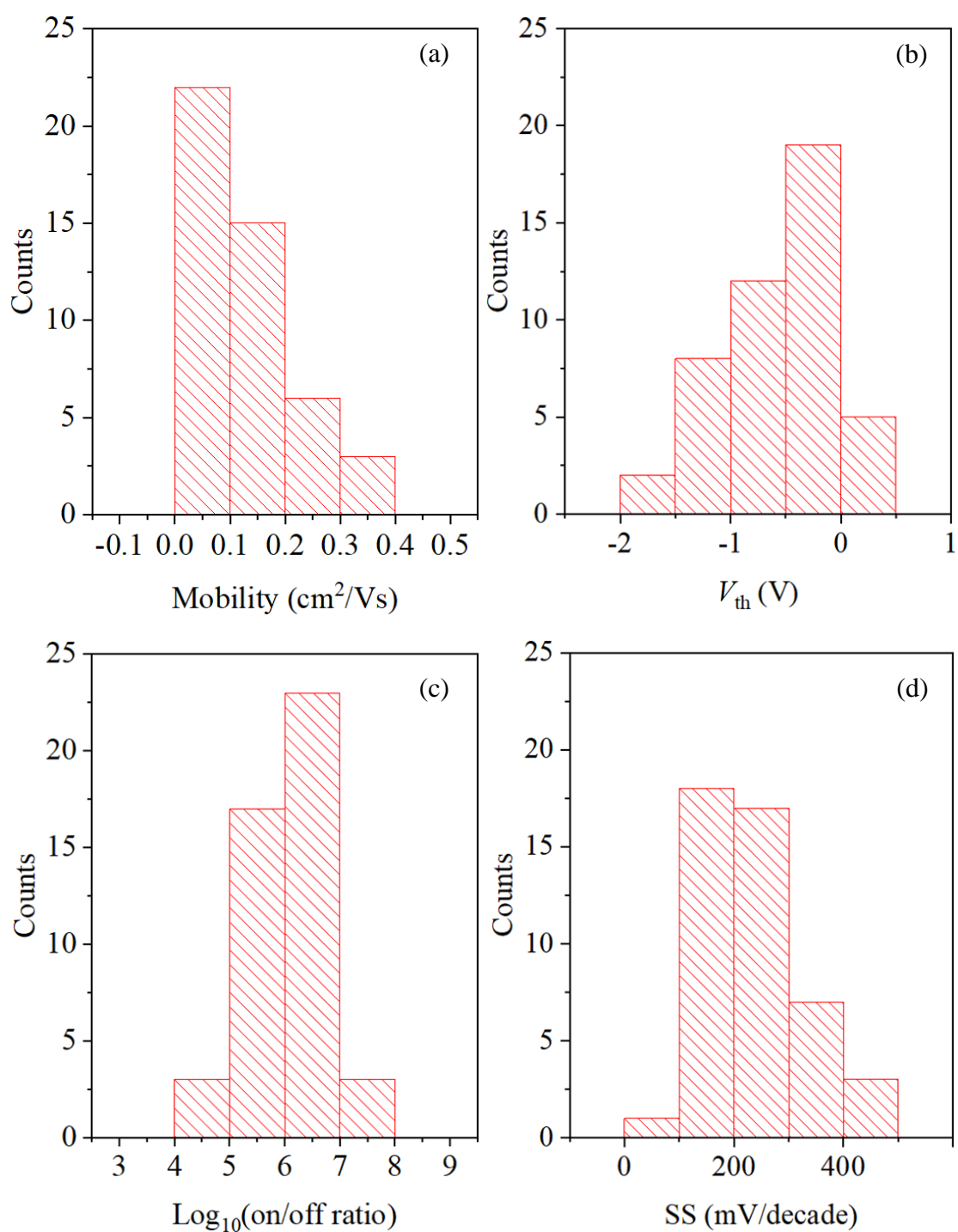


Figure 3.15. Histograms of 46 inkjet-printed OTFTs over the $4 \text{ cm} \times 4 \text{ cm}$ size flexible substrate: (a) mobility, (b) threshold voltage, (c) on/off ratio and (d) subthreshold slope.

3.7 Summary

In this chapter, the mechanism of the carrier transport in organic semiconductor, device structures, materials for different layers, fabrication process and the electrical

properties of the OTFT are introduced. Taking the manufacturability and device performance into consideration, a BGBC-structured OTFT device has been selected in this work. Materials used in this device include: PEN film for the flexible substrate, Ag for the electrodes, TIPS-pentacene for the semiconductor, PVC for the gate dielectric, and CYTOP for the encapsulation layer. All layers on the substrate have been deposited by the inkjet printing process, showing a better manufacturability compared with other fabricating process. Compared with the previously reported works, OTFTs fabricated in this work have shown relatively good yield and electrical properties, thus they are qualified to be the basic device for the further research about the self-healing of device and circuit interconnects in the following chapters.

4 SELF-HEALING OF INKJET PRINTED INTERCONNECTS

To reveal the feasibility of the PBSH technique in flexible circuits, this dissertation follows a wire-device-circuit logic. This chapter shows the self-healing of an open fault in inkjet-printed wires. Relationships between the healing time with the concentration, electric field strength, and external resistance are analysed in this chapter. Section 4.1 introduces the experimental set-up and shows results proving the healing of the open-fault. Section 4.2 analyses the relationships between the healing time with the concentration and figures out the most appropriate concentration by the calculation. Section 4.3 reveals the influence of the electric field strength on the healing time. Section 4.4 explores the dependence of the healing time on the length of open gap, and Section 4.5 analyses the relationships between the healing time with the external resistance. Finally, the stability of the healed pathway when reducing the external voltage is proved in Section 4.6.

4.1 Self-healing of Open-fault in the Wire

In this section the experimental set-up and some evidences proving the occurrence of the self-healing in the open gap are shown and discussed.

4.1.1 Experimental Set-up

The experimental set-up for the optical observation and electrical measurement of the self-healing are shown in Fig. 4.1. In this experiment, an Ag wire with the width of 200 μm was inkjet printed on a PEN substrate. An open gap was reserved in the middle of the printed wire. A Source Measure Unit (SMU) was connected to two terminals of

the printed wire. The SMU functions as a voltage source to provide direct voltage (volts D.C.). At the same time, it functions as an ammeter to measure the current flowing through the printed wire. A resistor was connected in series with the printed wire and the SMU. The function of this resistor was to limit the current in the circuit to protect the SMU, and to replace the external circuit and simulate the influence of the impedance of an external circuit on self-healing. A microscope lens connected to a charge coupled device (CCD) camera was fixed above the open gap to observe the movement of metal particles in the open gap.

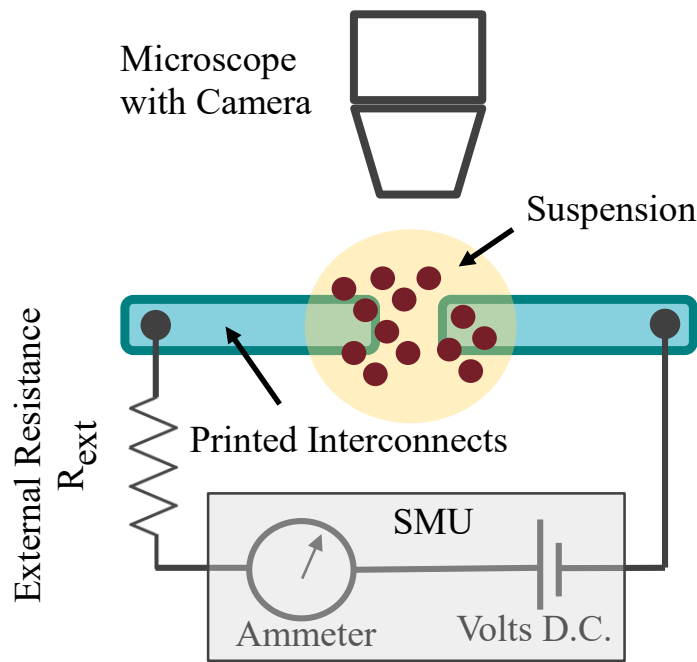


Figure 4.1. Schematic of the experimental set-up for measuring the self-healing in printed interconnects.

4.1.2 Self-healing in the Open Gap

The suspension with oleic acid (OA)-coated Ag particles was dropped to cover the open gap. Meanwhile the current flowing through the circuit and the movement of Ag particles in the open gap were recorded. According to the theory in Section 2.3, after dropping the suspension in the open gap, it takes time to drive metal particles to form the bridge. As soon as the conductive bridge is built, the current can return to the original level before the open-fault occurs. The result shown in Fig. 4.2 matches well with theory. In the first 33 seconds (s), the current stayed at the low level ($10^{-12} - 10^{-11}$ A), indicating the open state of the printed wire. The measured current did not equal 0

A because of the noise in the circuit and the SMU (will be analysed in Chapter 7). At the 33rd second, the conductive bridge was built and the current jumped to the original level (10^{-4} A) before the open-fault, which indicated the healing of the open gap in the interconnection. After that jump the current remained at the normal level, proving that the conductive bridge had been effective at healing the open-fault in the circuit.

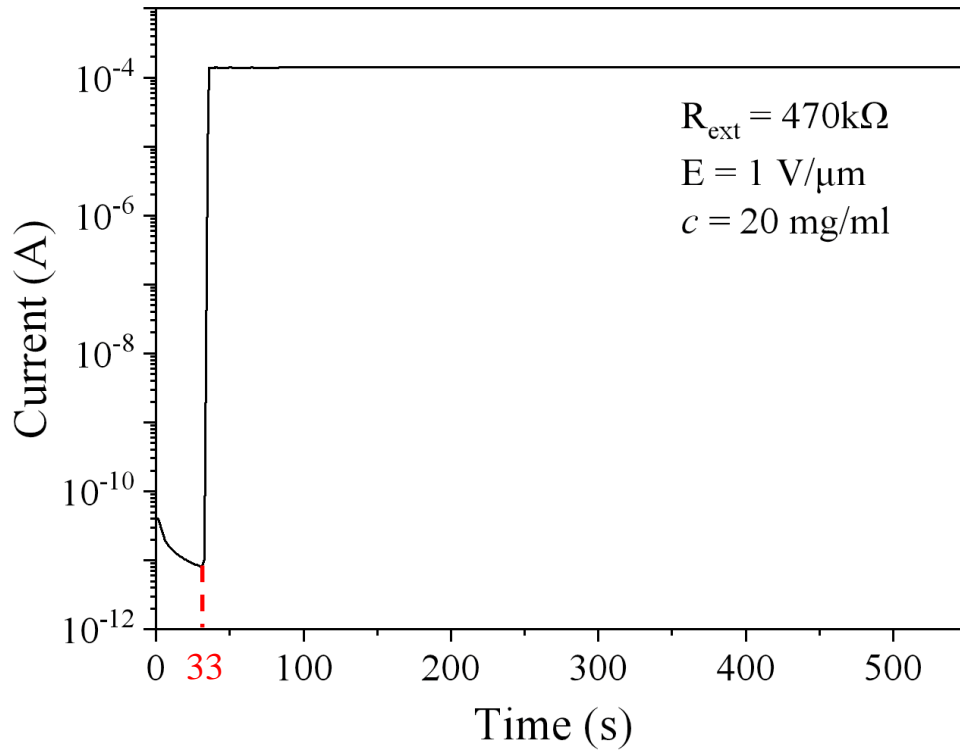


Figure 4.2. Self-healing of inkjet-printed interconnects on flexible substrates.

The movement of metal particles and the formation of the conductive bridge recorded by the CCD camera is shown in Fig. 4.3. In this process the OA-coated Ag particles were driven by the dipole-dipole attractive force arising from the electric field in the open gap. At time $t = 15$ s the bridge was built and due to the large external impedance, the potential difference across the open gap dropped to a low level, thus the electric field in the open gap was sharply weakened. After the time $t = 15$ s, the sintering occurred in the healed bridge, fixing the bridge across the open gap. As the strength of electric field weakened across the gap, Ag particles did not move and no new bridge formed in the open gap. The current flowed through the healed bridge and the whole circuit returned to the original state before the open-fault occurred. The SEM image of the healed bridge is shown in Fig. 4.3(f). A complete pathway is confirmed in this image, indicating the successful repairing of the open gap.

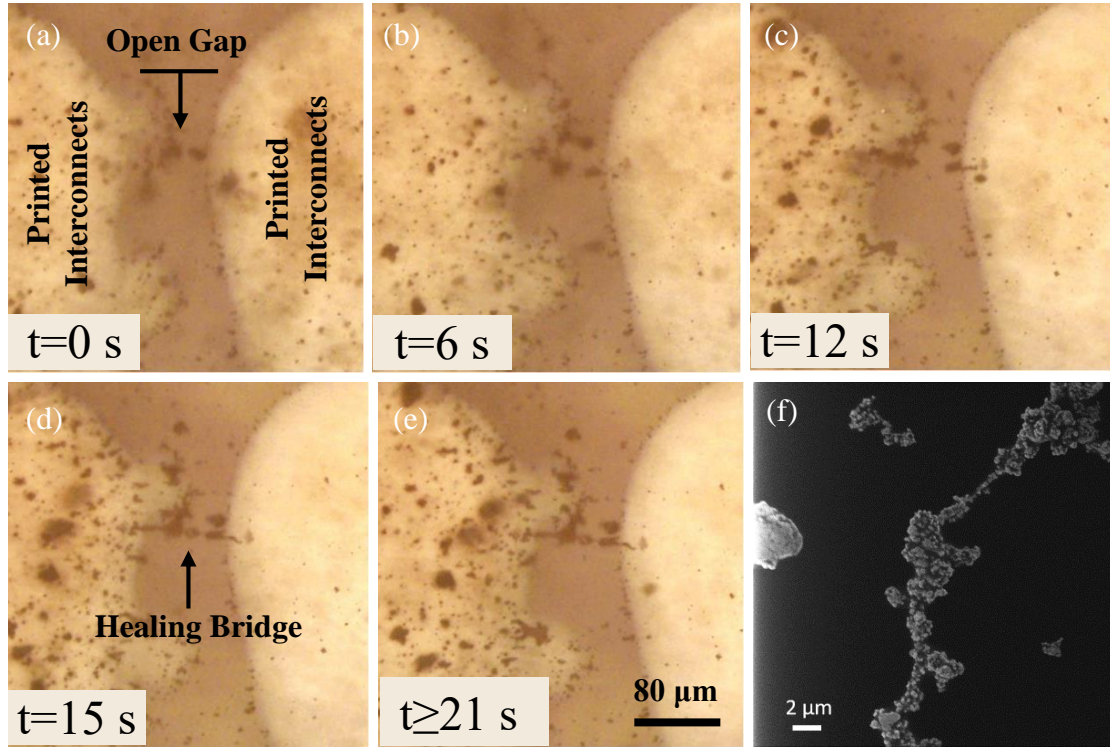


Figure 4.3. (a)-(e) Optical micro-photos showing the formation of the conductive bridge [48] (f) SEM image of the healed particle-based conductive bridge.

4.2 Dependence of Healing Time on Suspension Concentrations

This section discusses the impact of changing the concentration of Ag particles in the suspension. Three different concentrations, i.e., 10, 20, and 40 mg/mL were adopted in this work. For each concentration, 6 to 9 sets of data were collected. Fig.4.4(a) is typical dynamics of the current flowing through the printed wire circuit for different suspension concentrations. In this circuit, the length of the open gap was set as $s \approx 80 \mu\text{m}$, the external resistance was $R_{\text{ext}} \approx 220 \text{ k}\Omega$, and the electric field strength was fixed at $\xi \approx 1.1 \text{ V/mm}$. For each concentration, one typical data set is picked, as shown in Fig. 4.4(a). In this figure, suspensions with all these concentrations could heal the open fault, and the healing time decreased with the increase in the suspension concentration. The distribution of the healing time (τ_h) in experiments with different concentrations is shown in Fig. 4.4(b). The black dashed line represents the trend of the mean τ_h versus suspension concentration. The linear fitting of the data points in a log–log scale shows the slope of this dashed line to be $\Delta y/\Delta x \approx -2.13$, indicating that τ_h varies as the -2.13^{th} power of the concentration. The theoretical relationship between the healing time and

the concentration can be derived from equations in Section 2.3. By substituting Equation 2.7 into Equation 2.6, the following equation can be achieved:

$$t \sim \frac{\eta_f}{\epsilon_f} \frac{1}{\xi^2} (n_p r_p)^{-\frac{5}{3}} \quad (4.1)$$

In Equation 4.1, n_p is the number of particles in unit volume, which represents the concentration of particles in the suspension. Then by taking logarithm of both two sides, Equation 4.1 is presented as:

$$\log_{10} t \sim \log_{10} \left(\frac{\eta_f}{\epsilon_f} \frac{1}{\xi^2} \right) - \frac{5}{3} \log_{10} (n_p r_p) \quad (4.2)$$

In Equation 4.2 the constant coefficient for the concentration-related term $\log_{10}(n_p r_p)$ is $-5/3 \approx -1.67$. This theoretically derived coefficient is near the experimental result -2.13 , indicating the good agreement of the experimental result with the theoretical modelling.

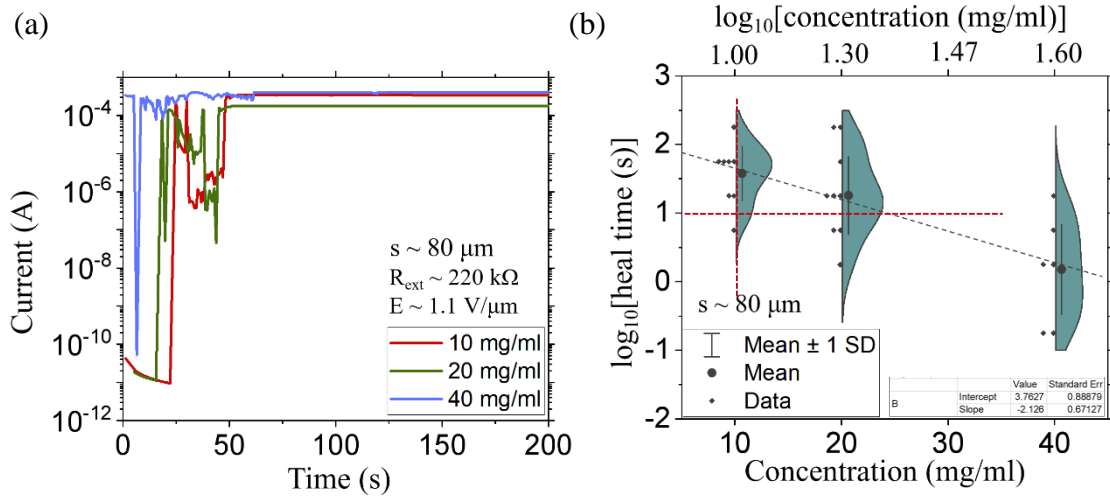


Figure 4.4. (a) Typical dynamics of current for suspension concentrations of 10, 20, and 40 mg/mL (b) The dependence of the healing time on suspension concentrations.

As seen from Fig. 4.4(b), the modified micro-particle suspension was inherently insulating when the concentrations were 10 and 20 mg/mL, and the healing was observed with $\tau_h \approx 10\text{--}100 \text{ s}$ and $\tau_h \approx 1\text{--}10 \text{ s}$, respectively. When the concentration reached 40 mg/mL, many samples showed the inherent conductivity as the open faults were repaired as soon as the suspension was dropped onto the open gap. For those nonconductive samples, the healing was much quicker than the former two concentrations with $\tau_h \approx 0.01\text{--}1 \text{ s}$. To avoid the crosstalk and to improve the reliability

of the healing circuit, the inherently insulating suspension is preferable. Therefore, the high concentration is undesirable for the self-healing in this work.

The optimum concentration for the Ag particle-based suspension can be calculated based on the previous research about using Cu particles for the self-healing [59]. Optimum concentrations for Ag and Cu particles in silicon oil in weight/volume are defined as ϕ_{Ag} and ϕ_{Cu} , respectively. And the suspension is assumed to have a two-dimensional (2D) spread. If the number of particles in unit volume is defined as n , for Ag and Cu particles in silicon oil, the number can be calculated as:

$$n_{Ag} = \phi_{Ag} / (4/3 \pi r_{Ag}^3 \rho_{Ag}) \quad (4.3)$$

$$n_{Cu} = \phi_{Cu} / (4/3 \pi r_{Cu}^3 \rho_{Cu}) \quad (4.4)$$

where r_{Ag} and r_{Cu} are radiuses of Ag and Cu particles. ρ_{Ag} and ρ_{Cu} are mass densities of these two particles. In the 2D geometry the distance between two particles is scaled as $(1/n)^{1/2}$, therefore, the particle distance in these two suspensions can be scaled as:

$$x_{Ag} \cong (1/n_{Ag})^{1/2} = [(4/3 \pi r_{Ag}^3 \rho_{Ag}) / \phi_{Ag}]^{1/2} \quad (4.5)$$

$$x_{Cu} \cong (1/n_{Cu})^{1/2} = [(4/3 \pi r_{Cu}^3 \rho_{Cu}) / \phi_{Cu}]^{1/2} \quad (4.6)$$

To estimate the optimum concentration of the Ag based on the optimum condition of the Cu, the healing time is aimed to be kept constant. According to Equation 2.6 $\tau_{h,Ag} \propto (x_{Ag}/r_{Ag})^5$ and $\tau_{h,Cu} \propto (x_{Cu}/r_{Cu})^5$, the healing time is defined constant $\tau_{h,Ag} = \tau_{h,Cu}$, therefore the relationship of these parameters is shown as:

$$x_{Ag}/r_{Ag} = x_{Cu}/r_{Cu} \quad (4.7)$$

By substituting Equations 4.5 and 4.6 into Equation 4.7:

$$(r_{Ag} \rho_{Ag})^{1/2} / (\phi_{Ag})^{1/2} = (r_{Cu} \rho_{Cu})^{1/2} / (\phi_{Cu})^{1/2} \quad (4.8)$$

Finally, the optimum concentration of the Ag is:

$$\phi_{Ag} = \phi_{Cu} \left(\frac{r_{Ag}}{r_{Cu}} \right) \left(\frac{\rho_{Ag}}{\rho_{Cu}} \right) \quad (4.9)$$

In the previous work, the optimum concentration of the Cu ϕ_{Cu} is concluded to be 150 mg/mL, so the optimum concentration of the Ag is calculated as:

$$\phi_{Ag} = 150 \times \left(\frac{0.5}{5} \right) \left(\frac{10.49}{8.96} \right) \approx 17.56 \text{ mg/mL} \quad (4.10)$$

The result is near 20 mg/mL, thus in subsequent experiments of this work, the Ag particle-based suspension with the concentration of 20 mg/mL was used.

4.3 Dependence of Healing Time on Electric Field

This section investigates the impact of the electric field (ξ) on the healing time. Experiments were performed using suspensions with the optimised concentration of 20 mg/mL, the length of the open gap was set to be $s \approx 80 \mu\text{m}$, and the external resistance connected to the printed wire was $R_{\text{ext}} \approx 220 \text{ k}\Omega$. For each sample, the actual length of the open gap was first measured, then an appropriate voltage was subsequently set in the SMU to be applied to the circuit, in this way a specific value of the electric field across the open gap could be achieved. By conducting the verification test, it was found that the healing was not consistent when $\xi < 0.6 \text{ V}/\mu\text{m}$. When $\xi > 1.3 \text{ V}/\mu\text{m}$, the healing occurred rapidly, but the corresponding voltages were too high, resulting in damage to the active devices like transistors. Therefore, electric field strengths selected in this work were 1.0, 1.1, 1.2, and 1.3 $\text{V}/\mu\text{m}$. For each electric field strength, about 12 sets of data were collected, and typical data sets are drawn in Fig. 4.5(a). The Ag particle-based suspensions could heal the open faults under all these electric fields, and the healing time decreased with the increase of the electric field strength.

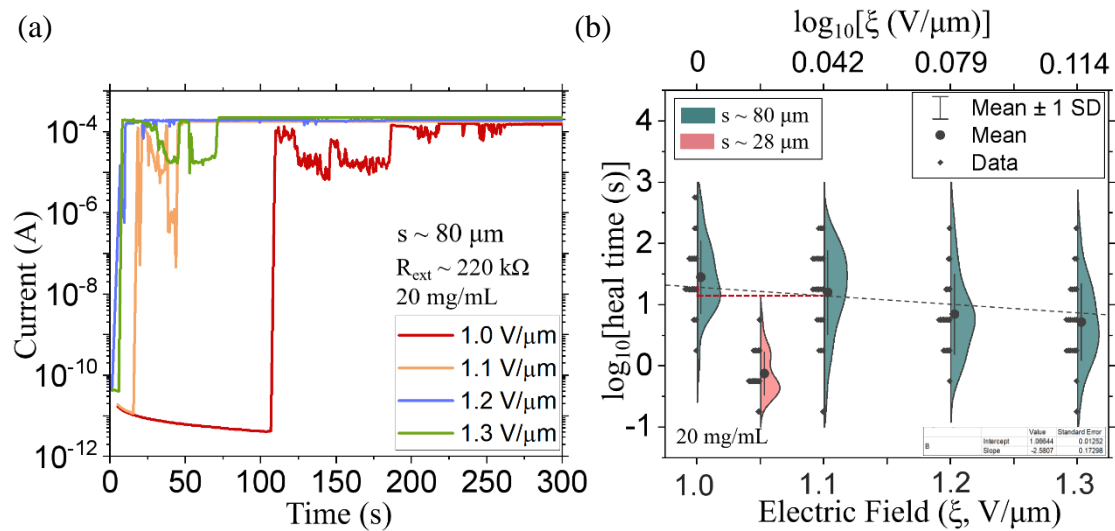


Figure 4.5. (a) Typical dynamics of current for the self-healing occurred under electric fields of 1.0, 1.1, 1.2, and 1.3 $\text{V}/\mu\text{m}$ (b) The dependence of the healing time on electric field strengths.

Fig. 4.5(b) shows the distribution of the healing time (τ_h) as a function of the electric field (ξ). The black dashed line reveals the trend of the mean τ_h versus ξ in a log–log scale. When fitting this line, the average value of the healing time for $\xi = 1.0 \text{ V}/\mu\text{m}$ was modified because one or two abnormal data points (like $\tau_h \approx 650 \text{ s}$) had a

great influence on the average result. The linear fitting of the data points on a log–log scale shows the slope of this dashed line to be $\Delta y/\Delta x \approx -2.58$, and this result indicated that τ_h varies as the -2.58^{th} power of the electric field strength. The theoretical relation between these two variables can be derived from Equation 4.1. By taking the logarithm of both sides, Equation 4.1 can be transformed to:

$$\log_{10} t \sim -2\log_{10}(\xi) + \log_{10} \left(\frac{\eta_f}{\epsilon_f} (n_p r_p) \right)^{-\frac{5}{3}} \quad (4.11)$$

In Equation 4.11 the constant coefficient for the electric field strength-related term $\log_{10}(\xi)$ is -2, which is approximate to the experimental result of -2.58. This result indicates that τ_h varies as around $1/\xi^2$ as predicted by theory.

As described earlier, this work follows a wire-device-circuit logic. To prove the feasibility of using the PBSH technique for TFT devices or circuits, the case of healing an open gap length of $s \approx 20 \mu\text{m}$ with $\xi \approx 1.05 \text{ V}/\mu\text{m}$ was also performed in this work, since this represents the typical operating voltage for TFTs. The result shown in Fig. 4.5(b) indicates that in this case the open gap can be repaired in a short time, and this result becomes the base for further studies in Chapter 5 and 6.

4.4 Dependence of Healing Time on Open Gap

This section explores the impact of the length of open gap (s) on the healing time (τ_h). Open gaps with the length of $s \approx 28 \mu\text{m}$ and $80 \mu\text{m}$ were purposely created in printed wires. Suspensions with the optimised concentration 20 mg/mL were utilised in this experiment to repair the open gap, and the electric field across the open gap was controlled to be in the range of $1.05 \sim 1.10 \text{ V}/\mu\text{m}$. Fig. 4.6(a) shows the time of healings occurred in different gaps ($s = 28$ and $80 \mu\text{m}$) when printed wires were connected to various external resistances. From this figure it can be concluded that the healing time becomes longer when the open gap is widened. To explain this phenomenon, Ag particles are assumed to be evenly aligned in the open gap and the distance between two particles is assumed to be constant. In that case the longer gap distance needs more Ag particles to form the conductive pathway. Fig. 4.6(b) analyses the dipole-dipole attraction forces in two-particle and four-particle systems, respectively. F_{12} represents the attraction force between Particle 1 and 2 experienced by Particle 1. Case 1 simulates the short gap condition and Case 2 simulates the long gap condition. In each case particles at the middle position are focused. In Case 1, Particle 1 only experiences one

attraction force F_{12} from Particle 2 while in Case 2, Particle 2 bears three forces: F_{21} , F_{23} , and F_{24} . According to Coulomb's law, the relationship between these forces is: $F_{12} = F_{23} = -F_{21} > F_{24}$, so when only considering the attraction force, the resultant force in Particle 1 (Case 1) F_{12} is larger than that in Particle 2 (Case 2) $F_{23} + F_{24} + F_{21} = F_{24}$. Derived from this model, the resultant force experienced by middle particles decreases with the increase of particle numbers, and weaker attraction force leads to longer times for particles to move over the same distance. Since the healing requires the connection of all particles in the bridge, the healing time (τ_h) becomes longer when it needs more time for driving middle particles.

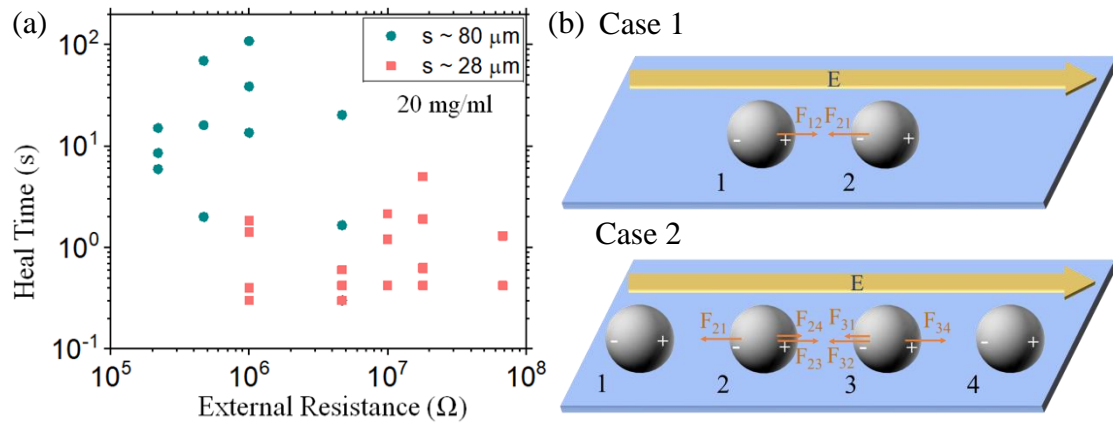


Figure 4.6. (a) Distribution of the healing time against the external resistance in different open gaps (b) Analysis of the dipole-dipole attraction force in Ag particles.

4.5 Dependence of Healing Time on External Resistance

This section discusses the impact of the external resistance (R_{ext}) on the healing time. As the initial field across the gap $\xi \sim V_{\text{ext}}/s$ is independent of R_{ext} , the time taken for the healing does not show any inner connection with R_{ext} . However, R_{ext} can determine the level of current flowing in the circuit, and further influence the dynamics of sintering in the healing bridge. Dynamics of the healing current for different external resistances were shown in Fig. 4.7. It was found that large open gaps (here $s \approx 80 \mu\text{m}$) did not show successful healing when the printed wire was connected to large R_{ext} (here when $R_{\text{ext}} > 4.7 \text{ M}\Omega$). On the other hand, successful healing was achieved for smaller open gaps ($s \approx 20 \mu\text{m}$) even when connecting to large R_{ext} (up to $R_{\text{ext}} \approx 68 \text{ M}\Omega$). The reason for this is the difference of the heat needed in short and long gaps to remove the insulating coating and sintering the particles. The heat needed for the healing increases

exponentially with the linear increase in the number of particles. Since the PBSH technique also aims to heal the interconnect fault in a high-impedance OTFT device and circuit, this result is significant and should be taken into consideration for the further experiments.

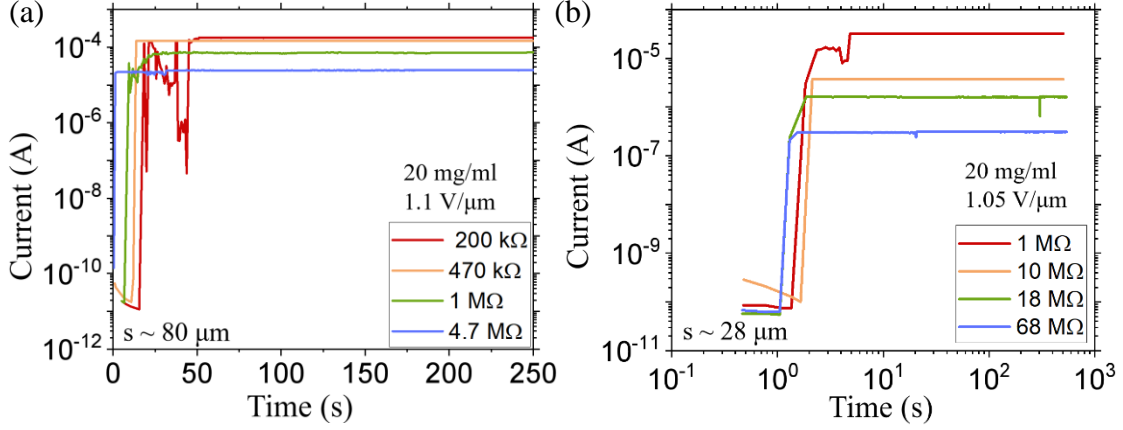


Figure 4.7. Dynamics of the healing current for different external resistances for (a) 80 and (b) 28 μm open gaps.

The impedance of the TFT is given by:

$$R_{TFT} = [\mu C_i (W/L) (V_{gs} - V_T - V_{DS})]^{-1} \quad (4.12)$$

As described in Section 2.5 and 2.6, the inkjet-printed OTFT fabricated in this work has an aspect ratio of $W/L = 1600 \mu\text{m}/80 \mu\text{m} = 20$. In addition, it has a mobility of $\mu = 0.1 \text{ cm}^2/\text{Vs}$ and the dielectric capacitance per unit area is $C_i \approx 10 \text{ nF}/\text{cm}^2$. The typical threshold voltage for this OTFT is $V_T = -1 \text{ V}$, and the gate–source voltage V_{gs} and drain–source voltage V_{ds} are set to be -30 V and -25 V , respectively. Bringing all these value into Equation 4.12 the impedance is calculated as $12.5 \text{ M}\Omega$. Based on this value and the result shown in Fig.4.7, it can be concluded that when the open gap is $s \approx 20 \mu\text{m}$, the self-healing of OTFT devices and circuits could be possible.

4.6 Stability of the Healing

The stability of the healing is a topic of concern in this work. As mentioned in Section 4.3, the healing does not occur under the low electric field (in this work, when $\xi < 0.6 \text{ V}/\mu\text{m}$). The concern is, if the high electric field under which the healing occurs drops to a low level, can the healed bridge sustain and continue to act as the pathway for the current? To give the answer to this concern, a stability test was designed. In this

experiment, the Ag wire with an open gap ($s \approx 28 \mu\text{m}$) was printed on the PEN substrate, and an external resistor ($R_{\text{ext}} \approx 1 \text{ M}\Omega$) was connected to this printed wire. The healing was then achieved by applying an external voltage $V_{\text{ext}} = 25 \text{ V}$ with the SMU and holding for 1000 s, then the voltage was reduced to 5 V, holding for 1000 s and subsequently set to 1 V for another 1000 s. The current in the circuit was continuously monitored through the experiment. The original electric field ξ_1 was $0.9 \text{ V}/\mu\text{m}$, which was above the threshold value for triggering the self-healing. However, in the later two cases, the theoretical electric field ξ_2 and ξ_3 were calculated to be $0.18 \text{ V}/\mu\text{m}$ and $0.04 \text{ V}/\mu\text{m}$, both of which were far below the threshold value for triggering the healing. As shown in Fig. 4.8(a), the open gap in the printed wire was repaired at the time $t \approx 30 \text{ s}$ (inset) under the electric field of $\xi_1 \approx 0.9 \text{ V}/\mu\text{m}$. After the healing, the current was kept at $I_1 \approx 25 \mu\text{A}$ during the first 1000 s. When the electric field dropped to $\xi_2 \approx 0.18 \text{ V}/\mu\text{m}$, the bridge did not break and the current at the level of $I_2 \approx 5 \mu\text{A}$ could stably flow through the healed bridge for the second 1000 s. As the electric field continued to decrease to $0.04 \text{ V}/\mu\text{m}$, the bridge still existed in the open gap and the low current ($I_3 \approx 1 \mu\text{A}$) could keep stable during the last 1000 s. Through this test, the current was observed to be stable and dependent on R_{ext} alone. This result indicates the permanence and low resistance of the healed bridge. The resistance of the healed bridge was measured when using the PBSH technique to heal open gaps ($s = 20 - 30 \mu\text{m}$). Fig. 4.8(b) is the histogram of resistances for steady-state healed bridges. The typical healing resistance in steady state is $\approx 400 \Omega$, and compared with the external resistance in the TFT-based circuit ($\text{M}\Omega$ level), the healing resistance can be neglected.

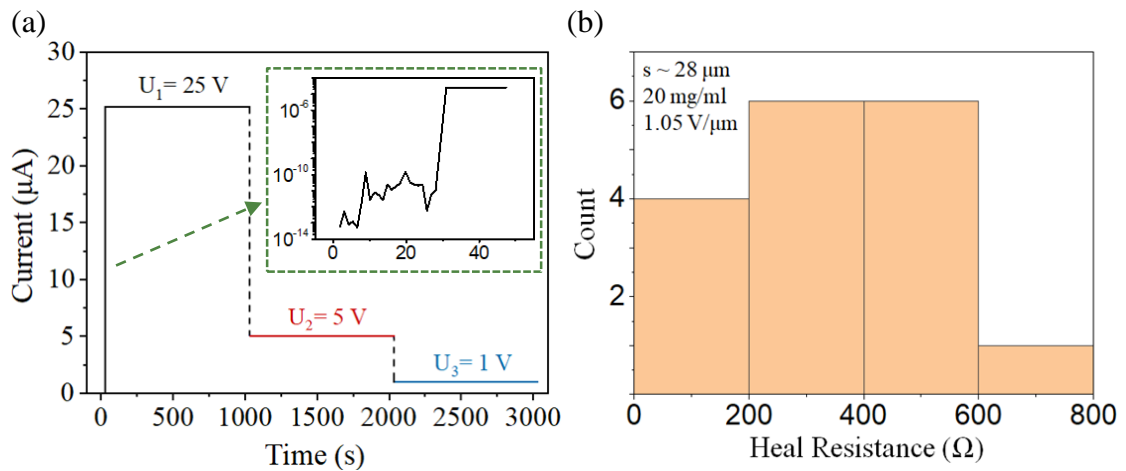


Figure 4.8. (a) The stability of the healing when the external voltage is sequentially lowered (b) The histogram of resistances for steady-state healed bridges.

4.7 Summary

In this chapter, self-healing in inkjet-printed interconnects has been investigated. The impact of suspension concentrations, electric field, length of open gap and external resistance on the healing time have been revealed by theoretical derivations and experimental results. The healing time is proven to decrease with the increase of the suspension concentration and electric field strength. In contrast, the increase of the length of open gap would lead to an increase in healing time. The external resistance does not directly determine the healing time, but it influences the dynamics of sintering in the healing bridge. Once the conductive pathway has formed and sintered across the open gap, the interconnection can be stable even when the external voltage drops to a level lower than the threshold voltage for the occurrence of the self-healing. The feasibility and stability of applying the PBSH technique to printed interconnects has given the possibility of using this technique in OTFT devices and circuits, which are to be presented in later chapters.

5 SELF-HEALING IN OTFT INTERCONNECTS

As mentioned in the previous chapter, this dissertation follows a wire-device-circuit logic. Chapter 4 has proven the feasibility of self-healing in printed interconnects. This chapter shows the self-healing of an open fault in OTFT device interconnects. Healings at both source and drain sides are discussed in this chapter. Section 5.1 introduces the experimental setup and the layout of OTFTs used in this experiment. Section 5.2 analyses the dynamics of the healing occurred at the source side while Section 5.3 focuses on the healing at the drain side. These sections prove the feasibility of the PBSH technique in OTFT device interconnects by showing the healing in both transfer and output curves.

5.1 Experimental Set-up

As described in Section 3.5, the inkjet-printed OTFT device with an inverted coplanar (BGBC) structure was utilised in this work. The schematic diagram and microscopic image of this printed OTFT are shown in Fig. 5.1(a). The source and drain electrodes were deposited along the top and bottom edges of the gate electrode. The area between these two electrodes is the channel region, and the distance between them is the channel length. To simplify the measurement, extended wires connecting to pads of source and drain electrodes were printed, as illustrated in Fig. 5.1(b). The measurement was conducted using the Semiconductor Characterisation System (SCS) and the probe station system. In this measurement, probe tips were placed on the pads of the Gate electrode and two extension wires. The SCS kept the source of the OTFT at ground, and provided dc bias voltages to the drain and gate electrodes, respectively.

Since the OTFT device used in this work is a p-type one, the voltage was set as $V_d < 0$ and $V_g < 0$ with respect to ground.

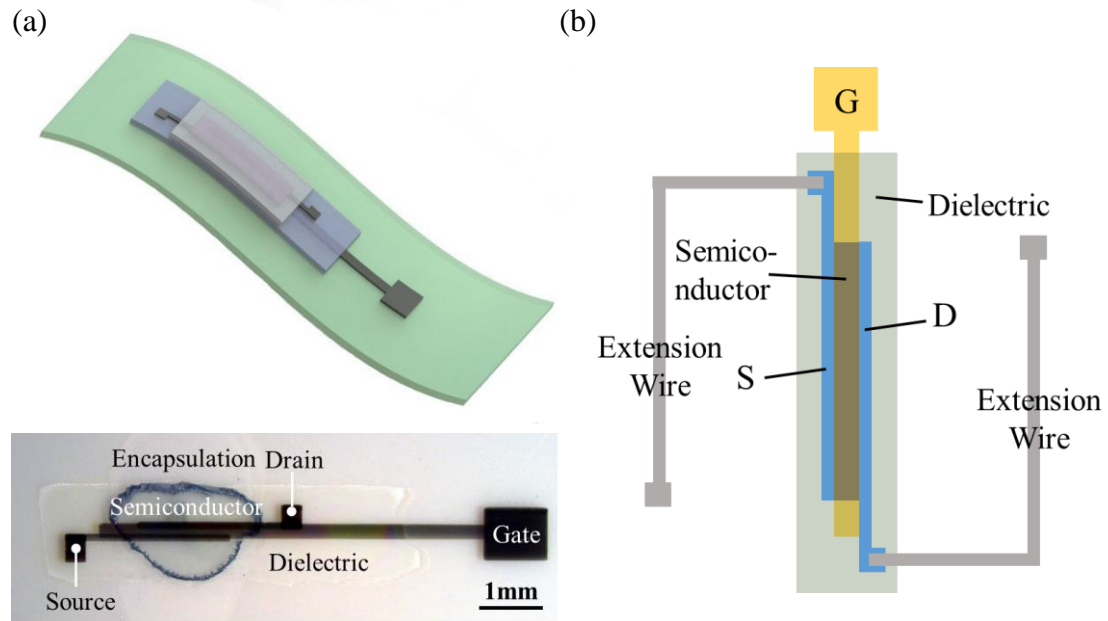


Figure 5.1. (a) Schematic and microscopic image of an OTFT printed on flexible substrate. (b) Layout and patterns of various layers in printed OTFT.

Self-healing in OTFT interconnects was characterised by the following steps: First, the original characteristics of the OTFT were measured, including the transfer and output characteristics. Then the open fault was purposely created in the extension wires, and the transfer curve was swept again showing the change of the current I_{ds} flowing through the drain and source electrodes. The last step was to drop the particle-based suspension on the open fault and sweep the transfer and output curves once again. The healing process was continuously monitored and the final current curve was compared with the original characteristics measured in the first step.

5.2 Self-healing of the Fault Located at the Source Side

In this work, both cases of the fault occurred at the source and drain sides were considered. In case 1, an open fault with the length of s was introduced in the extension wire between the ground probe and the source electrode. The equivalent circuit is shown in Fig. 5.2, here $V_h(t)$ is the voltage drop across the open gap, which is time-dependent and affects both the drain–source voltage (V_{ds}) as well as the gate–source voltage (V_{gs}) of the OTFT. The experiment was started by dropping the suspension onto

the open gap and then applying voltage bias at three terminals, i.e., the gate electrode, extension wires connecting to source and drain electrodes. The voltage bias applied to them were V_g ($V_g - V_T < 0$), ground, and V_d ($V_d < 0$), respectively. Meanwhile, the dynamics of the current flowing through the OTFT was monitored. To fully reveal the healing in interconnects, three results were shown in this experiment: the dynamics of the transfer curve ($I_{ds} - V_{gs}$), the output curve ($I_{ds} - V_{ds}$), and the curve showing the dependence of the drain-source current with time ($I_{ds} - t$).

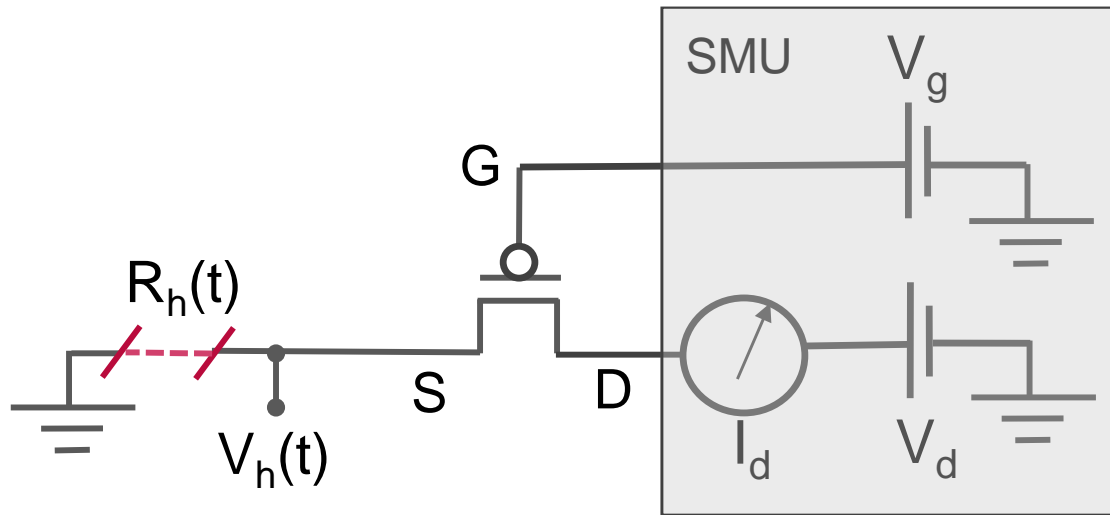


Figure 5.2. Schematic of the circuit for simulating the healing of the open fault at the source side of an OTFT.

During the sweep of the transfer curve, extension wires connecting to source and drain electrodes were applied with voltages $V_s = \text{GND}$ (ground) and $V_d = -25 \text{ V}$, while the voltage applied to the gate electrode V_g swept from 5 V to -25 V . At time $t = 0$, V_g was biased at a positive value, for p-type OTFT there was no passable channel for the transport of charge carriers (holes), so the impedance between source and drain R_{ds} was very large and $V_{ds} \approx V_d$, $V_h(t=0) \approx 0$. At this time no electric field existed in the open gap. When the gate voltage swept to the negative value whose absolute value was larger than that of the threshold voltage for the OTFT ($|V_g| > |V_T|$), the channel between source and drain formed and made it conductive between source and drain. At this time, the large resistance of the open fault led to $V_h(t) \approx V_d$ and caused an electric field $\zeta = V_d/s$ in the open gap. Then this electric field polarised metal particles in the suspension, and drove them to heal the fault. Before the completion of the healing there was no current flowing through source and drain ($I_{ds} \approx 0$), but once the healing was completed, the

current I_{ds} jumped to the original level before the open fault occurred. Fig. 5.3(a) gives the transfer curves of an OTFT without the open fault (original level, black line), with the open fault at the source side (circuit failed, red line), the sweep showing the healing (blue line), and another sweep taken after 5 min of the first healing (green line). Without the open fault, the device showed an off-current of $I_{off} \approx 10^{-12}$ A and an on-current of $I_{on} \approx 10^{-6}$ A, so the on-off current ratio was 10^6 . When the open fault occurred, the current kept constant below the off-current level ($10^{-14} \sim 10^{-12}$ A). Then after applying the suspension, the healing started when $V_g < 0$, $|V_g| > |V_T|$ and finished when $V_g \approx -7$ V. The healing is clearly shown in the blue line, jumping from the off-level to the on-level. After the completion of the healing, the blue line coincides with the black line, indicating the same electrical characteristics of the device before the failure and after the healing. The green line proves the stability of the healing, it shows that after 5 min of the healing, the healed bridge still existed, guaranteeing the normal operation of the OTFT device. Fig. 5.3(b) shows the output curve of the OTFT without the fault (original level, black line), the sweep immediately after the healing (blue line), and another sweep taken after 5 min of the first healing (green line). As shown in the figure the curve immediately after the healing coincides with the original output curve, and only has small variation after 5 min. This result indicates the effectiveness and stability of the healing in OTFT interconnects.

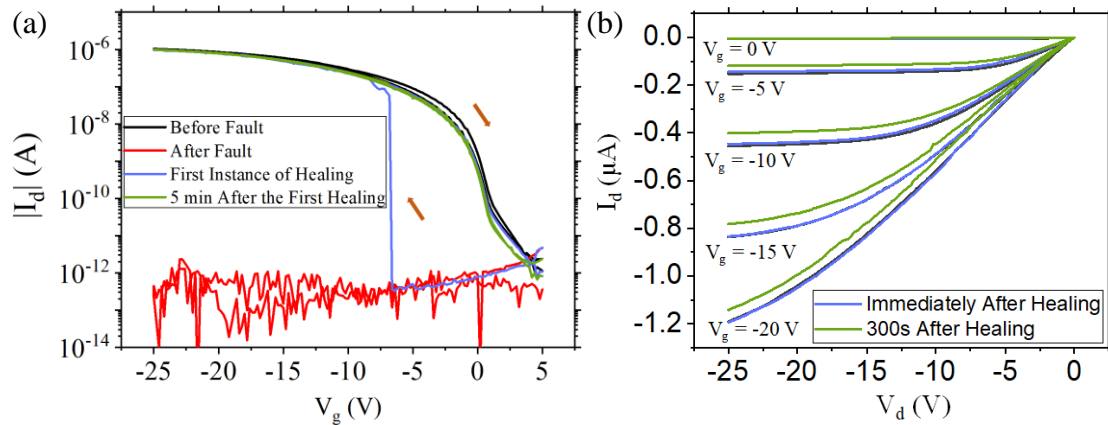


Figure 5.3. The (a) transfer and (b) output characteristics of the OTFT before and after the healing of the open fault at source side.

The curve showing the dependence of the drain-source current on the time ($I_{ds} - t$) was also measured in this experiment. Applied voltages remained constant and the current through the source and drain was monitored by the SCS. Fig. 5.4 shows the

dependence of I_{ds} on t when applying different V_d and V_g . In Fig. 5.4(a), the voltage applied on the gate electrode was $V_g = -25$ V. The red line showed no healing because the electric field across the open gap was $10/19 \approx 0.53$ V/ μm , which was less than the threshold value for the healing. The green line showed the most rapid healing since it had the largest electric field strength $20/12 \approx 1.67$ V/ μm and the shortest open gap 12 μm . This result has a good agreement with the theoretical conclusion in Section 4.3 and 4.4. In Fig. 5.4(b), the voltage applied on the extension wire connecting to the drain electrode was $V_d = -25$ V, and the voltages applied on the gate electrode were -5 V, -10 V and -15 V. All these voltages were larger than the threshold voltage (V_T) of the OTFT, so all OTFTs were kept in the ON state. As V_d was fixed, the red line takes longer time than the other two lines because of the longer gap distance and the weaker electric field. At the same time, the blue and green lines showed the same healing time since their gap distance was closed. This result also matched well with the relations predicted by theory in Section 4.3 and 4.4.

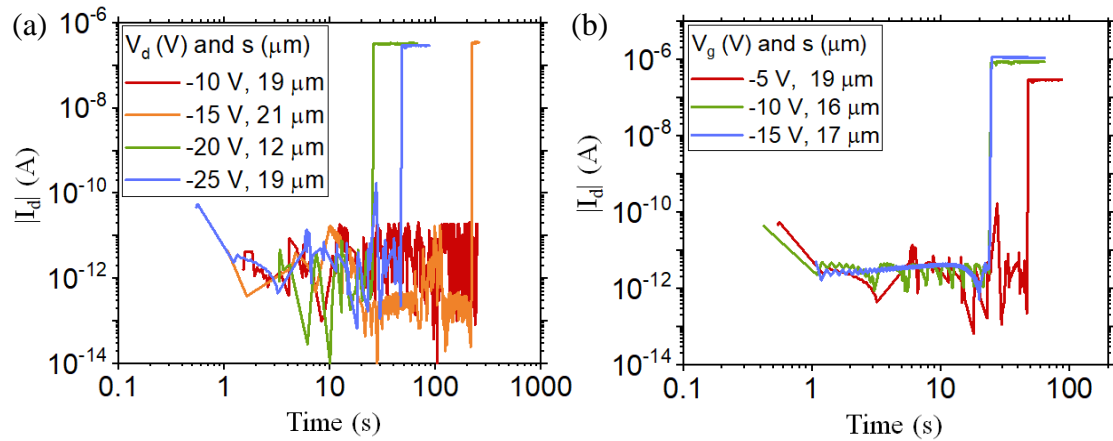


Figure 5.4. Dynamics of the source-drain current (I_{ds}) in the OTFT during self-healing of the open fault at the source side when applying (a) various drain voltages (V_d) and (b) various gate voltages (V_g).

5.3 Self-healing of the Fault Located at the Drain Side

In case 2, an open fault with the length of s was created in the extension wire between the V_d probe and the drain electrode. Different from case 1, in this case the open gap only affected the drain–source voltage (V_{ds}) and did not affect the gate–source voltage (V_{gs}). Fig. 5.5 illustrates the equivalent circuit for this experiment. The measuring process was the same as that in case 1. The voltage bias V_g ($V_g - V_T < 0$),

GND, and V_d ($V_d < 0$) were applied on the gate electrode and extension wires connecting to source and drain electrodes. The suspension was dropped onto the open gap and dynamics of the current flowing through source and drain (I_{ds}) was monitored. Also, the data to be measured in this case stayed the same with those in case 1: the dynamics of the transfer curve ($I_{ds} - V_{gs}$), the output curve ($I_{ds} - V_{ds}$), and the curve showing the dependence of the drain-source current on the time ($I_{ds} - t$).

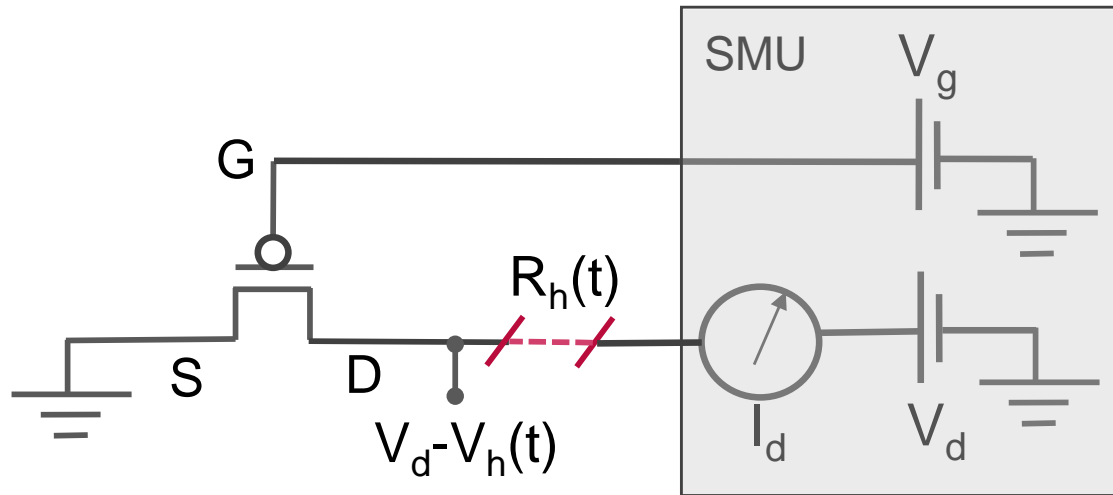


Figure 5.5. Schematic of the circuit for simulating the healing of the open fault at the drain side of an OTFT.

When measuring the healing in the transfer curve, extension wires connected to source and drain electrodes were applied by the voltage bias of $V_s = \text{GND}$ and $V_d = -20$ V, while the voltage applied on the gate electrode V_g swept from 3 V to -20 V. The difference between case 1 and case 2 was the initial stage of the healing. In case 1, at time $t = 0$, the OTFT was biased at the OFF state and the voltage across the open gap at the source side was $V_h(t=0) \approx 0$, so there was no electric field in the open gap and no healing occurred. The healing started to occur when V_g swept to the negative value and $|V_g| > |V_T|$. However, in this case, at time $t = 0$, the OTFT was biased at the OFF state but the voltage across the open gap at the drain side was $V_h(t=0) \approx V_d$, which means the electric field existed in the open gap and could drive particles to heal the open fault. Therefore, in this case, the healing started from the beginning of the voltage sweep. Fig. 5.6(a) gives the transfer curves of an OTFT without the open fault (original level, black line), with the open fault at the drain side (circuit failed, red line), the sweep showing

the healing (blue line), and another sweep taken after 5 min of the first healing (green line).

In the original transfer curve, this device showed an off-current of $I_{\text{off}} \approx 10^{-12}$ A and an on-current of $I_{\text{on}} \approx 10^{-6}$ A, thus the on-off current ratio was 10^6 . The current dropped to 10^{-14} - 10^{-12} A upon the occurrence of the open fault, indicating the failure of interconnects in the device. Then the suspension was applied, as the electric field V_d/s existed in the open field, the healing started immediately. The blue line in Fig. 5.6(a) showed a gradual process of the healing because the strength of the electric field was $\xi = 20/19.3 \approx 1.04$ V/ μm , and under this electric field it needed a long healing time as shown in Section 4.3. However, after the completion of the healing, the healed curve coincided well with the original transfer curve. The curve was swept again after 5 min of the healing, and the result (green line) showed a good stability of the healed interconnects. Fig. 5.6(b) shows the output curve of the OTFT without the fault (original level, black line), the sweep immediately after the healing (blue line), and another sweep taken after 5 min of the first healing (green line). These curves had the good match at the ON state region, which indicated the successful healing in interconnects. The variation and hysteresis in transfer and output curves near the OFF state region were because of the high density of defects at the semiconductor-insulator interface. In this region a lot of charge carriers were trapped by the defects, causing the degradation of the current. However, when all defect states were filled, charge carriers could fluently transport in the semiconductor and the current could return to the normal level.

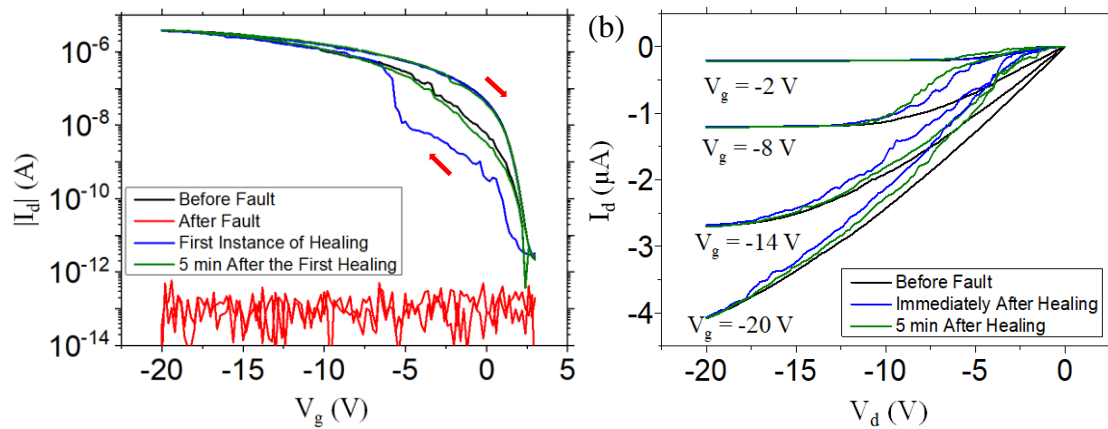


Figure 5.6. The (a) transfer and (b) output characteristics of the OTFT before and after the healing of the open fault at drain side.

Like in the previous experiment, the curve showing the dependence of the drain-source current on the time ($I_{ds} - t$) was measured, and the result was shown in Fig. 5.7. In Fig. 5.7(a), the gate electrode was supplied by the voltage bias of $V_g = -25$ V. Under the weak electric field $\xi = 10/17 \approx 0.59$ V/ μm , which was less than the threshold value for the healing, the healing could not occur in the open gap (red line). The green line was achieved with the condition of the strong electric field $\xi = 20/15 \approx 1.33$ V/ μm and the short open gap ($s = 15$ μm), so it had the shortest healing time in these experiments. In Fig. 5.7(b), the voltage bias of $V_d = -25$ V was supplied by the SCS, applying on the extension wire connecting to the drain electrode, and the voltages applied on the gate electrode were -5 V, -10 V and -15 V. Since these gate voltages were above the threshold voltage (V_T) of the OTFT, the devices remained at the ON state. As V_d was fixed at -25 V, the healing time was determined by the length of the open gap. In Fig. 5.7(b) the healing time decreased with the narrowing of the open gap, agreeing with the relations revealed in Section 4.3 and 4.4.

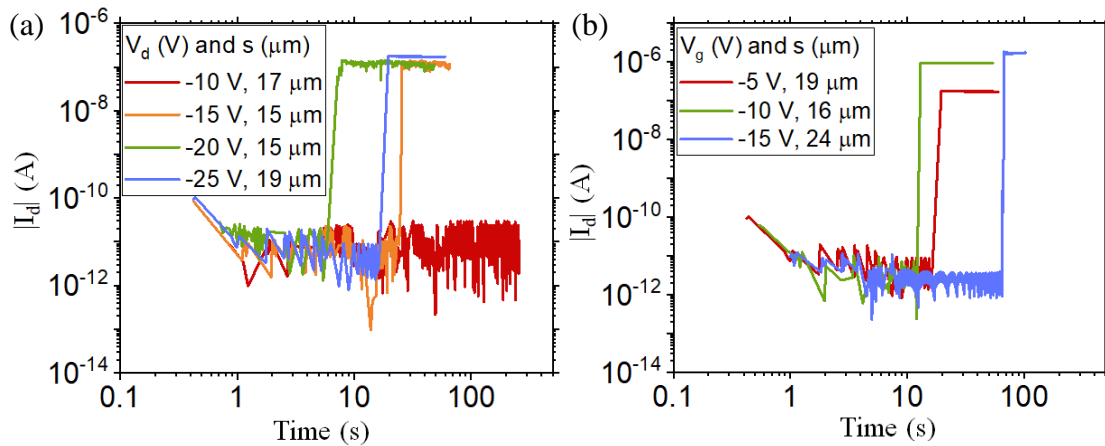


Figure 5.7. Dynamics of the source-drain current (I_{ds}) in the OTFT during self-healing of the open fault at the drain side when applying (a) various drain voltages (V_d) and (b) various gate voltages (V_g).

To further verify the relationship between the healing time and the electric field in OTFT interconnects, the dependence of the healing time on the electric field when applying various V_g in OTFT interconnects were counted in Fig. 5.8. The distributions of the data were fitted by the dashed line on a log-log scale. This line showed the trend of the mean τ_h versus ξ and had a slope of $-(2-1)/[0.3-(-0.2)] = -2$. This experimentally derived value conformed to the theoretical value derived from Equation 4.11. This

indicates that the self-healing of the open fault in the OTFT interconnects follows the same physical mechanism as the self-healing in wire interconnects. And when the self-healing occurs in OTFT interconnects, the gate-source voltage V_{gs} controls the ON/OFF state of the channel while the drain-source voltage V_{ds} modulates the electric field in the open gap, and further influences the healing time τ_h .

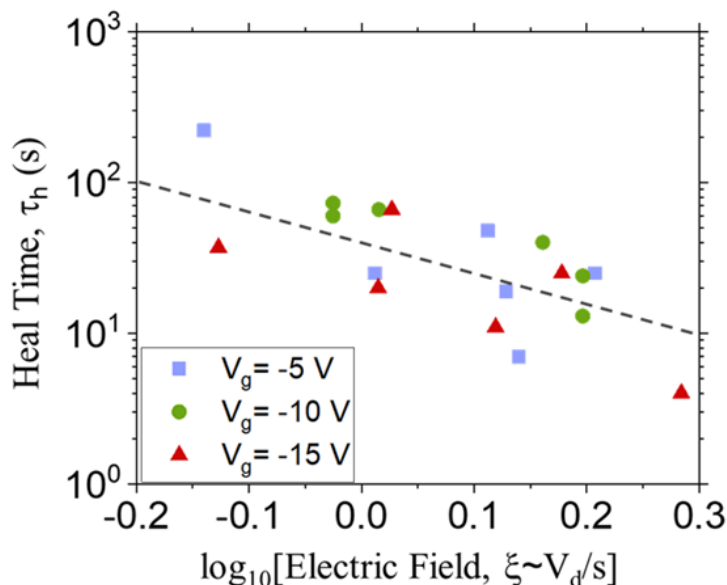


Figure 5.8. Impact of the electric field on the healing time with various gate voltages.

5.4 Summary

In this chapter, the self-healing in interconnects for inkjet-printed OTFT devices has been investigated. The open faults at the source and drain sides have been purposely created and the healing process has been monitored. In each case, the details of healings in the transfer curve ($I_{ds} - V_{gs}$), the output curve ($I_{ds} - V_{ds}$), and the dependence of the drain-source current on the time ($I_{ds} - t$) have been researched. All results indicate the successful healing of the open fault in OTFT interconnects. In addition, the healing in OTFT interconnects is proven to follow the same physical mechanisms as that in wire interconnects. The feasibility and stability of the self-healing in OTFT interconnects proved in this chapter have become the base for using the PBSH technique in OTFT-based circuits, which will be presented in the next chapter.

6 SELF-HEALING IN OTFT-BASED CIRCUITS

The feasibility of the self-healing in printed wire and OTFT interconnects has been proved in the previous chapters. This chapter analyses the self-healing of the open fault in OTFT-based circuits. Two circuits are investigated in this work: the current mirror and the common-source (CS) amplifier. Open faults are intentionally created in different nodes of the circuit, and healings of these open faults are discussed in this chapter. Section 6.1 introduces the experimental setup and the healing of open faults in different nodes for the current mirror circuit. Section 6.2 and Section 6.3 analyse the healing of open faults in the CS amplifier circuit. Here dynamics of both static characteristics and alternating current (AC) characteristics of the CS amplifier circuit before and after the healing are analysed in detail.

6.1 Self-healing in the Current Mirror

A current mirror is a circuit which functions to produce current in an output terminal by replicating the current flowing into or out of an input terminal. Conceptually, it is simply an ideal current amplifier with a gain of -1. There are two features of the current mirror: the first one is the relatively high output impedance which helps to keep the output current constant regardless of load conditions. Another one is the relatively low input impedance which helps to keep the input current constant regardless of drive conditions. Due to these features, the current mirror is often used in amplifier stages to provide bias currents and active loads.

6.1.1 Circuit and Characteristics

The current mirror has a symmetrical structure consisting of two transistors located at the input (reference) stage and the output stage, as illustrated in Fig. 6.1(a). The input part (left) is a current-to-voltage converter, in this part the gate is connected to the drain to incorporate negative feedback in the circuit. In the current mirror the two transistors are biased in the saturation region, in that case the drain-source current (I_{ds}) is controlled by the gate-source voltage (V_{gs}) with the equation:

$$I_{ds} = \frac{1}{2} \mu C_i \frac{W}{L} (V_{gs} - V_{th})^2 \quad (6.1)$$

and in turn I_{ds} can influence V_{gs} by the relation:

$$V_{gs} = V_{in} - RI_{ds} \quad (6.2)$$

By substituting Equation 6.2 into Equation 6.1, it can be concluded that the input current I_{in} can be controlled by changing the input voltage V_{in} . At the same time, V_{gs} converted from I_{in} can be the input signal for the output stage. As shown in Fig. 6.1(a), V_{gs} from the input stage is directly applied to the gate of the transistor in the output stage (right). As this transistor is also biased in the saturation region, the output current (I_{out}) is determined by Equation 6.1. When values of parameters for two transistors are the same, I_{out} equals to I_{in} , the copy of the current is achieved.

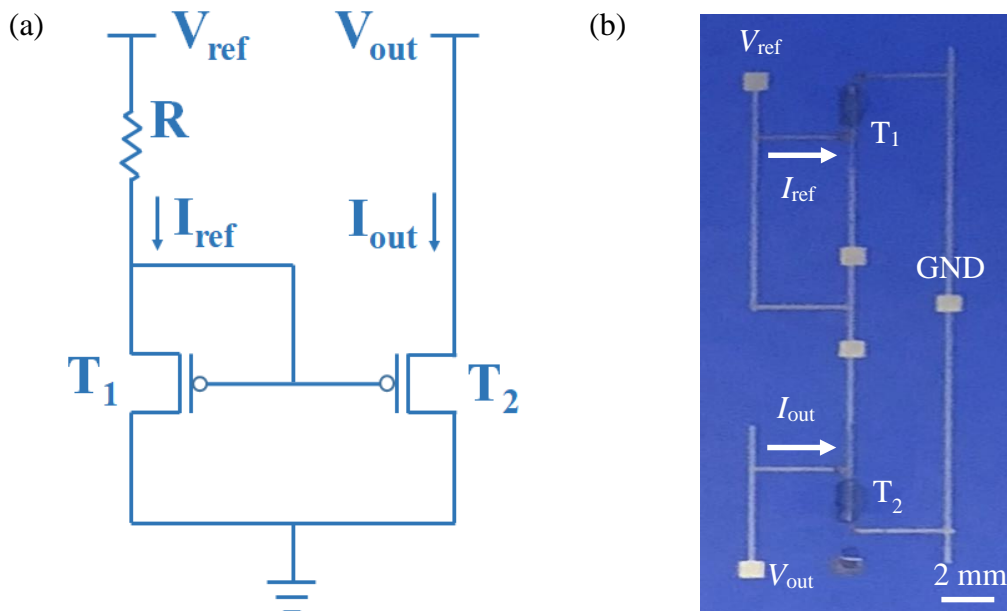


Figure 6.1. (a) Schematic circuit diagram and (b) Photo of an inkjet-printed current mirror.

To verify the function of the current mirror, a simulation was conducted using the simulation program with integrated circuit emphasis (SPICE). The version used in this work was Automatic Integrated Circuit Modelling Spice (AIM-Spice). In AIM-Spice simulation, the circuit was established by the netlist, and parameters for components are also defined in a netlist. In this work, the netlist for the current mirror circuit is shown in Appendix A. The input and output voltages were set as $V_{ref} = V_{out} = -25$ V, and parameters for OTFTs used in the simulation were extracted from inkjet-printed OTFTs in the current mirror circuit (Fig. 6.1(b)), which are summarised in Table 6.1.

Table 6.1 AIM-spice simulation: Parameters for OTFTs in current mirror

	Mobility (cm^2/Vs)	Aspect ratio (W/L)(μm)	Thickness of dielectric layer (nm)	FET models
TFT1	0.131	1600/80	500	Level=2
TFT2	0.146	1600/80	500	Level=2

The simulated and measured results are shown in Table 6.2. The current ratio of output and input currents was not 1 ($|I_{out}| / |I_{in}| \neq 1$), because a difference existed in the mobility of the two OTFTs located at the input and output stages, leading to the variation between these currents. In Table 6.2, the measured data approximated the simulated result, indicating the proper functioning of the printed current mirror circuit in the experiment. This conclusion is important as it is the basis for further study of the self-healing in the current mirror circuit.

Table 6.2 The simulated and measured currents in the current mirror.

	$ I_{ref} $ (μA)	$ I_{out} $ (μA)
AIM-spice simulated data	5.83	6.30
Experimental data	5.65	6.13

6.1.2 Self-healing in the Current Mirror Circuit

To study the impact of self-healing in the current mirror circuit, open-circuit faults ($s \approx 20$ μm) were purposely introduced in the circuit as shown in Fig. 6.2. Six cases were studied based on the location of the fault.

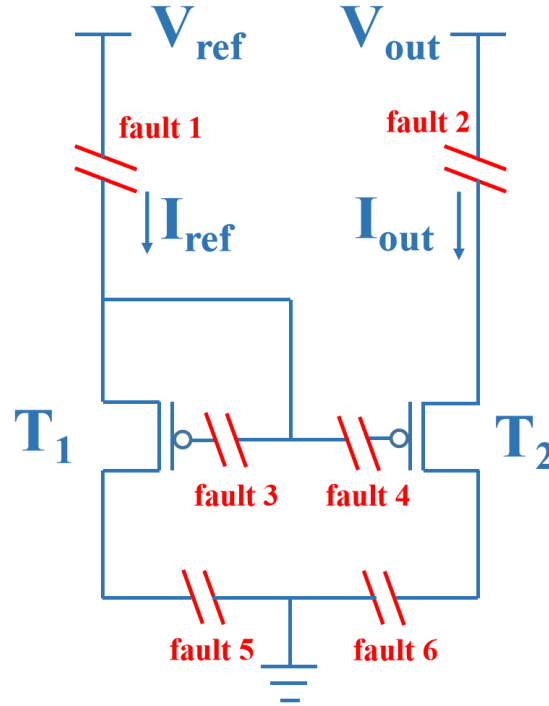


Figure 6.2. Schematic circuit diagram of a current mirror with faults located at various locations as defined by six cases.

In Case 1, the open fault occurred in the wire connecting the input voltage (V_{in}) and the common gate for drive and load TFT. This fault disabled the gate voltage for both TFTs, and cut the supply of the drain voltage for the drive TFT. So the voltage bias in the circuit was: for drive TFT (T_1), $V_{gs} = 0$ V and $V_{ds} = 0$ V, while for load TFT (T_2), $V_{gs} = 0$ V and $V_{ds} = -25$ V. In that case, there is no current flowing through the drain-source of the drive TFT ($I_{in} \approx 0$ A), and output current (I_{out}) dropped to the level when fixing $V_{gs} = 0$ V and $V_{ds} = -25$ V in the transfer characteristic curve. Subsequently, the suspension was dispensed over the region of the fault. At time $t = 0$ s, the electric field across the open gap was $\xi = 25/20 = 1.25$ V/ μm , which was over the threshold value for the self-healing. Under this electric field, particles in the suspension could be driven to form the conductive bridge to heal the open gap. As soon as the fault was repaired, both of input and output current jumped to the original level. The measured data were shown in Fig. 6.3(a), the original level for input and output current was $I_{in} \approx I_{out} \approx 6 \times 10^{-6}$ A, and after the occurrence of the open fault the input current dropped to $I_{in} \approx 10^{-14}$ A and the output current decreased to $I_{out} \approx 6 \times 10^{-9}$ A. Upon the drop of the suspension, the open gap was repaired at the time $t = 7$ s.

In Case 2, the open fault was in the interconnects joining the drain of the load TFT and the output voltage (V_{out}). This fault only cut the supply of the drain-source voltage (V_{ds}) for the load TFT and did not influence the voltage at other nodes. So the voltage bias in the circuit was: for drive TFT (T_1), $V_{gs} = -25$ V and $V_{ds} = -25$ V, while for load TFT (T_2), $V_{gs} = -25$ V and $V_{ds} = 0$ V. Therefore, the input current (I_{in}) would remain unchanged while the output current (I_{out}) would drop to $I_{out} \approx 0$ A. When dispensing the suspension over the fault region, particles were driven and healed the open gap under the electric field created by the output voltage V_{out} , causing the jump of I_{out} back to the original level. The measured data were shown in Fig. 6.3(b), the original level was $I_{in} \approx I_{out} \approx 6 \times 10^{-6}$ A. When the open fault occurred, the input current remained unchanged while the output current decreased to $I_{out} \approx 10^{-14}$ A. Then the open gap was quickly repaired ($\tau_h < 5$ s) upon the drop of the suspension.

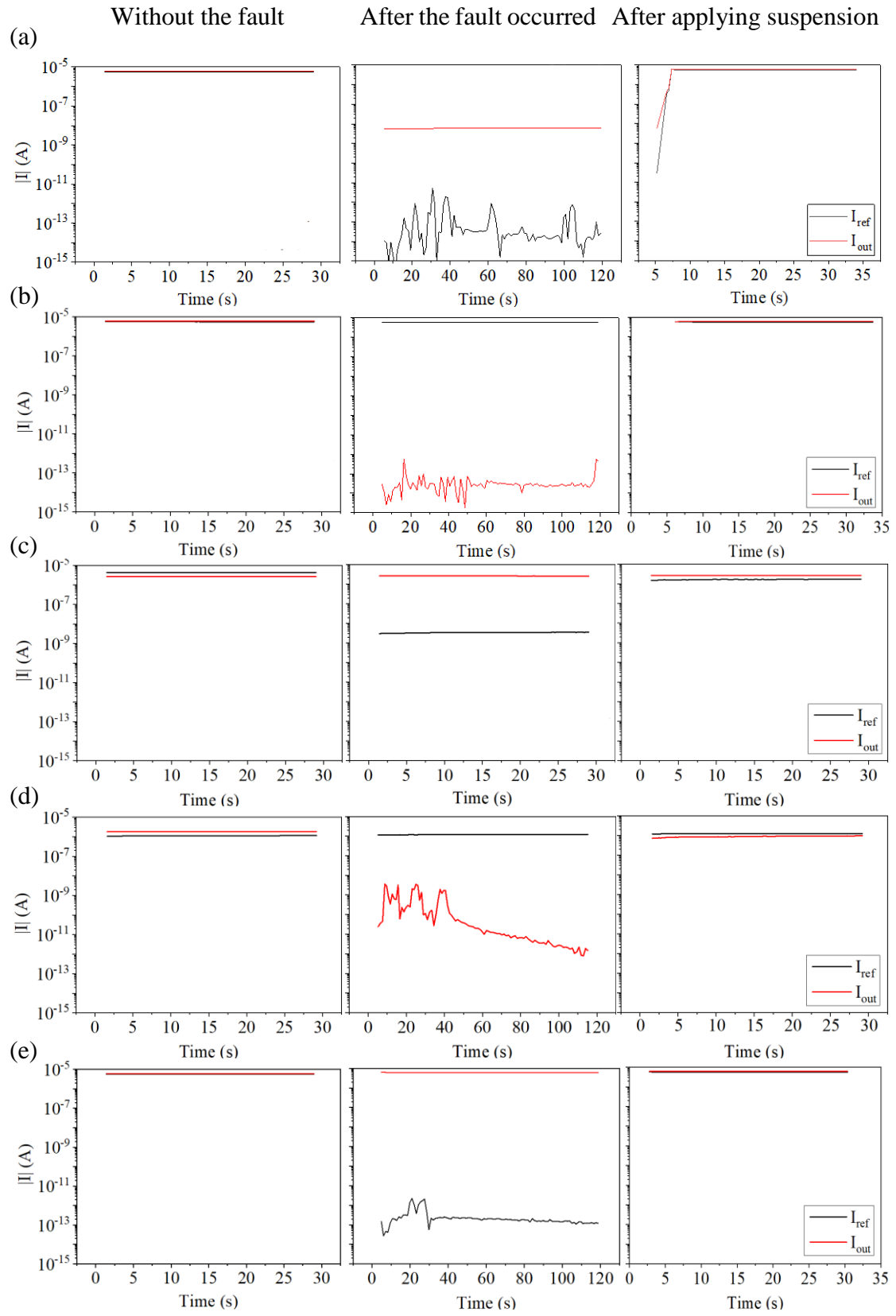
In Case 3, the diode-connect at the drive TFT side was cut, which disabled the supply of the gate voltage (V_{gs}) to the drive TFT. In that case, the voltage bias in the circuit was: for drive TFT (T_1), $V_{gs} = 0$ V and $V_{ds} = -25$ V, while for load TFT (T_2), $V_{gs} = -25$ V and $V_{ds} = -25$ V. So the input current (I_{in}) would drop to the level when taking $V_{gs} = 0$ V and $V_{ds} = -25$ V in the transfer characteristic curve and the output current (I_{out}) would remain unchanged. Due to the diode-connect structure, an electric field was created across the open gap by the input voltage (V_{in}). So the metallic micro-particle suspension could heal the open gap when being dispensed onto the fault region, bringing I_{in} back to the original level. Fig. 6.3(c) showed the measured current, the original level was $I_{in} \approx 4.3 \times 10^{-6}$ A and $I_{out} \approx 2.7 \times 10^{-6}$ A. When the open fault was introduced in the circuit, I_{in} dropped to $I_{in} \approx 3.1 \times 10^{-9}$ A while I_{out} remained unchanged. Subsequently, with the suspension, the healing was achieved in a short time ($\tau_h < 2.5$ s) and I_{in} returned to the original level.

In Case 4, the interconnection between the diode-connect node and gate of the load TFT was cut, which removed the gate voltage (V_{gs}) from the load TFT. Therefore, the voltage bias in the circuit was: for drive TFT (T_1), $V_{gs} = -25$ V and $V_{ds} = -25$ V, while for load TFT (T_2), $V_{gs} = 0$ V and $V_{ds} = -25$ V. In contrast to Case 3, the input current (I_{in}) would remain unchanged while the output current (I_{out}) would drop to the level when fixing $V_{gs} = 0$ V and $V_{ds} = -25$ V in the transfer characteristic curve. As the diode-connect structure provided gate voltage for both OTFTs in the circuit, like in Case 3, an electric field could also be created across the open gap by the input voltage (V_{in}),

driving particles in the suspension to heal the open fault. The experimental result was shown in Fig. 6.3(d), the original level was $I_{in} \approx 1 \times 10^{-6}$ A and $I_{out} \approx 1.8 \times 10^{-6}$ A. When the open fault was introduced in the circuit, I_{in} remained unchanged while I_{out} dropped to $I_{out} \approx 10^{-9} \sim 10^{-11}$ A. Like in Case 3, after dispensing the suspension over the fault region, the healing could be achieved in a short time ($\tau_h < 2.5$ s) and I_{out} returned to the original level.

In Case 5, the open fault was introduced in the interconnection connecting the source of the drive TFT and the ground (GND). This fault cut off the pathway for the drain-source current (I_{ds}) in the drive TFT but did not influence the load TFT. So with this fault the input current (I_{in}) would drop to $I_{in} \approx 0$ A while the output current (I_{out}) would remain unchanged. In the input part, the drive TFT acted as a resistor with large impedance. As there was no current flowing in the input part, the voltage across the open gap equalled to the input voltage (V_{in}), creating an electric field in the open gap and driving particles to heal the fault. The measured dynamics of the current were shown in Fig. 6.3(e), without the open fault the two currents were $I_{in} \approx I_{out} \approx 6 \times 10^{-6}$ A. The occurrence of the open fault brought I_{in} down to $I_{in} \approx 2 \times 10^{-13}$ A. After applying the suspension, particles were driven by the electric field and healed the open fault in a short time ($\tau_h < 2.5$ s).

Being symmetrical to Case 5, in Case 6, the open fault was introduced in the interconnection connecting the source of the load TFT and the ground (GND). The pathway for the drain-source current (I_{ds}) in the load TFT would be cut off by this fault. So with this fault the input current (I_{in}) would remain unchanged while the output current (I_{out}) would drop to $I_{out} \approx 0$ A. Like in Case 5, in the output part, the load TFT acted as a resistor with large impedance, and there was no current flowing in the output part, the voltage across the open gap equalled to the output voltage (V_{out}), creating an electric field in the open gap and driving particles to heal the fault. The measured dynamics of the current were shown in Fig. 6.3(f), the original level for I_{ds} in two OTFTs was $I_{in} \approx I_{out} \approx 6 \times 10^{-6}$ A, and the open fault in the output part brought I_{out} down to $I_{out} \approx 1 \times 10^{-13}$ A. By applying the suspension, the open fault was repaired when $t = 6.5$ s and I_{out} went back to the original level.



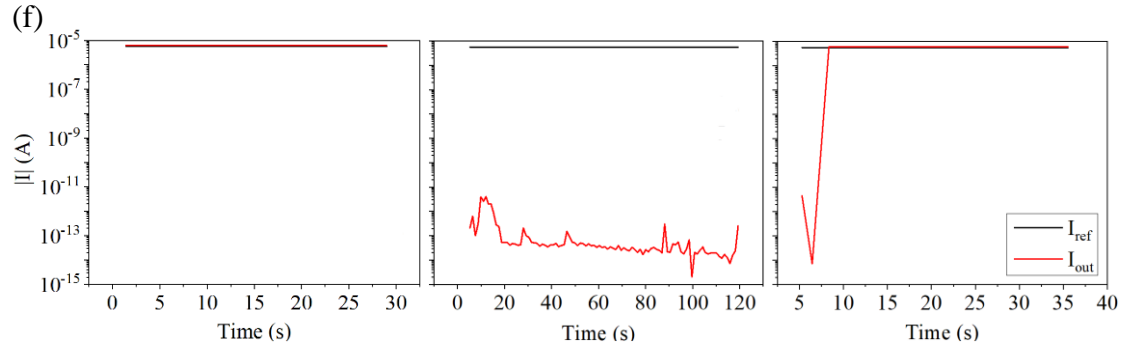


Figure 6.3. Self-healing in the current mirror circuit with the fault located at various locations as defined by six cases.

To summarise, in the above six cases, the PBSH technique repaired all open faults in the current mirror circuit. The voltage existed in all open gaps in these cases, as well as the electric field, which was the driving source for the self-healing in the interconnection. In addition, in all six cases, the healing did bring the input and output current back to the original level, which proves the effectiveness of the self-healing technique in the current mirror circuit.

6.2 Self-healing in the Common-source Amplifier (DC)

6.2.1 Circuit and Characteristics

Common-source (CS) amplifier is one of the most basic amplifiers in analogue circuits. Depending on the amplified parameters, it can be classified as either a transconductance amplifier or a voltage amplifier. In this work, a CS amplifier consisting of two transistors, i.e., a drive TFT (T_D) and a load TFT (T_L), was used to amplify the voltage. The configuration of the CS amplifier is shown in Fig. 6.4(a). It was driven with a dc supply voltage $V_{DD} = 30$ V. The input voltage (V_{in}), sweeping from 35 V to -5 V, was supplied to the drive TFT while the load TFT was diode-connected to ground. Fig 6.4(b) is the photo of the inkjet-printed CS amplifier fabricated in this work.

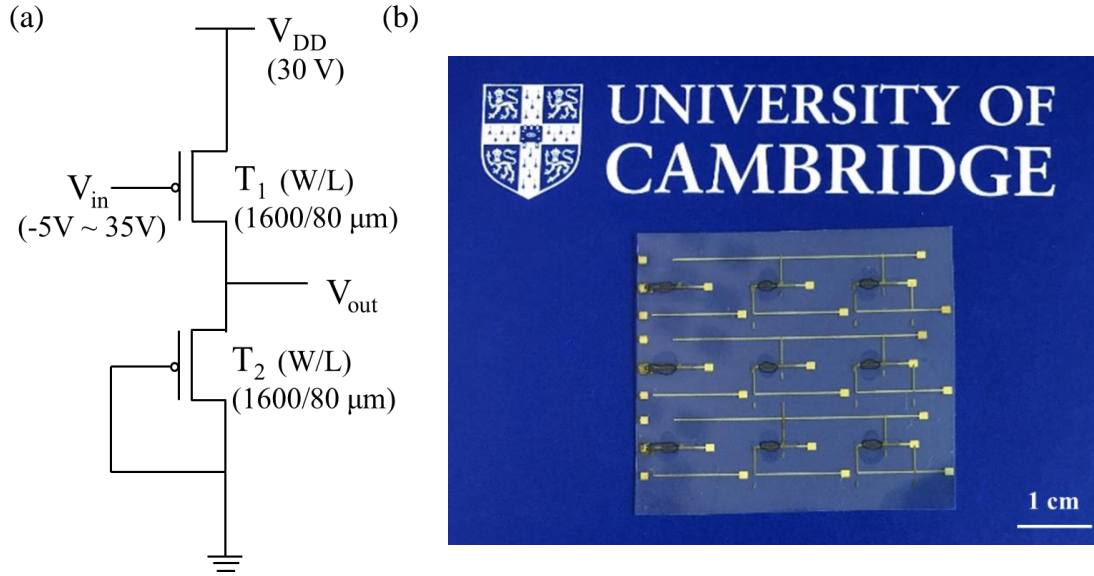


Figure 6.4. (a) Schematic circuit diagram and (b) Photo of an inkjet-printed common-source amplifier.

To analyse the electrical characteristics of the CS amplifier, the dynamics of the circuit performance was divided in three stages:

Stage 1: $V_{in} > 30V$

For the drive TFT, $V_{gs} = V_{in} - V_{DD} > 0 V$, the p-type OTFT was biased at the OFF state ($I_{ds(drive)} \approx 0 A$). So there was no current flowing through the drive TFT and $V_{out} \approx 0 V$. For the load TFT, the gate-source and drain-source voltages were calculated as $V_{gs} = -V_{out} \approx 0 V$, and $V_{ds} = -V_{out} \approx 0 V$. So the load TFT was also biased at the OFF state and $I_{ds(load)} = I_{ds(drive)} \approx 0 A$. In conclusion, in this stage, there was no current in the circuit and $V_{out} \approx 0 V$.

Stage 2: $V_{in} < 30V$ and $V_{out} < V_{in} - V_{th(drive)}$

For the drive TFT, as $V_{out} < V_{DD}$, $V_{in} < V_{DD}$, and $V_{th} < 0 V$, the absolute values of the drain-source (V_{ds}) and gate-source (V_{gs}) voltages were:

$$|V_{ds}| = |V_{out} - V_{DD}| = V_{DD} - V_{out} \quad (6.3)$$

$$|V_{gs} - V_{th}| = |V_{in} - V_{DD} - V_{th}| = V_{DD} - V_{in} + V_{th} \quad (6.4)$$

With $V_{out} < V_{in} - V_{th(drive)}$, the relationship between V_{ds} and V_{gs} turned into:

$$|V_{ds(drive)}| > |V_{gs(drive)} - V_{th}| \quad (6.5)$$

In this case, the drive TFT was biased in the saturation mode, and the drain-source current (I_{ds}) flowing through the drive TFT was:

$$I_{ds(drive)} = \frac{1}{2} \mu C_i \frac{W}{L} (V_{gs} - V_{th})^2 = \frac{1}{2} \mu C_i \frac{W}{L} (V_{DD} - V_{in} + V_{th})^2 \quad (6.6)$$

For the load TFT, it was diode-connected so the gate and drain electrodes were grounded. Therefore, the gate-source (V_{gs}) and drain-source (V_{ds}) voltages were calculated as $V_{gs} = -V_{out}$, and $V_{ds} = -V_{out}$, as $V_{th} < 0$ V, the relationship between V_{ds} and V_{gs} was:

$$|V_{ds(load)}| > |V_{gs(load)} - V_{th}| \quad (6.7)$$

So the load TFT was also biased in the saturation mode, and the drain-source current (I_{ds}) flowing through the load TFT was:

$$I_{ds(load)} = \frac{1}{2} \mu C_i \frac{W}{L} (V_{gs} - V_{th})^2 = \frac{1}{2} \mu C_i \frac{W}{L} (V_{out} + V_{th})^2 \quad (6.8)$$

In the CS amplifier circuit, the drain-source current in the drive and load TFTs should be equal, when the dielectric property and threshold voltage for the TFT remained constant $C_{i(drive)} = C_{i(load)}$ and $V_{th(drive)} = V_{th(load)}$, the following equation could be achieved:

$$\mu_{drive} \left(\frac{W}{L}\right)_{drive} (V_{DD} - V_{in} + V_{th})^2 = \mu_{load} \left(\frac{W}{L}\right)_{load} (V_{out} + V_{th})^2 \quad (6.9)$$

In conclusion, in this stage, the relationship between V_{in} and V_{out} was:

$$\sqrt{\frac{\mu_{drive} \left(\frac{W}{L}\right)_{drive}}{\mu_{load} \left(\frac{W}{L}\right)_{load}}} = \frac{V_{out} + V_{th(load)}}{V_{DD} - V_{in} + V_{th(drive)}} \quad (6.10)$$

Stage 3: $V_{in} < 30V$ and $V_{out} > V_{in} - V_{th(drive)}$

In this stage, the absolute values of the drain-source (V_{ds}) and gate-source (V_{gs}) voltages for the drive TFT were the same as Equation 6.3 and 6.4. With $V_{out} > V_{in} - V_{th(drive)}$, the relationship between V_{ds} and V_{gs} was described as:

$$|V_{ds(drive)}| < |V_{gs(drive)} - V_{th}| \quad (6.11)$$

Therefore, the drive TFT was also biased in the linear mode, and the drain-source current (I_{ds}) in the drive TFT was:

$$\begin{aligned} I_{ds(drive)} &= \mu C_i \frac{W}{L} \left(V_{gs} - V_{th} - \frac{V_{ds}}{2} \right) V_{ds} \\ &= \mu C_i \frac{W}{L} \left(V_{in} - V_{DD} - V_{th} - \frac{V_{out} - V_{DD}}{2} \right) (V_{out} - V_{DD}) \end{aligned} \quad (6.12)$$

For the load TFT, the diode-connected structure decided the same gate-source (V_{gs}) and drain-source (V_{ds}) voltages as in Stage 2. So the relationship between V_{ds} and V_{gs} followed Equation 6.7 and the drain-source current (I_{ds}) flowing through the load TFT followed Equation 6.8. Like in Stage 2, the current in the circuit should be equal and

the dielectric property and threshold voltage for the TFT were assumed to be the same:

$C_{i(drive)} = C_{i(load)}$ and $V_{th(drive)} = V_{th(load)}$, the following equation could be achieved:

$$\begin{aligned} \mu_{drive} \left(\frac{W}{L}\right)_{drive} \left(\frac{V_{out}+V_{DD}}{2} - V_{in} + V_{th}\right) (V_{DD} - V_{out}) \\ = \frac{1}{2} \mu_{load} \left(\frac{W}{L}\right)_{load} (V_{out} + V_{th})^2 \end{aligned} \quad (6.13)$$

In conclusion, in this stage, the relationship between V_{in} and V_{out} was:

$$\frac{2\mu_{drive} \left(\frac{W}{L}\right)_{drive}}{\mu_{load} \left(\frac{W}{L}\right)_{load}} = \frac{(V_{out}+V_{th})^2}{\left(\frac{V_{out}+V_{DD}}{2} - V_{in} + V_{th}\right)(V_{DD}-V_{out})} \quad (6.14)$$

To verify the function of the CS amplifier, the AIM-Spice simulation was conducted. The netlist for the CS amplifier circuit is shown in Appendix A and parameters for OTFTs in the simulation were extracted from inkjet-printed OTFTs in CS amplifier circuit used in this experiment, which were summarised in Table 6.3.

Table 6.3 AIM-spice simulation: Parameters for OTFTs in CS amplifier

	Mobility (cm ² /Vs)	Aspect ratio (W/L)(μm)	Thickness of dielectric layer (nm)	FET models
TFT1	0.291	1600/80	500	Level=2
TFT2	0.132	1600/80	500	Level=2

The simulated and measured results are shown in Fig.6.5, three stages for the dynamics of the circuit performance are marked in the simulated curves. For the simulated results, in Stage 1, V_{in} swept from 35 V to 30 V, and V_{out} remained constant at $V_{out} = 0$ V. in Stage 2, V_{in} swept from 30 V to 18.3 V, and V_{out} increased from 0 V to 18.1 V. In the simulation, the thickness of the dielectric layer and the aspect ratio of the drive and load TFTs were set to be the same. $V_{out}/(V_{DD}-V_{in})$ was calculated as 1.55, and $\sqrt{\mu_{drive}/\mu_{load}}$ was $\sqrt{0.291/0.132} \approx 1.48$. In Stage 3, V_{out} and V_{in} no longer followed the linear relationship. When neglecting the threshold voltage for OTFTs, $2V_{out}^2/[(V_{out} + V_{DD} - 2V_{in})(V_{DD} - V_{out})]$ was calculated as 4.80, and $2\mu_{drive}/\mu_{load}$ was $2 \times 0.291/0.132 = 4.41$. The proximity of the numerical result in Stage 2 and 3 indicated the coincidence of the simulated result with the theoretical model. In Fig. 6.5(b), the measured data showed the proximate curve compared with the simulated result, and the small variation was due to the difference of other parameters in real

OTFT devices and other components in the circuit. The proximate value of the measured electrical characteristics with the simulated results and the theoretical models indicated the proper function of the inkjet-printed CS amplifier circuits. This proper function was critical to the further study, as the feasibility and effectiveness of the self-healing should be proved in a working circuit.

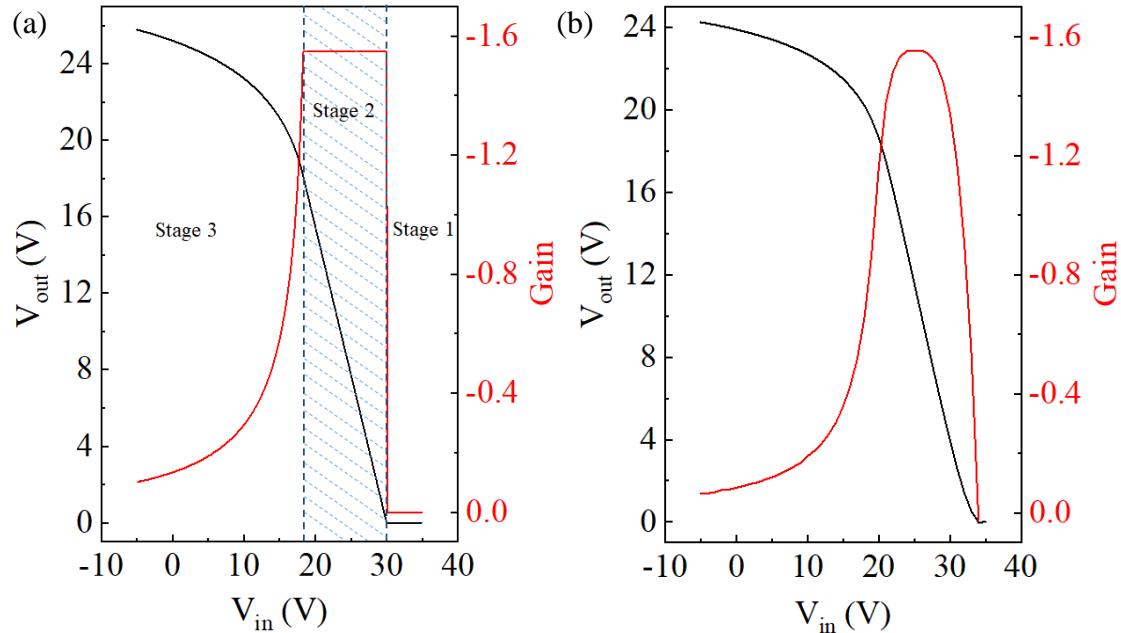


Figure 6.5. The (a) simulated and (b) measured curves of output voltage (V_{out}) and gain ($\Delta V_{out}/\Delta V_{in}$) as a function of input voltage (V_{in}) in the common-source amplifier.

6.2.2 Self-healing in the Common-source Amplifier Circuit (DC)

Like in the current mirror circuit, several open-circuit faults ($s \approx 20 \mu\text{m}$) were purposely introduced in the interconnects of the circuit as shown in Fig. 6.6. In the CS amplifier circuit, three cases were studied based on the location of the fault.

During the experiment, the transfer characteristics of the CS amplifiers for each case were measured before the occurrence of the fault by sweeping the input voltage V_{in} from +5 to -35 V with the corresponding output voltage V_{out} being measured. After the creation of the fault, the characteristics were measured again to check the circuit performance with the open fault. Subsequently, the metallic micro-particle suspension was dropped over the region of the fault and the transfer characteristics were measured again to check the healing of the open gap. Finally, the transfer characteristics were

swept one more time after 5 min of the first healing to examine the stability of the healed part.

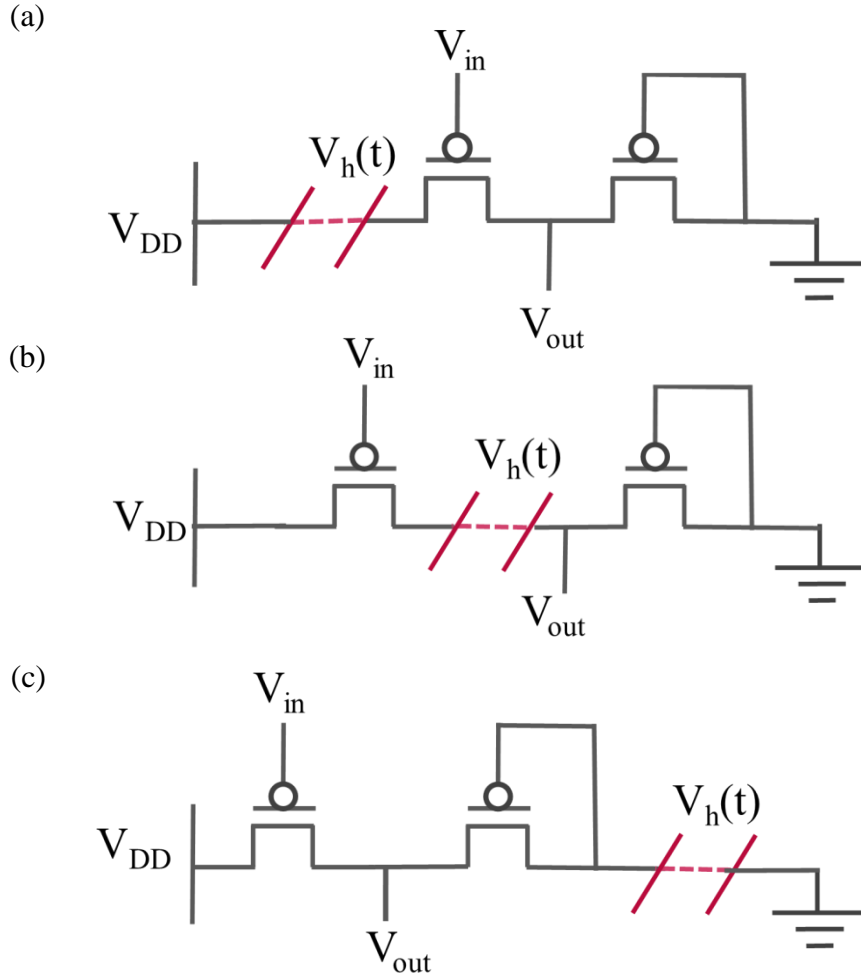


Figure 6.6. Schematic circuit diagram of a CS amplifier with faults located at various locations as defined by three cases.

In Case 1, the open fault was introduced in the wire connecting the supply voltage (V_{DD}) and the source electrode of the drive TFT (Fig. 6.6(a)). The supply voltage for the drive TFT was cut so $V_{ds(drive)}$ would drop to 0 V, then there was no current through the circuit and $V_{out} = 0$ V. After dispensing the suspension, at $t = 0$ s, the voltage across the open gap was $V_h(t=0) = 30$ V. With the distance of the open gap $s \approx 20$ μm , this voltage could create an electric field which was higher than the threshold field for the healing. Therefore, the field in the open gap could drive particles in the suspension to form the healing bridge. As analysed in Section 4.3, with the short open gap ($s \approx 20$ μm) and under the field of $\xi \approx 30/20 = 1.5$ V/ μm , the healing would be completed in a short time ($\tau_h < 1$ s). The measured result was revealed in Fig. 6.7(a), which coincided with

the analysis of the circuit dynamics. The fault dragged V_{out} down to 0 V and was found to be healed during the first sweep after the dispensing of the suspension. The completion of healing was seen by the abrupt change in V_{out} from “disabled” level to the original “working” level. After 5 min of the first instance of the healing, the transfer characteristic was proved to remain stable by a repeated sweep.

In Case 2, the open fault occurred in the interconnects joining the drain electrode of the drive TFT and the source electrode of the load TFT (Fig. 6.6(b)). The path for the current flowing through the circuit was cut off and the terminal for V_{out} was separated from the drive part, thus $V_{out} = 0$ V. When $V_{in} < 30$ V, $V_{gs(drive)} = V_{in} - V_{DD} < 0$ V, at this moment, the drive TFT was turned ON and would act as a resistor with high impedance. As there was no current in the circuit, the voltage across the open gap equalled to V_{DD} and the electric field would be created. With the suspension, the open fault could be quickly repaired. The measured data (Fig. 6.7(b)) followed the analysis of the circuit dynamics, and the healing could be stable as the curve measured 5 min after the first sweep overlapped the original curve of the CS amplifier operation.

In Case 3, the open fault cut the interconnects between the drain electrode of the load TFT and the ground (GND) (Fig. 6.6(c)). The whole circuit was disconnected with the ground and no current flowing in the circuit. In this case, when $V_{in} < 30$ V, the drive TFT was turned ON and both TFTs turned into resistors with high impedance. Therefore, the electrical potentials before the open gap were equal in the circuit and V_{out} would jump to $V_{out} = V_{DD}$. The voltage across the open gap also equalled to V_{DD} and the electrical field was created in the gap. After applying the suspension, the particles were driven by the field and healed the open fault. Once the open fault was repaired, V_{out} would drop from V_{DD} to the original working level. Another sweep was conducted 5 min after the first instance of the healing and the curve coincided with the transfer characteristics of the working CS amplifier, indicating the stability of the healing in this case.

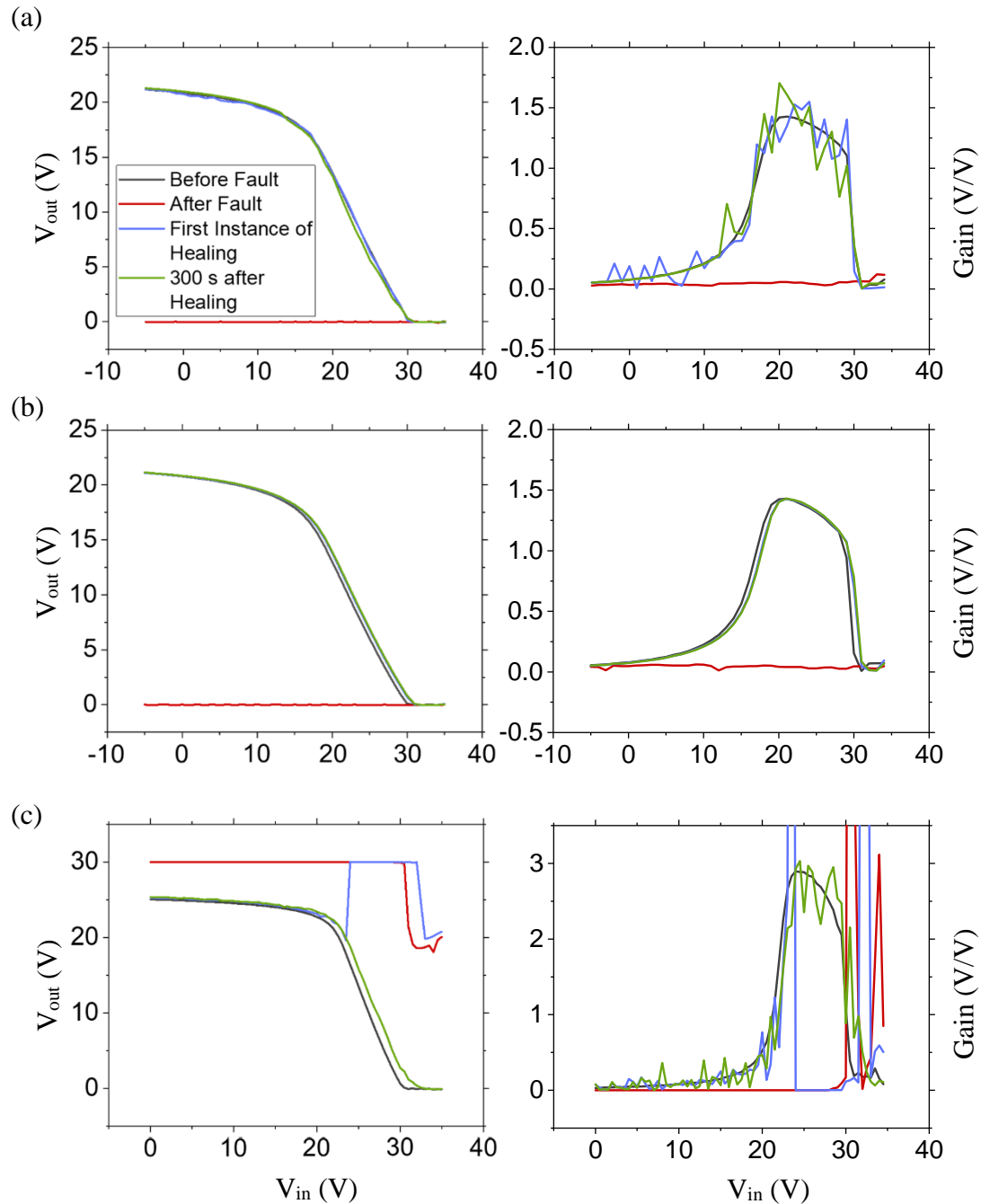


Figure 6.7. Self-healing in the common-source voltage amplifier circuit (left: $V_{out} - V_{in}$, right: Gain) with the fault located at various locations as defined by three cases.

6.3 Self-healing in the Common-source Amplifier (AC)

The main function of the amplifier is to amplify a signal, and in most cases, an alternating current (AC) signal. In real-world applications, it is usually used to amplify sensing, controlling and communicating signals. These wide-range applications make

the amplifier a key component in analogue circuits. To verify the feasibility of the PBSH technique in the CS amplifier when processing AC signals, the frequency response of the amplifier was measured for all cases in Fig. 6.6. The experimental setup for the AC signal measurement is shown in Fig. 6.8, and the photo of this setup is shown in Appendix B.

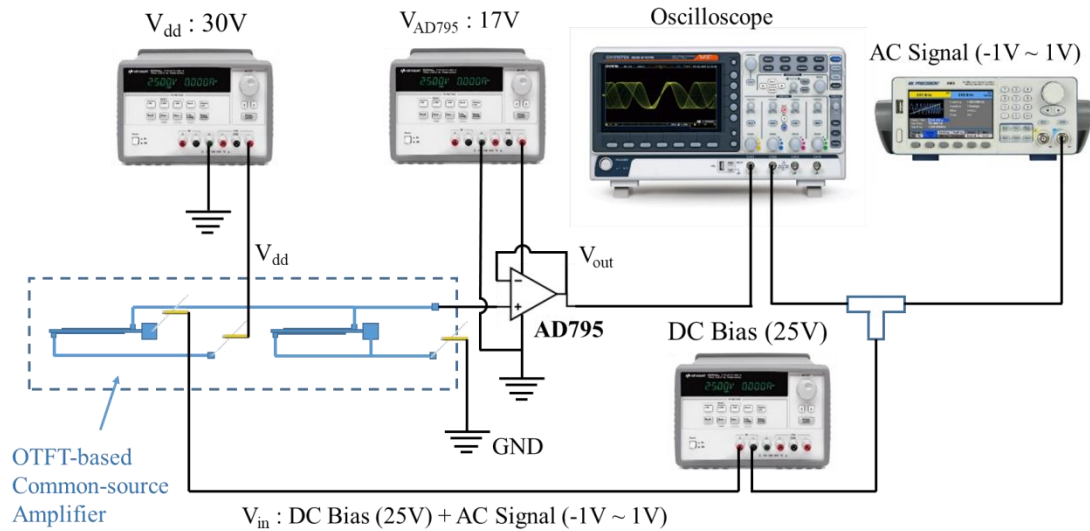


Figure 6.8. Schematic of the experimental setup for measuring the frequency response of the inkjet-printed CS amplifier.

In the measurement circuit, a unity gain buffer unit (AD795) was used. The function of this unit is to separate the CS amplifier circuit and the oscilloscope, therefore providing the stable output voltage shown on the oscilloscope. The connection diagram of this unity gain amplifier is included in Appendix C. In addition, from Fig. 6.5, it could be concluded that at $V_{in} \approx 25\text{ V}$, the voltage gain ($\Delta V_{out}/\Delta V_{in}$) could reach its peak value, so in the measurements the signal is expected to vary around this voltage bias point. Therefore, three power supplies were utilised in this experiment: One was placed to act as V_{DD} for the CS amplifier. Another one was used to supply power to activate the AD795 microchip. The final one was set to provide the DC bias carrying the AC signal. A signal generator was used to generate the sinusoidal signal with an amplitude of $\pm 1\text{ V}$ and frequencies from 0.1 to 10^5 Hz . This AC signal was series connected to the DC bias and acted as V_{in} to the CS amplifier. The oscilloscope was connected to monitor the input and output signals.

In this experiment, the input and output signals were monitored and peak voltages $v_{in(max)}$ and $v_{out(max)}$ under different frequencies were measured. The gain of the AC signal was calculated as:

$$Gain = \frac{v_{out(max)}}{v_{in(max)}} \quad (6.15)$$

The Bode magnitude plot was then drawn based on the signal gain measured under different frequencies. To verify the effectiveness of the healing to the AC signal in the CS amplifier, one curve was plotted after the amplifier was fabricated. After the healing of an open fault in each case, the signal gains under various frequencies were measured again and the corresponding curve was plotted. The Bode plot measured after the healing of open faults in all cases were summarised in Fig. 6.9.

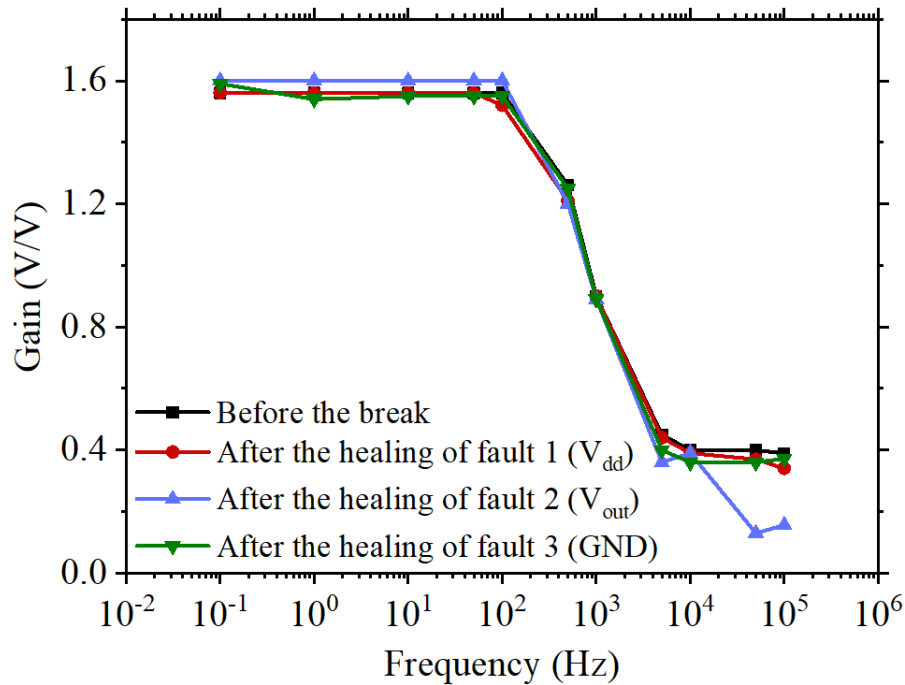


Figure 6.9. Frequency response of the CS amplifier before the fault and after the healing for each case.

Two conclusions can be drawn from the result shown in Fig. 6.9. The first one is that the amplifier showed a -3 dB cut-off frequency at around 500 Hz before and after the healing, irrespective of the location of the fault. The other one is that there was no significant change in the frequency response measured after the healing compared to that measured before the occurrence of the fault, indicating the feasibility and effectiveness of the self-healing in the CS amplifier when processing AC signals.

6.4 Summary

In this chapter, the self-healing in interconnects for current mirror and CS amplifier circuits has been investigated. The open faults have been created at various locations in circuits and these faults have been successfully healed in all cases. The healing can remain stable once the healed bridges have been formed in the open gap. For the CS amplifier, the frequency response has also been measured before the occurrence of the fault and after the completion of the healing. And the result indicates the effectiveness of the self-healing in the CS amplifier when processing AC signals. So far the self-healings in interconnects for wires, devices and circuits have all been proved feasible and effective. To further demonstrate the likelihood of applying the PBSH technique in the real-world application, more tests are to be conducted which will be discussed in the next chapter.

7 PERFORMANCE CHARACTERISATIONS OF THE PBSH TECHNIQUE

In the previous chapter, the PBSH technique has been proven effective in healing interconnects for wires, devices and circuits. This chapter continues to conduct several performance characterisations of the PBSH technique to further demonstrate the feasibility of this technique in real-world applications. Section 7.1 reveals the impact of the bending on the healed interconnects. Section 7.2 analyses the dynamics of the healing when double open faults exist in the interconnection. Section 7.3 gives the example of encapsulating the suspension in a patterned region, which is critical to achieve the manufacturability in real applications. Section 7.4 analyses the noise in the healed interconnects.

7.1 Bending

For the flexible electronics, mechanical stress is the main threat to its reliability, and in most cases the mechanical stress comes from the repeated bending in real life. Therefore, to prove the feasibility of applying the PBSH technique in flexible electronics, a study of the impact of the bending on the self-healing is essential. In this experiment, an OTFT device with extended wire was printed on the PEN substrate (the same pattern as used in Section 5.1). An open fault ($s \approx 20 \mu\text{m}$) was purposely introduced in the extended wire connecting to the source electrode. The experimental setup is shown in the inset of Fig. 7.1, the substrate was gently bent to have a radius of curvature of $r \approx 7 \text{ cm}$, and contacts were drawn out by probe tips connected to the SMU.

The micro Ag particle-based suspension was then dispensed in the region of the open gap and the SMU supplied voltages to measure the transfer characteristics of the OTFT. In Fig. 7.1, when the gate-source voltage (V_{gs}) was swept to -4 V, the curve showed an instant healing of the transfer characteristics of the OTFT. The healed part remained stable after 5 min of the first instance of the healing. Then, the substrate was removed from the probe station and subjected to repeated bending for 100 cycles. The transfer characteristics of the OTFT were measured again after the completion of this bending tests. The result revealed that even after 100 cycles of the bending the healed bridge still existed in the open gap and the OTFT device could still show the proper function. This means once the healing had been completed, it remains unaffected by the further bending.

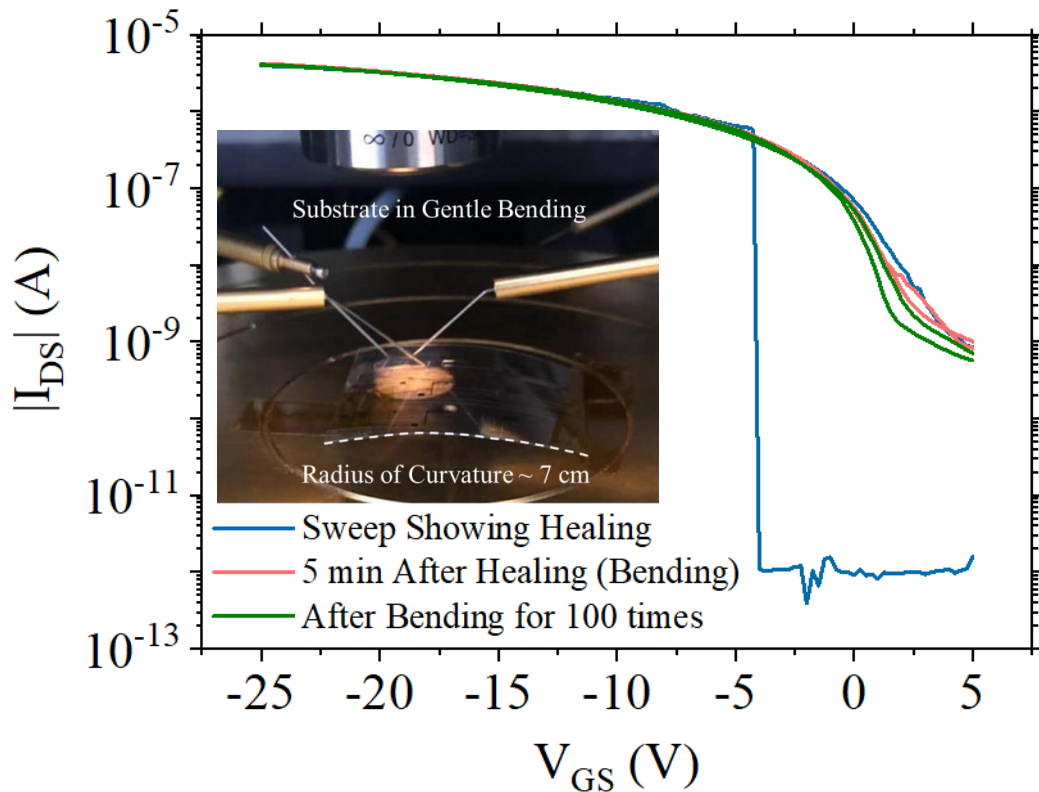


Figure 7.1. Self-healing with bending (bending radius ≈ 7 cm) and the demonstration of the healing stability after 100 bending cycles.

7.2 Double Faults

All experiments conducted in previous chapters only had one open fault in the interconnect. However, for the real flexible electronic circuits, the mechanical stress or

chemical corrosion usually creates two or more faults in interconnects. So it is essential to explore the ability of the PBSH technique for healing more than one fault. The experimental setup is shown in Fig. 7.2, this setup was the same as that used in studying the self-healing in printed interconnects (Chapter 4) but two open faults were created. The Ag-particle based suspension was dispensed in the open gaps. Then the SMU started to supply voltage and measured the current in the circuit.

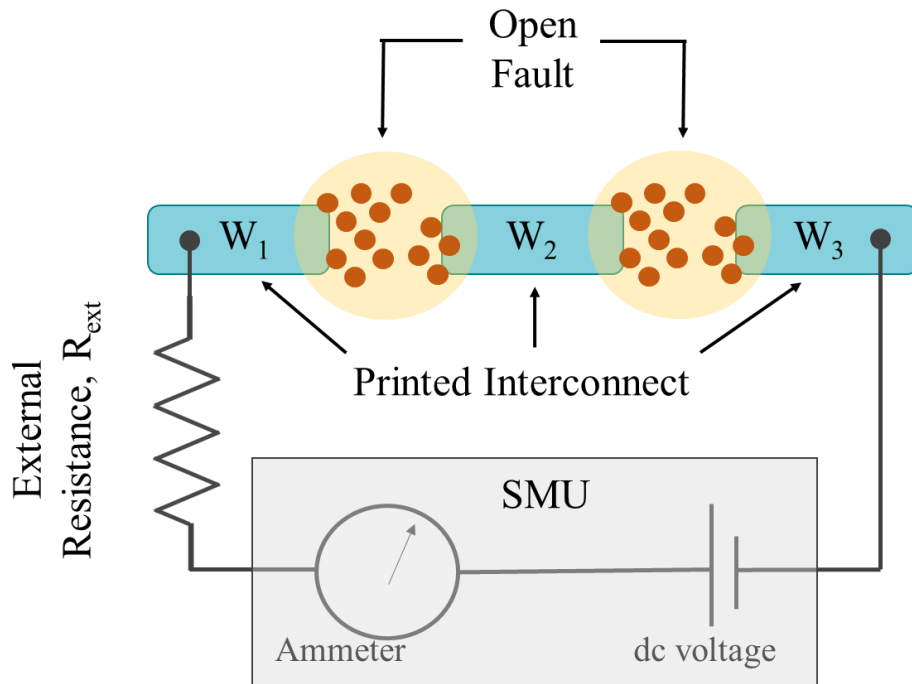


Figure 7.2. Schematic of the experimental setup for measuring the self-healing in printed interconnects with dual open faults.

As shown in Fig. 7.2, the two open faults divided the printed wire into three interconnect islands, W_1 , W_2 and W_3 . The electrical potential at W_1 equalled the supplied voltage, while at W_3 equalled ground (GND). The potential difference between W_1 and W_3 caused an electric field across these two islands. At the same time, the existence of W_2 narrowed the effective distance between the terminals of the potential difference (like inserting a metal plate into a plate condenser). If the distance of the two open gaps were assumed as d_1 and d_2 , the electric field across the gap was scaled as $V_{DD}/(d_1+d_2)$, here V_{DD} was the voltage supplied by the SMU. Driven by this electric field, Ag micro particles would move in the liquid and form the bridge to heal the open gap. However, because the strength of the electric field in this case was only half of that

with the single fault, the healing time became longer compared with the previous cases. In the experiment, circuits with various external resistors (0.47 M Ω , 0.99 M Ω , and 10.56 M Ω) were measured and results were shown in Fig. 7.3.

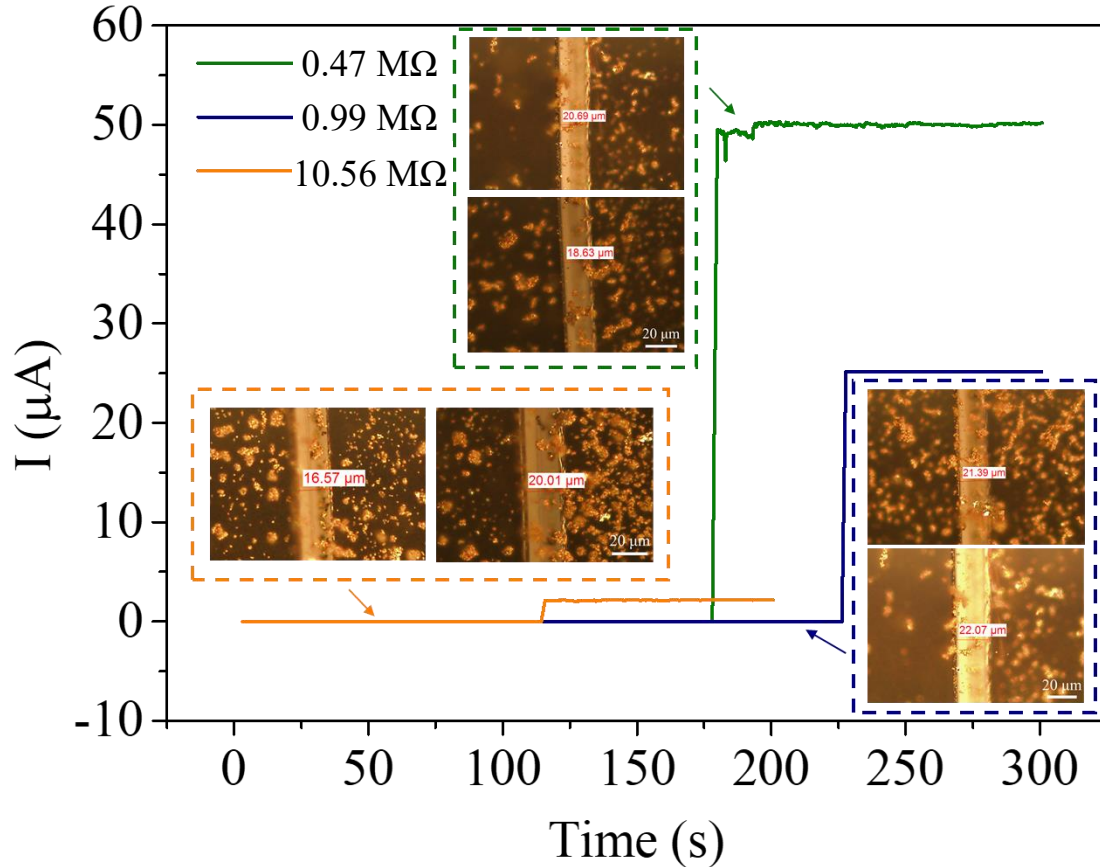


Figure 7.3. Dynamics of current showing the healing of dual faults for external resistors of 0.47, 0.99, and 10.56 M Ω (Inset) Microscopic images of open gaps in various interconnects.

The healing of the open faults was seen in all cases, and the healed current obeyed Ohm's law $I = V_{DD}/R_{ext}$, here $V_{DD} = 25$ V. The trend of the healing time (τ_h) followed the conclusion summarised in Section 4.3, as the effective gap distance $d_{eff} = d_1 + d_2$. These results have proved that the PBSH technique has the ability to heal more than one open fault in interconnects.

7.3 Packaging

All the above studies on the PBSH technique were performed by manually dispensing the metallic micro-particle suspension over the known location of the open

fault. However, to achieve manufacturability in the real-world applications, the suspension needs to be encapsulated in a specific region or contained along the interconnects without interfering with the circuit operation. There are two approaches to realise this goal, the first one is to utilise the inherently insulating nature of the suspension and fill the interconnect regions with it. The common size of open faults caused by mechanical stress in flexible electronics is in the range of $1 \sim 10 \mu\text{m}$. But the distance between two adjacent wires in the layout of the circuits is usually more than $100 \mu\text{m}$. Section 4.3 concluded that the electric field should be above a threshold value for driving metal particles to heal the faults. The large distance between different interconnects limits the maximum electric field between them and therefore avoids unwanted short circuits in the suspension -covered regions. The second approach is to borrow ideas from microfluidic techniques and restrict the suspension in an area patterned by the hydrophobic or oleophobic materials, or contain the suspension in micro-channels located along the interconnects. However, when it comes to high-density circuits, the increase in manufacturing complexity when applying this approach becomes a non-negligible issue.

This study adopted a combination of both concepts, and an approach as illustrated in Fig. 7.4 was processed. The pattern was designed on the protective film of the PEN substrate and was cut by scalpel. Then the protective film for the oleophobic region was peeled off and the surface of the PEN substrate was exposed to the ambient environment. Subsequently, the flexible substrate and a piece of watch glass holding drops of trichloro(1H,1H,2H,2H-perfluorooctyl) silane (97%, Sigma Aldrich) were placed in the dessicator and the air pressure inside was reduced to -0.08 Mpa using a vacuum pump. The low pressure inside the dessicator accelerated the volatilisation of the trichloro(1H,1H,2H,2H-perfluorooctyl) silane and then part of it would be deposited on the surface of the substrate. After this procedure, the exposed part was covered with the trichloro(1H,1H,2H,2H-perfluorooctyl) silane, which turned into the oleophobic region. And by peeling off the remaining protective film, the patterning of the oleophobic and oleophilic region was completed. The oleophilic regions were prepared for the printed OTFT devices and interconnects while the oleophobic regions were used to restrict the location of the suspension and separate different interconnects. The oleophobicity of the trichloro(1H,1H,2H,2H-perfluorooctyl) silane is due to its low surface energy caused by the fluorine atom and the polarity in the molecule. Thus the silicon oil used

as the liquid for the suspension could be incompatible with the trichloro(1H,1H,2H,2H-perfluorooctyl) silane and could be confined by the deposited oleophobic regions.

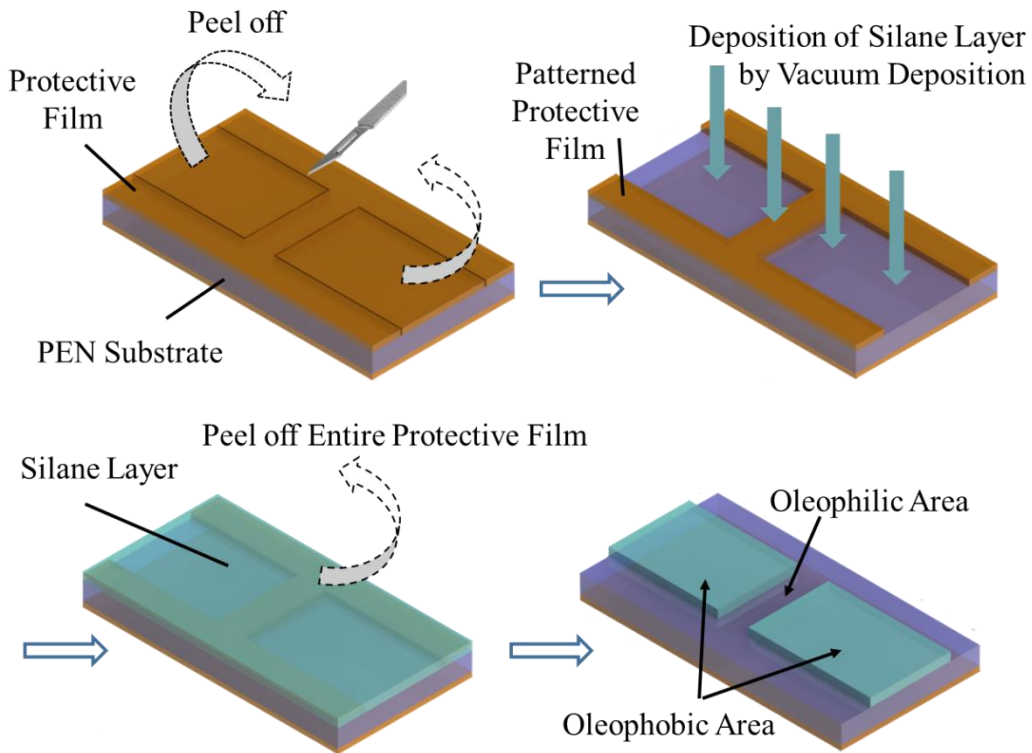


Figure 7.4. Method to package the suspension using an inkjet-printing compatible process and add self-healing ability to a circuit.

The suspension was dispensed freely over the substrate and remained confined in the oleophilic regions. Fig. 7.5(a) showed the comparison of the spread of the suspension with and without the trichloro(1H,1H,2H,2H-perfluorooctyl) silane treatment, and Fig. 7.5(b) gave the cross-sectional image of the confined suspension taken by microscope on a goniometer (Appendix D). Without the coating, the suspension spread and covered a large area of the circuits, after tens of minutes it spread and covered the whole surface of the substrate. With the coating, the suspension remained confined in the patterned oleophilic regions (marked by the rectangle dotted box) along the interconnects, and the suspension only healed the open faults that occurred in the covered area without interfering with other components in the circuit. The transfer characteristics of the OTFT device printed on the treated PEN substrate before the fault, after the fault and after the healing was shown in Fig. 7.6. The proper function of the OTFT device and the successful healing of the open faults in

interconnects were revealed in the result, proving that the ability of self-healing was unaffected by the oleophobic treatment. This approach preliminarily showed promise with regard to manufacturing flexible electronic platforms with the self-healing ability. However, to demonstrate the feasibility of applying the PBSH technique in higher-integrated circuit, further studies are needed to be conducted. These studies include methods for patterning the oleophobic and oleophilic regions with higher resolution, and metal particles with smaller size for the self-healing of the interconnects in large scale integrated (LSI) or even very large scale integrated (VLSI) circuits.

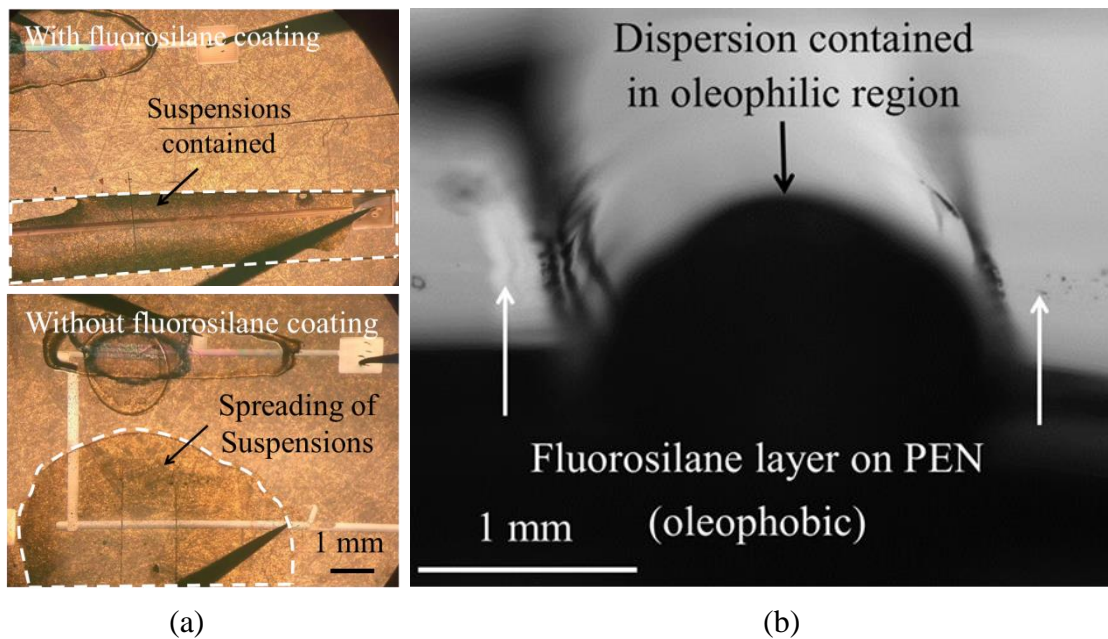


Figure 7.5. (a)The microscope photo and (b) The cross-sectional image demonstrating the containment of the suspension between trichloro(1H,1H,2H,2H-perfluorooctyl) silane -treated regions.

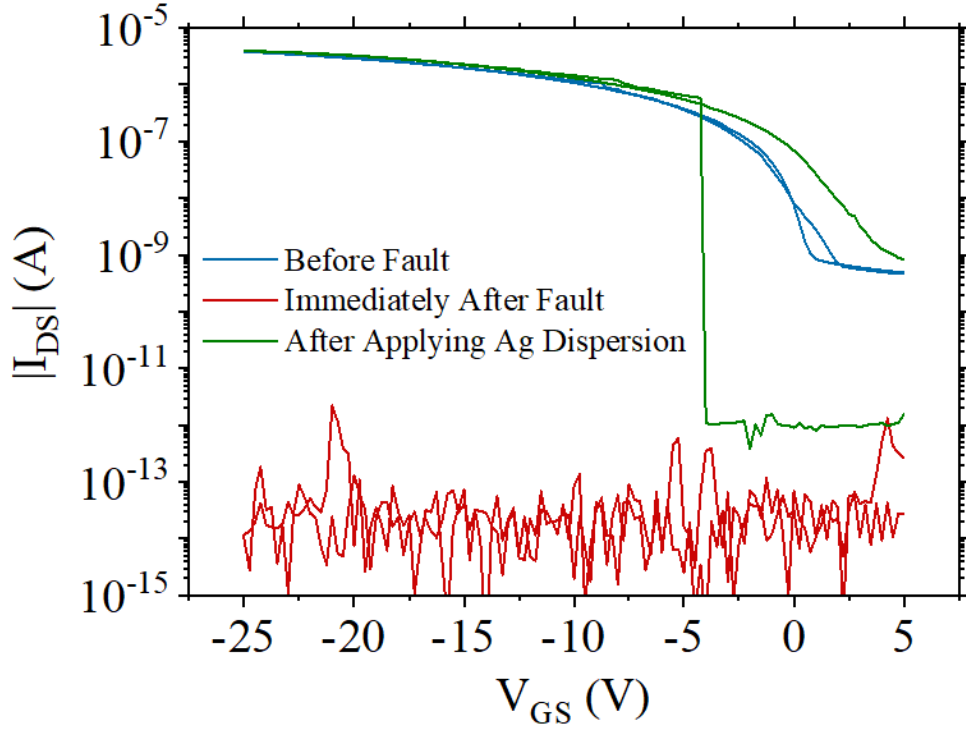


Figure 7.6. The transfer characteristics of the OTFT showing the successful self-healing with the trichloro(1H,1H,2H,2H-perfluorooctyl) silane-based packaging.

7.4 Noise

The noise in the self-healed interconnects was also studied in this work, as it is a critical parameter for analogue circuit operation, which determines the minimum level of the detectable signal and is particularly crucial at low frequencies where most flexible electronic circuits lie (<100 Hz). In most studies associated with the circuit, there are typically three types of noise, which includes thermal noise, flicker noise [136] and shot noise.

Thermal noise is caused by the thermal motion of charge carriers, and is mainly associated with the resistive devices. This noise is calculated as:

$$\langle i_{th}^2 \rangle = 4k_B T g_m \quad (7.1)$$

where k_B is Boltzmann's constant, T is the absolute temperature, and g_m represents the trans-conductance of the resistive devices like the transistor. In Equation 7.1, there is no frequency-related parameter, so the intensity remained unaffected over the whole frequency spectrum, proving the thermal noise to be a white noise.

Flicker noise results from the trapping-detrapping events of different time constants in electronic components. This noise is inversely proportional to the frequency (f), i.e., it is a noise with a $1/f$ spectrum, which is scaled as:

$$\langle i_{1/f}^2 \rangle = \frac{KI^2}{f} \quad (7.2)$$

where K is a coefficient depending on the density of the defect states in electronic components, and I is the direct current in the circuit. As the intensity is inversely proportional to the frequency, the flicker noise is a pink noise and it dominates at low frequencies.

Shot noise exists in active devices and it is due to the fluctuation in number of charge carriers. At low frequencies, it is a white noise, which is scaled as:

$$\langle i_s^2 \rangle = NqI \quad (7.3)$$

where N is a constant depending on the characteristics of the device, q is the elementary charge, and I is the direct current in the circuit. At low frequencies the intensity of the noise is independent of the frequency. However, at high frequencies, the coefficient N is greatly affected by the frequency, making shot noise prevail at high frequencies.

In this study, noise measurements of the healed interconnects were conducted with the two circuits shown in Fig. 7.7 in flat and bent (1cm bending radius) conditions. The photo of the measurement setup is shown in Appendix E. The measurements were performed in a copper shielded box, and a charge amplifier was connected to the circuit. There are two functions of this amplifier: one is to amplify the noise and the other one is to filter out the DC component of the noise current. A spectrum analyser was connected to the output port of the charge amplifier to measure the noise current at different frequencies. It is worth noting that to avoid the noise from AC power sources, both the amplifier and the circuit were powered by batteries.

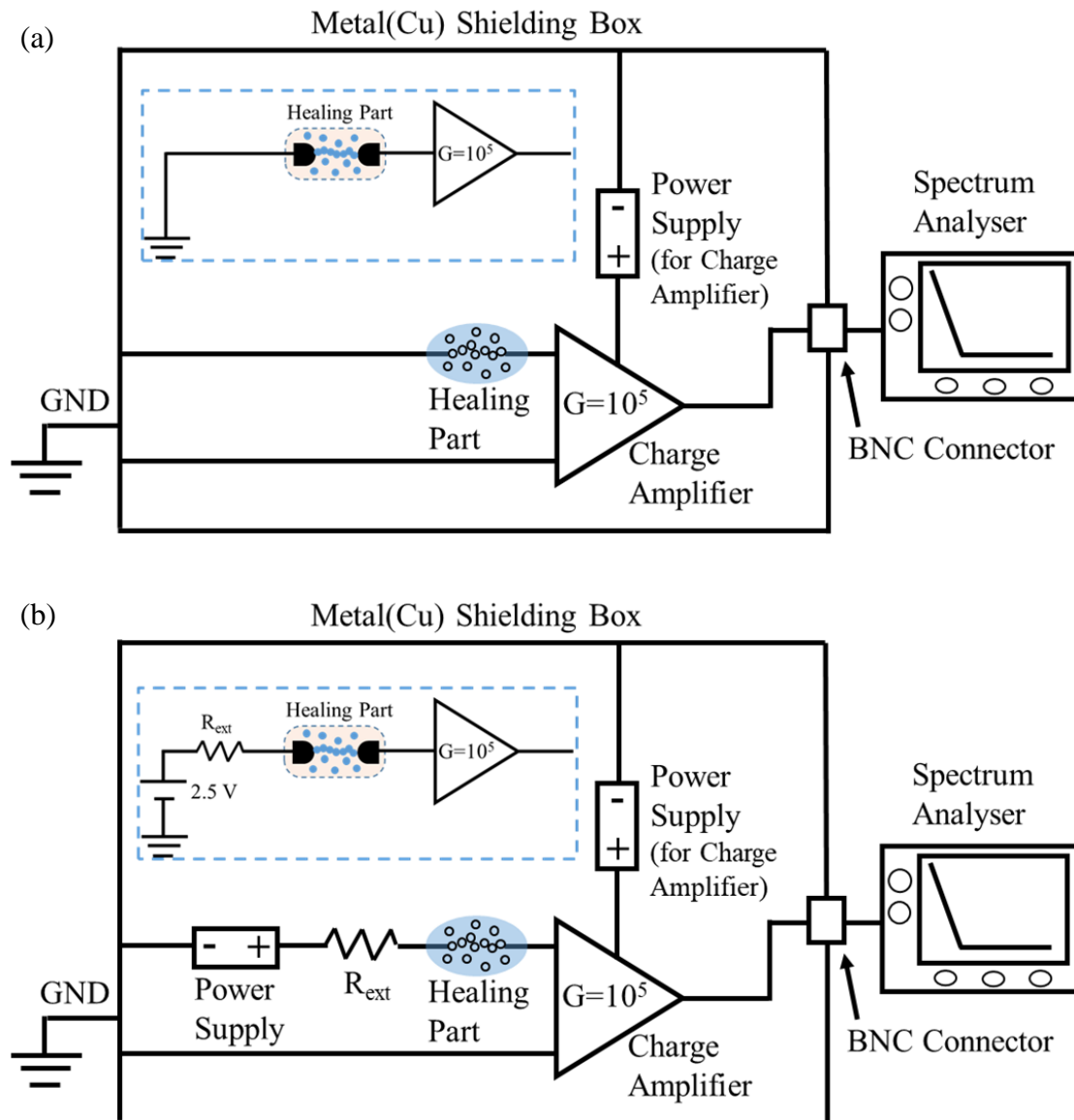


Figure 7.7. Schematic of the experimental setup for noise measurement (a)without the direct current (b)with the direct current.

Because of the absence of the active devices, the dominant noises in the circuit were thermal noise and flicker noise, and flicker noise existed when there was an external voltage supply or direct current in the circuit. First, the noise in open- and short-circuit conditions was measured. The result measured in the open-circuit condition represented the noise of the measurement setup, and the result from the short-circuit condition yielded the noise of the interconnection itself. Subsequently, the noise in the circuit having a DC voltage supply (2.5 V) were measured. The maximum current for the charge amplifier was 10^{-5} A, to protect the circuit, an external resistor with high resistance (980 k Ω) was connected in series with the healing part and the charge

amplifier. The noise caused by the external resistor was also measured for calibration. All data were shown in Fig. 7.8.

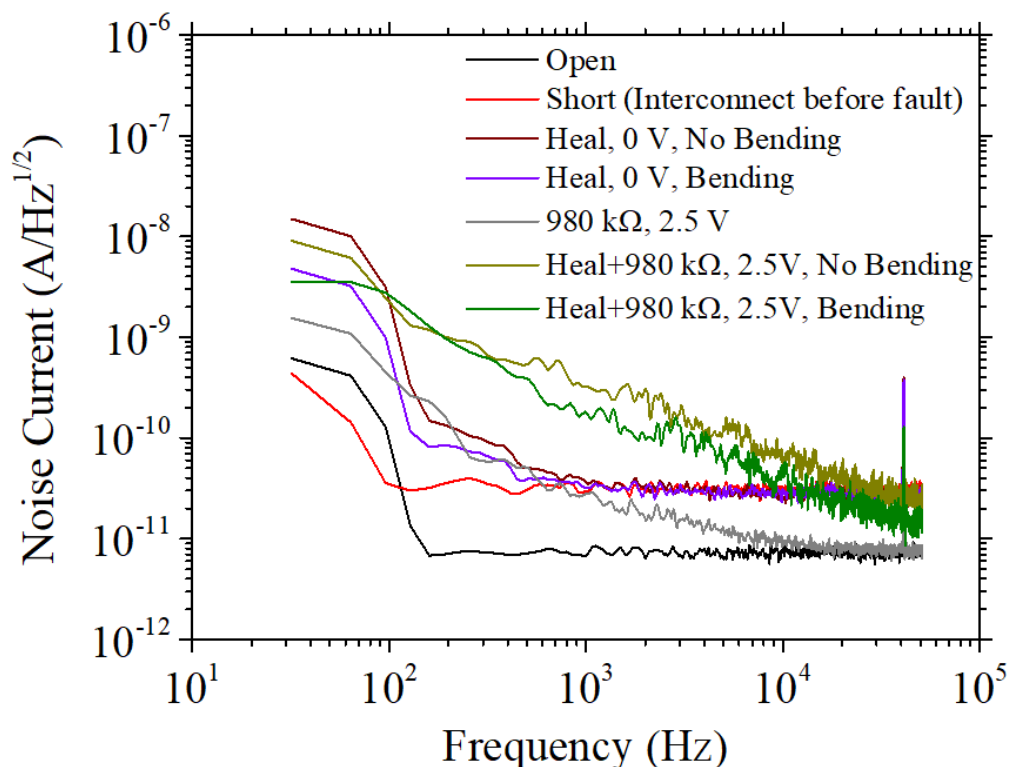


Figure 7.8. Measured noise currents in different cases.

When the DC voltage supply was absent, the noise measurement was expected to show only the thermal noise. The measured noise currents for the original and healed interconnects were about $0.03 \text{ nA}/\sqrt{\text{Hz}}$. When the DC voltage and the external resistor were added in the circuit, flicker noise was expected to appear in the circuit as well. In Fig. 7.8, the flicker noise was superior to the thermal noise at low frequencies. The external resistor dragged the thermal noise down to $0.01 \text{ nA}/\sqrt{\text{Hz}}$, and the flicker noise in the voltage source-resistor circuit without the healing part changed from $0.4 \text{ nA}/\sqrt{\text{Hz}}$ to $0.01 \text{ nA}/\sqrt{\text{Hz}}$ with the frequency sweeping from 100 Hz to 50 k Hz. For the healed voltage source-resistor circuit, the flicker noise was measured to be in the range of $3 \text{ nA}/\sqrt{\text{Hz}}$ to $0.02 \text{ nA}/\sqrt{\text{Hz}}$, which was higher than that in the circuit without the healing part. This could be explained by the increased trap density in the circuit. The healed bridge was formed by the metal particles, and the charge carriers should transport between these particles. In this process the boundaries of particles would become the barrier for the carrier transportation and increase the trap density in interconnects. Since

the flicker noise is associated with the trapping/detrapping effect, the noise current in the healed circuit would be higher than the original circuit without the healing.

7.5 Summary

In this chapter, several performance characterisations of the PBSH technique have been explored and summarised. First, the impact of the bending on the self-healing has been studied, the circuit can be repaired in the bent condition and the healing part can remain stable after being bent for 100 cycles. Then the healing of double faults has been explored. The double faults in all cases were successfully repaired and this result proved the ability of the PBSH technique to heal more than one open fault in interconnects. Subsequently, to achieve manufacturability in the real-world applications, the OTFT device and interconnects have been encapsulated in the oleophobic- and oleophilic-patterned substrate. The suspension used for the healing has been confined in the designed region along the interconnects. Meanwhile, the proper function of the OTFT device and the successful healing of the open faults in the interconnects have been achieved in this packaged circuit. Finally, the noise of the healed interconnects has been measured. The boundaries of particles increase the trap density in interconnects, leading to the larger flicker noise current in the circuit. The performance characterisations in this chapter have demonstrated the feasibility of the PBSH technique in real-world applications.

8 CONCLUSIONS AND FUTURE WORK

This research aims to thoroughly investigate the particle-based self-healing (PBSH) technique for improving the reliability of the organic thin-film transistors (OTFTs)-based flexible electronics. This is achieved following a division and combination logic: the research started with the separated investigations of the inkjet-printed OTFT device, circuits and the mechanisms of the PBSH technique, then these two parts were combined and the ability of the PBSH technique for healing the interconnects in flexible electronics was analysed and verified.

In the device part, a range of device structures and materials were investigated, and the proper structure and functional material systems which were compatible with the inkjet printing process were selected. In addition, the suitable fabrication process was explored and the inkjet printer was set with the optimised parameters. Finally, an inkjet-printed BGBC-structured OTFT with a TIPS-Pentacene-PVC material system was successfully fabricated. The fabrication process was proved to be reliable since the yield could reach 85%, and the devices fabricated in this work could achieved the average performance compared to devices fabricated by other process reported in previous work. Extracted from the measured data, the average mobility (μ) reached $0.13 \text{ cm}^2/\text{Vs}$, the average subthreshold swing (SS) value was down to 240 mV/dec , and the average on/off current ratio was up to 3.2×10^6 . The reliability of the process and the stability of the device performance are important for the follow-up experiments, as OTFT is the basic component for the flexible circuits constructed in this study.

In the circuit part, two basic circuits: the current mirror and the common-source (CS) amplifier were successfully built. Both devices and interconnects in the circuit

were inkjet-printed, and the proper functioning of these printed circuits was proved by comparing with the AIM-Spice simulated results. The current mirror is a basic module which is usually used in the power management circuit and the DC motor control circuit. And the CS amplifier is another widely used module in most analogue circuits for amplifying signals. Because of the popularity of these circuits in real-world applications, they were selected as the representative circuits for verifying the feasibility of applying the PBSH technique in flexible electronics.

In the self-healing part, the mechanism of the PBSH technique was analysed and its theoretical modelling was established. One issue for this technique was the inherent conductivity of the suspension, which would cause the short of the adjacent interconnects. To solve this issue, metal particles were modified by the oleic acid, and by this chemical pre-treatment, the suspension containing these metal particles showed the inherent insulativity. In that case, the self-healing could only occur when the electric field (ξ) across the open gap was over a threshold value (ξ_{th} , and in this work, $\xi_{th} \approx 0.6 \text{ V}/\mu\text{m}$).

After confirming the fabrication process of the OTFT-based flexible circuit and the preparation process of the particle-based suspension, the ability of the PBSH technique for healing the interconnects in flexible electronics was investigated. The whole investigation followed a wire-device-circuit logic. The first stage was to demonstrate the self-healing in inkjet-printed interconnects. In this stage, the PBSH technique has been proved to be effective in healing the open faults in interconnects, and the impacts of suspension concentration, electric field, length of open gap, and external resistance on the healing time have been revealed by the theoretical equations and experimental results. The second stage was to investigate the self-healing in interconnects for inkjet-printed OTFT devices. In this stage the self-healing of open-faults at source and drain sides has been respectively researched. Details of the healing in the transfer ($I_{ds} - V_{gs}$), the output ($I_{ds} - V_{ds}$) characteristics have been researched. All results indicate the successful healing of the open fault in OTFT interconnects, and the healing in OTFT interconnects followed the physical mechanisms summarised in wire interconnects. The final stage was to explore the self-healing in interconnects for flexible circuits: the current mirror and the CS amplifier. The open faults were created at various locations in circuits and all these faults have been successfully healed. For the CS amplifier, the frequency response has also been measured before the occurrence

of the fault and after the completion of the healing, indicating the effectiveness of the self-healing in the CS amplifier when processing AC signals.

To demonstrate the likelihood of applying the PBSH technique in the real-world application, more performance characterisations of the PBSH technique have been conducted. The bending test proves the reliability and stability of the healing in the bent condition. The dual-faults test verifies the ability of the PBSH technique for healing more than one open fault in interconnects. The proper functioning of the OTFT device and the successful healing of the open faults in the oleophobicly- and oleophilicly-treated substrate indicate the feasibility and manufacturability of the PBSH technique in the real-world integrated circuits. Finally, the noise of the healed interconnects has been measured. The boundaries of particles increase the trap density in interconnects, causing the larger flicker noise current in the circuit.

The study presented in this dissertation gives an idea of increasing the reliability of flexible circuits by providing them with an ability to heal themselves. However, due to time limitations, some detailed work could not be completed. In order to fabricate the flexible circuits with higher performance and further develop the PBSH technique for healing the large-scale circuits, the following work needs to be accomplished:

Optimisation of the inkjet-printed OTFTs. Although the material system used in this work (TIPS-Pentacene-PVC) is widely-used in OTFT research and the fabricated device has the relatively high performance compared with some OTFTs reported in previous work. There is still a large gap in device performance between organic TFT and oxide or low-temperature polycrystalline (LTPS) TFTs, while the later ones have been maturely developed for industrial applications. This is also the main reason limiting the large-scale fabrication and application of the OTFT-based electronics. This issue needs to be addressed by optimising the material (especially the organic semiconductor) and the fabrication process. The development of the material science in recent years has brought some new organic semiconductors and insulators with better electrical properties. And they are promising for developing the high-performance devices and circuits. In addition, in a complex circuit system, in most cases, both n-type and p-type TFTs are needed to build the complementary devices for improving the circuit performance. Thus the material systems for n-type OTFTs should also be investigated in the future work.

Preparation of the suspension with smaller particles. In this study the metal particles have the average particle size (APS) of 1 μm , and are applicable to healing the open gap with the size of 10 – 100 μm . However, for complex circuits, especially the large-scale integrated (LSI) or the very large-scale integrated (VLSI) circuits, dimensions of the device and the wire (including the wire spacing) become very small, usually scaling down to 0.1 – 1 μm level. Therefore, it is necessary to explore the self-healing technique using the metal particles with the APS of 0.1 μm or less. With the scaling down of the particle size, the specific surface area ($S = \text{surface area} / \text{mass}$) of the particle increases, leading to the strengthening of the adsorb-ability for metal particles. And in this case the oxidation becomes more likely to occur on the surface of particles, making the metal particles permanently nonconductive. To address this issue, the further research about the method of preparing the suspension with smaller particles should be conducted.

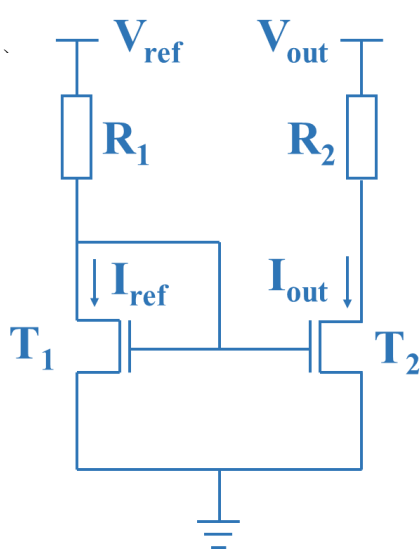
Optimisation of the chemical coating process. The pre-treatment with the oleic acid made the metallic micro-particle suspension inherently insulating, and set a threshold value of the electric field (ξ_{th}) for the occurrence of the self-healing. However, in this work, the relationship between the coating effect and treating parameters (composition, PH value, coating time, concentration) was not studied, and ξ_{th} for the self-healing could not be controlled. When the length of the open gap is fixed, the electric field is proportional to the voltage across the gap. If ξ_{th} is high, then the high voltage is needed in the circuit, and the large current caused by this high voltage may damage the components in the circuit. To protect the circuit and make the PSSH technique applicable to all types of circuits, it is necessary to further study and optimise the chemical coating process for metal particles.

Fabrication of the large-scale circuits. In this work, two basic circuits – the current mirror and the common-source (CS) amplifier were fabricated and used as demo circuits for verifying the effectiveness of the PSSH technique in healing the circuit interconnects. To further study the PSSH technique for healing circuits, the large-scale flexible circuits with more complex functions are needed. The fabrication of the all-inkjet-printed large-scale circuits is also a challenging topic in flexible electronics area. It requires the good uniformity of all transistors and the precise layouts and via holes in each layer. In addition, wires and devices in large-scale circuits usually have smaller dimensions, and this requires the higher resolution of the inkjet printing process. To

handle these challenges, more studies about the layout design and the optimisation of the inkjet printing process are needed. And organic materials with better uniformity are also needed to be investigated.

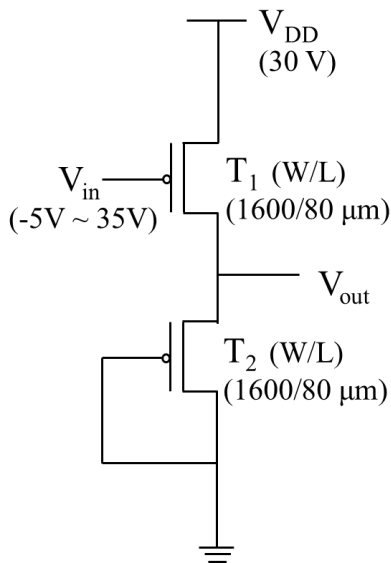
Packaging for the large-scale circuits. In Section 7.3, the packaging of the sample was achieved by the shadow mask and the low-pressure volatilisation. But in large-scale circuits, the shadow masks with higher precision and resolution are required. Thus the fabrication method of the shadow mask in this study should be altered and other masking process should be introduced in future study. To achieve the shadow mask with higher precision, the photolithography technique can be used. The photoresist used in the photolithography process can act as the shadow mask covering the oleophilic region, or directly act as the barrier confining the suspension in the specific region. In addition, it is important to develop a method to store the suspension along the interconnects, the proper storage and slow volatilisation of the insulating liquid is essential to unlock the possibility of using the PBSH technique in real-world applications.

APPENDIX A



TFT Current Mirror

```
vref 1 0 dc -25v
vout 4 0 dc -25v
r1 1 2 0
r2 4 3 0
T1 2 2 0 0 ptype1 l=80u w=1600u
T2 3 2 0 0 ptype2 l=80u w=1600u
.model ptype1 pmos(level=2) u0=0.131 tox=5e-7
.model ptype2 pmos(level=2) u0=0.146 tox=5e-7
```



TFT Common-Source Amplifier

```
vdd 1 0 dc 30
vin 3 0 dc 0.0 pulse(0 2 5ns 2ns 2ns 40ns)
T1 1 3 2 1 ptype1 l=80u w=1600u
T2 2 0 0 2 ptype2 l=80u w=1600u
.model ptype1 pmos(level=2) tox=5e-7 u0=0.291)
.model ptype2 pmos(level=2) tox=5e-7 u0=0.132)
```

Figure A. Schematic of the circuit and the netlist coding in AIM-Spice simulation for (a) Current mirror and (b) Common-source amplifier.

APPENDIX B

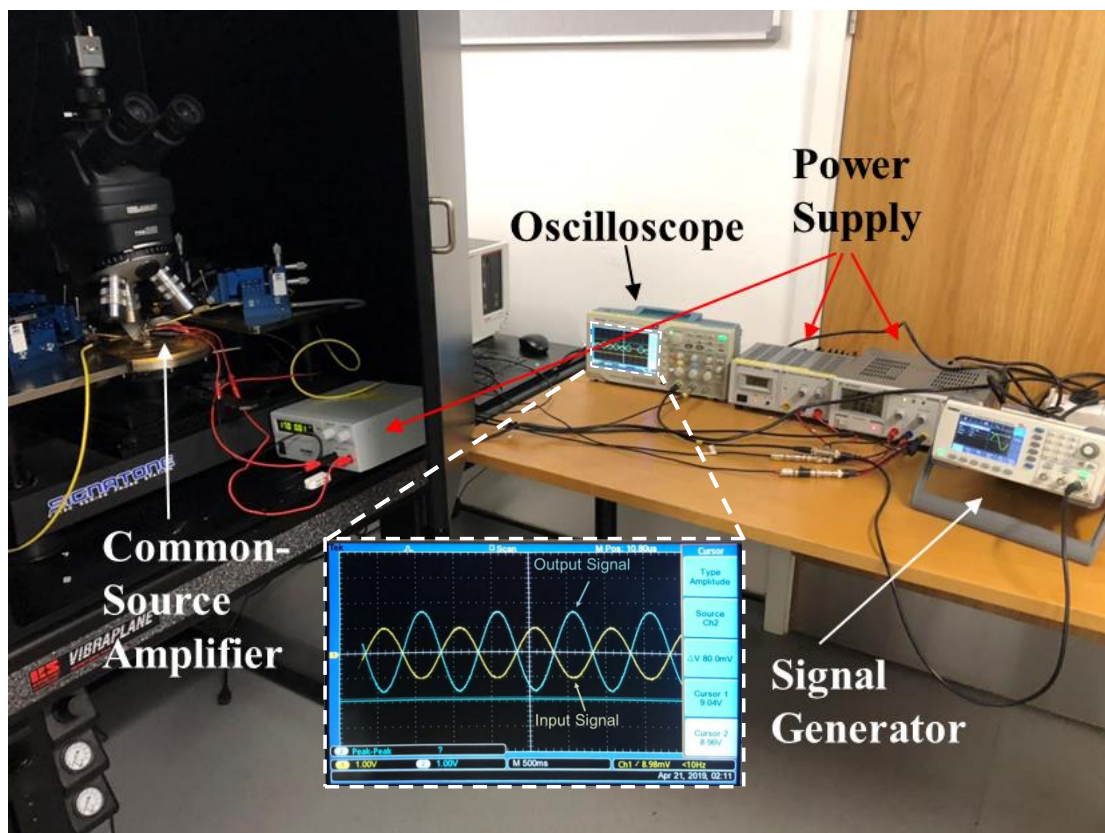


Figure B. Photograph of the experimental setup for measuring the AC signal processing by the common-source amplifier (Inset) The input and output signals shown on the oscilloscope.

APPENDIX C

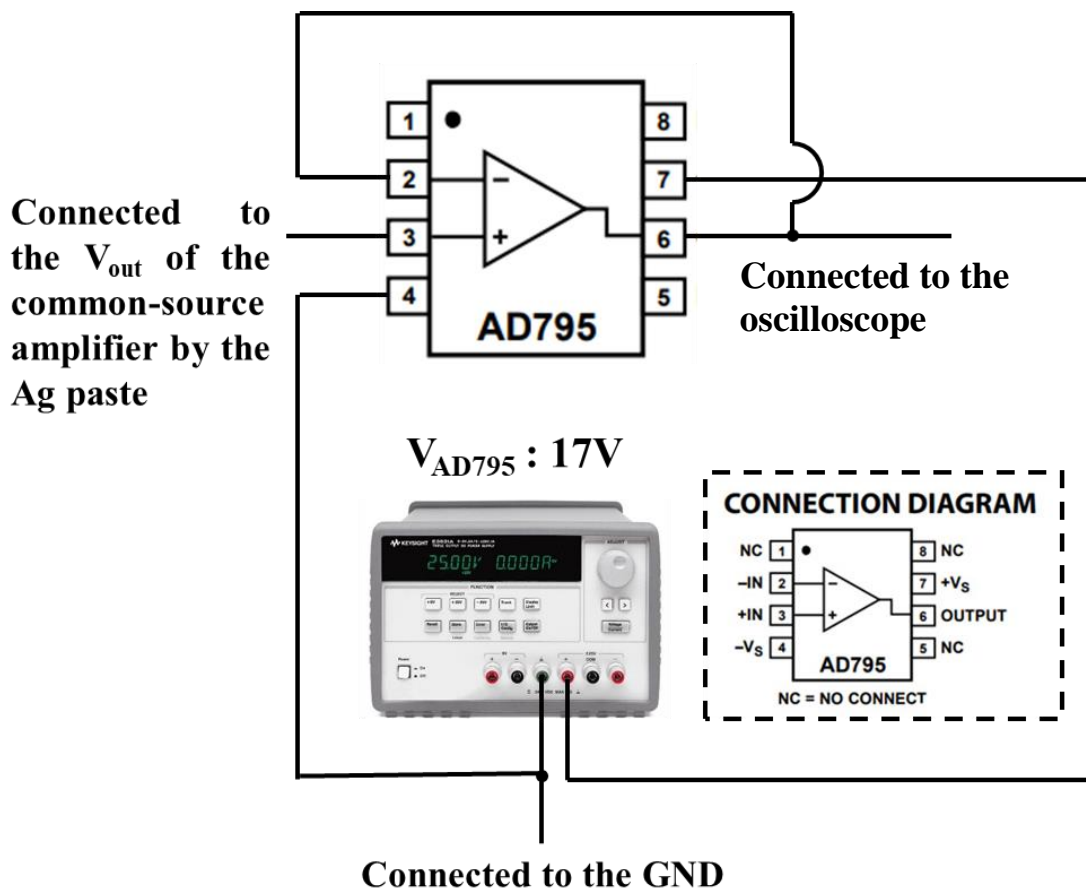


Figure C. Connection diagram of the AD795 chip.

APPENDIX D

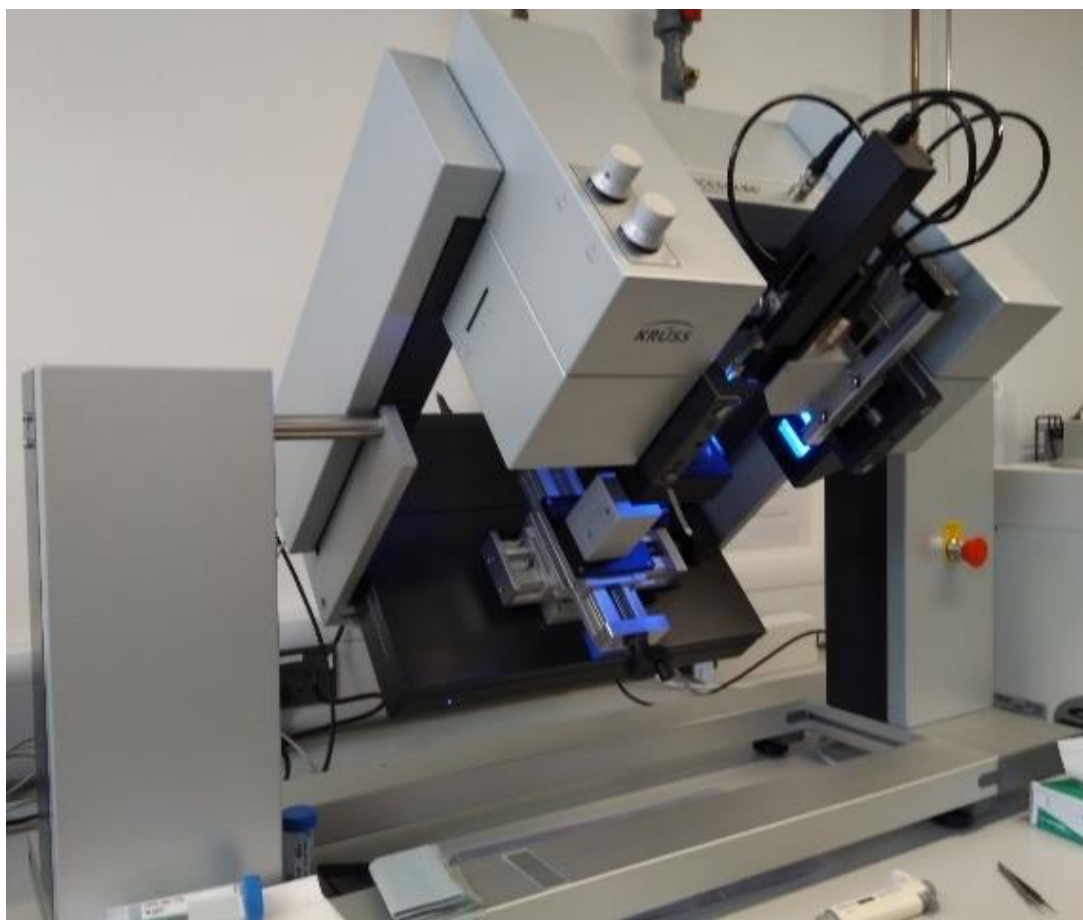


Figure D. Photography of the goniometer under tilting mode. The goniometer is used for visualising the stability of silicone oil over the silane coated and uncoated PEN substrate.

APPENDIX E

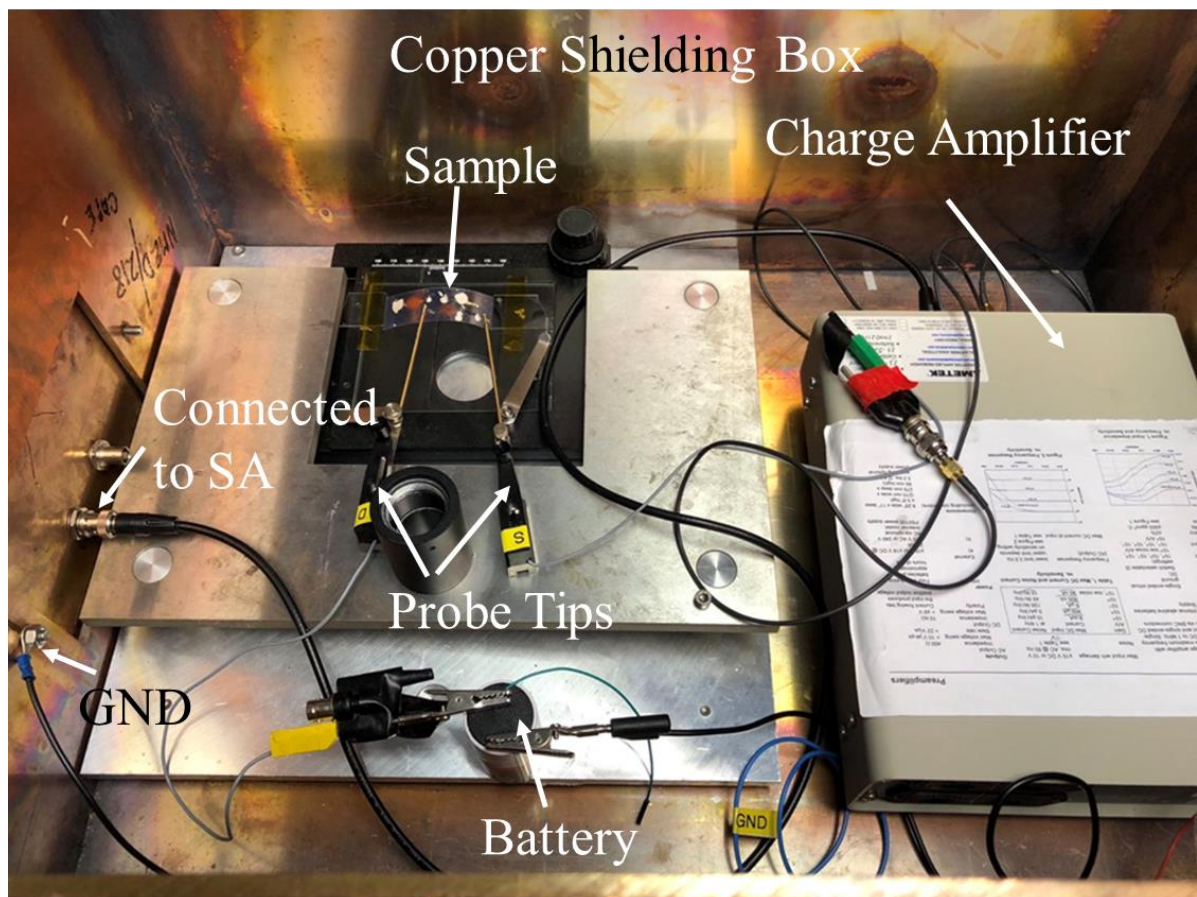


Figure E. Photography of the experimental setup for the noise measurement before covering the lid of the copper shielding box.

REFERENCES

- [1] Iwao Yagi, Nobukazu Hirai, Yoshihiro Miyamoto, Makoto Noda, Ayaka Imaoka, Nobuhide Yoneya, Kazumasa Nomoto, Jiro Kasahara, Akira Yumoto, and Tetsuo Urabe. A flexible full-color AMOLED display driven by OTFTs. *Journal of the Society for Information Display*, 16(1):15-20, 2008. ISSN: 1071-0922. doi: 10.1889/1.2835023.
- [2] Arokia Nathan, Arman Ahnood, Matthew T. Cole, Sungsik Lee, Yuji Suzuki, Pritesh Hiralal, Francesco Bonaccorso, Tawfique Hasan, Luis Garcia-Gancedo, Andriy Dyadyusha, Samiul Haque, Piers Andrew, Stephan Hofmann, James Moultrie, Daping Chu, Andrew J. Flewitt, Andrea C. Ferrari, Michael J. Kelly, John Robertson, Gehan A. J. Amaratunga, and William I. Milne. Flexible electronics: the next ubiquitous platform. *Proceedings of the IEEE*, 100:1486-1517, 2012. ISSN: 00189219. doi: 10.1109/JPROC.2012.2190168.
- [3] Tsuyoshi Sekitani, Ute Zschieschang, Hagen Klauk, and Takao Someya. Flexible organic transistors and circuits with extreme bending stability. *Nature Materials*, 9(12):1015-1022, 2010. ISSN: 1476-1122 doi: 10.1038/nmat2896.
- [4] Kaltenbrunner Martin, Sekitani Tsuyoshi, Reeder Jonathan, Yokota Tomoyuki, Kuribara Kazunori, Tokuhara Takeyoshi, Drack Michael, Schwodiauer Reinhard, Graz Ingrid, Bauer-Gogonea Simona, Bauer Siegfried, and Someya Takao. An ultra-lightweight design for imperceptible plastic electronics. *Nature*, 499(7459):458-463, 2013. ISSN: 0028-0836 doi: 10.1038/nature12314.
- [5] B. K. Charlotte Kjellander, Wiljan T. T. Smaal, Kris Myny, Jan Genoe, Wim Dehaene, Paul Heremans, and Gerwin H. Gelinck. Optimized circuit design for flexible 8-bit RFID transponders with active layer of ink-jet printed small molecule

semiconductors. *Organic Electronics*, 14(3):768-774, 2013. ISSN: 1566-1199. doi: 10.1016/j.orgel.2012.12.027.

[6] Takao Someya, Zhenan Bao, and George G. Malliaras. The rise of plastic bioelectronics. *Nature*, 540(7633):379-385, 2016. ISSN: 0028-0836. doi: 10.1038/nature21004.

[7] Tsukuru Minamiki, Tsuyoshi Minami, Ryoji Kurita, Osamu Niwa, Shin-Ichi Wakida, Kenjiro Fukuda, Daisuke Kumaki, and Shizuo Tokito. Accurate and reproducible detection of proteins in water using an extended-gate type organic transistor biosensor. *Applied Physics Letters*, 104(24):243703, 2014. ISSN: 0003-6951. doi: 10.1063/1.4883739.

[8] Benjamin C.-K. Tee, Alex Chortos, Andre Berndt, Amanda Kim Nguyen, Ariane Tom, Allister McGuire, Ziliang Carter Lin, Kevin Tien, Won-Gyu Bae, Huiliang Wang, Ping Mei, Ho-Hsiu Chou, Bianxiao Cui, Karl Deisseroth, Tse Nga Ng, and Zhenan Bao. A skin-inspired organic digital mechanoreceptor. *Science*, 350(6258):313-316, 2015. ISSN: 0036-8075. doi: 10.1126/science.aaa9306.

[9] Mallory Hammock, Alex Chortos, Benjamin Tee, Jeffrey Tok, and Zhenan Bao. The Evolution of Electronic Skin (E-Skin): A Brief History, Design Considerations, and Recent Progress. *Advanced Materials* 25(42):5997-6038, 2013. ISSN: 0935-9648. doi: 10.1002/adma.201302240.

[10] Sihong Wang, Jie Xu, Weichen Wang, Ging-Ji Nathan Wang, Reza Rastak, Francisco Molina-Lopez, Jong Won Chung, Simiao Niu, Vivian R Feig, Jeffery Lopez, Ting Lei, Soon-Ki Kwon, Yeongin Kim, Amir M Foudeh, Anatol Ehrlich, Andrea Gasperini, Youngjun Yun, Boris Murmann, Jeffery B-H Tok, and Zhenan Bao. Skin electronics from scalable fabrication of an intrinsically stretchable transistor array. *Nature*, 555(7694):83-88, 2018. ISSN: 0028-0836. doi: 10.1038/nature25494.

[11] Jie Xu, Sihong Wang, Ging Ji Nathan Wang, Chenxin Zhu, Shaochuan Luo, Lihua Jin, Xiaodan Gu, Shucheng Chen, Vivian R. Feig, and John W. F. To. Highly stretchable polymer semiconductor films through the nanoconfinement effect. *Science*, 355(6320):59, 2017. ISSN: 0036-8075. doi: 10.1126/science.aah4496.

[12] Li Ding, Jiaqing Zhao, Yukun Huang, Wei Tang, Sujie Chen, and Xiaojun Guo. Flexible-blade Coating of Small Molecule Organic Semiconductor for Low Voltage

Organic Field Effect Transistor. *IEEE Electron Device Letters*, 38(3):338, 2017. ISSN: 0741-3106. doi: 10.1109/LED.2017.2657651.

[13] Henning Sirringhaus, TH. Kawase, Rh. Friend, Tatsuya Shimoda, Michael Inbasekaran, Weishi Wu, and Edmund P. Woo. High-Resolution Inkjet Printing of All-Polymer Transistor Circuits. *Science*, 290(5499):2123-2126, 2000. ISSN: 0036-8075. doi: 10.1126/science.290.5499.2123.

[14] Tomi Hassinen, Teemu Ruotsalainen, Petri Laakso, Raimo Penttilä and Henrik Sandberg. Roll-to-roll compatible organic thin film transistor manufacturing technique by printing, lamination, and laser ablation. *Thin Solid Films*, 571(1):212-217, 2014. ISSN: 0040-6090. doi: 10.1016/j.tsf.2014.10.086.

[15] Makoto Noda, Norihito Kobayashi, Mao Katsuhara, Akira Yumoto, Shinichi Ushikura, Ryouichi Yasuda, Nobukazu Hirai, Gen Yukawa, Iwao Yagi, and Kazumasa Nomoto. An OTFT-driven rollable OLED display. *Journal of the Society for Information Display*, 19(4):316-322, 2011. ISSN: 1071-0922. doi: 10.1889/JSID19.4.316.

[16] Galaxy Z Fold2 5G, URL <https://www.samsung.com/uk/smartphones/galaxy-z-fold2/>.

[17] Daniel Lu, and C. P. Wong. Materials for Advanced Packaging. 2009. ISBN: 978-0-387-78218-8. doi: 10.1007/978-0-387-78219-5.

[18] Tsuyoshi Sekitani, Yusaku Kato, Shingo Iba, Hiroshi Shinaoka, Takao Someya, Takayasu Sakurai, and Shinichi Takagi. Bending experiment on pentacene field-effect transistors on plastic films. *Applied Physics Letters*, 86(7):073511, 2005. ISSN: 0003-6951. doi: 10.1063/1.1868868.

[19] James R. Black. Electromigration - A brief survey and some recent results. *IEEE Transactions on Electron Devices*, 16(4):338-347, 1969. ISSN: 0018-9383. doi: 10.1109/t-ed.1969.16754.

[20] Y. W. Lin, Jia-Hong Ke, Hsin-Yi Chuang, Yi-Shao Lai, and C. R. Kao. Electromigration in flip chip solder joints under extra high current density. *Journal of Applied Physics*, 107(7):073516, 2010. ISSN: 0021-8979. doi: 10.1063/1.3371711.

- [21] Jens Lienig, and Matthias Thiele. The Pressing Need for Electromigration-Aware Physical Design. *International Symposium on Physical Design*, 2018, 4:144-151, 2018. doi: 10.1145/3177540.3177560.
- [22] Jin Ge, Li Sun, Fu-Rui Zhang, Ye Zhang, Lu-An Shi, Hao-Yu Zhao, Hong-Wu Zhu, Hai-Long Jiang, and Shu-Hong Yu. A Stretchable Electronic Fabric Artificial Skin with Pressure-, Lateral Strain-, and Flexion-Sensitive Properties. *Advanced Materials*, 28(4):722-728, 2016. ISSN: 0935-9648 doi: 10.1002/adma.201504239.
- [23] Ming-Yuan Cheng, Chan-Mo Tsao, Yu-Tze Lai, and Yao-Joe Joseph Yang. The development of a highly twistable tactile sensing array with stretchable helical electrodes. *Sensors and Actuators A: Physical*, 166(2):226-233, 2011. ISSN: 0924-4247. doi: 10.1016/j.sna.2009.12.009.
- [24] Darren S. Gray, Joe Tien, and Christopher S. Chen. High-conductivity elastomeric electronics. *Advanced Materials*, 16(5):393-397, 2004. ISSN: 0935-9648. doi: 10.1002/adma.200306107.
- [25] Dominique Brosteaux, Fabrice Axisa, Mario Gonzalez, and Jan Vanfleteren. Design and fabrication of elastic interconnections for stretchable electronic circuits. *IEEE Electron Device Letters*, 28(7):552-554, 2007. ISSN: 0741-3106. doi: 10.1109/LED.2007.897887.
- [26] Beno ̂t Huyghe, Hendrik Rogier, Jan Vanfleteren, and Fabrice Axisa. Design and manufacturing of stretchable high-frequency interconnects. *IEEE Transactions on Advanced Packaging*, 31(4):802-808, 2008. ISSN: 1521-3323. doi: 10.1109/TADVP.2008.927811.
- [27] You Yu, Jifang Zeng, Chaojian Chen, Zhuang Xie, Ruisheng Guo, Zhilu Liu, Xuechang Zhou, Yong Yang, and Zijian Zheng. Three-dimensional compressible and stretchable conductive composites. *Advanced Materials*, 26(5):810-815, 2014. ISSN: 0935-9648. doi: 10.1002/adma.201303662.
- [28] Xuchun Gui, Anyuan Cao, Jinqian Wei, Hongbian Li, Yi Jia, Zhen Li, Lili Fan, Kunlin Wang, Hongwei Zhu, and Dehai Wu. Soft, highly conductive nanotube sponges and composites with controlled compressibility. *ACS Nano*, 4(4):2320-2326, 2010. ISSN: 1936-0851. doi: 10.1021/nn100114d.

- [29] Han-Byeol Lee, Chan-Wool Bae, Le Thai Duy, Il-Yung Sohn, Do-Il Kim, You-Joon Song, Youn-Jea Kim, and Nae-Eung Lee. Mogul-Patterned Elastomeric Substrate for Stretchable Electronics. *Advanced Materials*, 28(16):3069-3077, 2016. ISSN: 0935-9648. doi: 10.1002/adma.201505218.
- [30] Zongping Chen, Wencai Ren, Libo Gao, Bilu Liu, Songfeng Pei, and Hui-Ming Cheng. Three-dimensional flexible and conductive interconnected graphene networks grown by chemical vapour deposition. *Nature Materials*, 10(6):424-428, 2011. ISSN: 1476-1122. doi: 10.1038/nmat3001.
- [31] Phillip Lee, Jooyeon Ham, Jinhwan Lee, Sukjoon Hong, Seungyong Han, Young Duk Suh, Sang Eon Lee, Junyeob Yeo, Seung Seob Lee, Dongjin Lee, and Seung Hwan Ko. Highly Stretchable or Transparent Conductor Fabrication by a Hierarchical Multiscale Hybrid Nanocomposite. *Advanced Functional Materials*, 24(36):5671-5678, 2014. ISSN: 1616-301X. doi: 10.1002/adfm.201400972.
- [32] Ha-Chul Jung, Jin-Hee Moon, Dong-Hyun Baek, Jae-Hee Lee, Yoon-Young Choi, Joung-Sook Hong, and Sang-Hoon Lee. CNT/PDMS composite flexible dry electrodes for long-term ECG monitoring. *IEEE Transactions on Biomedical Engineering*, 59(5):1472-1479, 2012. ISSN: 0018-9294. doi: 10.1109/TBME.2012.2190288.
- [33] Yi Hou, Dongrui Wang, Xiao-Man Zhang, Hang Zhao, Jun-Wei Zha, and Zhi-Min Dang. Positive piezoresistive behavior of electrically conductive alkyl-functionalized graphene/polydimethylsilicone nanocomposites. *Journal of Materials Chemistry C*, 1(3):515-521, 2013. ISSN: 2050-7526. doi: 10.1039/c2tc00114d.
- [34] Lin Li, and Deborah D. L. Chung. Electrically conducting powder filled polyimidesiloxane. *Composites*, 22(3):211-218, 1991. ISSN: 0010-4361. doi: 10.1016/0010-4361(91)90321-7.
- [35] Mi-Sun Lee, Kyongsoo Lee, So-Yun Kim, Heejoo Lee, Jihun Park, Kwang-Hyuk Choi, Han-Ki Kim, Dae-Gon Kim, Dae-Young Lee, SungWoo Nam, and Jang-Ung Park. High-performance, transparent, and stretchable electrodes using graphene-metal nanowire hybrid structures. *Nano Letters*, 13(6):2814-2821, 2013. ISSN: 1530-6984. doi: 10.1021/nl401070p.

- [36] Jiajie Liang, Kwing Tong, and Qibing Pei. A Water-Based Silver-Nanowire Screen-Print Ink for the Fabrication of Stretchable Conductors and Wearable Thin-Film Transistors. *Advanced Materials*, 28:5986-5996, 2016. ISSN: 0935-9648. doi: 10.1002/adma.201600772.
- [37] Wei Xu, Qingsong Xu, Qijin Huang, Ruiqin Tan, Wenfeng Shen, and Weijie Song. Electrically conductive silver nanowires-filled methylcellulose composite transparent films with high mechanical properties. *Materials Letters*, 152:173-176, 2015. ISSN: 0167-577X. doi: 10.1016/j.matlet.2015.03.111.
- [38] Lingnan Song, Amanda C. Myers, Jacob J. Adams, and Yong Zhu. Stretchable and reversibly deformable radio frequency antennas based on silver nanowires. *ACS Applied Materials & Interfaces*, 6(6):4248-4253, 2014. ISSN: 1944-8244. doi: 10.1021/am405972e.
- [39] Vincent Martinez, Flurin Stauffer, Mohammed O. Adagunodo, Csaba Forro, Janos Voros, and Alexandre Larmagnac. Stretchable Silver Nanowire-Elastomer Composite Microelectrodes with Tailored Electrical Properties. *ACS Applied Materials & Interfaces*, 7(24):13467-13475, 2015. ISSN: 1944-8244. doi: 10.1021/acsami.5b02508.
- [40] Hristiyan Stoyanov, Matthias Kollosche, Sebastian Risse, Remi Wache, and Guggi Kofod. Soft conductive elastomer materials for stretchable electronics and voltage controlled artificial muscles. *Advanced Materials*, 25(4):578-583, 2013. ISSN: 0935-9648. doi: 10.1002/adma.201202728.
- [41] Darren J. Lipomi, Jennifer A. Lee, Michael Vosgueritchian, Benjamin C. K. Tee, John A. Bolander, and Zhenan Bao. Electronic Properties of Transparent Conductive Films of PEDOT:PSS on Stretchable Substrates. *Chemistry of Materials*, 24(2):373-382, 2012. ISSN: 0897-4756. doi: 10.1021/cm203216m.
- [42] Chung-Ki Cho, Woo-Jin Hwang, Kyoungtae Eun, Sung-Hoon Choa, Seok-In Na, and Han-Ki Kim. Mechanical flexibility of transparent PEDOT:PSS electrodes prepared by gravure printing for flexible organic solar cells. *Solar Energy Materials and Solar Cells*, 95(12):3269-3275, 2011. ISSN: 0927-0248. doi: 10.1016/j.solmat.2011.07.009.
- [43] Mary M. Caruso, Stuart R. Schelkopf, Aaron C. Jackson, Alexandra M. Landry, Paul V. Braun, and Jeffrey S. Moore. Microcapsules containing suspensions of carbon

nanotubes. *Journal of Materials Chemistry*, 19(34):6093-6096, 2009. ISSN: 0959-9428. doi: 10.1039/b910673a.

[44] Susan A. Odom, Timothy P. Tyler, Mary M. Caruso, Joshua A. Ritchey, Matthew V. Schulmerich, Scott J. Robinson, Rohit Bhargava, Nancy R. Sottos, Scott R. White, Mark C. Hersam, and Jeffrey S. Moore. Autonomic restoration of electrical conductivity using polymer-stabilized carbon nanotube and graphene microcapsules. *Applied Physics Letters*, 101(4):043106, 2012. ISSN: 0003-6951. doi: 10.1063/1.4737935.

[45] Susan A. Odom, Mary M. Caruso, Aaron D. Finke, Alex M. Prokup, Joshua A. Ritchey, John H. Leonard, Scott R. White, Nancy R. Sottos, and Jeffrey S. Moore. Restoration of Conductivity with TTF-TCNQ Charge-Transfer Salts. *Advanced Functional Materials*, 20(11):1721-1727, 2010. ISSN: 1616-301X. doi: 10.1002/adfm.201000159.

[46] Sen Kang, Amanda R. Jones, Jeffrey S. Moore, Scott R. White, and Nancy R. Sottos. Microencapsulated Carbon Black Suspensions for Restoration of Electrical Conductivity. *Advanced Functional Materials*, 24(20):2947-2956, 2014. ISSN: 1616-301X. doi: 10.1002/adfm.201303427.

[47] Eric J. Markvicka, Michael D. Bartlett, Xiaonan Huang, and Carmel Majidi. An autonomously electrically self-healing liquid metal-elastomer composite for robust soft-matter robotics and electronics. *Nature Materials*, 17:618-624, 2018. ISSN: 1476-1122. doi: 10.1038/s41563-018-0084-7.

[48] Li Ding, Pushkaraj Joshi, James Macdonald, Virendra Parab, and Sanjiv Sambandan. Self-healing Thin-film Transistor Circuits on Flexible Substrates. *Advanced Electronic Materials*, 7(3):2001023, 2021. ISSN: 2199-160X. doi: 10.1002/aelm.202001023.

[49] Dae-Hyeong Kim, Zhuangjian Liu, Yun-Soung Kim, Jian Wu, Jizhou Song, Hoon-Sik Kim, Yonggang Huang, Keh-chih Hwang, Yongwei Zhang, and John A. Rogers. Optimized structural designs for stretchable silicon integrated circuits. *Small*, 5(24):2841-2847, 2009. ISSN: 1613-6810. doi: 10.1002/sml.200900853.

- [50] Chuan Fei Guo, Tianyi Sun, Qihan Liu, Zhigang Suo, and Zhifeng Ren. Highly stretchable and transparent nanomesh electrodes made by grain boundary lithography. *Nature Communications*, 5:3121, 2014. ISSN: 2041-1723. doi: 10.1038/ncomms4121.
- [51] Manthiriyappan Sureshkumar, Hyo Yeol Na, Kyung Hyun Ahn, and Seong Jae Lee. Conductive nanocomposites based on polystyrene microspheres and silver nanowires by latex blending. *ACS Applied Materials & Interfaces*, 7(1):756-764, 2015. ISSN: 1944-8244 doi: 10.1021/am5071392.
- [52] Desalegn Alemu, Hung-Yu Wei, Kuo-Chuan Ho, and Chih-Wei Chu. Highly conductive PEDOT:PSS electrode by simple film treatment with methanol for ITO-free polymer solar cells. *Energy & Environmental Science*, 5(11):9662-9671, 2012. ISSN: 1754-5692. doi: 10.1039/c2ee22595f.
- [53] Lijun Lu, Xiangdong Wei, Ye Zhang, Guoqiang Zheng, Kun Dai, Chuntai Liu, and Changyu Shen. A flexible and self-formed sandwich structure strain sensor based on AgNW decorated electrospun fibrous mats with excellent sensing capability and good oxidation inhibition properties. *Journal of Materials Chemistry C* 5(28):7035-7042, 2017. ISSN: 2050-7534. doi: 10.1039/C7TC02429K.
- [54] Yunjeong Heo, Youngkyu Hwang, Hoon Sun Jung, Sung-Hoon Choa, and Heung Cho Ko. Secondary Sensitivity Control of Silver-Nanowire-Based Resistive-Type Strain Sensors by Geometric Modulation of the Elastomer Substrate. *Small*, 13(23):1700070, 2017. ISSN: 1613-6810. doi: 10.1002/smll.201700070.
- [55] Daihua Zhang, Kounghmin Ryu, Xiaolei Liu, Evgueni Polikarpov, James Ly, Mark E. Tompson, and Chongwu Zhou. Transparent, Conductive, and Flexible Carbon Nanotube Films and Their Application in Organic Light-Emitting Diodes. *Nano Letters*, 6(9):1880-1886, 2006. ISSN: 1530-6984. doi: 10.1021/nl0608543.
- [56] Etienne Palleau, Stephen Reece, Sharvil C. Desai, Michael E. Smith, and Michael D. Dickey. Self-healing stretchable wires for reconfigurable circuit wiring and 3D microfluidics. *Advanced Materials*, 25(11):1589-1592, 2013. ISSN: 0935-9648. doi: 10.1002/adma.201203921.
- [57] Philippe Cordier, Francois Tournilhac, Corinne Soulie-Ziakovic, and Ludwik Leibler. Self-healing and thermoreversible rubber from supramolecular assembly. *Nature*, 451(7181):977-980, 2008. ISSN: 0028-0836 doi: 10.1038/nature06669.

- [58] Jinxing Li, Oleg E. Shklyae, Tianlong Li, Wenjuan Liu, Henry Shum, Isaac Rozen, Anna C. Balazs, and Joseph Wang. Self-Propelled Nanomotors Autonomously Seek and Repair Cracks. *Nano Letters*, 15(10):7077-7085, 2015. ISSN: 1530-6984. doi: 10.1021/acs.nanolett.5b03140.
- [59] Virendra Parab, Oppili Prasad, Sreelal Pillai, and Sanjiv Sambandan. Electric Field Assisted Self-Healing of Open Circuits with Conductive Particle-Insulating Fluid Dispersions: Optimizing Dispersion Concentration. *Scientific Reports*, 9(1):19700, 2019. ISSN: 2045-2322 doi: 10.1038/s41598-019-55801-8.
- [60] Zhengxia Xu, and Guoxin Hu. Simple and green synthesis of monodisperse silver nanoparticles and surface-enhanced Raman scattering activity. *RSC Advances*, 2(30):11404-11409, 2012. ISSN: 2046-2069. doi: 10.1039/c2ra21745g.
- [61] Yongqiang Lu, and Jan D. Miller. Carboxyl Stretching Vibrations of Spontaneously Adsorbed and LB-Transferred Calcium Carboxylates as Determined by FTIR Internal Reflection Spectroscopy. *Journal of Colloid and Interface Science*, 256(1):41-52, 2002. ISSN: 0021-9797. doi: 10.1006/jcis.2001.8112.
- [62] Fredrik Söderlind, Henrik Pedersen, Rodrigo M. Petoral, Per-Olov Käll, and Kajsa Uvdal. Synthesis and characterisation of Gd₂O₃ nanocrystals functionalised by organic acids. *Journal of Colloid and Interface Science*, 288(1):140-148, 2005. ISSN: 0021-9797. doi: 10.1016/j.jcis.2005.02.089.
- [63] Lyudmila M. Bronstein, Xinlei Huang, John Retrum, Abrin Schmucker, Maren Pink, Barry D. Stein, and Bogdan Dragnea. Influence of Iron Oleate Complex Structure on Iron Oxide Nanoparticle Formation. *Chemistry of Materials*, 19(15):3624-3632, 2007. ISSN: 0897-4756. doi: 10.1021/cm062948j.
- [64] Srinivasa R. Raghavan, Jun Hou, Gregory L. Baker, and Saad A. Khan. Colloidal Interactions between Particles with Tethered Nonpolar Chains Dispersed in Polar Media: Direct Correlation between Dynamic Rheology and Interaction Parameters. *Langmuir*, 16(3):1066-1077, 2000. ISSN: 0743-7463. doi: 10.1021/la9815953.
- [65] Yingying Chen, Xiaojun Quan, Zhongyong Wang, Chiahsun Lee, Zizhao Wang, Peng Tao, Chengyi Song, Jianbo Wu, Wen Shang, and Tao Deng. Stably dispersed high-temperature Fe₃O₄/silicone-oil nanofluids for direct solar thermal energy

harvesting. *Journal of Materials Chemistry A*, 4(44):17503-17511, 2016. ISSN: 2050-7488. doi: 10.1039/c6ta07773k.

[66] Gilles Horowitz. Organic field-effect transistors. *Advanced Materials*, 10(5):365-377, 1998. ISSN: 0935-9648. doi: 10.1002/(SICI)1521-4095(199803)10:53.0.CO;2-U.

[67] Ian G. Hill. Numerical simulations of contact resistance in organic thin-film transistors. *Applied Physics Letters*, 87(16):163505, 2005. ISSN: 0003-6951. doi: 10.1063/1.2112189.

[68] David Gundlach, Lisong Zhou, J. A. Nichols, Thomas N. Jackson, P. V. Necliudov, and Michael S. Shur. An experimental study of contact effects in organic thin film transistors. *Journal of Applied Physics*, 100(2):99-348, 2006. ISSN: 0021-8979. doi: 10.1063/1.2215132.

[69] Yongbo Yuan, Gaurav Giri, Alexander L. Ayzner, Arjan P. Zoombelt, Stefan C. B. Mannsfeld, Jihua Chen, Dennis Nordlund, Michael F. Toney, Jinsong Huang, and Zhenan Bao. Ultra-high mobility transparent organic thin film transistors grown by an off-centre spin-coating method. *Nature Communications*, 5:3005, 2014. ISSN: 2041-1723. doi: 10.1038/ncomms4005.

[70] Yong Xu, Huabin Sun, Eul Yong Shin, Yen Fu Lin, and Yong Young Noh. Planar-Processed Polymer Transistors. *Advanced Materials*, 28(38):8531-8537, 2016. ISSN: 0935-9648. doi: 10.1002/adma.201601589.

[71] David Gundlach, J. Royer, S. K. Park, Sankar Subramanian, Oana D. Jurchescu, Behrang H. Hamadani, Andrew J. Moad, R. Joseph Kline, Lucile C. Teague, Oleg Kirillov, Curt A. Richter, James G. Kushmerick, Lee Richter, Sean Parkin, Thomas N. Jackson, and John E. Anthony. Contact-induced crystallinity for high-performance soluble acene-based transistors and circuits. *Nature Materials*, 7(3):216-221, 2008. ISSN: 1476-1122. doi: 10.1038/nmat2122.

[72] Michael G. Kane, John Campi, Mark S. Hammond, Frank P. Cuomo, B. Greening, Christopher D. Sheraw, J. A. Nichols, David Gundlach, Jiunn-Ru Huang, and Chung-Chen Kuo. Analog and digital circuits using organic thin-film transistors on polyester substrates. *IEEE Electron Device Letters*, 21(11):534-536, 2000. ISSN: 0741-3106. doi: 10.1109/55.877202.

- [73] Enrico Sowade, Kalyan Yoti Mitra, Eloi Ramon, Carme Martinez-Domingo, Fulvia Villani, Fausta Loffredo, Henrique L. Gomes, and Reinhard R. Baumann. Up-scaling of the manufacturing of all-inkjet-printed organic thin-film transistors: Device performance and manufacturing yield of transistor arrays. *Organic Electronics*, 30:237-246, 2016. ISSN: 1566-1199. doi: 10.1016/j.orgel.2015.12.018.
- [74] Florian Eder, Hagen Klauk, Marcus Halik, Ute Zschieschang, Günter Schmid, and Christine Dehm. Organic electronics on paper. *Applied Physics Letters*, 84(14):2673-2675, 2004. ISSN: 0003-6951. doi: 10.1063/1.1690870.
- [75] Yun Li, Chuan Liu, Yong Xu, Takeo Minari, Peter Darmawan, and Kazuhito Tsukagoshi. Solution-processed organic crystals for field-effect transistor arrays with smooth semiconductor/dielectric interface on paper substrates. *Organic Electronics*, 13(5):815-819, 2012. ISSN: 1566-1199. doi: 10.1016/j.orgel.2012.01.021.
- [76] Toshiharu Teranishi, Satoshi Hasegawa, Takami Shimizu, and Mikio Miyake. Heat-Induced Size Evolution of Gold Nanoparticles in the Solid State. *Advanced Materials*, 13(22):1699-1701, 2001. ISSN: 0935-9648. doi: 10.1002/1521-4095(200111)13:223.O.CO;2-3.
- [77] Dongjo Kim, Sunho Jeong, and Jooho Moon. Synthesis of silver nanoparticles using the polyol process and the influence of precursor injection. *Nanotechnology*, 17(16):4019-4024, 2006. ISSN: 0957-4484. doi: 10.1088/0957-4484/17/16/004.
- [78] Wei Tang, Linrun Feng, Jiaqing Zhao, Qingyu Cui, Sujie Chen, and Xiaojun Guo. Inkjet printed fine silver electrodes for all-solution-processed low-voltage organic thin film transistors. *Journal of Materials Chemistry C*, 2(11):1995-2000, 2014. ISSN: 2050-7526. doi: 10.1039/c3tc32134g.
- [79] Kien F. Teng, and Robert W. Vest. Metallization of Solar Cells with Ink Jet Printing and Silver Metallo-Organic Inks. *IEEE Transactions on Components Hybrids and Manufacturing Technology*, 11(3):291-297, 1988. ISSN: 2156-3950. doi: 10.1109/33.16656.
- [80] Cheong Min Hong, and Sigurd Wagner. Inkjet printed copper source/drain metallization for amorphous silicon thin-film transistors. *IEEE Electron Device Letters*, 21(8):384-386, 2000. ISSN: 0741-3106. doi: 10.1109/55.852958.

- [81] Jung Pyo Hong, Aee Young Park, Seonghoon Lee, Jihoon Kang, Nayool Shin, and Do Y. Yoon. Tuning of Ag work functions by self-assembled monolayers of aromatic thiols for an efficient hole injection for solution processed triisopropylsilylethynyl pentacene organic thin film transistors. *Applied Physics Letters*, 92(14):143311, 2008. ISSN: 0003-6951. doi: 10.1063/1.2907691.
- [82] Bert De Boer, Afshin Hadipour, M. Magdalena Mandoc, Teunis Van Woudenberg, and Paul W. M. Blom. Tuning of Metal Work Functions with Self-Assembled Monolayers. *Advanced Materials*, 17(5):621-625, 2005. ISSN: 0935-9648. doi: 10.1002/adma.200401216.
- [83] Ian H. Campbell, Shai Rubin, Thomas A. Zawodzinski, Joel D. Kress, Richard L. Martin, D. L. Smith, Nikolay N. Barashkov, and John P. Ferraris. Controlling Schottky energy barriers in organic electronic devices using self-assembled monolayers. *Physical Review B*, 54(20):R14321-R14324, 1996. ISSN: 1098-0121. doi: 10.1103/PhysRevB.54.R14321.
- [84] Samrana Kazim, F. Javier Ramos, Peng Gao, Mohammad Khaja Nazeeruddin, Michael Grätzel, and Shahzada Ahmad. A dopant free linear acene derivative as a hole transport material for perovskite pigmented solar cells. *Energy & Environmental Science*, 8(6):1816-1823, 2015. ISSN: 1754-5692. doi: 10.1039/c5ee00599j.
- [85] Chen Jiang, Hyung Woo Choi, Xiang Cheng, Hanbin Ma, David Hasko, and Arokia Nathan. Printed subthreshold organic transistors operating at high gain and ultralow power. *Science*, 363(6428):719-723, 2019. ISSN: 0036-8075. doi: 10.1126/science.aav7057.
- [86] Dario Natali, and Mario Caironi. Charge Injection in Solution-Processed Organic Field-Effect Transistors: Physics, Models and Characterization Methods. *Advanced Materials*, 24(11):1357-1387, 2012. ISSN: 0935-9648. doi: 10.1002/adma.201104206.
- [87] Chuan Liu, Yong Xu, and Yong-Young Noh. Contact engineering in organic field-effect transistors. *Materials Today*, 18(2):79-96, 2015. ISSN: 1369-7021. doi: 10.1016/j.mattod.2014.08.037.
- [88] Akira Tsumura, Hiroshi Koezuka, and Torahiko Ando. Macromolecular electronic device: Field-effect transistor with a polythiophene thin film. *Applied Physics Letters*, 49(18):1210-1212, 1986. ISSN: 0003-6951. doi: 10.1063/1.97417.

- [89] Chang Jui-Fen, Sun Baoquan, Dag W. Breiby, Martin M. Nielsen, Theis I Slling, Mark Giles, Iain McCulloch, and Henning Sirringhaus. Enhanced Mobility of Poly(3-hexylthiophene) Transistors by Spin-Coating from High-Boiling-Point Solvents. *Chemistry of Materials*, 16(23):4772-4776, 2004. ISSN: 0897-4756. doi: 10.1021/cm049617w.
- [90] Kang Jun Baeg, Mario Caironi, and Yong Young Noh. Toward Printed Integrated Circuits based on Unipolar or Ambipolar Polymer Semiconductors. *Advanced Materials*, 25(31):4210-4244, 2013. ISSN: 0935-9648. doi: 10.1002/adma.201205361.
- [91] Beng S Ong, Yiliang Wu, Ping Liu, and Sandra Gardner. High-Performance Semiconducting Polythiophenes for Organic Thin-Film Transistors. *Journal of the American Chemical Society*, 126(11):3378-3379, 2004. ISSN: 0002-7863. doi: 10.1021/ja039772w.
- [92] Iain Mcculloch, Martin Heeney, Clare Bailey, Kristijonas Genevicius, and Michael F. Toney. Liquid-crystalline semiconducting polymers with high charge-carrier mobility. *Nature Materials*, 5(4):328-333, 2006. ISSN: 1476-1122. doi: 10.1038/nmat1612.
- [93] Yong Young Noh, Ni Zhao, Mario Caironi, and Henning Sirringhaus. Downscaling of self-aligned, all-printed polymer thin-film transistors. *Nature Nanotechnology*, 2(12):784-789, 2007. ISSN: 1748-3387 doi: 10.1038/nnano.2007.365.
- [94] Paul S. K. Amegadze, and Yong Young Noh. Development of high-performance n-type organic thin-film transistors using a small-molecule polymer blend. *Thin Solid Films*, 556:414-418, 2014. ISSN: 0040-6090. doi: 10.1016/j.tsf.2014.01.004.
- [95] Jing Guo, Guodong Li, Heiko Reith, Lang Jiang, and Yuanyuan Hu. Doping High-Mobility Donor–Acceptor Copolymer Semiconductors with an Organic Salt for High-Performance Thermoelectric Materials. *Advanced Electronic Materials*, 6(3):1900945, 2020. ISSN: 2199-160X. doi: 10.1002/aelm.201900945.
- [96] Xinran Zhang, Hugo Bronstein, Auke J. Kronemeijer, Jeremy Smith, Youngju Kim, R. Joseph Kline, Lee J. Richter, Thomas D. Anthopoulos, Henning Sirringhaus, Kigook Song, Martin Heeney, Weimin Zhang, and Dean M. DeLongchamp. Molecular origin of high field-effect mobility in an indacenodithiophene-benzothiadiazole copolymer.

Nature Communications, 4(7):2238, 2013. ISSN: 2041-1723. doi: 10.1038/ncomms3238.

[97] Deepak Venkateshvaran, Mark Nikolka¹, Aditya Sadhanala, Vincent Lemaur, Mateusz Zelazny, Michal Kepa, Michael Hurhangee, Auke Jisk Kronemeijer, Vincenzo Pecunia, Iyad Nasrallah, Igor Romanov, Katharina Broch, Iain McCulloch, David Emin, Yoann Olivier, Jerome Cornil, David Beljonne, and Henning Sirringhaus. Approaching disorder-free transport in high-mobility conjugated polymers. *Nature*, 515(7527):384-388, 2014. ISSN: 0028-0836. doi: 10.1038/nature13854.

[98] Hoi Nok Tsao, Don M. Cho, Insun Park, Michael Ryan Hansen, Alexey Mavrinskiy, Do Y. Yoon, Robert Graf, Wojciech Pisula, Hans Wolfgang Spiess, and Klaus Muellen. Ultrahigh mobility in polymer field-effect transistors by design. *Journal of the American Chemical Society*, 133(8):2605-2612, 2011. ISSN: 0002-7863. doi: 10.1021/ja108861q.

[99] Linrun Feng, Chen Jiang, Hanbin Ma, Xiaojun Guo, and Arokia Nathan. All ink-jet printed low-voltage organic field-effect transistors on flexible substrate. *Organic Electronics*, 38:186-192, 2016. ISSN: 1566-1199. doi: 10.1016/j.orgel.2016.08.019.

[100] Ying Diao, Benjamin C-K. Tee, Gaurav Giri, Jie Xu, Do Hwan Kim, Hector A. Becerril, Randall M. Stoltenberg, Tae Hoon Lee, Gi Xue, Stefan C. B. Mannsfeld, and Zhenan Bao. Solution coating of large-area organic semiconductor thin films with aligned single-crystalline domains. *Nature Materials*, 12(7):665-671, 2013. ISSN: 1476-1122. doi: 10.1038/nmat3650.

[101] Sung Kyu Park, Thomas N. Jackson, John E. Anthony, and Devin A. Mourey. High mobility solution processed 6,13-bis(triisopropyl-silylethynyl) pentacene organic thin film transistors. *Applied Physics Letters*, 91(6):063514, 2007. ISSN: 0003-6951. doi: 10.1063/1.2768934.

[102] Sung Kyu Park, John E. Anthony, and Thomas N. Jackson. Solution-Processed TIPS-Pentacene Organic Thin-Film-Transistor Circuits. *IEEE Electron Device Letters*, 28(10):877-879, 2007. ISSN: 0741-3106. doi: 10.1109/LED.2007.905374.

[103] Huai-Yuan Tseng, and Vivek Subramanian. All inkjet-printed, fully self-aligned transistors for low-cost circuit applications. *Organic Electronics*, 12(2):249-256, 2011. ISSN: 1566-1199. doi: 10.1016/j.orgel.2010.11.013.

- [104] Xiaoya Hou, Siu Choon Ng, Jie Zhang, and Joseph Sylvester Chang. Polymer nanocomposite dielectric based on P(VDF-TrFE)/PMMA/BaTiO₃ for TIPs-pentacene OFETs. *Organic Electronics*, 17:247-252, 2015. ISSN: 1566-1199. doi: 10.1016/j.orgel.2014.12.012.
- [105] Robby Janneck, Nicolas Pilet, Satya Prakash Bommanaboyena, Benjamin Watts, Paul Heremans, Jan Genoe, and Cedric Rolin. Highly Crystalline C8-BTBT Thin-Film Transistors by Lateral Homo-Epitaxial Growth on Printed Templates. *Advanced Materials*, 29(44):1703864, 2017. ISSN: 0935-9648. doi: 10.1002/adma.201703864.
- [106] Takafumi Uemura, Yuri Hirose, Mayumi Uno, Kazuo Takimiya, and Jun Takeya. Very High Mobility in Solution-Processed Organic Thin-Film Transistors of Highly Ordered [1]Benzothieno[3,2-b]benzothiophene Derivatives. *Applied Physics Express*, 2(11):111501-111503, 2009. ISSN: 1882-0778. doi: 10.1143/APEX.2.111501.
- [107] Richard Hamilton, Jeremy Smith, Simon Ogier, Martin Heeney, John E. Anthony, Iain McCulloch, Janos Veres, Donal D. C. Bradley, and Thomas D. Anthopoulos. High-Performance Polymer-Small Molecule Blend Organic Transistors. *Advanced Materials*, 21(10):1166-1171, 2009. ISSN: 0935-9648. doi: 10.1002/adma.200801725.
- [108] Devin A. Mourey, Sung Kyu Park, Dalong A. Zhao, Jie Sun, Yuanyuan V. Li, Sankar Subramanian, Shelby F. Nelson, David H. Levy, John E. Anthony, and Thomas N. Jackson. Fast, simple ZnO/organic CMOS integrated circuits. *Organic Electronics*, 10(8):1632-1635, 2009. ISSN: 1566-1199. doi: 10.1016/j.orgel.2009.08.021.
- [109] Simon Hunter, Jeremy W. Ward, Marcia M. Payne, John E. Anthony, Oana D. Jurchescu, and Thomas D. Anthopoulos. Low-voltage polymer/small-molecule blend organic thin-film transistors and circuits fabricated via spray deposition. *Applied Physics Letters*, 106(22):223304, 2015. ISSN: 0003-6951. doi: 10.1063/1.4922194.
- [110] Jingjing Chang, Chunyan Chi, Jie Zhang, and Jishan Wu. Controlled Growth of Large-Area High-Performance Small-Molecule Organic Single-Crystalline Transistors by Slot-Die Coating Using A Mixed Solvent System. *Advanced Materials*, 25(44):6442–6447, 2013. ISSN: 0935-9648. doi: 10.1002/adma.201301267.
- [111] Adrien Pierre, Mahsa Sadeghi, Marcia M. Payne, Antonio Facchetti, and Ana Claudia Arias. All-Printed Flexible Organic Transistors Enabled by Surface Tension-

Guided Blade Coating. *Advanced Materials*, 26(32):5722-5727, 2014. ISSN: 0935-9648. doi: 10.1002/adma.201401520.

[112] Gaurav Giri, Eric Verploegen, Stefan C. B. Mannsfeld, Sule Atahan-Evrenk, Do Hwan Kim, Sang Yoon Lee, Hector A. Becerril, Alán Aspuru-Guzik, Michael F. Toney, and Zhenan Bao. Tuning charge transport in solution-sheared organic semiconductors using lattice strain. *Nature*, 480(7378):504-508, 2011. ISSN: 0028-0836. doi: 10.1038/nature10683.

[113] Claudia M. Duffy, Jens W. Andreasen, Dag W. Breiby, Martin M. Nielsen, Masahiko Ando, Takashi Minakata, and Henning Sirringhaus. High-Mobility Aligned Pentacene Films Grown by Zone-Casting. *Chemistry of Materials*, 20(23):7252-7259, 2008. ISSN: 0897-4756. doi: 10.1021/cm801689f.

[114] Wojciech Pisula, Anoop Menon, Michael Stepputat, Ingo Lieberwirth, Ute Kolb, Adam Tracz, Henning Sirringhaus, Tadeusz Pakula, and Klaus Müllen. A Zone-Casting Technique for Device Fabrication of Field-Effect Transistors Based on Discotic Hexa-peri-hexabenzocoronene. *Advanced Materials*, 17(6):684–689, 2005. ISSN: 0935-9648. doi: 10.1002/adma.200401171.

[115] Song Yun Cho, Jung Min Ko, Jongsun Lim, Jun Young Lee, and Changjin Lee. Inkjet-printed organic thin film transistors based on TIPS pentacene with insulating polymers. *Journal of Materials Chemistry C*, 1(5):914-923, 2013. ISSN: 2050-7526. doi: 10.1039/c2tc00360k.

[116] Muhammad R. Niazi, Ruipeng Li, Maged Abdelsamie, Kui Zhao, Dalaver H. Anjum, Marcia M. Payne, John Anthony, Detlef M. Smilgies, and Aram Amassian. Contact-Induced Nucleation in High-Performance Bottom-Contact Organic Thin Film Transistors Manufactured by Large-Area Compatible Solution Processing. *Advanced Functional Materials*, 26(14):2371–2378, 2015. ISSN: 1616-301X. doi: 10.1002/adfm.201502428.

[117] Jihoon Kang, Nayool Shin, Do Young Jang, Vivek M. Prabhu, and Do Y. Yoon. Structure and properties of small molecule-polymer blend semiconductors for organic thin film transistors. *Journal of the American Chemical Society*, 23(3):366-376, 2013. ISSN: 0002-7863. doi: 10.1002/adfm.201201389.

- [118] B. K. Charlotte Kjellander, Wiljan T. T. Smaal, John E. Anthony, and Gerwin H. Gelinck. Inkjet Printing of TIPS-PEN on Soluble Polymer Insulating Films: A Route to High-Performance Thin-Film Transistors. *Advanced Materials*, 22(41):4612-4616, 2010. ISSN: 0935-9648. doi: 10.1002/adma.201001697.
- [119] Linrun Feng, Wei Tang, Xiaoli Xu, Qingyu Cui, and Xiaojun Guo. Ultralow-Voltage Solution-Processed Organic Transistors With Small Gate Dielectric Capacitance. *IEEE Electron Device Letters* 34(1):129-131, 2013. ISSN: 0741-3106. doi: 10.1109/LED.2012.2227236.
- [120] He Yan, Zhihua Chen, Yan Zheng, Christopher Newman, and Antonio Facchetti. A high-mobility electron-transporting polymer for printed transistors. *Nature*, 457(7230):679-686, 2009. ISSN: 0028-0836. doi: 10.1038/nature07727.
- [121] Jinhua Li, Zhenhua Sun, and Feng Yan. Solution processable low-voltage organic thin film transistors with high-k relaxor ferroelectric polymer as gate insulator. *Advanced Materials*, 24(1):88-93, 2012. ISSN: 0935-9648. doi: 10.1002/adma.201103542.
- [122] Flora M. Li, Arokia Nathan, Yiliang Wu, and Beng S. Ong. Organic thin-film transistor integration using silicon nitride gate dielectric. *Applied Physics Letters*, 90(13):133514, 2007. ISSN: 0003-6951. doi: 10.1063/1.2718505.
- [123] Sung Hoon Kim, Sun Hee Lee, Youn Goo Kim, and Jin Jang. Ink-Jet-Printed Organic Thin-Film Transistors for Low-Voltage-Driven CMOS Circuits With Solution-Processed AlO_x Gate Insulator. *IEEE Electron Device Letters*, 34(2):307-309, 2013. ISSN: 0741-3106. doi: 10.1109/LED.2012.2228461.
- [124] Xiao Hong Zhang, Shree Prakash Tiwari, Sung Jin Kim, and Bernard Kippelen. Low-voltage pentacene organic field-effect transistors with high-k HfO₂ gate dielectrics and high stability under bias stress. *Applied Physics Letters*, 95(22):223302, 2009. ISSN: 0003-6951. doi: 10.1063/1.3269577.
- [125] Donald A. Neamen. *Semiconductor Physics And Device: Basic Principles*, Fourth Edition. 2012. ISBN: 978-0-07-352958-5.
- [126] Jaeyoung Jang, Se Hyun Kim, Sooji Nam, Dae Sung Chung, and Jae Bon Koo. Hysteresis-free organic field-effect transistors and inverters using photocrosslinkable

poly(vinyl cinnamate) as a gate dielectric. *Applied Physics Letters*, 92(14):143306, 2008. ISSN: 0003-6951. doi: 10.1063/1.2907974.

[127] Jochen Laubender, L. Chkoda, Moritz M. Sokolowski, and Eberhard Umbach. The influence of oxygen and air on the characteristics of organic light-emitting devices studied by in vacuo measurements. *Synthetic Metals*, 111-112:373-376, 2000. ISSN: 0379-6779. doi: 10.1016/S0379-6779(99)00331-8.

[128] Matteo Rapisarda, Daniela Simeone, Guglielmo Fortunato, Antonio Valletta, and Luigi Mariucci. Pentacene thin film transistors with (polytetrafluoroethylene) PTFE-like encapsulation layer. *Organic Electronics*, 12(1):119-124, 2011. ISSN: 1566-1199. doi: 10.1016/j.orgel.2010.10.018.

[129] Lae Ho Kim, Kyunghun Kim, Seonuk Park, Yong Jin Jeong, and Chan Eon Park. Al₂O₃/TiO₂ nanolaminate thin film encapsulation for organic thin film transistors via plasma-enhanced atomic layer deposition. *ACS Applied Materials & Interfaces*, 6(9):6731-6738, 2014. ISSN: 1944-8244. doi: 10.1021/am500458d.

[130] Hsiao-Wen Zan, and Ting-Yu Hsu. Stable Encapsulated Organic TFT With a Spin-Coated Poly(4-Vinylphenol-Co-Methyl Methacrylate) Dielectric. *IEEE Electron Device Letters*, 32(8):1131-1133, 2011. ISSN: 0741-3106. doi: 10.1109/LED.2011.2155026.

[131] Product specification of CYTOP CT-SOLV180, 2014.

[132] Kris Myny, Soeren Steudel, Steve Smout, Peter Vicca, François Furthner, B. Van Der Putten, Anil K. Tripathi, Gerwin H. Gelinck, Jan Genoe, Wim Dehaene, and Paul Heremans. Organic RFID transponder chip with data rate compatible with electronic product coding. *Organic Electronics*, 11(7):1176-1179, 2010. ISSN: 1566-1199. doi: 10.1016/j.orgel.2010.04.013.

[133] Kengo Nakayama, Yuri Hirose, Junshi Soeda, Masahiro Yoshizumi, Takafumi Uemura, Mayumi Uno, Wanyan Li, Myeong Jin Kang, Masakazu Yamagishi, and Yugo Okada. Patternable solution-crystallized organic transistors with high charge carrier mobility. *Advanced Materials*, 23(14):1626-1629, 2011. ISSN: 0935-9648. doi: 10.1002/adma.201004387.

[134] Kenjiro Fukuda, Tomohito Sekine, Daisuke Kumaki, and Shizuo Tokito. Profile Control of Inkjet Printed Silver Electrodes and Their Application to Organic Transistors.

ACS Applied Materials & Interfaces, 5(9):3916-3920, 2013. ISSN: 1944-8244. doi: 10.1021/am400632s.

[135] Soon-Won Jung, Kang-Jun Baeg, Sung-Min Yoon, In-Kyu You, Jong-Keun Lee, Young-Soon Kim, and Yong-Young Noh. Low-voltage-operated top-gate polymer thin-film transistors with high capacitance poly(vinylidene fluoride-trifluoroethylene)/poly(methyl methacrylate) dielectrics. *Journal of Applied Physics*, 108(10):102810, 2010. ISSN: 0021-8979. doi: 10.1063/1.3511697.

[136] F. N. Hooge, T.G.M. Kleinpenning, and Lode K.J. Vandamme. Experimental studies on 1/f noise. *Reports on Progress in Physics*, 44(5):479, 2000. ISSN: 0034-4885. doi: 10.1088/0034-4885/44/5/001.